



UNIVERSITY OF
BIRMINGHAM

Development of Plastic Design Procedures for Stainless Steel Indeterminate Structures

A thesis submitted to University of Birmingham
for the degree of Doctor of Philosophy

By

Georgios Kokosis

Department of Civil Engineering

University of Birmingham

Birmingham B15 2TT

United Kingdom

May 2019

UNIVERSITY OF
BIRMINGHAM

University of Birmingham Research Archive

e-theses repository

This unpublished thesis/dissertation is copyright of the author and/or third parties. The intellectual property rights of the author or third parties in respect of this work are as defined by The Copyright Designs and Patents Act 1988 or as modified by any successor legislation.

Any use made of information contained in this thesis/dissertation must be in accordance with that legislation and must be properly acknowledged. Further distribution or reproduction in any format is prohibited without the permission of the copyright holder.

ABSTRACT

Given the significant environmental impact of the construction industry, drastic improvements in terms of innovation and sustainability of the construction sector are required. To this end, the use of highly sustainable materials and the exploitation of their full potential is of paramount importance and will lead to more efficient utilization of resources and reduced carbon footprint. Stainless steel is gaining increasing usage in the construction industry owing to its excellent corrosion resistance, aesthetic appeal and a combination of favourable structural properties. The high initial material cost warrants the development of novel design procedures, in line with the observed structural response, which fully utilizes its merits and improve cost-effectiveness and sustainability of structural stainless steel design. Due to lack of available experimental data plastic design of stainless steel indeterminate structures is currently not permitted by Eurocode 3: Part 1.4 despite the excellent material ductility and the existence of a Class 1 slenderness limit, thereby compromising design efficiency. This dissertation focuses on the structural behaviour and design of stainless steel continuous beams and portal frames.

A comprehensive experimental study on eight simply supported and four two-span continuous beams employing austenitic and duplex stainless steel rectangular hollow sections (RHS) is reported in this thesis. An FE model was developed and validated against the reported experimental tests. The validated FE models were used to conduct parametric studies, in order

to obtain structural performance data over a range of cross-sectional slendernesses, cross-section aspect ratios, moment gradients and loading and structural arrangements.

The behaviour of stainless steel frames has been investigated based on a comprehensive FE study. As no experimental results on the behaviour of stainless steel frames have been reported to date, experimental tests on pin-ended frames employing cold-formed steel RHS are utilized to validate an FE model. Upon successful replication of the failure modes and overall structural behaviour, parametric studies were conducted to study the effect of key parameters on the ultimate response of stainless steel frames. The parameters investigated involve the material grade used, the degree of static indeterminacy (i.e. whether pin-ended or fixed-ended frames), the cross-section slenderness and the member slenderness. The importance of material strain-hardening at cross-section level, moment redistribution at system level and sway sensitivity/2nd order effects were determined and quantified.

Based on the obtained results, it was concluded that the current Eurocode 3: Part 1.4 approach significantly underestimates the strength of continuous beams and portal frames. This is because the formation of successive plastic hinges and moment redistribution in indeterminate structures with adequate deformation capacity as well as the effect of strain-hardening at cross-sectional level are not accounted for. It is shown that accounting for both strain-hardening and moment redistribution is of paramount importance for design. To this the application of a strain-based design approach, which rationally accounts for local buckling at cross-section level, in conjunction with traditional plastic analysis concepts are extended to the design of stainless steel indeterminate structures.

ACKNOWLEDGEMENTS

The work reported in this thesis was carried out under the supervision of Dr Marios Theofanous, to whom I would like to express my sincere gratitude for his patience, valuable advice and continuous encouragement throughout my postgraduate studies.

I would like also to acknowledge the financial support that received by the Engineering and Physical Sciences Research Council (EPSRC) under grant agreement EP/P006787/1. The experimental work of this project was conducted in the Structures Laboratory of the Department of Civil and Mechanical Engineering, University of Birmingham. I would like to thank the technicians Mark Carter, David Cope and Michael Vanderstam where the completion of the experimental work would not have been possible without their effort. Special thanks are also due to Dr Michaela Gkantou and fellow PhD students Mohamed Elflah and Nikolaos Tziavos for their assistance in the laboratory.

The quiet and inspiring working environment provided by both administrative staff and academic of the Department, in particular Mohamed Elflah, Orhan Yapici, Meshal Almatrafi, Helena Neville, Lydia Hotlom and others has significantly contribute to the successful completion of this research. Special thanks should be extended to Dr Samir Dirar, Dr Pedro Martinez-Vazquez and Prof Charalampos Baniotopoulos for their valuable comments and

vast help on the thesis and Dr Asaad Faramarzi who gave me the opportunity to work on a very interesting project based on Auxetic Reinforced Concrete beyond the scope of the herein presented research.

The patience and the support exhibited by Jacob Frizis, Loizos Liagakis and Prokopis Mountrichas during the last four years is gratefully acknowledge. Special thanks are due to Panagiotis Kallitsas for organizing weekly football games.

Finally, I would like to thank my parents and my fiancée for their unconditional love and support throughout my post graduate studies, without which the completion of this thesis would not have been possible.

CONTENTS

Abstract	ii
Acknowledgements	iv
Contents	vi
Notation	xii
List of figures	xvii
List of tables	xxvi

CHAPTER 1 INTRODUCTION

1.1 Background.....	1
1.2 Aims and objectives.....	3
1.3 Outline of thesis.....	4

CHAPTER 2 LITERATURE REVIEW

2.1 Stainless steel.....	8
2.2 Design of stainless steel structures.....	12
2.2.1 Cross-sectional resistance.....	13
2.2.2 Resistance of indeterminate structures.....	15
2.2.2.1 Influence of second order effects.....	17
2.2.2.2 Influence of strain-hardening.....	19
2.2.3 The Continuous Strength Method (CSM)	20
2.2.3.1 CSM for indeterminate structures.....	24
2.3 Material modelling.....	27
2.4 Corner material properties.....	29
2.5 Numerical modelling.....	30
2.5.1 Type of element.....	31

2.5.2 Material modelling.....	32
2.5.3 Type of analysis.....	33
2.5.4 Imperfections.....	34
2.6 Published experimental data on the response of indeterminate structures.....	36
2.6.1 Carbon and cold-formed steel structures.....	36
2.6.2 Stainless steel structures.....	46
2.7 Knowledge gap.....	50

CHAPTER 3 EXPERIMENTAL TESTS ON STAINLESS STEEL

BEAMS

3.1 Tested cross-sections.....	51
3.2 Tensile coupon tests.....	53
3.3 3-Point bending tests.....	57
3.4 4-Point bending tests.....	59
3.5 Tests on continuous beams.....	60
3.6 Results.....	63
3.6.1 Simply supported beam test results.....	63
3.6.2 Continuous beam test results.....	67

CHAPTER 4 NUMERICAL MODELLING OF STAINLESS STEEL**BEAMS**

4.1 Development of the models.....	70
4.2 Validation of the FE models.....	76
4.2.1 Validation of the FE models against tests by Theofanous et al. (2014)	76
4.2.2 Validation of the FE models against tests by Gkantou et al. (2019).....	82
4.3 Parametric studies.....	87

CHAPTER 5 NUMERICAL INVESTIGATION OF STAINLESS STEEL**PORTAL FRAMES**

5.1 Development of model.....	91
5.1.1 Modelling using beam elements.....	92
5.1.2 Modelling using shell elements.....	96
5.2 Validation.....	104
5.2.1 Beam elements.....	104
5.2.2 Shell elements.....	110

5.3 Parametric Studies.....	115
-----------------------------	-----

CHAPTER 6 DISCUSSION OF RESULTS AND DESIGN

RECOMMENDATIONS

6.1 Design of stainless steel simply supported beams.....	118
6.2 Design of stainless steel continuous beams.....	121
6.3 Behaviour and design of stainless steel frames.....	132
6.3.1 Levels of structural behaviour.....	132
6.3.2 Numerical results and failure modes.....	135
6.3.3 Assessment of design methods without moment redistribution.....	145
6.3.4 Assessment of design methods allowing for moment redistribution.....	155
6.3.5 Design recommendations.....	160

CHAPTER 7 CONCLUSION AND FUTURE RESEARCH

7.1 Conclusions.....	162
7.2 Suggestions for future research.....	164

REFERENCES.....167

**APPENDIX A PLANNED TESTS ON STAINLESS STEEL PORTAL
FRAMES**

A.1 Frame layout.....177

A.2 Connections and base.....181

A.3 Construction sequence.....187

A.4 Instrumentation.....189

NOTATION

A	Cross-sectional area
a_g	Geometric shape factor = W_{pl}/W_{el}
B	Outer cross-section width
b	Internal flat element width
COV	Coefficient of variation
CSM	Continuous Strength Method
E	Young's modulus
$E_{0.2}$	Tangent modulus at 0.2% offset strain
EC	Eurocode
F_{Ed}	Design load on structure
$f_{0.2}$	0.2% proof stress
f_{cr}	Elastic buckling stress
FE	Finite element
F_{coll}	Plastic collapse load

F_{nom}	Nominal stress
F_u	Ultimate load
$F_{u,\text{FE}}$	Predicted ultimate load based on finite element analysis
$F_{u,\text{pred}}$	Predicted ultimate load
f_y	Material yield strength
$f_{y,\text{mill}}$	Mill certificate yield stress
f_p	Proof stress
f_{true}	True stress
f_u	Material ultimate tensile strength
$f_{u,\text{mill}}$	Mill certificate ultimate tensile stress
h	Section height
h_w	Internal web height between flanges
I	Second moment of area
k	Dimensionless strain-hardening parameter
k_c	Curvature
L	Length between centrelines of supports
LC	Load combinations
L_0	Initial length
LVDT	Linear Variable Differential Transformer
MA	Major axis
M_{CSM}	Bending resistance predicted by the CSM

M_{EC3}	Bending resistance predicted by EC3
M_{Ed}	Design bending moment
M_{el}	Elastic moment capacity
M_{hinge}	Bending moment at plastic hinge i
MI	Minor axis
M_{pl}	Plastic moment capacity
M_u	Ultimate test moment capacity
N	Applied load
N_{coll}	Plastic collapse load
N_{CSM}	Compression resistance/collapse load predicted by the CSM
N_{EC3}	Compression resistance/collapse load predicted by the EC3
N_{Ed}	Design axial force
N_u	Ultimate test load
n	Strain hardening exponent used in Ramberg-Osgood model
$n_{0.2,1.0}$	Strain hardening exponent used in Ramberg-Osgood model
PFC	Parallel flange channel
RHS	Rectangular hollow section
R	Rotation capacity
R-O	Ramber-Osgood
r_i	Internal corner radius
SHS	Square hollow section

t	Thickness
t_f	Flange thickness
t_w	Web thickness
COV	Coefficient of variation
CSM	Continuous strength method
W_{el}	Elastic section of modulus
W_{pl}	Plastic section modulus
α_{cr}	Factor by which a set of loads acting on a structure has to be multiplied to cause elastic instability of a structure in a global sway mode
α_p	Factor by which a set of loads acting on a structure has to be multiplied to cause the formation of a plastic collapse mechanism based on a rigid plastic analysis
α_u	Factor by which set of loads acting on a structure has to be multiplied to cause the formation of a plastic collapse mechanism based on a rigid plastic analysis and allowing for second order effects
ε_e	Elastic strain
ε_f	Plastic strain at fracture
ε_{hinge}	Strain at hinge i
ε_{nom}	Nominal strain
ε_{ln}^{pl}	Log plastic strain
ε_p	Plastic strain
$\bar{\lambda}_p$	Plate slenderness
θ	Rotation of a cross section

θ_i	Rotation at hinge i
θ_{pl}	Elastic rotation at the plastic moment
θ_{rot}	Total rotation upon reaching the plastic moment on the unloading path
θ_u	Total rotation at plastic hinge when the moment-rotation curve falls back below M_{pl}
κ_{pl}	Elastic part of total curvature at midspan when M_{pl} is reached on the ascending branch
$\bar{\lambda}$	Non-dimensional slenderness
$\bar{\lambda}_p$	Non-dimensional local plate slenderness
ν	Poisson's ratio
ρ	Reduction factor due to local buckling
σ_{cr}	Elastic critical buckling stress of plate element
σ	Stress
σ_{nom}	Engineering stress
σ_{true}	True stress
σ_u	Ultimate tensile stress
$\sigma_{u,mill}$	Ultimate tensile stress as given in the mill certificate
$\sigma_{0.2}$	Proof stress at 0.2% offset strain
$\sigma_{0.2,mill}$	Proof stress at 0.2% offset strain as given in the mill certificate
$\sigma_{1.0}$	Proof stress at 1.0% offset strain
$\sigma_{1.0,mill}$	Proof stress at 1.0% offset strain as given in the mill certificate

LIST OF FIGURES

Fig. 2.1: Stress-strain curves for typical stainless steel and carbon steel grades.....	12
Fig. 2.2: Plastic hinge at the mid-span of a simply supported beam.....	16
Fig. 2.3: Second-order effects.....	18
Fig. 2.4: Bilinear elastic-strain hardening material model.....	24
Fig. 2.5: Plastic collapse mechanism for two-span continuous beam.....	25
Fig. 2.6: Corner properties extended to a distance t	32
Fig. 2.7: Corner properties extended to a distance $2t$	32
Fig. 2.8: Mitutoyo Coordinate Measuring Machine.....	35
Fig. 2.9: M_u/M_{el} versus $b/t\epsilon$ for assessment of Class 3.....	39
Fig. 2.10: M_u/M_{pl} versus $b/t\epsilon$ for assessment of Class 2.....	39

Fig. 2.11: Rotation capacity versus $b/t\epsilon$ for assessment of Class 1.....	40
Fig. 2.12: Definition of rotation capacity from moment-rotation graphs.....	40
Fig. 2.13: Rotation capacity R versus web slenderness λ_w for AISC 4100 Class 1 limit.....	41
Fig. 2.14: Rotation capacity R versus web slenderness λ_w for AS 4100 Class 1 limit.....	42
Fig. 2.15: Rotation capacity R versus web slenderness λ_w for Eurocode 3 Class 1 limit.....	42
Fig. 2.16: Theoretical collapse mode shapes.....	44
Fig. 2.17: Layout of portal frames.....	45
Fig. 2.18: Layout of frame tests.....	46
Fig. 3.1: Locations of flat and corner coupons.....	54
Fig. 3.2: Stress – strain curves of the tensile coupons (100×50×3-D and 100×50×2).....	55
Fig. 3.3: Flat and corner tensile coupons.....	56
Fig. 3.4: Schematic 3-point bending test arrangement and instrumentation (dimensions in mm).....	58

Fig. 3.5: Overall setup for 3-point bending tests.....	58
Fig. 3.6: Schematic 4-point bending test arrangement and instrumentation (dimensions in mm).....	59
Fig. 3.7: Overall setup for 4-point bending tests.....	60
Fig. 3.8: Schematic continuous beam test arrangement and instrumentation (dimensions in mm).....	62
Fig. 3.9: Overall setup for continuous beams.....	62
Fig. 3.10: Normalized moment-rotation and moment-curvature response.....	64
Fig. 3.11: Failure modes of 3-point bending and 4-point bending tests.....	65
Fig. 3.12: Load – displacement continuous beam tests	68
Fig. 3.13: Normalized force-end-rotation continuous beam tests.....	69
Fig. 3.14: Evolution of support to span moment ratio with increasing displacement.....	69
Fig. 4.1: Engineering stress-strain and true stress-log plastic curves.....	72
Fig. 4.2: Mesh configuration.....	74
Fig. 4.3: Buckling mode shape for 3-point bending beam.....	75

Fig. 4.4: Buckling mode shape for continuous beam.....	76
Fig. 4.5: Normalised moment-rotation curves for the section 60×60×3.....	77
Fig. 4.6: Normalised moment-rotation curves for the section 60×40×3- MI.....	78
Fig. 4.7: Comparison between experimental and numerical failure modes for three-point bending tests.....	79
Fig. 4.8: Load – mid-span displacement response for the section 60×40×3- MI.....	81
Fig. 4.9: Load – mid-span displacement response for the section 60×60×3.....	81
Fig. 4.10: Comparison between experimental and numerical failure modes for continuous beams with point loads applied at mid-span and at one third from the centre span	82
Fig. 4.11: Normalised moment-rotation curves for the section 150×50×2 3-point bending test.....	84
Fig. 4.12: Normalised moment-rotation curves for the section 150×50×5 4-point bending test.....	84
Fig. 4.13: Load – mid-span displacement response for the section 150×50×3 –D Continuous beam.....	85

Fig. 4.14: Comparison between experimental and numerical failure modes for simply supported and continuous beams.....	85
Fig. 4.15: Load cases considered in the parametric studies (LC1 to LC5).....	88
Fig. 4.16: Additional load cases considered in the parametric studies.....	89
Fig. 5.1: Position of applied loads (dimensions in mm).....	95
Fig. 5.2: Frame sway mode shape.....	96
Fig. 5.3: Profile cut of cross sections at knee joints.....	97
Fig. 5.4: Extended corner material properties.....	98
Fig. 5.5: Kinematic coupling applied at column bases.....	99
Fig. 5.6: Lateral restrain.....	99
Fig. 5.7: Tie constrain.....	100
Fig. 5.8: RHS mesh configuration.....	101
Fig. 5.9: Knee joint and apex joint connection plates mesh configurations.....	101
Fig. 5.10: Local buckling mode shapes.....	103
Fig. 5.11: Frame sway mode shape.....	104

Fig. 5.12: Vertical load – vertical displacement apex for Frame	
1.....	105
Fig. 5.13: Vertical load – horizontal displacement at North knee joint for Frame	
1.....	106
Fig. 5.14: Vertical load – vertical displacement apex for Frame	
2.....	106
Fig. 5.15: Vertical load – horizontal displacement at North knee joint for Frame	
2.....	107
Fig. 5.16: Vertical load – vertical displacement apex for Frame	
3.....	107
Fig. 5.17: Vertical load – horizontal displacement at North knee joint for Frame	
3.....	108
Fig. 5.18: Comparison between experimental and numerical failure mode for Frame	
3.....	109
Fig. 5.19: Vertical load – vertical displacement apex for Frame	
1.....	111
Fig. 5.20: Vertical load – horizontal displacement at North knee joint for Frame	
1.....	111
Fig. 5.21: Vertical load – vertical displacement apex for Frame	
2.....	112

Fig. 5.22: Vertical load – horizontal displacement at North knee joint for Frame 2.....	112
Fig. 5.23: Vertical load – vertical displacement apex for Frame 3.....	113
Fig. 5.24: Vertical load – horizontal displacement at North knee joint for Frame 3.....	113
Fig. 5.25: Comparison between experimental and numerical failure mode for Frame 3.....	114
Fig. 5.26: Loading arrangement adopted in the parametric studies.....	116
Fig. 6.1: Assessment of the Eurocode Class 2 slenderness limits for internal elements in compression.....	120
Fig. 6.2: Assessment of the Eurocode Class 1 slenderness limits for internal elements in compression.....	121
Fig. 6.3: F_{pred}/F_u against the $\bar{\lambda}_p$ for the four design methods for LC1.....	128
Fig. 6.4: F_{pred}/F_u against the $\bar{\lambda}_p$ for the four design methods for LC3.....	129
Fig. 6.5: F_{pred}/F_u against the $\bar{\lambda}_p$ for the four design methods for LC4.....	129

Fig. 6.6: F_{pred}/F_u against the $\bar{\lambda}_p$ for the four design methods for LC1.1.....	130
Fig. 6.7: F_{pred}/F_u against the $\bar{\lambda}_p$ for the four design methods for LC2.1.....	130
Fig. 6.8: F_{pred}/F_u against the $\bar{\lambda}_p$ for the four design methods for LC2.....	131
Fig. 6.9: F_{pred}/F_u against the $\bar{\lambda}_p$ for the four design methods for LC5.....	132
Fig. 6.10: Failure modes for frames employing slender (top) and stocky (bottom) beam- columns.....	136
Fig. 6.11: Combined plastic mechanism of a pin-ended frame.....	137
Fig. 6.12: Accuracy of design methods not allowing for moment redistribution as a function of a_{cr}	154
Fig. 6.13: Accuracy of design methods allowing for moment redistribution as a function of a_{cr}	159
Fig. A.1: Portal frames layout (dimensions in mm).....	179
Fig. A.2: Overall setup for portal frames (dimensions in mm).....	180
Fig. A.3: Location of connections.....	182
Fig. A.4: Cut requirements for beams (dimensions in mm).....	182

Fig. A.5: Cut requirements for columns (dimensions in mm).....	183
Fig. A.6: Base plate connection (dimensions in mm).....	184
Fig. A.7: 300×100 steel channels.....	184
Fig. A.8: Column to sleeve arrangement.....	185
Fig. A.9: Loading plate arrangement (dimensions in mm).....	186
Fig. A.10: Butt welds.....	187
Fig. A.11: Column base arrangement.....	188
Fig. A.12: Connection of the spreader beam to portal frames.....	189
Fig. A.13: Location of strain gauges, LVDTs and inclinometers (dimensions in mm).....	190

LIST OF TABLES

Table 2.1: Simply supported, continuous beams and frame tests for carbon steel.....	37
Table 2.2: Simply supported and continuous beam tests for stainless steel.....	47
Table 2.3 Assessment of design methods for continuous beams allowing for plastic design.....	48
Table 3.1: Mean measured dimensions of tested cross-sections.....	53
Table 3.2: Tensile coupon test results.....	54
Table 3.3: Material properties.....	57
Table 3.4: Key experimental results from 3-point and 4-point bending tests.....	66
Table 3.5: Key results from continuous beam tests.....	68
Table 4.1: Ratios of the numerical ultimate moments over the experimental ultimate moments.....	78

Table 4.2: $F_{u,FE}/F_{u,test}$ for the imperfection amplitudes considered.....	80
Table 4.3: Validation of FE models against the test results.....	83
Table 4.4: Material properties.....	88
Table 4.5: Material properties.....	89
Table 5.1: Cross section geometries for portal frame tests.....	93
Table 5.2: Horizontal load for each portal frame test.....	95
Table 5.3: Material properties.....	97
Table 5.4: $F_{u,FE, beam elements}/F_{u,test}$ for the imperfection amplitudes considered.....	109
Table 5.5: $F_{u,FE}/F_{u,test}$ for frames discretised with shell and beam elements.....	114
Table 5.6: Frame variation considered in the parametric studies.....	117
Table 6.1: Assessment of design methods for simply supported beams.....	120
Table 6.2: Assessment of design methods for plastic design of stainless steel continuous beams – experimental results.....	123
Table 6.3: Assessment of design methods for plastic design of stainless steel continuous beams – numerical results.....	126

Table 6.4: Design parameters for various levels of response and design methods.....	135
Table 6.5: Plastic mechanism for the support conditions and load patterns considered.....	137
Table 6.6: Key design parameters for fixed-based frames.....	140
Table 6.7: Key design parameters for pinned-based frames.....	142
Table 6.8: Assessment of design methods without moment redistribution for fixed-based frames	147
Table 6.9: Assessment of design methods without moment redistribution for pinned-based frames.....	150
Table 6.10: Assessment of design methods allowing for moment redistribution	156
Table A.1: Section sizes and plates for each frame.....	186

CHAPTER 1

INTRODUCTION

1.1. BACKGROUND

Stainless steel is a sustainable and novel construction material that can be utilized in a range of structural applications due to its favourable structural properties. In addition to its high stiffness, strength and ductility it possesses high durability, which makes it an ideal solution for exposed structural elements in aggressive environments, since it eliminates the need for a protective coating (Baddoo, 2008; Gedge, 2008). The key characteristic of stainless steel from a metallurgical viewpoint is that contains a minimum of 10.5% chromium, which provides stainless steel with a thin layer of chromium oxide that protects it from corrosion, which builds on the external surface of stainless steel and can heal itself if damaged (BSSA, 2004). As result of its excellent corrosion resistance stainless steel reduces the cost of maintenance and repair over the life-cycle of building components (Gardner et al., 2007). Therefore, life-cycle costing and sustainability considerations (Rossi, 2014) make stainless steels more attractive

when cost is considered over the full life of the project, due to the minimum maintenance required and the high potential to recycle or reuse the material at the end of life of the project.

The exploitation of the inelastic range of the material's stress-strain curve is of high importance for the design of stocky sections, where high deformations develop prior to the occurrence of local buckling, contrary to slender sections which will fail at stresses lower than the material's nominal yield stress. Based on the European structural design codes for carbon steel (EN 1993-1-1+A1, 2014) and stainless steel (EN 1993-1-4+A1, 2015) four behavioural classes of cross-sectional response are defined, based on the susceptibility of the cross-sections to local buckling as determined by comparing the width to thickness ratio of the most slender cross-section element to specified slenderness limits. According to EN 1993-1-1, indeterminate carbon steel structures which are classified as Class 1, are assumed to have sufficient deformation capacity to permit plastic design to be applied, i.e. the cross-sections that are classified as Class 1 are assumed able to undergo large inelastic rotations without a loss of strength to permit moment redistribution to occur and a mechanism to develop.

Contrary, EN 1993-1-4 does not allow the application of plastic design for stainless steel structures, despite their excellent material ductility (Gardner, 2005) and the existence of Class 1 in the relevant design standard (EN 1993-1-4+A1, 2015). This is arguably due to lack of available test data at the time when the design codes were drafted or revised. Deficiencies in current design guidance put stainless steel at a disadvantage compared to other metallic materials thereby hindering its use in applications where it might be the optimal solution.

1.2. AIM AND OBJECTIVES

This thesis aims at addressing a gap in current knowledge and to provide long overdue technical performance data on the plastic behaviour of stainless steel indeterminate structures. The focus lies on stainless steel tubular (i.e. SHS and RHS) cross-sections as they are the most commonly used in the construction industry. The findings of this thesis will inform the next generation of relevant design standards thus enabling designers to make informed decisions when selecting a structural material for a given project and promoting the use of stainless steel in construction with profound economic and environmental benefits. It is envisaged that the developed plastic design procedures will be incorporated in future revision of EN1993-1-4.

To achieve the above mentioned research aim, the following list of objectives has been set:

1. Obtain materials properties of austenitic and duplex stainless steel material via coupon tests to facilitate subsequent analysis of member and system tests.
2. Experimental testing of simply supported stainless steel beams to obtain the cross-sectional response for a range of cross-section slenderness.
3. Experimental testing on continuous stainless steel beams to obtain the effect of cross-section slenderness on the potential of moment redistribution in indeterminate structures.
4. Develop and validate Finite Element model for stainless steel continuous beams against published tests data in addition to the experimental data obtained as part of this study.
5. Study the ultimate response of various configurations on continuous beams via a comprehensive Finite Element parametric study for a wide range of cross-section slenderness, cross-section aspect ratios and structural configurations.

6. Assess the adequacy of existing Class 1 limits specified in EN 1993-1-4, based on the generated Finite Element and experimental results.
7. Validate Finite Element model for stainless steel portal frames against relevant experimental data.
8. Study the ultimate response of stainless steel frames via a comprehensive Finite Element parametric study considering the effect of static indeterminacy and of cross-sectional, member and frame slenderness on the moment redistribution and ultimate load.
9. Assess codified design equations for sway sensitive frames on the basis of the numerical results.
10. Develop design procedures for stainless steel indeterminate structures, accounting for both strain-hardening at cross-sectional level and moment redistribution as well as 2nd order effects where relevant.

1.3. OUTLINE OF THESIS

In this chapter, the novelties of stainless steel as a construction material, together with its applications are briefly introduced. Moreover, the drawbacks of the current European structural stainless steel design specifications EN 1993-1-4 +A1 (2015) are outlined.

In Chapter 2, a literature review that is relevant to the present thesis is provided. The review contains a brief introduction on stainless steel grades and a comparison of their structural merits against those of conventional carbon steel. Furthermore, the structural steel design

specifications (EN 1993-1-1+A1, 2014; EN 1993-1-4+A1, 2015) together with their inability to allow for strain-hardening in strength calculations are presented. An outline of the Continuous Strength Method (CSM), its benefits and its extension to allow for moment redistribution in a similar way with the traditional plastic analysis procedure is provided. Moreover, important topics including laboratory testing, material modelling and finite element (FE) modelling of both carbon steel and stainless steel continuous beams and portal frames are introduced.

Once the most significant parameters pertinent to the plastic response and design of stainless steel indeterminate structures were identified, a comprehensive laboratory testing program, involving tensile coupon tests on flat and corner material, and a series of 3 Point bending, 4 Point bending and continuous beam tests of cold-formed rectangular hollow sections (RHS), was conducted as presented in Chapter 3. A full account of the employed experimental setup and instrumentation as well as key experimental results are reported. These include the ratio of the ultimate moment to the elastic and plastic moment resistance (M_u/M_{el} and M_u/M_{pl} respectively) and the rotation capacity R for the simply supported beam tests, and the experimental load at collapse F_u , the vertical displacement δ_u , the end-rotation of the most heavily loaded span θ_u at collapse and the theoretical plastic collapse load F_{coll} for the continuous beam tests.

In Chapter 4, nonlinear finite element models employing shell elements were developed and validated against the laboratory test results reported in Chapter 3 and the fifteen test results reported by Theofanous et al., (2014). After, the successful replication of the experimental results, parametric studies were carried out to expand the available structural performance

data for various geometric parameters, such as cross-sectional slenderness, cross section aspect ratio, moment gradient and loading and structural arrangements, and to assess existing design codes (EN 1993-1-4+A1, 2015) and design recommendations for the design of stainless steel continuous beams employing tubular cross-sections of varying slenderness.

Similar to Chapter 4, Chapter 5 reports a comprehensive FE study (geometrically and materially nonlinear imperfection analysis - GMNIA) on stainless steel frames with pinned and fixed bases. The suitability of the use of both beam elements, widely available in most design consultancies, and shell elements, mainly used by researchers, and the effect on the accuracy of the results is investigated. Due to the absence of any experimental tests on stainless steel frames, test data on frames made of other metallic materials were sought in the published literature for the validation of the numerical models. The most relevant test data were deemed to be the three tests on pinned-based portal frames employing cold-formed steel RHS reported by Wilkinson and Hancock (1999), as they were reported in sufficient detail to allow their numerical replication and they employed the same cross-section shape (RHS) and a material exhibiting similarities with stainless steel in terms of non-linear stress-strain response and absence of a yield plateau. Upon successful validation against these three experimental tests, parametric studies were conducted to study the ultimate response of stainless steel portal frames and investigate the combined effects of i) material strain-hardening, ii) cross-section slenderness, iii) moment redistribution and iv) second-order effects (i.e. frame sway) on the ultimate load carrying capacity.

In chapter 6, the design methods related to the performance and design of stainless steel simply supported, continuous beams and portal frames are discussed. In more detail, the conventional

Eurocode methodology based on an elastic-perfectly plastic material idealisation with or without moment redistribution, and the Continuous Strength Method (CSM) with or without allowing for moment redistribution were revisited and compared. The well-established Merchant-Rankine equation in conjunction with a modified CSM for indeterminate structures is proposed as a versatile design methodology for the incorporation of second order effects, strain-hardening at cross-sectional level and moment redistribution at system level in the design of stainless steel frames.

Chapter 7, conclusions are summarised and a methodology for plastic design of indeterminate stainless steel structures is proposed. Furthermore, suggestions for future research on stainless steel portal frames and stainless steel connections are presented, in order to promote the more widespread utilization stainless steel in construction.

Finally, Appendix A gives an overview of a series of tests that were planned for stainless steel frames, which were however not conducted due to laboratory related restrictions. Although unfinished, the planned tests took significant time and energy and have been included in the thesis as a guidance for future research.

CHAPTER 2

LITERATURE REVIEW

2.1. STAINLESS STEEL

Carbon steel is composed of iron (Fe) and other elements which are used in steelmaking, such as carbon (C), manganese (Mn) and silicon (Si). Stainless steel is a type of steel containing a minimum of 10.5% chromium. Due to the addition of chromium into the steel a formation of a thin, self-repairing layer of chromium oxide (Cr_2O_3) takes place on the surface of the steel. This layer varies in thickness from 1-10 nanometers and it is responsible for the ability of the steel to resist corrosion. As the film is stable and non-porous, the steel cannot react further with the oxygen in the atmosphere, thus the passive layer protects it from oxidation. There are three factors that determine the stability of passive layer; the composition of the steel, its surface treatment and last but not least the corrosive nature of its environment (ESDEP, 1997; Euro Inox, 2006). Hence different stainless steel grades have different corrosion resistance characteristics in different environment.

The grades of structural stainless steel vary according to their microstructure and alloying elements thus resulting in differences in terms of strength, ductility, weldability, toughness and the level of corrosion resistance. The grades of stainless steel can be classified into the following five basic groups:

i. Austenitic stainless steel

This type of stainless steel it is based on 17-18% of chromium and 8-11% of nickel additions. Also, austenitic stainless steel has a modified crystal structure in comparison with the carbon steel. Due to the above features, austenitic stainless steel except from exceptional corrosion resistance, has high ductility, it is readily weldable and is adaptably cold forming. Furthermore, its corrosion resistance can be improved with the addition of molybdenum. Also, it can be strengthened by cold forming and has advanced toughness over a wide range of temperatures in comparison with the other steel grades (ESDEP, 1997).

ii. Ferritic stainless steel

Ferritic stainless steel has a chromium content of 10.5-18% and contains less nickel in comparison with the austenitic. Also, it has the same atomic structure with carbon steel, which leads to reduced ductility, reduced formability and reduced corrosion resistance than austenitic grade. Furthermore, ferritic stainless steel similarly to austenitic can be strengthened by cold forming and not by heat treatment, whilst it is also strongly magnetic, a property that it less pronounced in austenitic stainless steel (ESDEP, 1997).

iii. Duplex stainless steel

Duplex stainless steels typically, contain 21-26% chromium, 4-8% nickel and 0.1-4.5% molybdenum additions. Duplex stainless steel can offer very high strength (higher than the austenitic stainless steel) and decent corrosion resistance (inferior to the one offered by austenitic grades). Similarly to austenitic and ferritic, duplex stainless steel cannot be strengthened by heat treatment but only by cold working (ESDEP, 1997). Recent addition to the duplex stainless steel family are the lean duplex stainless steel grades (EN 1.4162 and EN 1.4362) which contain a small quantity of nickel, approximately 1.5%. Therefore, both the initial material cost and cost fluctuation are reduced. Although it has low nickel content, lean duplex stainless steel displays a good combination of corrosion resistance, fatigue resistance and strength together with adequate weldability (Theofanous and Gardner, 2010).

iv. Martensitic stainless steel

Martensitic stainless steel has a mixed microstructure to ferritic and carbon steel. Due to its high carbon content, martensitic can be strengthened by heat treatment contrary with the above grades of stainless steel. The ductility of martensitic stainless steel is more limited than the above stainless steel grades and its corrosion resistance is similar to ferritic stainless steel. Martensitic stainless steels are not readily weldable due to the high carbon content and require pre-heat treatment and post weld heat treatment to produce welds of adequate ductility. Due to their low ductility and difficulties in welding, martensitic stainless steels are not used in construction (ESDEP, 1997).

v. Precipitation hardened stainless steel

The precipitation hardening stainless steels (PH) also called as age hardening are chromium 17% and nickel 4% containing steels. Precipitation hardening steel can be strengthened to high level by heat treatment but no as high as martensitic stainless steel, due to its lower content of carbon steel. It is also characterized of very high tensile strength and toughness, and it is mainly used in aerospace industry and for certain heavy-duty connections in buildings. Moreover, it should be mentioned that precipitation hardening steel has better corrosion performance than martensitic and ferritic stainless steel and very similar to austenitic grades. Like martensitic stainless steels, precipitation hardening stainless steels are not used in the construction industry (ESDEP, 1997).

Fig. 2.1 depicts the strain curve for a typical carbon steel and typical stainless steel alloys. It can be observed that carbon steel displays a linear elastic behaviour up to the yield stress, followed by plateau and then by a strain hardening region til failure. Contrary a more rounded response with no well-defined yield stress is observed for the stress-strain curve of the stainless steel. Moreover, as it is stated on Fig. 2.1 a conventional yield point is defined for stainless steel as the 0.2% proof strength, which is used as the nominal yield strength for structural stainless steel design (Euro Inox, 2006) to maintain consistency with conventional carbon steel design guidance.

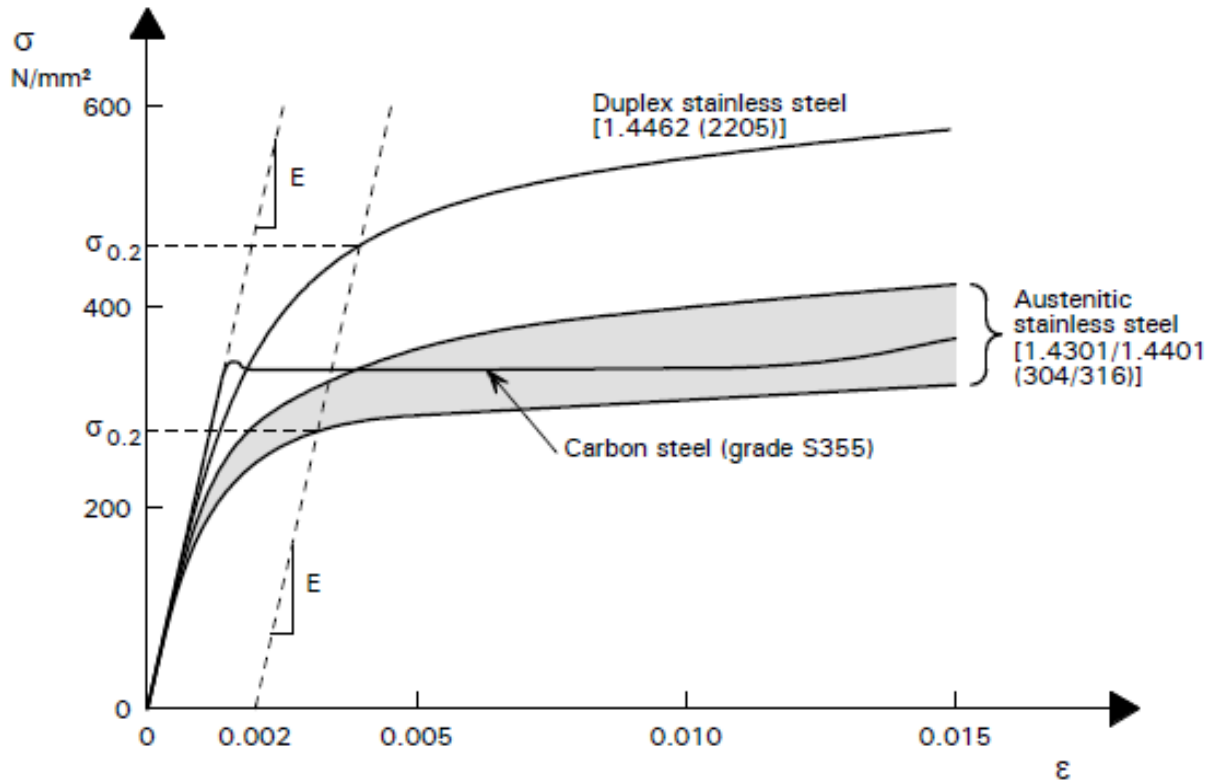


Fig. 2.1: Stress – strain curves for typical stainless steel and carbon steel grades (BSSA)

2.2. DESIGN OF STAINLESS STEEL STRUCTURES

The design of stainless steel structures is covered by a number of international design codes (EN 1993-1-4+A1, 2015; AS/NZS 4673, 2001; SELASCE 8-02, 2002; AISC Design Guide 27, 2013), which have either recently been introduced (AISC Design Guide 27, 2013) or are currently being amended (EN 1993-1-4+A1, 2015; AS/NZS 4673, 2001; SELASCE 8-02, 2002) in light of recent experimental tests, thus indicating the worldwide interest stainless steel has received in recent years. Despite the absence of a well-defined yield stress, all current design standards for stainless steel adopt an equivalent yield stress and assume bilinear (elastic, perfectly-plastic) behaviour for stainless steel as for carbon steel in an attempt to maintain consistency with traditional carbon steel design guidance. Neglecting the significant

strain-hardening inherent in stainless steel has been shown to lead to overly conservative design, particularly for stocky stainless steel components (Rasmussen and Hancock, 1993; Gardner and Nethercot, 2004; Young and Lui, 2005; Zhou and Young, 2005; Zhao et al., 2015). It should be stated that in this thesis emphasis is given to EN 1993-1-4+A1 (2015).

As the focus of this thesis is on the design of stainless steel indeterminate structures employing tubular members, the cross-sectional resistance and the system resistance of indeterminate structures is discussed in detail below. No discussion on member resistance (i.e. member buckling) is provided since tubular members are not prone to lateral torsional buckling (LTB), hence the discussion would be pointless for continuous beams, whilst the effect of member buckling on the beam-columns of frames is explicitly considered via the GMNIA via the incorporation of member imperfections in addition to the system and cross-sectional imperfections.

2.2.1. Cross-sectional resistance

Four behavioural classes are defined in EN 1993-1-4+A1 (2015), in order to account for the effect of local buckling on the moment resistance and rotation capacity of steel cross-sections. EN 1993-1-4+A1 (2015) does not allow explicitly for strain-hardening in strength calculations, although strain-hardening is implicitly relied upon e.g. to reach the plastic moment resistance M_{pl} at finite strains. This approach mimics the one adopted by EN 1993-1-1+A1 (2014) for structural steel cross-sections.

For the design of slender sections, which are expected to fail in the elastic region of the material response, traditionally the effective width concept pioneered by Von Karman (1932) and further developed by Winter (1947), is adopted as the main design methodology in most international design codes (EN 1993-1-4+A1, 2015; AS/NZS 4673, 2001; SEI/ASCE 8-02, 2002; AISC Design Guide 27, 2013). The effective width concept stipulates that part of the plated cross-sectional elements subjected to compression or bending are ineffective, whilst in the remaining effective parts, the width of which is determined as a function of their slenderness, stresses can reach the nominal yield stress. An alternative design approach termed the Direct Strength Method (DSM) was pioneered by Schafer and Pekoz (1998) as a rational means to design slender members of complex cross-sectional geometry accounting for the effect of element interaction and considering all possible buckling modes. The fundamental idea of the DSM is that, the strength of a member can be directly determined, if all the elastic critical stresses associated with the buckling modes of local, distortional and member buckling and the load that causes the section to yield are determined (Schafer, 2008). The method has been validated against numerous experimental results on cold-formed steel sections and is able to account for interaction between the various buckling modes. Another advantage of the method is the elimination of the tedious effective properties calculation for slender sections, whilst a disadvantage is that it necessitates the use of software like CUFSM (Li and Schafer, 2010) to obtain the elastic critical buckling stresses.

Several design approaches that allow for the effect of strain-hardening on the response of stocky steel cross-sections have been proposed. Kemp (2002) proposed a design approach for I-sections, which takes into consideration strain-hardening and permits the determination of moment capacities up to 8% higher than the plastic moment resistance on the basis of bi-linear

moment-curvature relationship. The critical curvature at which failure occurs can be determined as a function of steel properties and local and lateral buckling slenderness (Kemp, 2002), thereby explicitly considering interaction between flange local buckling, web local buckling and lateral torsional buckling. A few years later, the resistance of class 3 sections in bending was studied (Lechner et al., 2008); it was proposed that part of the plastic capacity can be exploited for Class 3 sections, depending on how close the slenderness of the Class 3 elements is to the Class 2 and Class 3 slenderness limits. In 2008 Lechner proposed a linear transition from Class 2 to Class 4.

The most recently proposed design approach for the design of stocky sections allowing for strain-hardening was developed initially for stainless steel hollow sections by Gardner and Nethercot (2004), expanded to carbon steel (Gardner, 2008; Liew and Gardner, 2015), aluminum alloy and high strength steel structures (Gardner and Ashraf, 2006) and further developed to allow for element interaction by Theofanous and Gardner (2012). The current version of the method (Afshan and Gardner, 2014) has been adopted by the Design Guide 27: Structural Stainless Steel AISC (2013). This method is excessively utilized in this project, which aims to expand it to indeterminate stainless steel structures and therefore it is discussed in detail in Section 2.2.3.

2.2.2. Resistance of indeterminate structures

Structural steel due to its high ductility is able to withstand considerable deformation beyond the elastic limit, without fracture. According to EN 1993-1-1+A1 (2014), plastic design is permitted for indeterminate carbon steel structures which are classified as Class 1. Plastic

analysis is based on the successive formation of plastic hinges throughout the structure, which are assumed to be able to maintain their plastic moment resistance whilst rotating, thus allowing moment redistribution within the structure. A plastic hinge is a yielded zone where an infinite rotation is assumed to occur at a constant plastic moment M_p of the section. The formation of plastic hinges leads to progressive reduction in stiffness of the structure and to a possible collapse when a mechanism is formed. In case where a point load is applied at the center of a simply supported beam, the maximum strain will take place at the midspan where a plastic hinge will be formed (Fig. 2.2) (Owens, 1994).

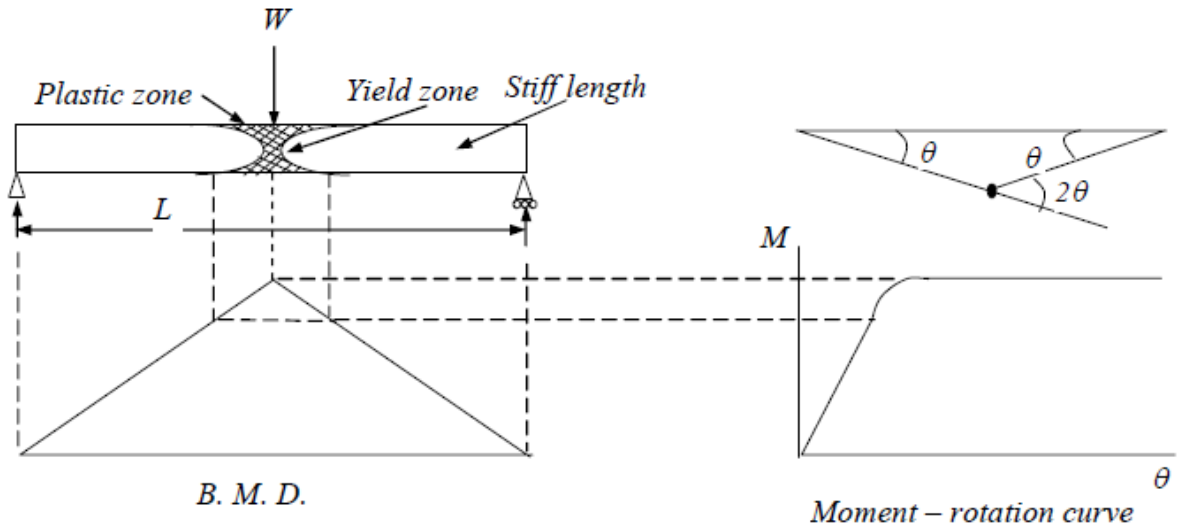


Fig. 2.2: Plastic hinge at mid-span of a simply supported beam (Owens, 1994)

Therefore, with the use of the plastic analysis method the ultimate capacity at which a plastic collapse mechanism first forms can be calculated. The plastic analysis method requires three conditions to be satisfied: equilibrium, mechanism and plasticity. The first condition (static equilibrium) means that equilibrium needs to be achieved between the externally applied loads and the internal forces and moments that resist those loads. The term mechanism means that when the ultimate plastic load is reached, sufficient number of plastic hinges has formed in a

kinematically admissible manner and the structure is no longer stable. Finally, the plasticity condition stipulates that at no point within the structure stresses higher than the yield stress are permitted, which for beam elements means that the full plastic moment capacity of the section should not be exceeded.

For the calculation of the plastic collapse load either the static, based on the lower bound theorem, or the kinematic method, based on the upper bound theorem can be used (Bruneau et al., 1998). Commonly the kinematic method is used, which assumes that the plastic deformation is restricted to discrete hinges and that rigid links exist between these hinges, which are assumed to remain undeformed, i.e. the elastic deformations are ignored. The virtual work method is invoked based on which the internal energy dissipated at the plastic hinges is equated to the work done by the external loads. Since the kinematic method is based on the upper bound theorem, all possible mechanisms have to be examined and the one with the lowest collapse load is the critical one.

2.2.2.1. Influence of second order effects

The main difference between frames and continuous beams is that the frames are potentially sensitive to second order effects. The linear analysis, also known as first order analysis does not take into account any changes into the geometry during the loading process, where in reality there will always be changes in geometry which could lead to a collapse load either exceeding or failing short of the predicted load calculated during the linear analysis (Wood, 1958). The geometric nonlinearities (second order effects) may result either from effects which are caused from deflections within the length of members $P-\delta$ or effects which are

based on displacements of the overall frame P- Δ (Trahair et al., 2008). For a better understanding of the distinction between deflections that arise within the length of a member and the displacements of the overall structure the Fig. 2.3 is illustrated further below. In accordance with the EN 1993-1-1+A1 (2014) the parameter α_{cr} , which is the critical factor by which the design loading would have to be increased to cause elastic instability of the frame, needs to be checked against the provided limiting values. In case, where α_{cr} is larger than 10 or 15 for elastic analysis or plastic analysis respectively, second order effects do not need to be considered, as they are deemed sufficiently small and can be ignored. The parameter α_{cr} is given by Eq. 1 (EN 1993-1-1+A1, 2014):

$$\alpha_{cr} = \frac{F_{cr}}{F_{Ed}} \quad (1)$$

where F_{cr} is the elastic critical buckling load for global sway instability based on initial elastic stiffness and F_{Ed} is the design loading acting on the structure.

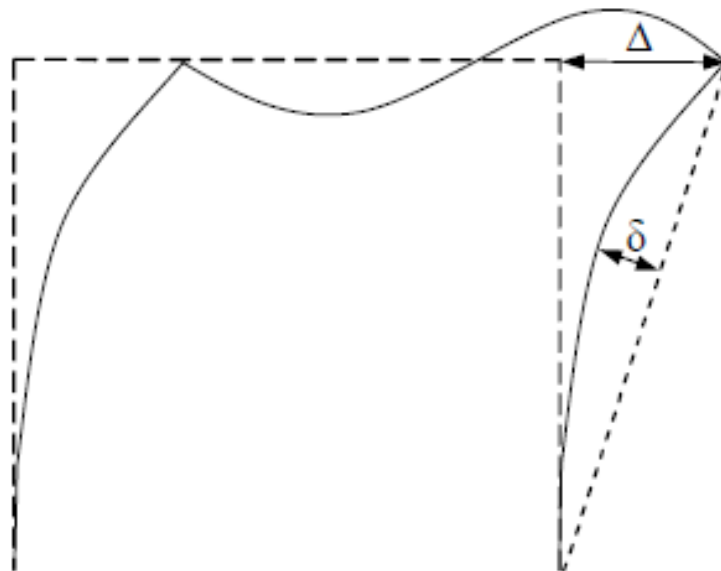


Fig. 2.3: Second-order effects (Wang, 2011)

In cases where α_{cr} is smaller than the limiting value for elastic or plastic analysis (10 and 15 respectively), the effects of the deformed geometry on the structural response have to be considered either by conducting a geometrically nonlinear analysis, in which the load is applied incrementally and the deformed geometry is explicitly considered, or by amplifying the bending moments obtained from 1st order analysis by the amplification factor given by Eq. 2:

$$k_{amp} = \frac{1}{1 - \frac{1}{\alpha_{cr}}} \quad (2)$$

To account for the combined effects of deformed geometry and moment redistribution where $\alpha_{cr} < 15$, the well-established Rankine equation (Eq. 3) can be used which gives the inverse of the ultimate collapse load factor α_u as a sum of the inverse of the plastic collapse load factor α_p obtained from traditional plastic analysis and the inverse of the critical load factor α_{cr} :

$$\frac{1}{\alpha_u} = \frac{1}{\alpha_p} + \frac{1}{\alpha_{cr}} \quad (3)$$

2.2.2.2. Influence of strain-hardening

As observed from the frame tests that were conducted by Baker and Eickhoff (1995), the strain-hardening properties of steel frames can lead to an enhanced capacity beyond the plastic collapse load. Strain-hardening and its properties were described by Davies (1966), who recommended an approach which would allow to estimate the increase in bending moment beyond the plastic moment M_{pl} at a plastic hinge location. Subsequently, it was proved that

by considering a region of constant flexural moment, the moment resistance may extend beyond the value of the full plastic moment and remain constant under a continuous increased rotation at a hinge location (Byfield and Nethercot 1998; Kemp et al., 2002; Liam et al., 2005). Thereafter, a detailed investigation on the combined effect of the detrimental influence of local buckling and lateral torsional buckling and the beneficial effect of strain hardening on the load carrying capacity of a structure was conducted (Davies, 2006). It was concluded that due to the limiting information regarding the influence of strain-hardening on the behaviour of the structure it would be insufficient to explicitly include strain-hardening into the design procedure.

All aforementioned studies were on carbon steel structures, where the effect of strain-hardening is inferior compared to stainless steel structures. The balance between the beneficial effect of strain-hardening and the detrimental influence of second order effects is crucial, as they counteract each other. In accordance with EN 1993-1-1+A1 (2014), for plastic analysis of frames the consideration of a critical factor $\alpha_{cr}=15$ required, since higher deformations are expected prior to the attainment of a frame's collapse load.

2.2.3. The Continuous Strength Method (CSM)

The Continuous Strength Method is a design method for the treatment of local buckling of stainless steel cross-sections which are subjected to compression or bending. The method is based on the experimentally derived base curve, i.e. an empirical curve calibrated against the available data given from stub column tests, which relates the slenderness $\bar{\lambda}_p$ of a cross section to its deformation capacity ε_{LB} . For plated cross sections, the cross-section slenderness

parameter is related to the cross-section slenderness, which conservatively can be taken as the plate slenderness $\bar{\lambda}_p$ of the most slender constituent element as given in Eq. 4 (Gardner and Theofanous, 2008):

$$\bar{\lambda}_p = \sqrt{\frac{f_y}{f_{cr}}} = \sqrt{\frac{\sigma_{0.2}}{\sigma_{cr}}} = \sqrt{\frac{12 (1-\nu)^2 \sqrt{235}}{\pi \sqrt{210000} \sqrt{k_\sigma}}} \frac{b}{t\epsilon} \quad (4)$$

where σ_{cr} is the elastic critical buckling stress of the plate element, $\sigma_{0.2}$ is the proof stress, ν is the Poisson's ration, b is the flat element width measured between centerlines of adjacent faces, t is the plate thickness and k_σ is a buckling factor allowing for different boundary and loading conditions.

A more robust approach leading to increased strength predictions necessitates the use of either a finite element or a finite strip based software that can predict the elastic critical buckling stress f_{cr} of a cross-section accounting for the effects of element interaction. Alternatively, analytical expressions derived by Seif and Schafer (2010) for the most common shapes of structural cross-sections can be employed to explicitly account for element interaction in the determination of the critical buckling stress. This approach is followed in this thesis and the cross-section slenderness is calculated on the basis of a rational cross-section analysis using the freely available software CUFSM (Li and Scahfer, 2011).

The deformation capacity ϵ_{LB} of a cross-section in compression is defined as the compressive strain corresponding to ultimate load and is given by the Eq. 5 (Gardner and Nethercot, 2004a):

$$\varepsilon_{LB} = \frac{\delta_u}{L_0} \quad (5)$$

where δ_u is the axial shortening at ultimate load and L_0 is the stub column initial length. Furthermore, this deformation capacity is normalized to the elastic strain corresponding to the 0.2% proof stress $\sigma_{0.2}$ is denoted as ε_0 (Eq. 6) and the resulting normalized deformation capacity is determined as a function of cross-section slenderness $\bar{\lambda}_p$ (Eq. 7):

$$\varepsilon_0 = \frac{\sigma_{0.2}}{E} \quad (6)$$

$$\frac{\varepsilon_{csm}}{\varepsilon_y} = \frac{0.25}{\bar{\lambda}_p^{3.6}} \text{ but } \leq \min \left\{ 15; \frac{0.1 \varepsilon_u}{\varepsilon_y} \right\} \text{ for } \bar{\lambda}_p \leq 0.68 \quad (7)$$

A more rounded response with no well-defined yield stress is observed for the stress-strain curve of the stainless steel as illustrated in Fig. 2.1. For stainless steel the stress-strain relationship has been described by Ramberg-Osgood (1943). In the CSM the improved material model which is modified by Gardner and Nethercot (2004) and can either based on the two stage Ramberg-Osgood equation (Ownes and Knowles, 1994; Rasmussen, 2003) was originally proposed (Gardner and Nethercot, 2004a). The equation for this improved stress-strain relationship (Eq. 17) provided in section 2.3.

For cross-sections in compression, the cross-section compression resistance is defined as the local buckling stress σ_{LB} multiplied by the gross cross-section area A_g (Eq. 8). Moreover, for cross-sections in bending the ultimate moment capacity $M_{c,Rd}$ is given by Eq. 9 where the

obtained stress distribution is integrated over the cross-section (Gardner and Theofanous, 2008):

$$N_{c,Rd} = \sigma_{LB} A_g \quad (8)$$

$$M_{c,Rd} = \int_A \sigma y dA \quad (9)$$

where y is the distance from the neutral axis of the section.

Using an accurate material model that truly captures the stress-strain law complicates the design particularly for cross-sections in bending as it necessitates the use a long non-linear inversion of the stress-strain law (Abdella, 2006) and additionally the use of numerical integration when the flexural strength is sought.

To simplify the design procedure whilst still accounting for strain-hardening a bilinear stress-strain approximation was proposed that allows an explicit determination of the moment resistance without the need for numerical integration. As shown in Fig. 2.4, the material response is assumed linear elastic up to the nominal yield strength, where after a strain-hardening branch follows with a slope E_{sh} defined by Eq. 10:

$$E_{sh} = \frac{f_u - f_y}{0.16 \varepsilon_u - \varepsilon_y} \quad (10)$$

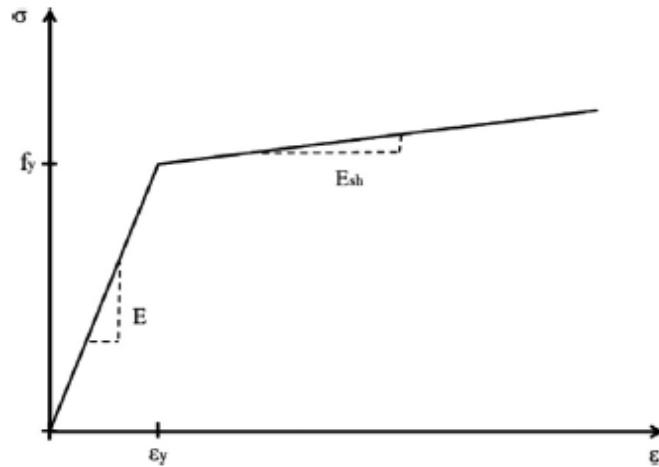


Fig. 2.4: Bilinear elastic-strain hardening material model (Theofanous et al., 2014)

Using the bilinear material assumption, the ultimate moment resistance M_{csm} for RHS and SHS are determined explicitly by Eq. 11 (Gardner and Wang, 2011):

$$\frac{M_{csm}}{M_{pl}} = 1 + \frac{E_{sh} W_{el}}{E W_{pl}} \left(\frac{\epsilon_{csm}}{\epsilon_y} - 1 \right) - \left(1 - \frac{W_{el}}{W_{pl}} \right) \left(\frac{\epsilon_{csm}}{\epsilon_y} \right)^{-2} \quad (11)$$

2.2.3.1. CSM for indeterminate structures

The significance of material non-linearity for stainless indeterminate structures at cross section and at system level is not taken into consideration by the design code EN 1993-1-4+A1 (2015), which leads to conservative strength predictions. Better capacity predictions obtained when the material strain-hardening or the moment redistribution is taken into account. CSM which allows for moment redistribution in similar way with the traditional plastic analysis procedure and for exploitation of material strain-hardening was applied in carbon steel structures by Gardner, Wang and Liew (2011). The applicability of this method to indeterminate stainless steel structures was assessed by Theofanous et al. (2014). The

maximum CSM cross-section resistance is allocated at the location of the critical plastic hinge and only a degree of strain-hardening is allowed at the subsequent hinges. The main feature of this method is that adopting an elastic-linear hardening response rather than the traditional rigid-plastic material response. According with Theofanous et al. (2014), in order to determine the design strengths of indeterminate stainless steel structures based on CSM design procedure the following steps are required:

1. Similar to traditional plastic design the identification of the location of the plastic hinges of number i and the determination of the respective hinge rotations θ_i are required. For example, in the case of five-point bending as shown in Fig. 2.5, $\theta_1=2\delta/L_2$ and $\theta_2=\delta/L_1+\delta/L_2$.

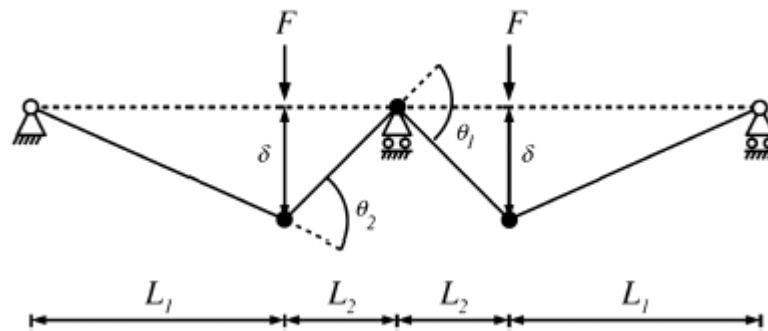


Fig. 2.5: Plastic collapse mechanism for two-span continuous beam (Theofanous et al., 2014)

2. Calculation of the cross-section slenderness λ_p at the position of each hinge is required; λ_p is calculated based on Eq. 8 which is aforementioned at section 2.2.3.1.
3. Determination of the level of the strain (ϵ_{CSM}) where a cross section can endure from the base curve at each hinge (Eq. 12):

$$\left(\frac{\varepsilon_{\text{csm}}}{\varepsilon_y}\right)_i = \frac{0.25}{(\bar{\lambda}_p)^{3.6}} \text{ but } \left(\frac{\varepsilon_{\text{csm}}}{\varepsilon_y}\right)_i \leq \min\left\{15; \frac{0.1\varepsilon_u}{\varepsilon_y}\right\} \text{ for } (\bar{\lambda}_p)_i \leq 0.68 \quad (12)$$

4. For each collapse mechanism, the rotation demand α_i of each of the i hinges need to be determined according to Eq. 13:

$$\alpha_i = \frac{\theta_i h_i}{\left(\frac{\varepsilon_{\text{csm}}}{\varepsilon_y}\right)_i} \quad (13)$$

where θ_i is the relative rotation derived from kinematics considerations for the collapse mechanism considered, h_i is the section height at the considered location and $(\varepsilon_{\text{csm}}/\varepsilon_y)$ is the corresponding normalized strain ratio at the hinge.

5. The deformation demands in terms of strains at other plastic hinges locations are then assigned relative to that of the critical hinge (Eq. 14):

$$\left(\frac{\varepsilon_{\text{csm}}}{\varepsilon_y}\right)_i = \frac{\alpha_i}{\alpha_{\text{crit}}} \left(\frac{\varepsilon_{\text{csm}}}{\varepsilon_y}\right)_{\text{crit}} \leq \left(\frac{\varepsilon_{\text{csm}}}{\varepsilon_y}\right)_i \quad (14)$$

6. Then the cross section bending moment capacity M_i at each plastic hinge on the corresponding strain ratio $(\varepsilon_{\text{csm}}/\varepsilon_y)_i$ is calculated based on the Eq. 11.
7. Finally, the collapse load of the system is determined by equating the external work done by the applied load to the internal work resulting from the hinge rotations (Eq. 15):

$$\sum_j (F_j \delta_j) = \sum_i (M_i \theta_i) \quad (15)$$

2.3. MATERIAL MODELLING

Material modelling is one the most critical aspects in FE simulations, since it heavily affects the quality and accuracy of the obtained results. The stress-strain curve of some metallic materials such as aluminium alloys and stainless steel is rounded with no clearly defined yield point. The first attempt to describe this response was made by Ramberg and Osgood (1943) and further developed by Hill (1944), resulting in the classic Ramberg-Osgood equation (Eq. 16):

$$\varepsilon = \frac{\sigma}{E_0} + 0.002 \left(\frac{\sigma}{\sigma_{0.2}} \right)^n \quad (16)$$

where σ =engineering stress, E_0 =material Young's modulus, n =strain hardening exponent and $\sigma_{0.2}$ = 0.2% proof stress. The three material parameters, namely E_0 , $\sigma_{0.2}$ and n are determined experimentally. In 1990, a large number of Austenitic and Duplex stainless steel beams were tested by Groth and Johansson (1990); in order to determine the mechanical properties of stainless steel. The test specimens had a thickness range 1.5 to 6.35 mm, a width of 16 mm and length equal to 270 mm. The present database is used in this project to choose material parameters for the parametric studies.

The limitations of the Ramberg-Osgood expression were discussed by Mirambell and Real (2000), who highlighted that the original Ramberg-Osgood equation significantly overestimates the stresses at strains higher than 0.2%, hence resulting in unsafe strength

predictions for high strains. A remedy was proposed, where the single curve of the Ramberg-Osgood equation was replaced with a two-stage model. Beyond the 0.2% proof stress until failure a second Ramberg-Osgood curve is fitted, which more accurately captures the observed material response. For the full description of the material response two further material parameters, namely the ultimate tensile stress and the second strain-hardening exponent are utilized in addition to the three material parameters of the original Ramberg-Osgood model (Mirambell and Real, 2000). The two-staged Ramberg-Osgood model was further developed by Rasmussen (2003) who proposed explicit equation for the determination of the additional material parameters as a function of the three basic ones. In order to capture the compressive response of stainless steel, for which not ultimate tensile stress exists, Gardner and Nethercot (2004a) recommended, that the ultimate stress is substituted with the 1% of proof stress $\sigma_{1.0}$ (Eq. 17), a material parameter readily available from the mill certificates for stainless steel material:

$$\varepsilon = \frac{(\sigma - \sigma_{0.2})}{E_{0.2}} + \left(\varepsilon_{t1.0} - \varepsilon_{t0.2} - \frac{\sigma_{1.0} - \sigma_{0.2}}{E_{0.2}} \right) \left(\frac{\sigma - \sigma_{0.2}}{\sigma_{1.0} - \sigma_{0.2}} \right)^{n_{0.2,1.0}} \quad (17)$$

where E_0 and $E_{0.2}$ are the Young's modulus and the tangent modulus at 0.2% offset strain, respectively, $\sigma_{0.2}$ and $\sigma_{1.0}$ are the proof stresses at 0.2% and 1% offset strains, respectively, $\varepsilon_{t0.2}$ and $\varepsilon_{t1.0}$ are the total strains $\sigma_{0.2}$ and $\sigma_{1.0}$, respectively and n and $n_{0.2,1.0}$ are strain hardening exponents.

An extension to the two-staged Ramberg Osgood was proposed by Quach et al. (2008), who proposed a three-stage material model that better approximates the material response throughout the full strain range. The proposed model consists of the two-stage material

response as proposed by Gardner and Nethercot (2004a), which is supplemented by an assumed linear equation between strain and true stress valid from 2% strain till the ultimate tensile stress is reached and was intended to be used in numerical modelling of cold-forming processes. A review of all relevant material models together with a generalisation of the Ramberg Osgood material law is reported by Hradil et al. (2013).

2.4. CORNER MATERIAL PROPERTIES

In a cold-formed cross section the stress-strain properties of the flat region vary from the properties of the corner region, due to the material response in deformation. The strength in the corner regions of cold-formed steel square hollow sections (SHS) and rectangular hollow sections (RHS) is higher than the strength in flat regions due to plastic deformation. A power model was proposed by Karren (1967) in order to measure the increase of strength in corner regions for carbon stainless steel. This model was based on the strain experienced in the sheet material during corner forming, where it was observed that the strain that produced in the corner forming is related to the ratio of the internal radius of the corner and the thickness of the material r_i/t . In 2005 Karren's model was modified by Ashraf et al. (2005) for stainless steel, which employs the 0.2% proof stress $\sigma_{0.2, mill}$ (Eq. 18) for the unformed material:

$$\sigma_{0.2,c} = \frac{1.881\sigma_{0.2, mill}}{\left(\frac{r_i}{t}\right)^{0.194}} \quad (18)$$

After, a continuous study of cold-rolled box sections Gardner and Nethercot (2004a) came to the conclusion that since the corner has been work-hardened to a sufficient extent in order to be operating in the relatively flat part of the material stress-strain curve, the 0.2% proof

strength of the corner material it could be expressed as a fixed percentage of the ultimate stress of the flat material (Eq. 19):

$$\sigma_{0.2c}=0.85\sigma_u \quad (19)$$

where $\sigma_{0.2c}$ is the 0.2% proof strength of the corner material and σ_u the ultimate stress of the flat material. Therefore, based on the Eq.19 the fixed percentage found to be 85%.

Cruise and Gardner (2008), quantified the effect of the ratio of the radius-to-thickness ratio on the strength of cold-formed stainless steel section corners by executing a large number of experimental tests on material coupons as well as hardness tests which they correlated to the nominal yield strength of the material. More recent studies on the corner material response of cold formed sections were conducted by Rossi et al. (2009), whilst Afshan et al. (2013) reported a series of experimental tests on flat and corner carbon steel as well as austenitic, duplex and ferritic stainless steel coupons extracted from cold-formed tubular sections. Based on the obtained results by Afshan et al. (2013), Rossi et al. (2013) proposed predictive models for the corner strength enhancements of steel and stainless steel cold-formed sections.

2.5. NUMERICAL MODELLING

Nowadays general purpose finite element (FE) software is widely used both in practice and research, to simulate and predict the response of structural components and complete structures. In order to be confident in the numerical results, the generated model has to be validated. Therefore, usually a limited number of experiments published in the literature are simulated numerically and the generated FE models are said to be validated when they can

numerically replicate the experimental response with sufficient accuracy. Upon validation, parametric studies are performed to establish the key factors controlling the response of the modelled structure and study a large number of structural components/structures. Parametric studies are typically conducted by changing either the geometry (slenderness or thickness) or the mechanical properties of the model (Wang, 2011). Both numerical models and laboratory tests are of vital importance to reach conclusions on the response of the studied elements/structures and for the development of relevant design guidance. The main advantage of FE parametric studies is that they are a quick and low cost approach in comparison with the laboratory tests. In the following, a brief summary of the overarching assumptions underpinning the FE modelling of stainless steel structures is given.

2.5.1. Type of element

For the modelling of thin-walled metallic members the most commonly used type of elements are the shell elements, which are typically employed to discretize the mid-plane of the simulated structural members. Contrary to beam elements, shell elements are able to capture localized deformations at cross-sectional level; hence they can be used for the analysis of structures where local buckling is expected. Nevertheless, the general purpose FE software ABAQUS allows the representation of local buckling effects in a beam element model with the use of M1 command in the input of moment-curvature response (Zienkiewicz and Taylor, 2005). Furthermore, it should be stated that in the documentation of ABAQUS there is a number of various shell elements. In this report a 4-noded doubly curved shell element with finite membrane strains and reduced integration called S4R shell element will be used as this element is able to capture both thin and thick shell response (i.e. its formulation is based on

the Reissner-Mindlin plate theory), it allows for large membrane strains at high deformations and it was shown to perform well in similar studies (Gardner and Nethercot, 2004; Ashraf et al., 2006; Theofanous and Gardner, 2010).

2.5.2. Material modelling

In cold-formed and stainless steel cross-sections the enhanced material properties of the corner regions were shown to extend beyond the curved corner portions. For carbon steel was found that the corner properties extend to a distance equal to the material thickness t (Fig. 2.6) (Karren, 1967). In 2004, a parametric study was conducted for cold-formed stainless steel stub columns with extended corner properties to t and $2t$ beyond the curved corner portions (Fig. 2.7). The outcome of this research was that the FE models with corner properties extended to $2t$ beyond the curved corner portions provide better results than the FE models extended to t beyond the curved corner portions (Gardner and Nethercot, 2004).

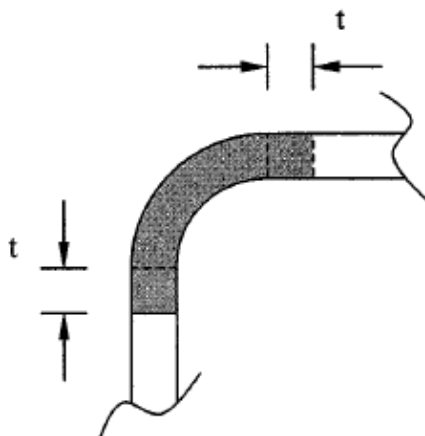


Fig. 2.6: Corner properties extended to a distance t (Karren, 1967)

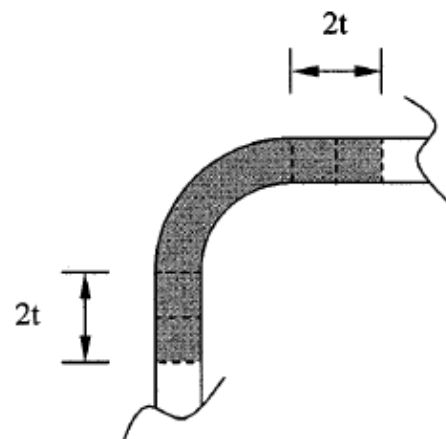


Fig. 2.7: Corner properties extended to a distance $2t$ (Gardner and Nethercot, 2004)

For the FE model the continuous engineering stress-strain curve measured from the coupon test needs to be converted into the true stress σ_{true} -log plastic strain $\epsilon_{\text{ln}}^{\text{pl}}$ format and introduced in the FE software (ABAQUS) as a piecewise multilinear curve. The engineering stress-strain curve is discretized and represented through a sufficient large number of points to capture the shape of the continuous curve and then these points are converted into true stress-log plastic strain with the use of Eq. 20 and 21:

$$\sigma_{\text{true}} = \sigma_{\text{nom}} (1 + \epsilon_{\text{nom}}) \quad (20)$$

$$\epsilon_{\text{ln}}^{\text{pl}} = \ln (1 + \epsilon_{\text{nom}}) - \frac{\sigma_{\text{true}}}{E} \quad (21)$$

2.5.3. Type of analysis

During the numerical simulation the following steps are required. First, a linear buckling analysis need to be conducted, in order to extract the buckling mode shapes associated with the lowest critical buckling stress. Then, these buckling mode shapes are utilized in the nonlinear static analysis, to introduce the shape of the geometric imperfections. For the execution of the nonlinear static analysis, the RIKS procedure is used. The RIKS method, which is a variant of the arc length method, is generally used to predict unstable, geometrically nonlinear collapse of a structure. Moreover, RIKS method uses the load magnitude as an additional unknown; it solves simultaneously for loads and displacements (ABAQUS, 2007) and is therefore capable of tracing the post ultimate response of structures and hence capture the full load-deformation history of a structure.

2.5.4. Imperfections

The initial geometric imperfections are defined as deviations of the real component geometry from the idealised one. They are attributed to the fabrication process of structural components and can have a significant effect on the structural response, particularly when it is governed by buckling. Eigenvalue analysis is of vital importance for the acquisition of the required buckling mode shapes, where the first local buckling mode shape is commonly assumed as the initial imperfection (Wang, 2011). This is a modelling convenience and has been shown to yield satisfactory results. Depending on the half wavelength over which buckling occurs, the initial geometric imperfections can be classified as local, distortional, global ($P-\delta$) and system ($P-\Delta$). Where more than one type of imperfections can occur, a linear combination of the relevant imperfection mode shapes can be considered thus allowing their effect (as well as the effect of their interaction) on the structural behaviour to be quantified.

The imperfection amplitude needs to be added into the FE models. The value of the amplitude can be determined with one of the following four methods:

- A Mitutoyo Coordinate Measuring Machine with an accuracy of 0.001 mm can be used for the measurement of the geometric imperfections (Fig. 2.8). The Mitutoyo machine uses a standard touch probe for the inspection of any local imperfection at the mid length of the specimen (Young, 2005).



Fig. 2.8: Mitutoyo Coordinate Measuring Machine (Young, 2005)

- Derivation of local buckling imperfection from analytical predictive model (Dawson and Walker, 1972). Dawson and Walker model predicts imperfection amplitudes based on both geometric and material properties of cross-sections.
- Use of the imperfection spectrum in order to determine the imperfection magnitude in a specific eigenmode, which called modal imperfection (Schafer and Pekoz, 1998).
- Consider the amplitude of local imperfection as a fixed fraction of the component thickness t ($t/10$, $t/100$ and $t/500$) (Ashraf and Gardner, 2006; Chan and Gardner, 2008b; Gardner and Theofanous, 2008; Wang, 2011).

2.6. PUBLISHED EXPERIMENTAL DATA ON THE RESPONSE OF INDETERMINATE STRUCTURES

The focus of this project is the structural response of stainless steel indeterminate structures. Given the relatively limited results on stainless steel indeterminate structures, which currently include only tests on two span continuous beams, experimental data on carbon steel indeterminate structures will also be considered. Relevant test data on simply supported beams tested in 3-point and 4-point bending configuration will also be reviewed, as they offer an insight on both the strength and the deformation capacity of the cross-sections which act as plastic hinges in the indeterminate structures. In this thesis tests on continuous beams are reviewed, whilst literature review on carbon steel frames (i.e. not stainless steel frames have been tested to date) will be conducted later on and included in subsequent chapters.

2.6.1. Carbon and cold-formed steel structures

A total of forty-seven simply supported beam tests, twelve continuous beam tests and forty-two frame tests (Table 2.1) were carried out for both hot-rolled and cold-formed steel sections (Gardner, Saari, and Wang, 2010; Kwon, Chung and Kim, 2006; Wilkinson and Handcock, 1998; Wilkinson and Handcock, 1999; Low, 1959; Baker and Eickoff, 1955).

Table 2.1: Simply supported, continuous beams and frame tests for carbon steel

References resources	Section type	No. of simply beam tests	No. of continuous beam tests	No. of portal frames
Gardner, Saari and Wang, 2010	6 RHS & 12 SHS	6	12	-
Wilkinson and Handcock, 1998; 1999	38 RHS & 3 SHS	41	-	3
Baker and Eickoff, 1955	I-section	-	-	2
Low, 1959	Square solid section Rectangular solid section	-	-	34
Kwon, Chung and Kim, 2006	Closed Cold-Formed section	-	-	3

Gardner et al. (2010), considered both cold-formed and hot-rolled tubular sections, and assessed the slenderness limits given in EN 1993-1-1+A1 (2014). In Fig. 2.9 the maximum moment recorded in the tests is normalized by the elastic moment capacity M_{el} and plotted on the vertical axis, allowing assessment of the Class 3 slenderness limit which is the slenderness parameter used by EN 1993-1-1+A1 (2014) for cross-section classification. The ultimate moment M_u was normalized by the plastic moment M_{pl} and plotted against the slenderness of the compression flange of the beams $b/t\epsilon$ (Fig. 2.10) which is the slenderness parameter used by EN 1993-1-1+A1 (2014) for cross-section classification. It was concluded that the slenderness limits for Class 2 and Class 3 are in agreement with the Eurocode 3 slenderness limits. For the assessment of Class 1 slenderness limit, the rotation capacity R was plotted against the slenderness of the respective section (Fig. 2.11). The rotation capacity R of the test specimens was determined based on the following Eq. 22:

$$R = \frac{\theta_{rot}}{\theta_{pl}} - 1 \quad (22)$$

where θ_{pl} is the elastic rotation at the plastic moment and θ_{rot} is the total rotation upon reaching the plastic moment on the unloading path. The above mentioned symbols and the determination of rotation capacity are illustrated in Fig. 2.12, where M is the bending moment at mid-span and θ the rotation of the plastic hinge.

Following the assessment of Class 1 limit, it was stated that further investigation is required, since a number of test specimens show a rotation capacity less than three $R < 3$, which is not in agreement with the rotation capacity given from Eurocode 3 (EN 1993-1-1+A1, 2014), where the rotation capacity R must be larger than 3 ($R > 3$). Finally, it was shown that the material strain hardening leads to higher load-carrying capacities for stocky sections compared to those predicted from the given design approaches, particularly for cold-formed sections for which strain-hardening is more pronounced. Therefore, the use of the Continuous Strength Method (CSM) was proposed for as a means to rationally incorporate strain-hardening in the design of structures employing sufficiently stocky cross-sections (Gardner, Saari, and Wang, 2010).

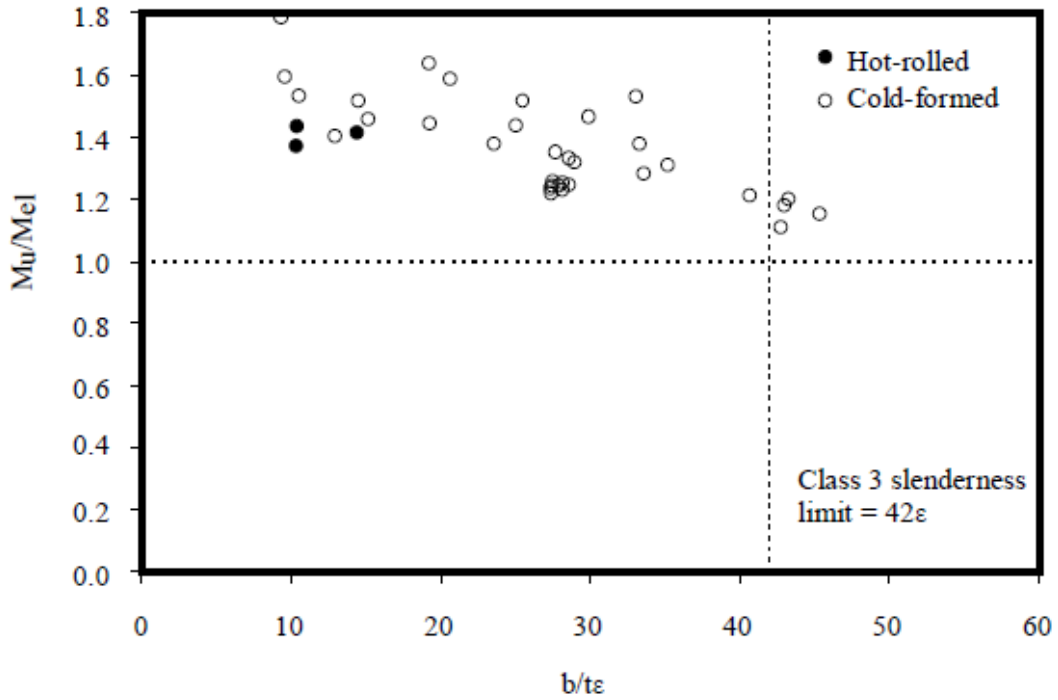


Fig. 2.9: M_u/M_{el} versus $b/t\epsilon$ for assessment of Class 3 (Gardner, Saari and Wang, 2010)

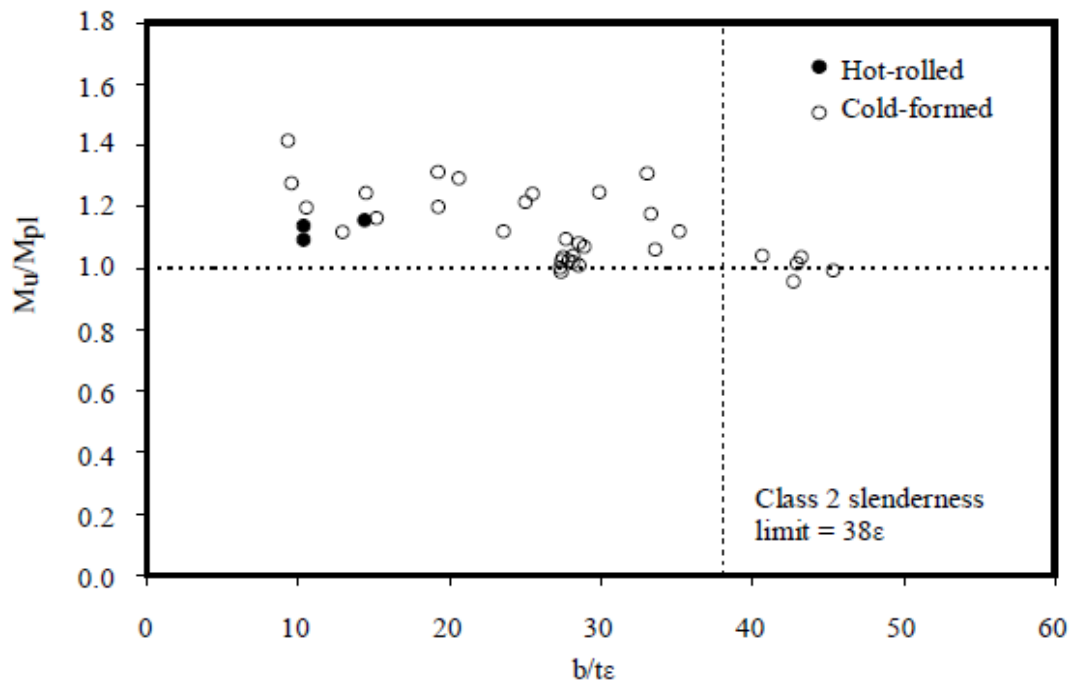


Fig. 2.10: M_u/M_{pl} versus $b/t\epsilon$ for assessment of Class 2 (Gardner, Saari and Wang, 2010)

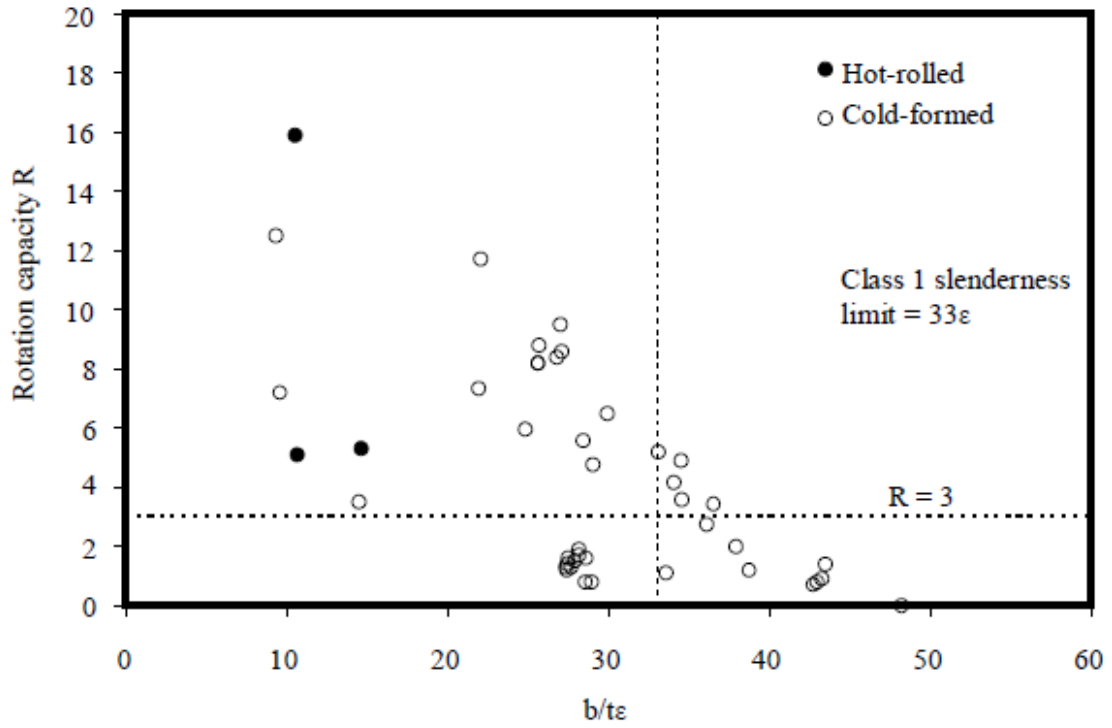


Fig. 2.11: Rotation capacity versus b/ϵ for assessment of Class 1 (Gardner, Saari and Wang, 2010)

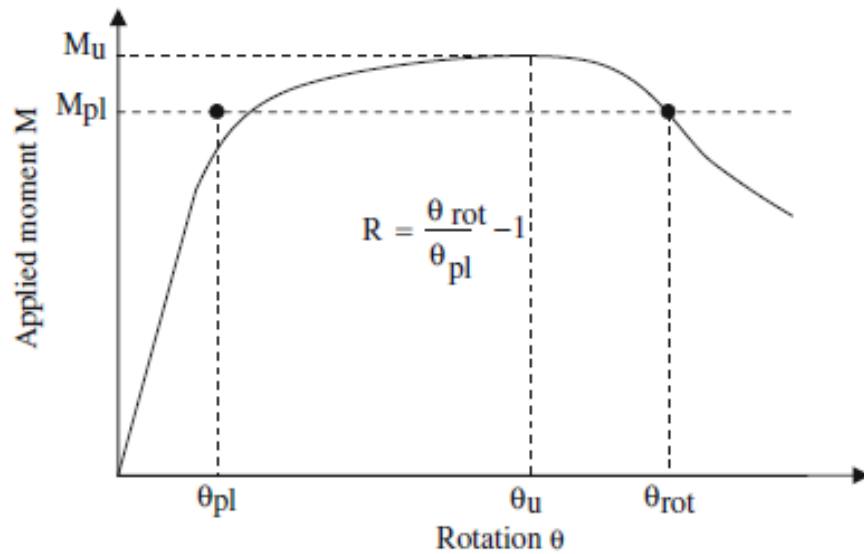


Fig. 2.12: Definition of rotation capacity from moment-rotation graphs (Gardner, Saari and Wang, 2010)

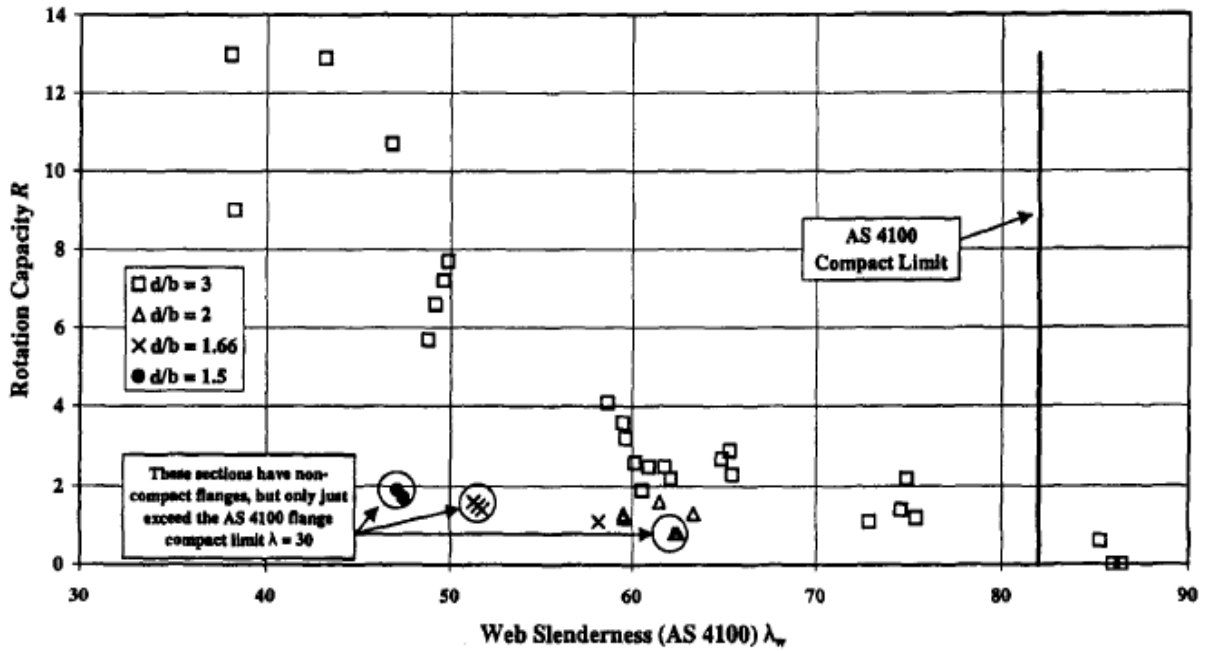


Fig. 2.14: Rotation capacity R versus web slenderness λ_w for AS 4100 Class 1 limit (Wilkinson and Hancock, 1998)

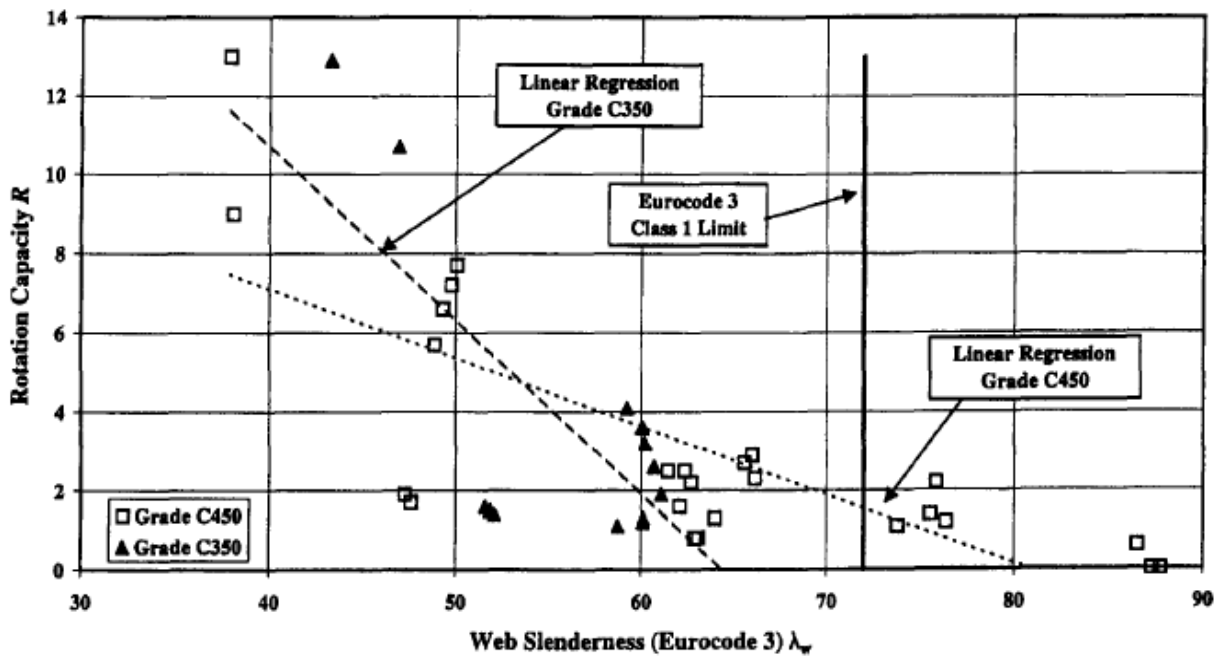


Fig. 2.15: Rotation capacity R versus web slenderness λ_w for Eurocode 3 Class 1 limit (Wilkinson and Hancock, 1998)

In 1956, two real scale pitched roof portal frames of five meters span and two and a half meter height, erected four meters apart and braced by two eaves beams, purlins and sheeting rails, were tested by Baker and Eickoff. The purpose of this tests was to asses both elastic design methods (Baker, 1954) and plastic design methods (Baker 1950; Neal and Symonds, 1952; Horne, 1952; Baker and Heyman, 1956), in order to produce a structure which will not fail until the applied load exceeds its working load. For a better understanding of the collapse modes that can occur in portal frames for different ratios of horizontal load to vertical load, Baker and Eickoff produced the diagram shown at Fig. 2.16. During the design process, an assumption was made that at collapse the plastic hinges would form at the points B, D, F and G, despite the fact that plastic hinges did not form at points B and F due to the local increase in the depth, which was formed during the construction of the joints. Based on the collapse load of the portal frames which was recorded as 14.2 tons, it was concluded that the effect of strain hardening at the location of plastic hinges lead to a load carrying capacity higher than the theoretical one and hence the effects of both strain-hardening and lateral instability need to be taken into consideration for the achievement of a satisfactorily ultimate load prediction.

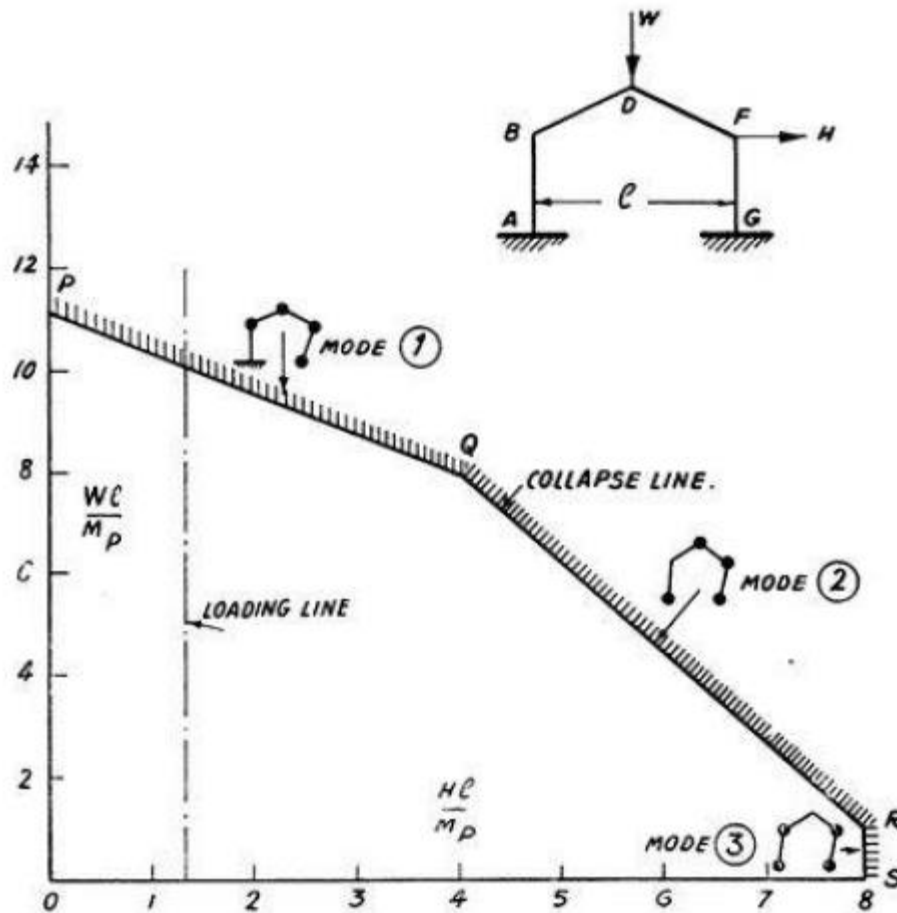


Fig. 2.16: Theoretical collapse mode shapes (Baker and Eickoff, 1955)

Three tests of cold-formed rectangular hollow section portal frames were conducted by Wilkinson and Hancock (1999), in order to investigate the ultimate load capacity of RHS portal frames, to assess if the formation of a plastic collapse mechanism in such frames is possible given the reduced ductility and the absence of a yield plateau associated with cold-formed steel members and to study the rotation capacity requirements for portal frames made of cold-formed steel. The frame layout is shown in Fig. 2.17, where each frame had a span of 7 m and a total height of 4 m. Each frame was tested under combined vertical and horizontal loads, where for the most efficient application of these loads a gravity load simulator (Yarimci et al., 1967) which had been attached to the strong floor, was used. This loading system allows

the direction of the applied load to remain vertical even when the frame starts to sway. According to the results, it was concluded that plastic collapse mechanism was formed in all three frames, with local buckling occurring in the locations where the plastic hinges are formed. Furthermore, it was observed that the ultimate load that was obtained by the frame tests was smaller or similar to the loads obtained from plastic analysis. This inconsistency was attributed to second order effects and moment-axial force interaction, which has not been taken into consideration during the plastic analysis procedure.

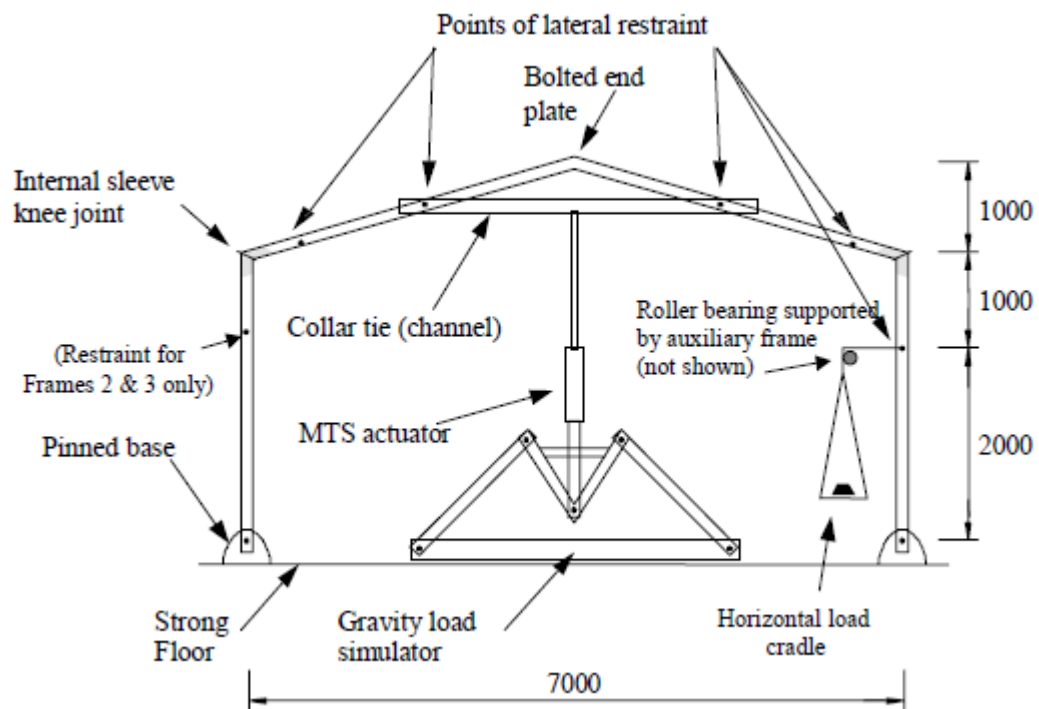


Fig. 2.17: Layout of portal frames (dimensions in mm) (Wilkinson and Hancock, 1999)

More recently, three steel closed cold-formed section portal frames were tested by Kwon et al. (2006). This research was mostly related to the study of cold-formed steel connections and less related to portal frames. The test layout is shown in Fig. 2.18, where the frames were tested under a combination of constant vertical and increasing horizontal load to failure. Based

on the obtained results it was concluded that test results were much lower than the calculated load, which does take into consideration the material nonlinearity and the fracture of the connections.

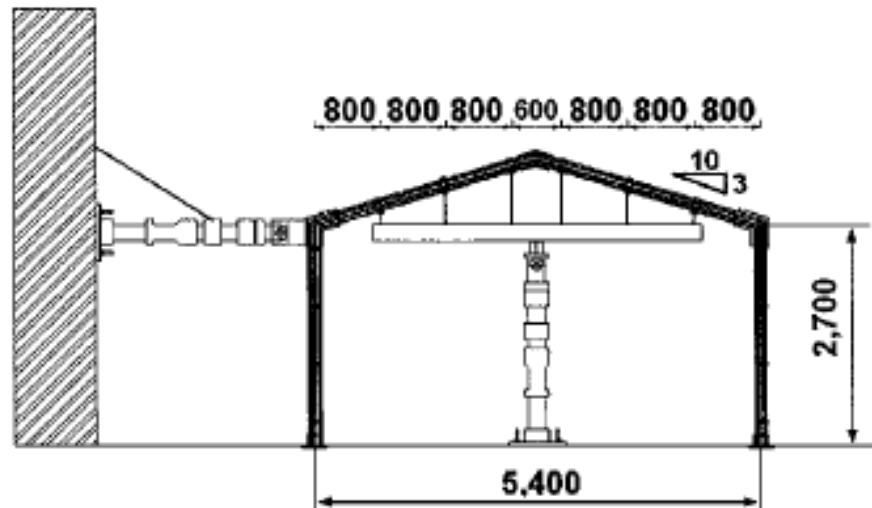


Fig. 2.18: Layout of frame tests (dimensions in mm) (Kwon, Chung and Kim, 2006)

2.6.2. Stainless steel structures

As previously stated no experimental tests on stainless steel frames exist to date. All available test data on stainless steel continuous beams are collected from the published literature. The accompanying tests on simply supported stainless steel beams reported in the same studies are also considered as they give essential information on the moment-rotation response of the cross-sections studied in the continuous beam tests. Considering all available test data on stainless steel simply supported beams is beyond the scope of this thesis; a summary of tests until 2008 was reported by Gardner and Theofanous (2008).

Table 2.2: Simply supported and continuous beam tests for stainless steel

References resources	Stainless steel grades	Section type	No. of simply beam tests	No. of continuous beam tests
Mirambell and Real, 2000	Austenitic	4 RHS, 4 SHS & 4 H-sections	6	6
Arrayago and Real, 2016	Ferritic	10 RHS & 11 SHS	12	9
Theofanous et al., 2014	Austenitic & Lean Duplex	6 RHS, 9 SHS & 16 I-sections	13	18

The main objective of the experimental investigation of Mirambell and Real (2000) was to study the flexural behaviour of stainless steel beams, mainly focusing on the calculation of deflections. Inadvertently they provided the first set of experimental tests on stainless steel indeterminate structures. A total of six simply supported and six continuous beam tests were tested. The cross sections of the tested beams were square hollow sections (SHS), rectangular hollow sections and I-sections. For both the simply supported beams and for the continuous beams tests, the loads were applied at mid-span.

Further investigation on determinate and indeterminate stainless steel structures was carried out by Theofanous et al. (2014). The effect of slenderness on the resistance and rotation capacity of the cross-sections, as well as the suitability of the slenderness limits based on the dated European design provisions (EN1993-1-4, 2006) which have been recently updated (EN1993-1-4+A1, 2015), was assessed on the basis of a series of tests on two span continuous beams employing SHS, RHS and I-sections. The same sections were also tested as simply supported beams in the 3-point and 4-point bending configuration to obtain fundamental data

on the moment-rotation (moment-curvature) response of the sections considered. The adaptation of the CSM for the design of stainless steel continuous beams was shown to give very accurate and consistent results for stocky sections (Table 2.3) in comparison with the results for EN 1993-1-4 (2006) and the EN 1993-1-4 (2015). In Table 2.3 the predicted collapse load F_{pred} is normalized by the experimental obtained collapse load F_u . Nevertheless, it was clearly stated that additional research is required for the extension of this method to more general cases (i.e. more structural systems and more loading configurations need be tested) (Theofanous et al., 2014), which is done in the framework of this thesis.

Table 2.3: Assessment of design methods for continuous beams allowing for plastic design (Theofanous et al., 2014)

Specimen	EN 1993-1-4, 2006		EN 1993-1-4+A1, 2015		CSM for indeterminate	
	Class	F_{pred}/F_u	Class	F_{pred}/F_u	$\epsilon_{csm}/\epsilon_y$	F_{pred}/F_u
SHS 50×50×3-1	1	0.68	1	0.68	10.5	0.91
SHS 50×50×3-2	1	0.68	1	0.68	11.1	0.91
SHS 60×60×3-1	1	0.72	1	0.72	8.9	0.93
SHS 60×60×3-2	1	0.76	1	0.76	8.9	0.98
SHS 100×100×3-1	4	0.68	4	0.71	1.1	N/A
SHS 100×100×3-2	4	0.68	4	0.72	1.1	N/A
RHS 60×40×3-MA-1	1	0.63	1	0.63	10.2	0.84
RHS 60×40×3-MA-2	1	0.63	1	0.63	10.2	0.85
RHS 60×40×3-MI-1	3	0.52	1	0.69	5.6	0.84
RHS 60×40×3-MI-2	3	0.43	1	0.71	5.6	0.85
I-200×140×6×6-1	4	0.64	4	0.68	1.2	N/A
I-200×140×8×6-1	4	0.65	3	0.66	2.7	N/A
I-200×140×10×8-1	1	0.79	1	0.79	8.5	0.91
I-200×140×12×8-1	1	0.72	1	0.72	15.0	0.93

Specimen	EN 1993-1-4, 2006		EN 1993-1- 4+A1, 2015		CSM for indeterminate	
	Class	F_{pred}/F_u	Class	F_{pred}/F_u	$\epsilon_{csm}/\epsilon_y$	F_{pred}/F_u
I-200×140×6×6-2	4	0.53	4	0.56	1.2	N/A
I-200×140×8×6-2	4	0.57	3	0.57	2.7	N/A
I-200×140×10×8-2	1	0.84	1	0.84	8.9	0.95
I-200×140×12×8-2	1	0.82	1	0.82	15.0	1.02
Mean		0.66		0.70		0.91
COV		0.16		0.11		0.06

* N/A = Cross-sections are not applicable for the Continuous Strength Method

More recently, simply supported and continuous test were conducted by Arrayago and Real (2016). Four three-point, eight four-point bending tests and 9 continuous beam tests over two spans were conducted. The focus of their tests was on ferritic stainless steels, which were not previously considered. Similarly to the investigation by Afshan and Gardner (2013), the experimental results from the simply supported beam tests were used to assess the adequacy of the cross-sectional slenderness limits provided by EN 1993-1-4 (2006) and those proposed by Gardner and Theofanous (2008), which were recently adopted by Eurocode (EN 1993-1-4+A1:2015). For Class 3 and Class 2 it was observed that the new cross-section classification limits (EN 1993-1-4+A1, 2015) are more accurate than those provided previously by EN 1993-1-4 (2006). Furthermore, it was stated that the definition of Class 1 limit requires further investigation. The continuous beams were tested in order to investigate the effect and level of moment redistribution at failure and to further assess the applicability of plastic design for ferritic stainless steel structures. The researchers came to the conclusion that when different stainless steel grades are used for the design of steel members better predictions are provided

by the Continuous Strength Method (CSM) regarding the collapse loads for indeterminate beams; the most accurate ultimate capacity predictions according the classical plastic design and EN 1993-1-4 (2006) approach are obtained by the new cross section classification limits (EN 1993-1-4+A1, 2015).

2.7. KNOWLEDGE GAP

The present literature review has revealed that despite the significant existing research on stainless steel structures, there is a lack of suitable guidance for the design of indeterminate stainless steel structures, mainly due to the limited number of tests conducted to date, which have focused only on continuous beams. According to EN 1993-1-1+A1 (2014), indeterminate carbon steel sections classified as Class 1, are assumed to have sufficient deformation capacity to permit plastic design of indeterminate structures. Contrary, EN 1993-1-4+A1 (2015) doesn't allow plastic design for stainless steel structures, despite their excellent material ductility and despite the existence of Class 1. This thesis aims at augmenting the limited results currently available on the structural response of stainless steel indeterminate structures, improve current understanding on their response and ultimately devise an efficient design approach suitable for incorporation in future revisions of EN 1993-1-4+A1 (2015) as discussed in the aim and objectives.

CHAPTER 3

EXPERIMENTAL TESTS ON STAINLESS STEEL BEAMS

The experimental study reported in this Chapter was presented by the PhD candidate at the 5th International Experts Seminar on Stainless Steel Structures on 20/09 in London. The research reported herein was published by Gkantou et al. (2019).

3.1. TESTED CROSS-SECTIONS

Physical tests on simply supported beams loaded in the 3-point bending and in the 4-point bending configuration and on two-span continuous beams loaded at mid-spans were conducted in the Structures Laboratory at the University of Birmingham. In addition, tensile tests on flat and corner coupons extracted from the finished cross-sections were carried out in the lab of the department of Metallurgy and Materials at the University of Birmingham.

Four RHS with a nominal outer web depth H and a nominal outer flange width B equal to 100 mm and 50 mm respectively were employed in the experimental study reported herein. The employed sections cover not only a wide range of local slendernesses, but also different material grades and production techniques. Three of the sections were cold-formed from Grade EN 1.4301/1.4307 austenitic stainless steel and had a nominal thickness t of 2 mm, 3 mm and 5 mm. The fourth section was fabricated by welding two parallel flange channel sections cold-formed from Grade 1.4462 duplex stainless steel along the flange tips and had a nominal thickness of 3 mm. Hence the austenitic cold-formed RHS had a seam weld along the centreline of one of the webs (i.e. longer faces), whilst the fabricated duplex RHS had a longitudinal weld along the centreline of each flange. It is noteworthy that the welded duplex section was fabricated due to difficulties associated with sourcing cold-formed duplex stainless steel RHS in small quantities (as required for a research project), whilst austenitic stainless steel RHS were readily available. Moreover, despite the lower nickel content which is expected to lead to a lower price (Theofanous and Gardner, 2010), lean duplex stainless steels were even more expensive than their ordinary duplex counterparts, unless a large quantity was requested. Clearly several issues with the supply chain need to be addressed to take advantage of the benefits of such novel structural materials. Prior to testing careful measurements were taken for each beam specimen. Since all beam specimens for each section were cut from the same length of tubes, the measurements were averaged for each nominal cross-section and are reported in Table 3.1, where r_i refers to the internal corner radius and the remaining symbols have been previously defined. The subscript D following the section designation denotes the specimen in duplex stainless steel.

Table 3.1: Mean measured dimensions of tested cross-sections

Cross-section	Material Grade	B (mm)	H (mm)	t (mm)	r _i (mm)
RHS 100×50×2	EN 1.4301/1.4307	50.04	100.13	1.90	1.70
RHS 100×50×3	EN 1.4301/1.4307	49.97	100.17	2.90	2.25
RHS 100×50×5	EN 1.4301/1.4307	50.19	100.42	4.93	2.56
RHS 100×50×3-D	EN 1.4462	50.19	100.44	2.87	2.56

3.2. TENSILE COUPON TESTS

Two flat material coupons (i.e. one from the mid-width of the web and one from the mid-width of the flange) and one corner coupon were extracted from each of the four cross-sections considered herein as shown in Fig. 3.1 and were tested according to EN ISO 6892-1 (Rasmussen, 2003). For the austenitic sections, the flat coupons did not contain the weld, whilst for the duplex section one of the flat coupons contained the weld along the coupon length. The obtained results are summarized in Table 3.2, where E is the Young's modulus, $\sigma_{0.2}$ is the 0.2% proof stress, $\sigma_{1.0}$ is the 1.0% proof stress, σ_u is the ultimate tensile stress, ϵ_f is the plastic strain at fracture and n and $n_{0.2,1.0}$ are material parameters used in the two-stage Ramberg-Osgood model (Real and Mirambell 2008; Rasmussen, 2003; Gardner and Nethercot, 2004) material model, which is adopted in the numerical modelling as discussed in the next section. Typical stress-strain curves are depicted in Fig. 3.2 for the RHS 100×50×2 and the duplex RHS 100×50×3 material coupons, where the corner coupons are seen to possess enhanced material strength. Typical coupons before, during and after testing are also depicted in Fig. 3.3.

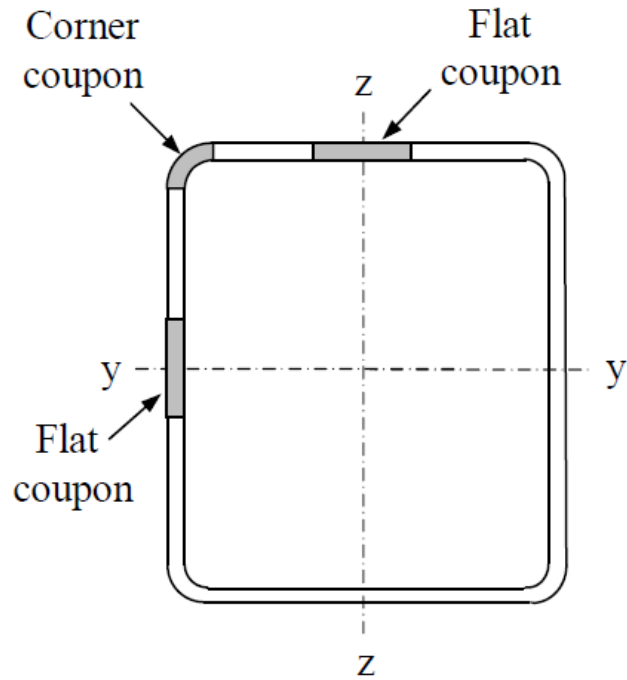


Fig. 3.1: Locations of flat and corner coupons

Table 3.2: Tensile coupon test results

Specimen	E (N/mm ²)	$\sigma_{0.2}$ (N/mm ²)	$\sigma_{1.0}$ (N/mm ²)	σ_u (N/mm ²)	ϵ_f %	Compound R-O coefficients	
						n	n _{0.2,1.0}
RHS 100×50×5 Flange	190000	481	533	746	0.55	8.5	3.25
RHS 100×50×5 Web	201700	490	535	758	0.54	8.0	3.25
RHS 100×50×5 Corner	198000	697	800	839	0.48	10.0	3.80
RHS 100×50×3 Flange	200600	458	507	699	0.57	8.0	2.90
RHS 100×50×3 Web	193800	473	506	698	0.58	10.0	2.30
RHS 100×50×3 Corner	201000	510	626	698	0.46	6.0	3.90
RHS 100×50×2 Flange	193800	450	482	774	0.55	9.0	2.25

Specimen	E (N/mm ²)	$\sigma_{0.2}$ (N/mm ²)	$\sigma_{1.0}$ (N/mm ²)	σ_u (N/mm ²)	ϵ_f %	Compound R-O coefficients	
						n	n _{0.2,1.0}
RHS 100×50×2 Web	200600	434	473	769	0.56	8.0	2.20
RHS 100×50×2 Corner	203000	545	650	809	0.34	6.0	4.50
RHS 100×50×3 Flange-D	203600	576	643	822	0.34	12.0	2.50
RHS 100×50×3 Web-D	198300	582	637	808	0.29	12.0	2.50
RHS 100×50×3 Corner-D	190000	718	840	893	0.24	6.0	4.75

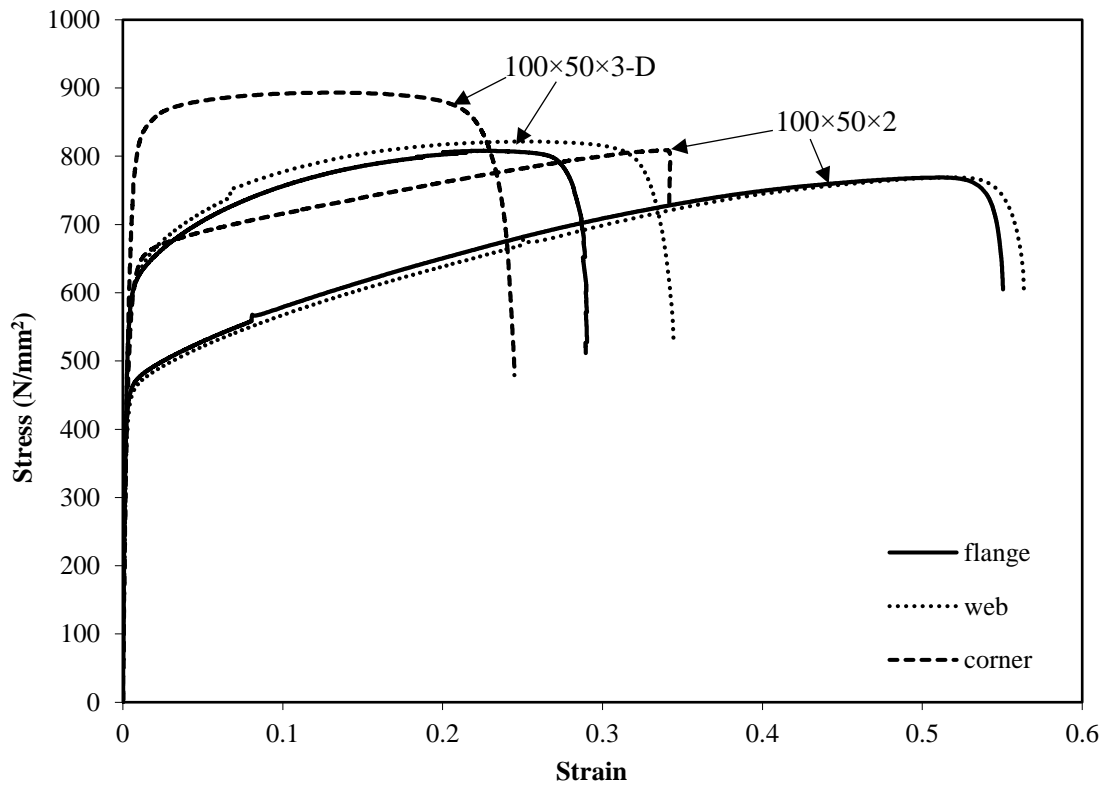


Fig. 3.2: Stress - strain curves of the tensile coupons (100×50×3-D and 100×50×2)

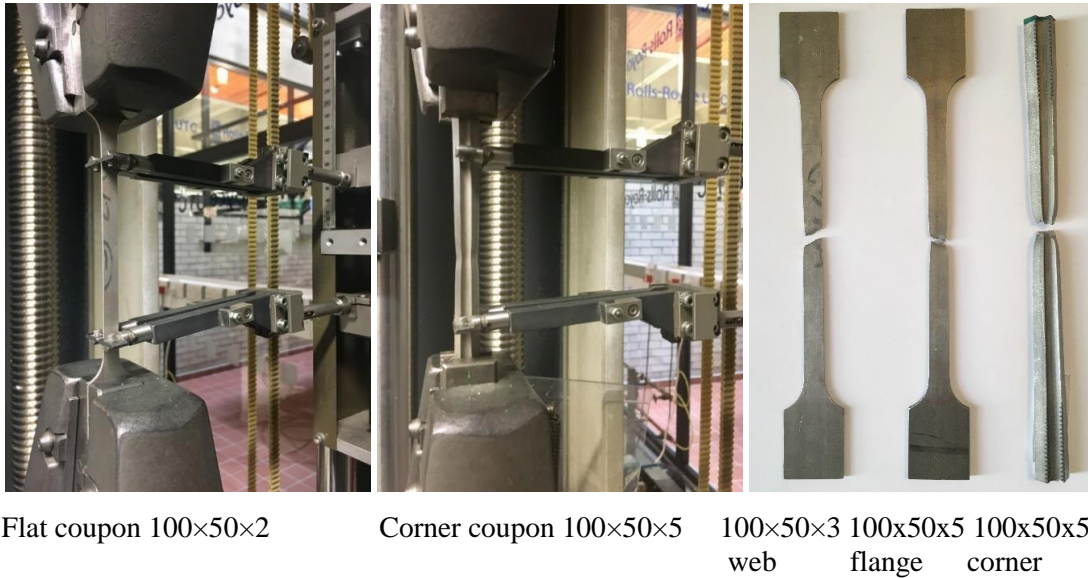


Fig. 3.3: Flat and corner tensile coupons

The key material properties stated in the mill certificates for the sheet material used for the fabrication of the cross-sections are summarized in Table 3.3. As expected the proof stress and ultimate stress values corresponding to coupons extracted from the finished sections are significantly higher compared to the mill certificate values for the austenitic cross-sections, since during the cold-forming production process the coil material properties are significantly enhanced (Cruise and Gardner, 2008). A far inferior level of enhancement can be observed for the duplex cross-sections, arguably due to the different fabrication process.

Table 3.3: Material properties

Cross-section	Material Grade	$\sigma_{0.2}$ (N/mm ²)	$\sigma_{1.0}$ (N/mm ²)	σ_u (N/mm ²)	ϵ_f %
RHS 100×50×2	EN 1.4307/1.4301	324	356	634	54
RHS 100×50×3	EN 1.4307/1.4301	312	348	625	55
RHS 100×50×5	EN 1.4307/1.4301	310	351	639	54
RHS 100×50×3	EN 1.4462	555	-	765	32

3.3. 3-POINT BENDING TESTS

For each of the four cross-sections, one beam was tested in the 3-point bending configuration to study the response in major axis bending. The test arrangement and employed instrumentation for the 3-point bending tests is schematically shown in Fig. 3.4, whilst the overall setup is depicted in Fig. 3.5. All specimens had a total length of 1500 mm and the simply supported conditions were achieved with the use of steel rollers, which allowed both the rotation about the axis of bending and the axial displacement at the ends of the beams. The rollers were placed 75 mm inwards from each beam end, as a result the span of the beams was 1350 mm as shown in Fig. 3.4. In order to prevent web crippling (Cruise and Gardner, 2008), wooden blocks which were closely matching the dimensions of the tested beams, were inserted into the tubular specimens at the loading point and the supports.

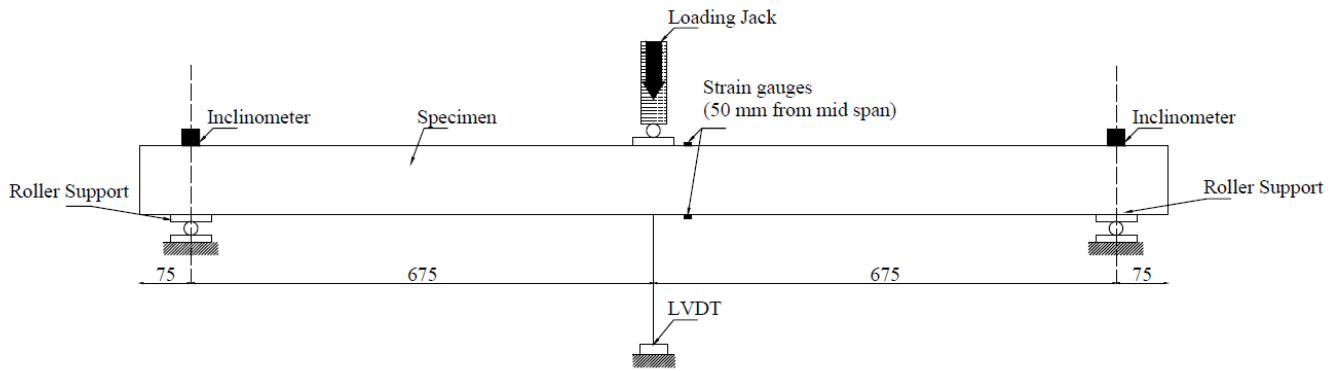


Fig. 3.4: Schematic 3-point bending test arrangement and instrumentation (dimensions in mm)



Fig. 3.5: Overall setup for 3-point bending tests

All beams tested in the 3-point bending configuration were loaded at mid-span by a hydraulic actuator at a rate of 1.5mm/min. Two inclinometers were placed at the supports, as shown in Fig. 3.4, in order to measure the end-rotations of the three-point bending tests. For each specimen, an angle grinder with a flapper wheel was used to remove the mill scale from the steel surface at the gauges location. Once acetone was applied to remove the collected dust on

the specified locations, two strain gauges were attached; one at the top and one at the bottom flange, at a distance of 50 mm from the loading point, in order to measure the extreme tensile and compressive strains that occur during the bending tests. Moreover, one LVDT was located at the loading point of the 3-point bending tests, in order to measure the vertical deflection of the mid-span. The Squirrel data logger was used for recording the load, strains, end-rotations and mid-span displacements at 2 sec intervals.

3.4. 4-POINT BENDING TESTS

The 4-point bending test arrangement was similar to the 3-point bending tests, as shown schematically in Fig. 3.6. Two equal point loads were applied at a distance equal to one-third of the clear span length from each end support via a spreader beam, which was positioned between the loading jack and two steel rollers, resting on the top flange of the specimens at the loading points and loaded at mid-span via a hydraulic actuator. As with the 3-point bending tests, wooden blocks were inserted within the tubes at the two loading points and supports to prevent web crippling.

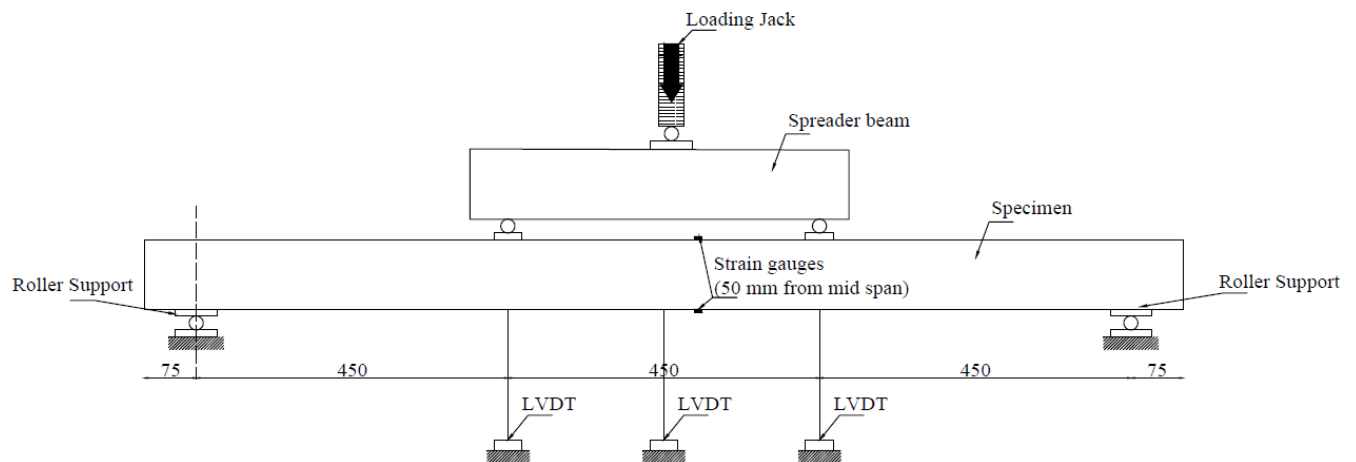


Fig. 3.6: Schematic 4-point bending test arrangement and instrumentation (dimensions in mm)

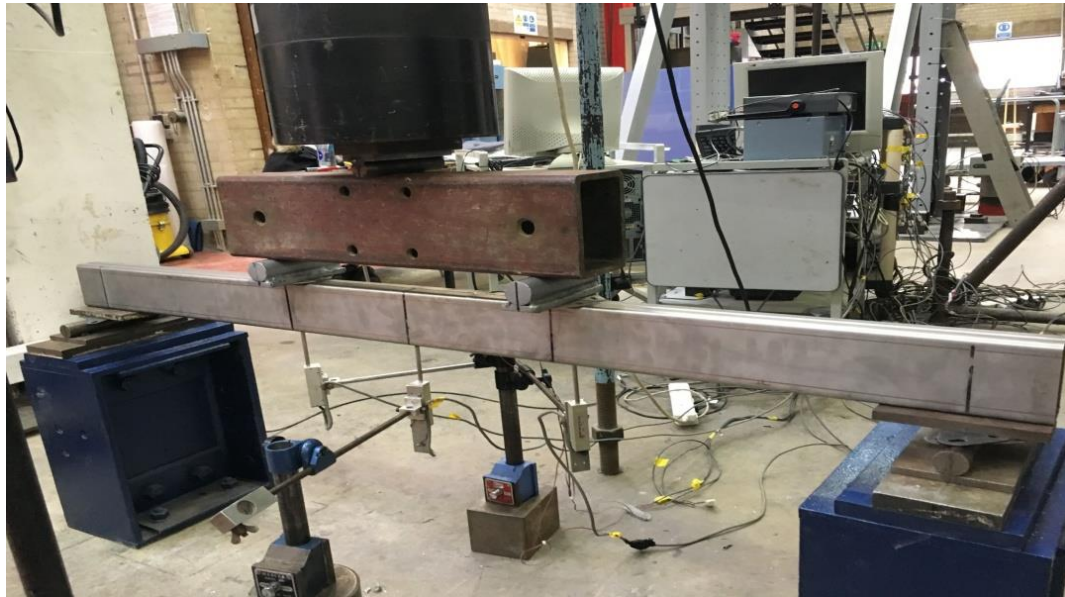


Fig. 3.7: Overall setup for 4-point bending tests

The overall setup is depicted in Fig. 3.7. Identical to the 3-point bending tests, two strain gauges were attached on the polished surfaces at a distance 50 mm from the mid-point of the span; one at the top and one at the bottom flange, in order to measure the extreme tensile and compressive strains. Three LVDTs were used in order to measure the vertical displacement of the beam; two LVDTs were placed at the loading points and one at the mid-span.

3.5. TESTS ON CONTINUOUS BEAMS

In order to determine the redistribution capacity of austenitic and duplex stainless steel continuous beams, four two-span structural configurations were subsequently conducted on the same cross-section sizes and material employed for the simply supported beams. All specimens had a total length of 3000 mm. Preliminary investigations were conducted in order to find a loading configuration that would allow significant moment redistribution, without repeating the structural arrangements examined in past publications (Mirambell and Real,

2000; Real and Mirambell, 2005; Theofanous et al., 2014; Arrayago and Real, 2016). It was decided to configure two equal spans with the one being doubly loaded compared to the other (i.e. one span loaded with a concentric load “ $P/3$ ” and the other one with “ $2P/3$ ”, where P the reference total load), considering the case of major axis bending only.

The continuous beam test arrangement is shown schematically in Fig. 3.8. The simply supported conditions were achieved with the use of steel rollers at the three supports. The clear span between the supports was 1425 mm. The instrumentation included two load cells, four inclinometers, four strain gauges and two LVDTs. The load cells were used to measure the reaction forces. The inclinometers were used to measure the rotations in the two end supports and in the two sides of the central support. As with the 3-point bending and 4-point bending tests, an angle grinder with a flapper wheel and acetone were used, in order to remove the mill scale and the collected dust from the gauges location. The strain gauges were affixed at a distance 50 mm from the mid-span and from the “ $2P/3$ ” loading point and their readings were used to ensure that no axial restraint was provided by the end rollers. The LVDTs were used to record the two vertical mid-span displacements. Similarly to the simply supported beams, in order to prevent web crippling failure wooden blocks were inserted in the tubular specimens at the loading points and the supports. In order to prevent local bearing failure, steel blocks of 15 mm thickness were used for the application of the load and at the end rollers. A spreader beam eccentrically loaded, was used to ensure the required loading configuration. The load was assigned vertically with a loading rate of 1.5 mm/min. The Squirrel data logger was used for recording the load, strains, end-rotations, reaction forces and mid-span displacements at 2 sec intervals. A photograph from the overall set up is given in Fig. 3.9.

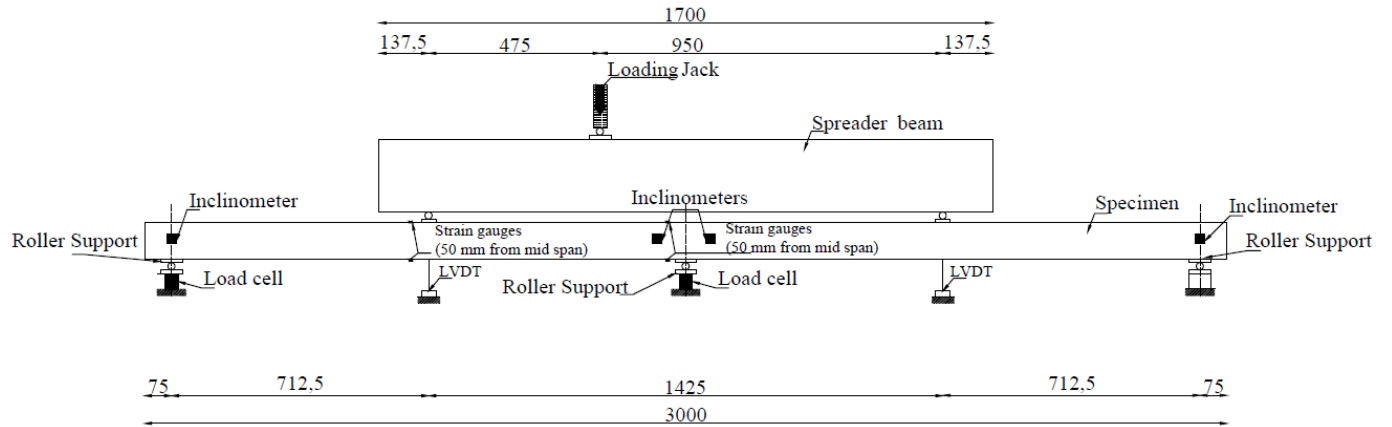


Fig. 3.8: Schematic continuous beam test arrangement and instrumentation (dimensions in mm)



Fig. 3.9: Overall setup for continuous beams

3.6. RESULTS

3.6.1. Simply supported beam test results

In Fig. 3.10, the moment-rotation and moment-curvature response of all specimens are depicted for the 3-point bending and 4-point bending tests respectively. To facilitate the comparison between the responses exhibited by the tested sections, the curves are displayed in a non-dimensional format, where the moments are normalized by the plastic moment resistance M_{pl} and the rotations θ and curvatures k are normalized by the elastic part of the rotation θ_{pl} or elastic part of the curvature k_{pl} corresponding to M_{pl} respectively, which are obtained from Eq. 23 and 24:

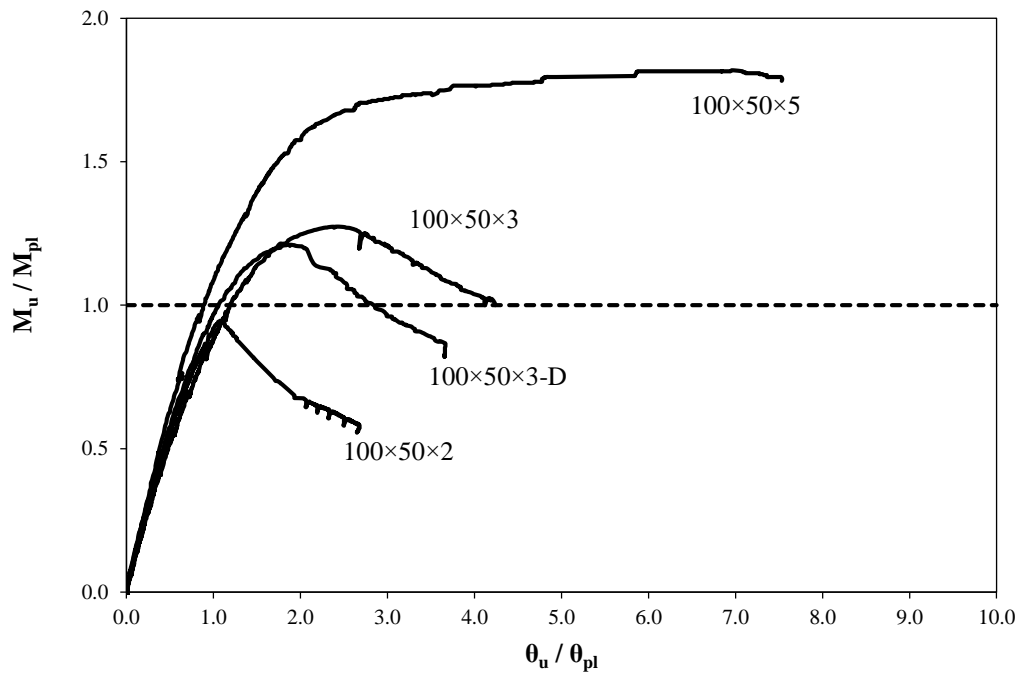
$$\theta_{pl} = \frac{M_{pl}L}{2EI} \quad (23)$$

$$k_{pl} = \frac{M_{pl}}{EI} \quad (24)$$

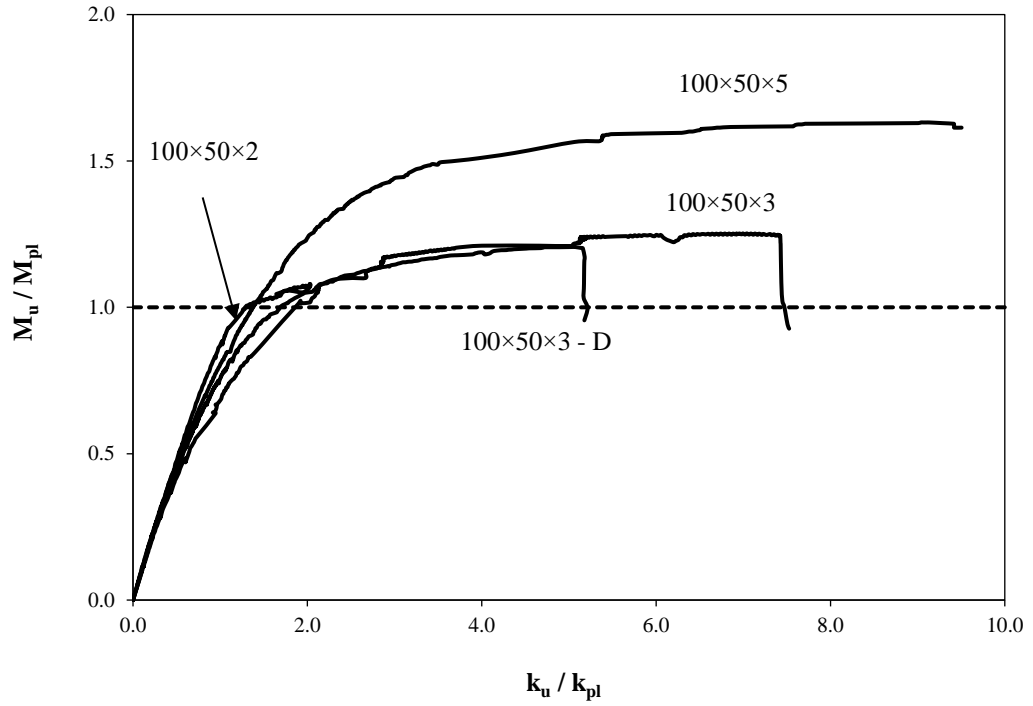
Key experimental results, including the moment resistance M_u , the ratios of the ultimate moment to the elastic and plastic moment resistance (M_u/M_{el} and M_u/M_{pl} respectively) and the rotation capacity R are reported in Table 3. The rotation capacity is defined by Eq. 25, where θ_u (k_u) refers to the total rotation (total curvature) at mid-span when the moment-rotation (moment-curvature) curve falls back below M_{pl} and are obtained from the tests (Refer to Chapter 2, Fig. 2.12 for a detailed description of rotation capacity from moment rotation graphs). No rotation capacity is defined for specimens failing prior to reaching M_{pl} . All failed specimens are depicted in Fig. 3.11. All failure modes relate to local buckling of the

compression flange and the upper part of the web. For the 3-point tests the local buckling was observed adjacent to the mid-span, where the load was applied. As for the 4-point test, the local buckling was observed, adjacent to one of the two loads location. It should be noted that significant inelastic deformations are evident for stockier sections, whilst local buckling occurred in the more slender sections with little evidence of permanent deformation:

$$R = \frac{\theta_u}{\theta_{pl}} - 1 \qquad R = \frac{k_u}{k_{pl}} - 1 \qquad (25)$$



a) 3-point bending tests



b) 4-point bending tests

Fig. 3.10: Normalized moment-rotation and moment-curvature response



a) 3-point bending tests



b) 4-point bending tests

Fig. 3.11: Failure modes of 3-point bending and 4-point bending tests

Table 3.4: Key experimental results from 3-point and 4-point bending tests

Cross-section	Test configuration	M_u (kNm)	M_u/M_{el}	M_u/M_{pl}	R
RHS 100×50×2	3-point bending	7.41	1.18	0.96	N/A
RHS 100×50×3		15.51	1.59	1.28	3.23
RHS 100×50×5		36.86	2.33	1.82	6.53
RHS 100×50×3-D		18.08	1.50	1.20	1.76
RHS 100×50×2	4-point bending	8.46	1.35	1.10	0.48
RHS 100×50×3		15.21	1.56	1.25	6.46
RHS 100×50×5		33.08	2.09	1.63	8.51
RHS 100×50×3-D		18.13	1.51	1.21	4.21

* N/A = Not applicable for cross-section with no rotational capacity R

3.6.2. Continuous beam test results

The key results are summarized in Table 3.5, where F_u is the experimental load at collapse, δ_u is the vertical displacement at “2P/3” loading point at collapse, θ_u is the end-rotation of the most heavily loaded span at collapse and F_{coll} is the theoretical plastic collapse load evaluated in line with classical plastic analysis procedures, considering rigid-plastic material response. As anticipated, all specimens failed by developing a distinct plastic hinge at “2P/3” loading point, followed by a second plastic hinge at the central support. The experimental response is shown in Fig. 3.12, where the load is plotted against the vertical displacement at “2P/3” loading point for all four specimens. The load normalized by the F_{coll} is plotted against the maximum end-rotation in Fig. 3.13. The evolution of the support to span moment ratio (M_{supp}/M_{span}) against the increasing vertical displacement at “2P/3” loading point is shown in Fig. 3.14 for the most slender and the stockiest specimen. The horizontal lines of 1.29 and 1.0 correspond to the theoretical moment ratios of the elastic and rigid plastic analysis respectively and the vertical lines pass through the displacement at which the ultimate load occurred. As can be seen for the stockiest 100×50×5 specimen, the moment ratio is equal to the elastic ratio at the initial stages of loading and fall to unity (i.e. the plastic ratio) at the ultimate load, after yielding, plastic spreading and moment redistribution has taken place. The specimen 100×50×2 failed in smaller strains, before significant moment redistribution had occurred. Given that the aforementioned specimen achieved very small deformation capacity in the respective 4-point test, this response was anticipated. Note that as it will be discussed in Chapter 4, this is a Class 2 section according to Eurocode (EN 1993-1-4+A1, 2015) (i.e. not aimed for plastic design).

Table 3.5: Key results from continuous beam tests

Cross-section	Class (EN 1993-1-4+A1, 2015)	F_u (kN)	F_{coll} (kN)	δ_u (mm)	θ_u (deg)
RHS 100×50×2	2	47.94	48.66	15.44	1.59
RHS 100×50×3	1	78.85	76.73	19.55	2.01
RHS 100×50×5	1	216.60	128.04	46.86	6.02
RHS 100×50×3-D	1	108.86	94.88	30.95	4.16

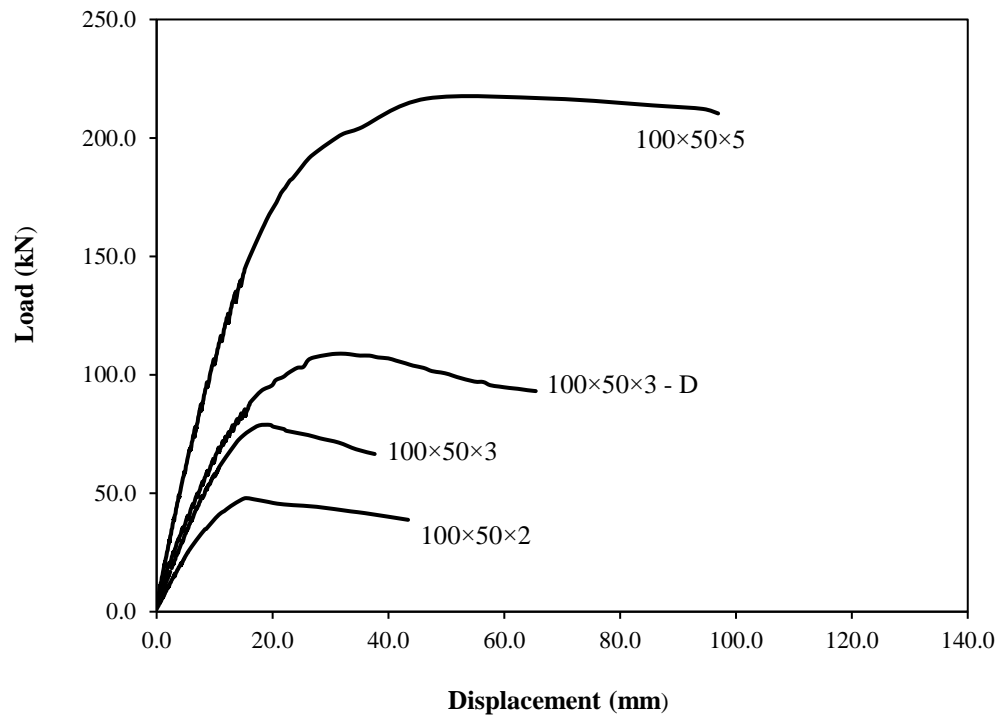


Fig. 3.12: Load-displacement continuous beam tests

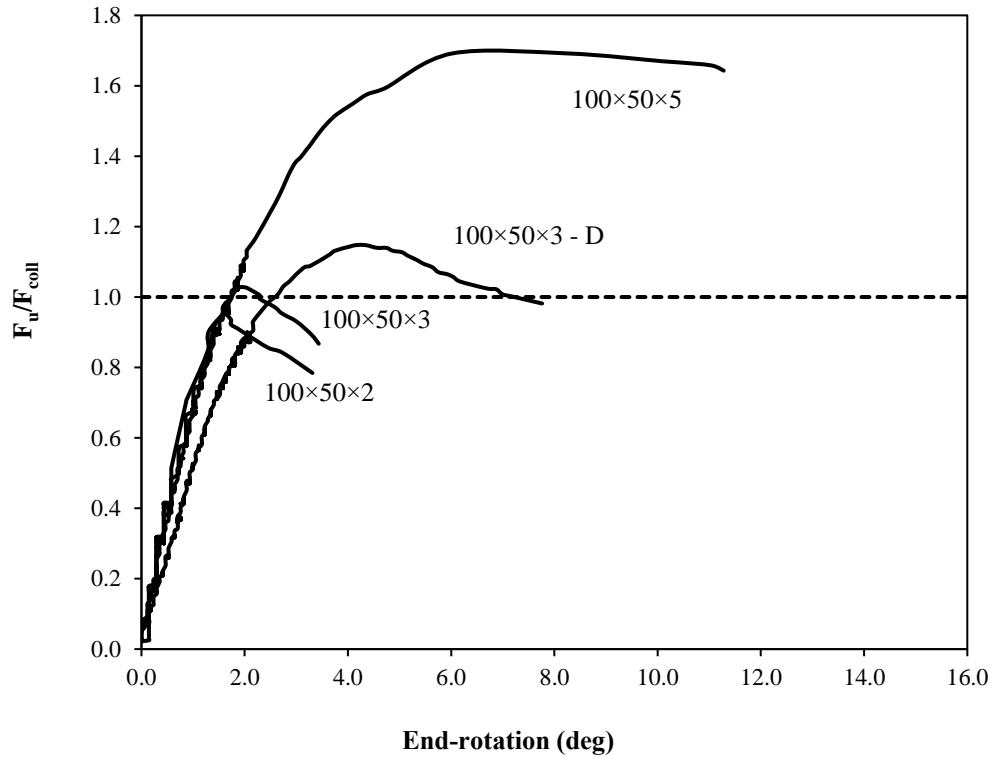


Fig. 3.13: Normalized force-end-rotation continuous beam tests

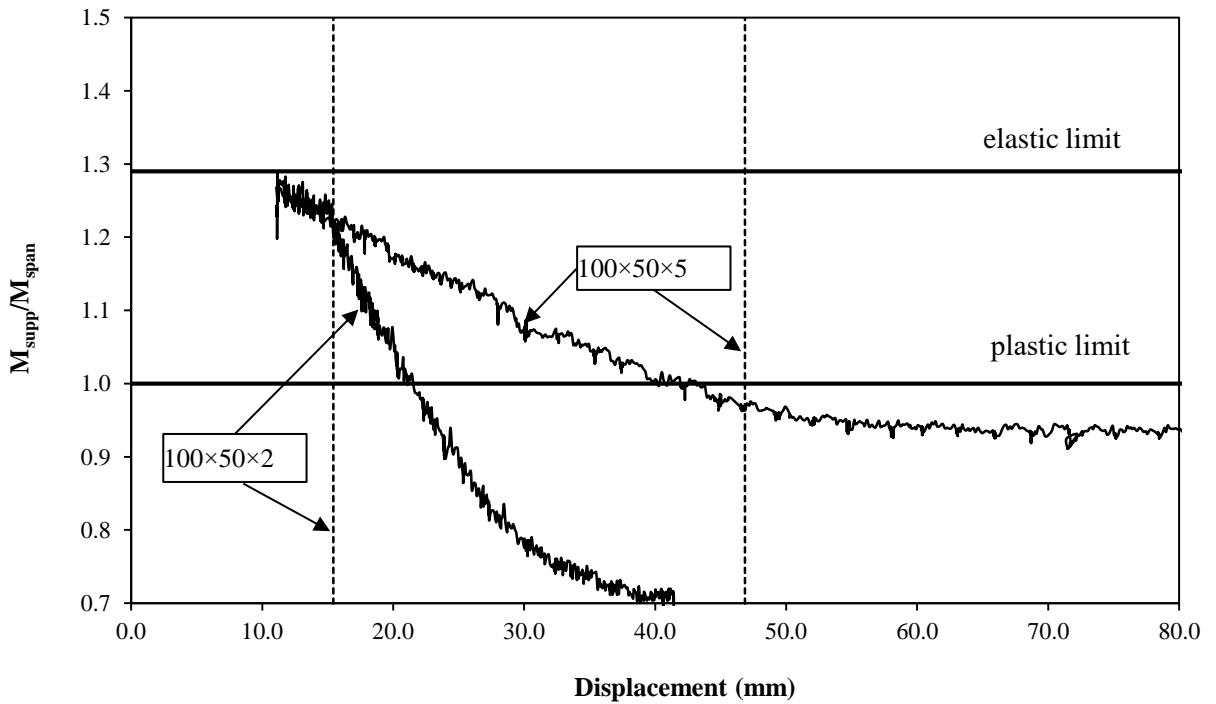


Fig. 3.14: Evolution of support to span moment ratio with increasing displacement

CHAPTER 4

NUMERICAL MODELLING OF STAINLESS STEEL BEAMS

The numerical study reported in this Chapter was presented by the PhD candidate at the 5th International Experts Seminar on Stainless Steel Structures on 20/09 in London. The research reported herein was published by Gkantou et al. (2019).

4.1. DEVELOPMENT OF THE MODELS

Finite element models of stainless steel SHS and RHS were developed and validated against twelve test data reported by Gkantou et al. (2019) and fifteen test data reported by Theofanous et al. (2014). All the numerical studies in this thesis were produced with the use of finite element analysis package ABAQUS (2007).

Finite element models were developed using Shell elements in accordance with the modelling recommendations set in (Gardner and Nethercot, 2004). For the initial modelling of bending

tests, the reduced integration 4-noded shell elements termed S4R were used, which are suitable for either thin or thick shell applications (ABAQUS, 2007) and allow for finite membrane strains, a highly desirable feature when modelling plate buckling at large strains. Precise geometric dimensions were incorporated on the FE models based on the measured section geometries reported by Gkantou et al. (2019) and Theofanous et al. (2014). To increase computational efficiency, the symmetry in boundary conditions, loading and failure mode was exploited and only half the cross-section in the plane of loading was simulated, whilst suitable symmetry boundary conditions were applied along the plane of symmetry. The assumed material response was incorporated the plastic response of stainless steel by assuming the Von Mises yield criterion and an isotropic hardening rule. The material properties reported by Gkantou et al. (2019) and Theofanous et al. (2014) were utilized in the FE models. Based on ABAQUS requirements, the continuous engineering stress-strain curve measured by the coupon test was converted into the true stress σ_{true} -log plastic strain ϵ_{ln}^{pl} format and introduced in ABAQUS as a piecewise multilinear curve. The engineering stress-strain curve was discretized and represented by a total number of 25 points and then these points were converted into true stress-log plastic strain with the use of Eq. 19 and Eq. 20 as it was mentioned in literature review (Chapter 2). The engineering stress-strain and the true stress-log plastic curves, which were used for the validation of the models in ABAQUS are shown in Fig. 4.1 below.

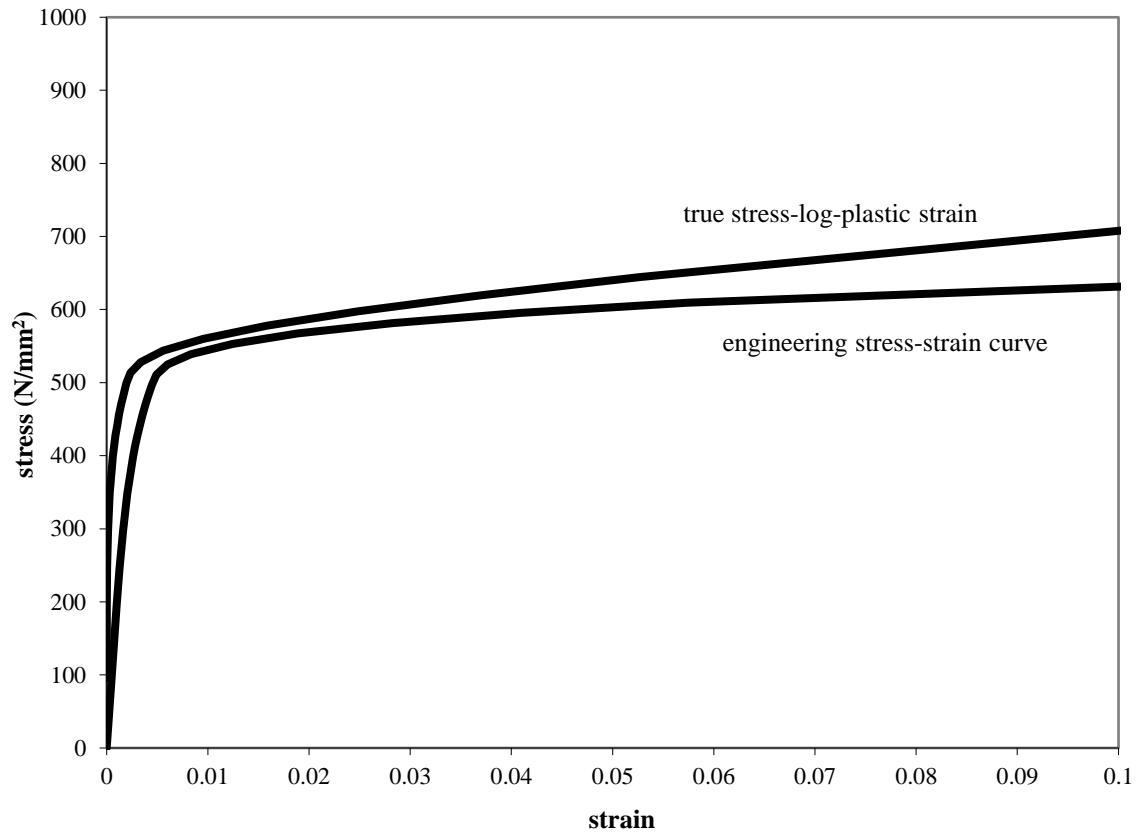


Fig. 4.1: Engineering stress-strain and true stress-log plastic curves

Since all modelled sections are cold-formed, enhanced strength is expected in the corner regions. This is due to the significant strength enhancements that produced in corner regions by the plastic deformation during forming. Moreover, these strength enhancements extend beyond the curve corners into the flat regions as discussed in the literature review. Based on a series of parametric studies (Gardner and Nethercot, 2004; Ashraf et al., 2006), it was concluded that for accurate results, the corner properties should be assumed to extend to a distance equal twice the thickness of the section beyond the curved corner regions. This approach has been followed herein.

In order to achieve accurate results within reasonable computational time, a uniform mesh density throughout the models is employed. A suitable mesh size was found to vary between 4 mm to 6 mm, whilst a minimum of 3 elements was employed along each of the 4 curved quarter circular corner regions of the cross-sections as shown in Fig. 4.2. The end supports for both simply supported and continuous beam models were constrained with the use of kinematic coupling in order to avoid deformations in these points. For the simply supported beams distributing coupling was used at the loading points. Similarly, to the simply supported beams, distributing coupling was used at the loading points and at the mid support of the continuous beams. The distributing coupling allows relative deformation of the cross-section and at the same time allows a distribution of stresses, so that the stiffer points take more load. This was in line with the use of wooden blocks inserted in the sections subjected to a point load, which stiffened the sections locally and allowed the loads to be distributed throughout the section but did not completely prevent any cross-section deformation.

In the simply supported beams, the left-hand side support was modelled as a roller support by restraining the translational degrees of freedom (DoF) at the bottom of the flange; the point load was applied at the web top corner arc junction, in order to prevent the section from squashing locally under the point load. In the continuous beams the left-hand side and the mid support were modelled as roller supports by restraining the translational DoF at the bottom of the flange. In the same way with the simply supported beams the point loads were applied at the web top corner arc junction.

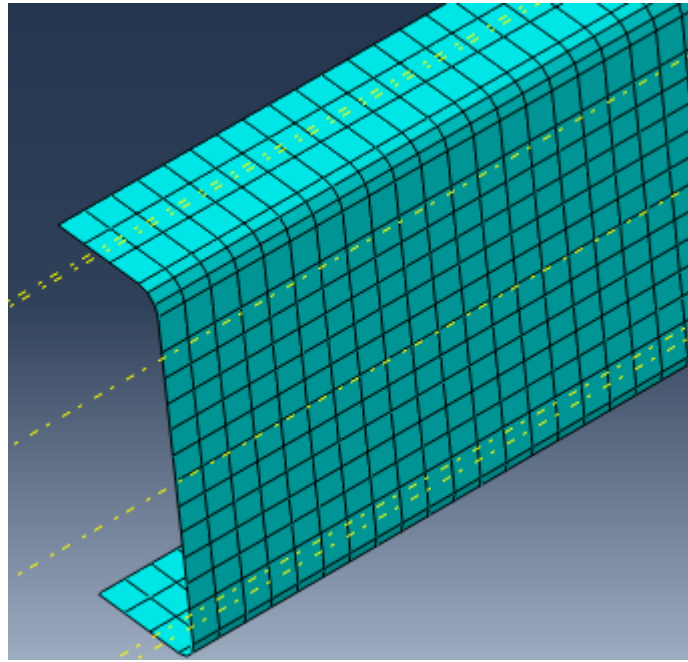


Fig. 4.2: Mesh configuration

Initial geometric imperfections can influence the structural responses of structural members. Therefore, it is of high importance to account for these initial imperfections in the numerical simulations. According previous studies (Zhou et al., 2013), local geometric imperfections can be incorporated in the FE models in the form of the lowest elastic buckling mode shape and the amplitude of local imperfection can be considered as a fixed fraction of the component thickness t ($t/10$, $t/100$) (Chan and Gardner, 2008b).

To conclude, for the numerical simulation of the FE models the following steps were conducted. First, a linear buckling analysis was conducted, in order to extract the buckling mode shapes associated with the lowest critical buckling stress (Fig. 4.3 and Fig. 4.4). Then, these buckling mode shapes were utilized in the nonlinear static analysis, to introduce the shape of the geometric imperfections. For the performance of the nonlinear static analysis, the RIKS procedure was used. The RIKS method, which is a variant of the arc length method, is

generally used to predict unstable, geometrically nonlinear collapse of a structure. Additionally, RIKS method uses the load magnitude as an additional unknown; it solves simultaneously for loads and displacements (ABAQUS, 2007) and is therefore capable of tracing the post ultimate response of structures.

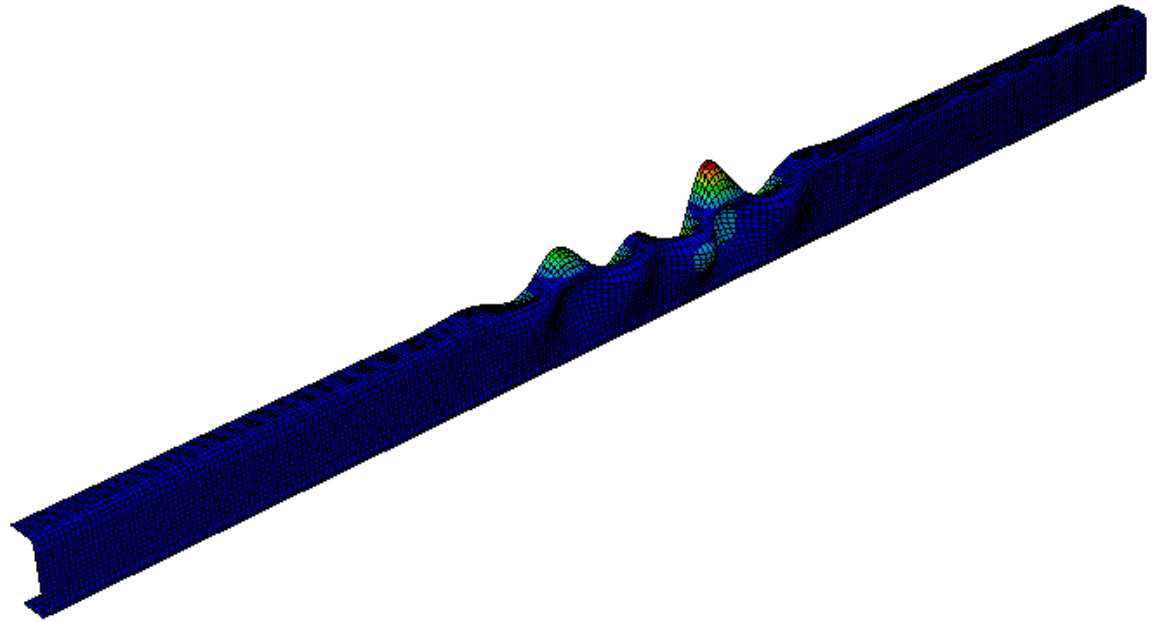


Fig. 4.3: Buckling mode shape for 3-point bending beam

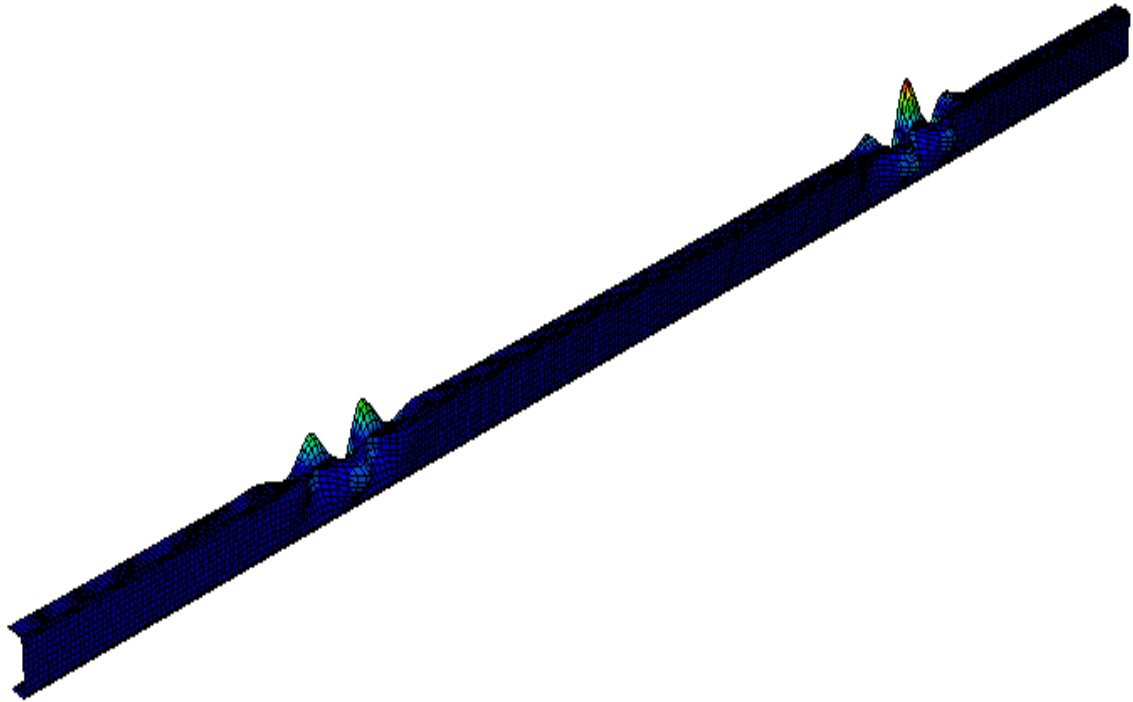


Fig. 4.4: Buckling mode shape for continuous beam

4.2. VALIDATION OF THE FE MODELS

In this section the numerical results are compared against the test results reported by Gkantou et al. (2019) and Theofanous et al. (2014), to assess the accuracy of the models and to verify their suitability for performing parametric studies.

4.2.1. Validation of the FE models against tests by Theofanous et al. (2014)

According to the experimental tests (Theofanous et al., 2014), the simply supported SHS and RHS beams had a total length of 1200 mm; the beams were supported by two roller supports, which allowed free axial displacement. The clear span between the roller supports was 1100

mm, since the rollers were placed 50 mm inward from each beam end. To prevent web crippling at the supports points and at the loading point wooden blocks were placed. In order to validate the simply supported beams the normalized moment M/M_{pl} was plotted against the normalized rotation θ/θ_{pl} for both numerical and experimental results (Fig. 4.5 and Fig. 4.6). Based on the results excellent agreement between the experimental and numerical response in terms of initial stiffness, ultimate load and post ultimate response can be observed. For the optimum prediction of the initial imperfection amplitude, the ratios of the numerical ultimate moment over the experimental ultimate moment for the predicted imperfection amplitudes $t/10$ and $t/100$ are presented in Table 4.1. Typical experimental and numerical failure modes are shown in Fig. 4.7.

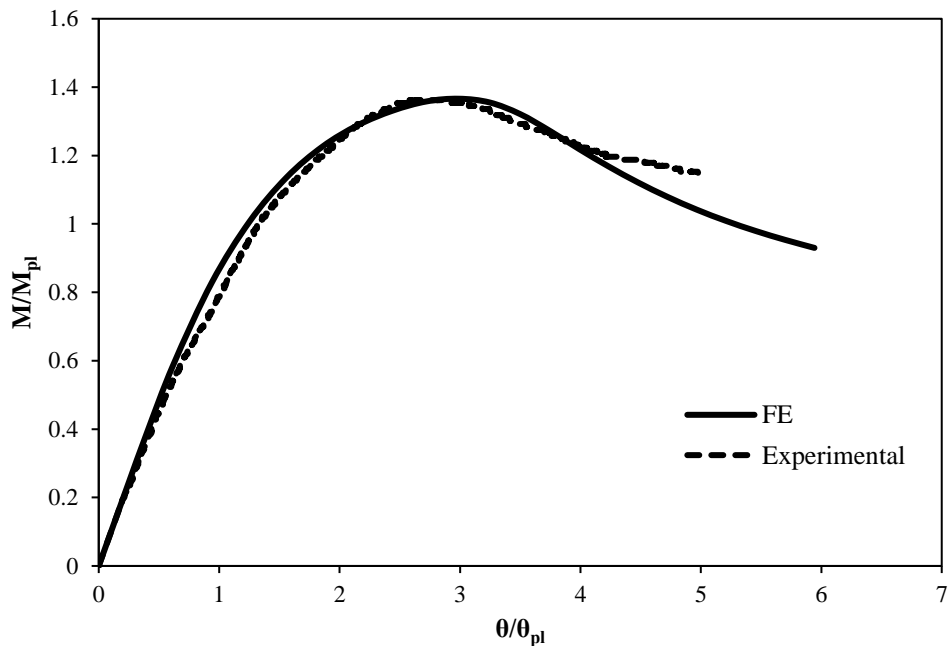


Fig. 4.5: Normalised moment-rotation curves for the section 60×60×3

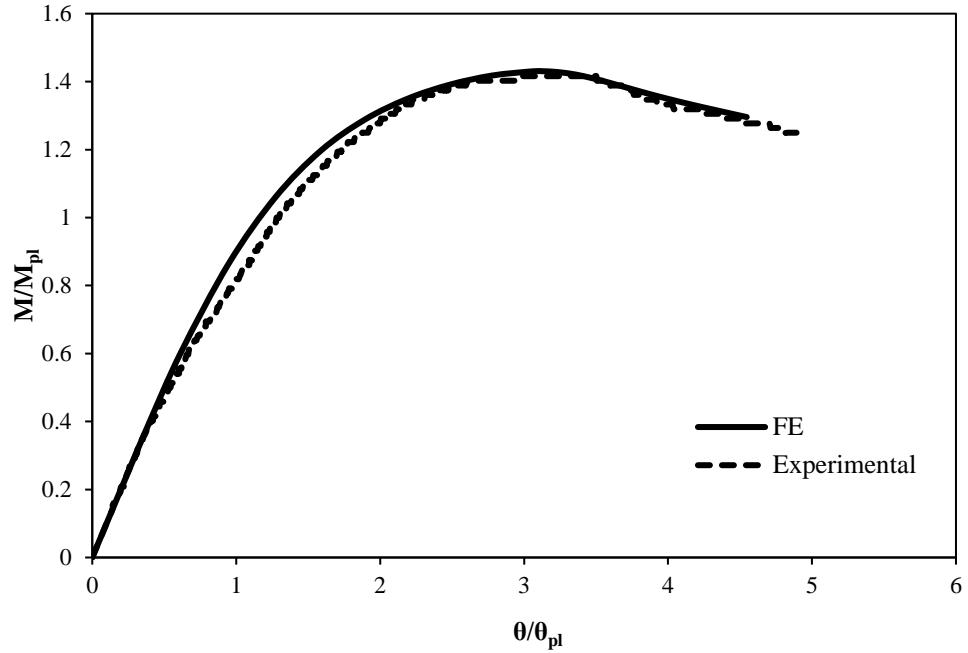


Fig. 4.6: Normalised moment-rotation curves for the section 60×40×3-MI

Table 4.1: Ratios of the numerical ultimate moments over the experimental ultimate moments

Section	$M_{u,FE} / M_{u,Test}$		
	No imper.	t/10	t/100
50×50×3	1.013	1.019	1.016
60×60×3	1.014	1.008	1.016
100×100×3	1.024	1.023	1.012
60×40×3-Major	1.081	1.053	1.086
60×40×3-Major	1.011	0.987	1.009
Mean	1.028	1.018	1.028
COV	1.011	0.024	0.032

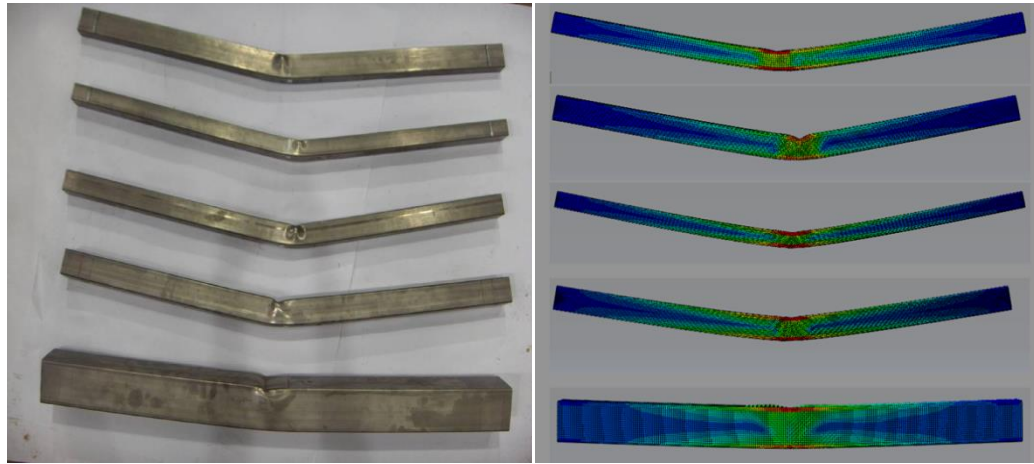


Fig. 4.7: Comparison between experimental and numerical failure modes for three-point bending tests

The continuous SHS and RHS beams had a total length of 2400 mm; the beams were supported by three roller supports, where the end rollers allowed free axial displacements. The clear span between the roller supports was 1100 mm, whilst at the end of each specimen further 100 mm was provided. At the support points and at the loading points wooden blocks were placed in order to prevent web crippling. Two symmetrical loading configurations were conducted. For the first one the loads were applied at the mid-span and in the second configuration the loads were applied at a distance equal to one-third of the clear span length from the central support.

Table 4.2 presents the ratios of the numerical ultimate loads over the experimental ultimate loads for continuous beams, for the predicted imperfection amplitudes of $t/10$ and $t/100$. It is clear that better results are taken when the initial imperfection amplitude of $t/100$ is used. Furthermore, for all the specimens the applied load F and the corresponding average of point loads displacement were compared between the experimental and finite element results. Overall excellent agreement between the numerical and the experimental results was achieved. The bending response was accurately predicted, including the initial stiffness, the ultimate

moment capacity and the failure modes (Fig. 4.8 and Fig. 4.9). This model was therefore employed in parametric studies, which are presented in this thesis. The comparison between experimental and numerical failure modes is shown in Fig. 4.10.

Table 4.2: $F_{u,FE}/F_{u,test}$ for the imperfection amplitudes considered

Sections	$F_{u,FE}/F_{u,test}$		
	No imp.	t/10	t/100
50×50×3-1	0.971	0.941	0.972
50×50×3-2	0.950	0.936	0.949
60×60×3-1	0.979	0.948	0.972
60×60×3-2	1.029	1.029	1.029
100×100×3-1	1.029	1.010	1.017
100×100×3-2	1.040	1.027	1.028
60×40×3-MA-1	1.011	0.991	1.010
60×40×3-MA-2	1.022	0.997	1.022
60×40×3-MI-1	0.974	0.971	0.971
60×40×3-MI-2	0.955	0.936	0.952
MEAN	0.996	0.979	0.992
COV	0.034	0.038	0.032

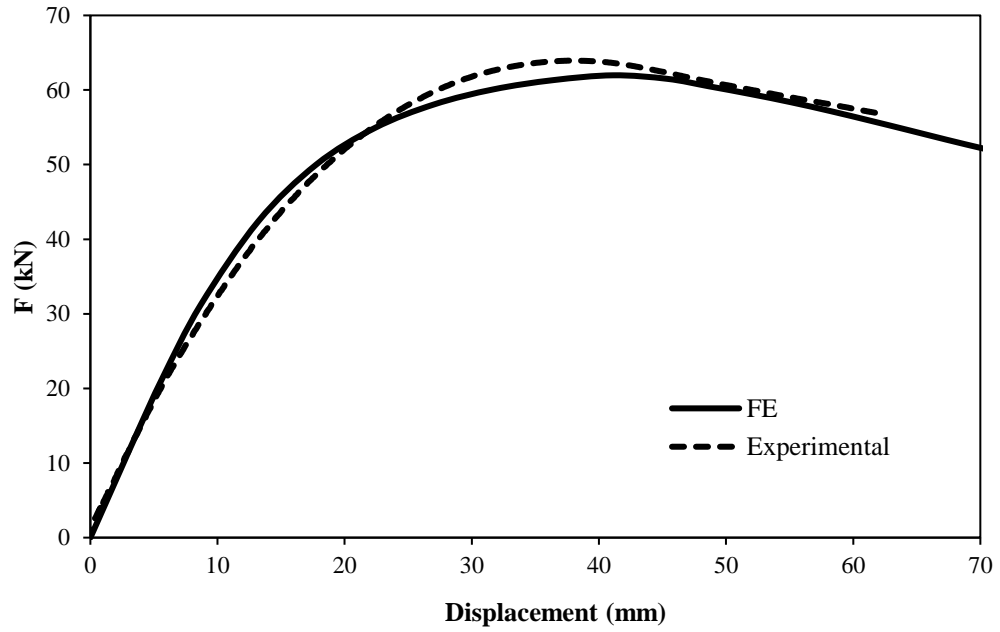


Fig. 4.8: Load – mid-span displacement response for the section 60×40×3-MI

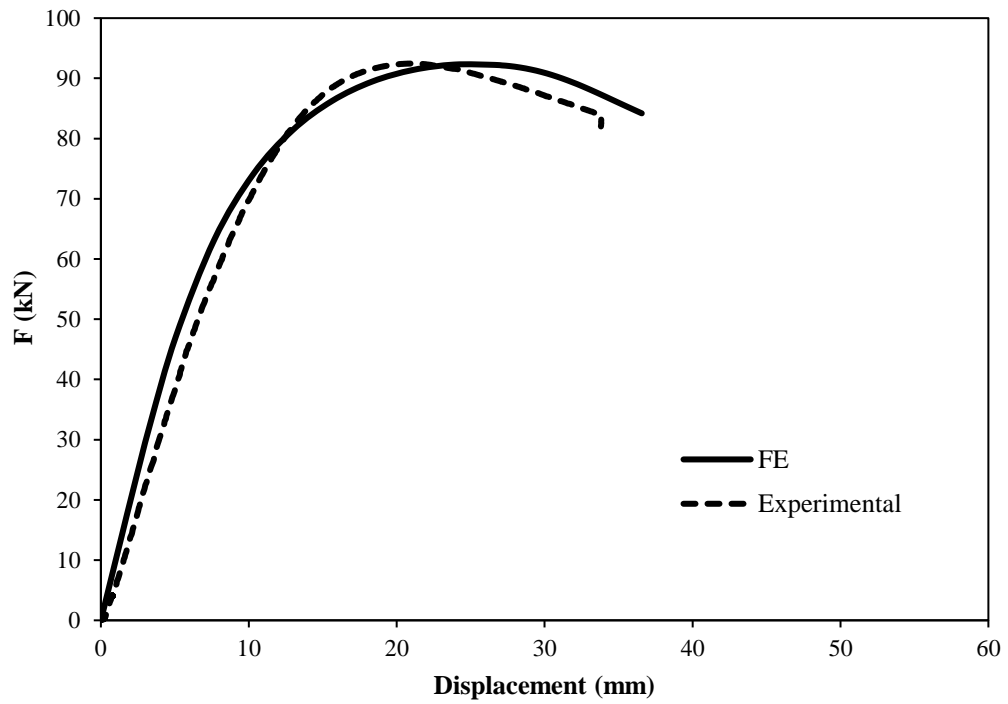


Fig. 4.9: Load – mid-span displacement response for the section 60×60×3

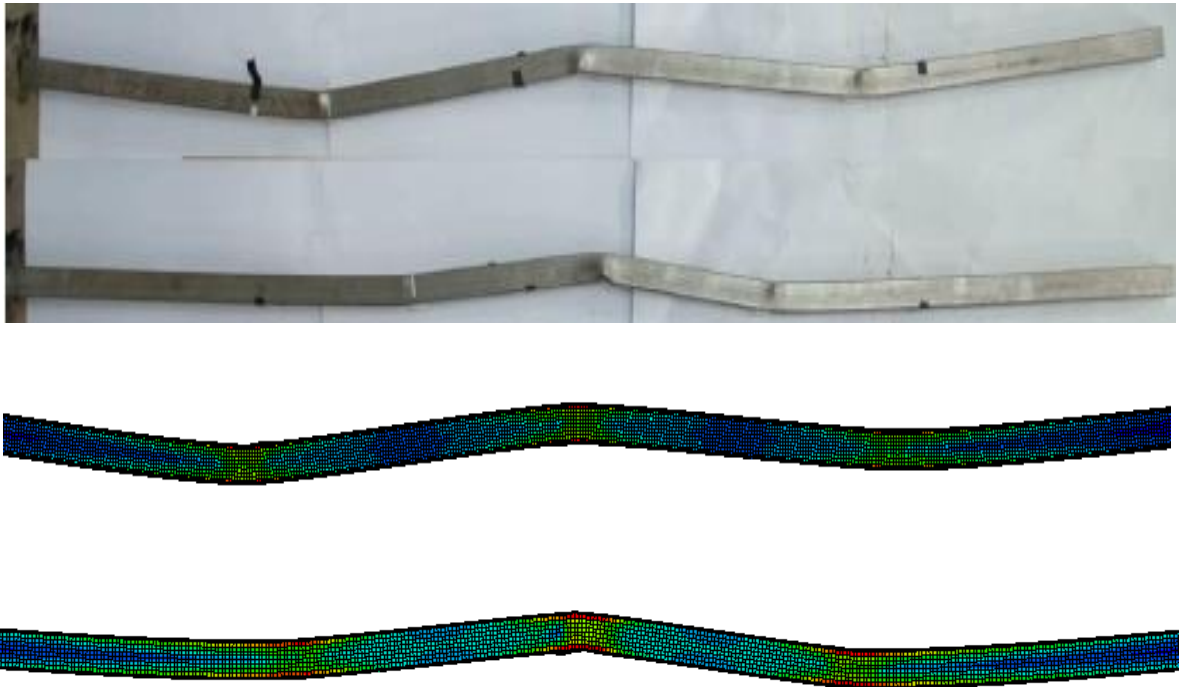


Fig. 4.10: Comparison between experimental and numerical failure modes for continuous beams with point loads applied at mid-span and at one third from the centre span

4.2.2. Validation of the FE models against tests by Gkantou et al. (2019)

Following the aforementioned modelling assumptions in section 4.1, the numerical results are compared with the experimental results that were produced by Gkantou et al. (2019), in the laboratory of University of Birmingham. Table 4.3 shows the numerical over experimental ultimate load ratios for the geometric imperfection amplitudes $t/10$, $t/50$ and $t/100$ that are considered. It can be observed that the 3-point bending models display the highest sensitivity to the initial geometric imperfection amplitude considered, whilst the 4-point bending models and the continuous beam models are less affected. In order to validate the 3-point bending and 4-point bending models the normalized moment M/M_{pl} was plotted against the normalized rotation θ/θ_{pl} for both numerical and experimental results (Fig. 4.11 and Fig. 4.12), while for

the continuous beam tests typical load-deformation curves are shown in Fig. 4.13. A good agreement between the experimental and numerical response in terms of initial stiffness, ultimate load and post ultimate response can be observed. Overall, best agreement between the numerical and the experimental results has been achieved for the $t/100$ imperfection magnitude which was adopted for the subsequent parametric studies. Finally, typical experimental and numerical failure modes are illustrated in Fig. 4.14.

Table 4.3: Validation of FE Models against the test results

	$F_{u,FE}/F_{u,test}$	$F_{u,FE}/F_{u,test}$	$F_{u,FE}/F_{u,test}$
Sections	$t/10$	$t/50$	$t/100$
3-point bending			
RHS 100×50×2	1.04	1.05	1.05
RHS 100×50×3	0.94	0.98	0.99
RHS 100×50×5	0.88	0.93	0.94
RHS 100×50×3-D	0.98	1.03	1.04
Mean	0.96	1.00	1.01
COV	0.07	0.05	0.05
4-point bending			
RHS 100×50×2	0.98	1.03	1.03
RHS 100×50×3	0.92	0.97	0.98
RHS 100×50×5	0.95	1.02	1.02
RHS 100×50×3-D	0.97	0.99	0.99
Mean	0.96	1.00	1.01
COV	0.03	0.03	0.02
Two span continuous beams			
RHS 100×50×2	0.91	0.92	0.92
RHS 100×50×3	1.04	1.04	1.04
RHS 100×50×5	0.89	0.90	0.91
RHS 100×50×3-D	0.95	0.95	0.95
Mean	0.95	0.95	0.96
COV	0.07	0.06	0.06
Overall Mean	0.95	0.98	0.99
Overall COV	0.05	0.05	0.05

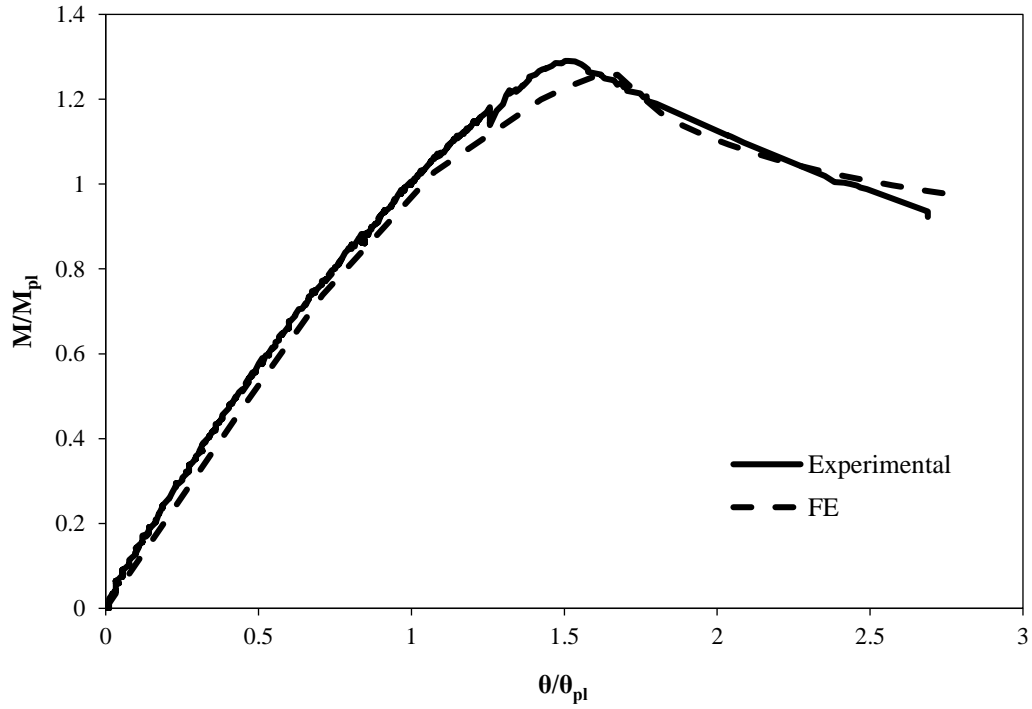


Fig. 4.11: Normalised moment-rotation curves for the section 100x50x2 3-point bending test

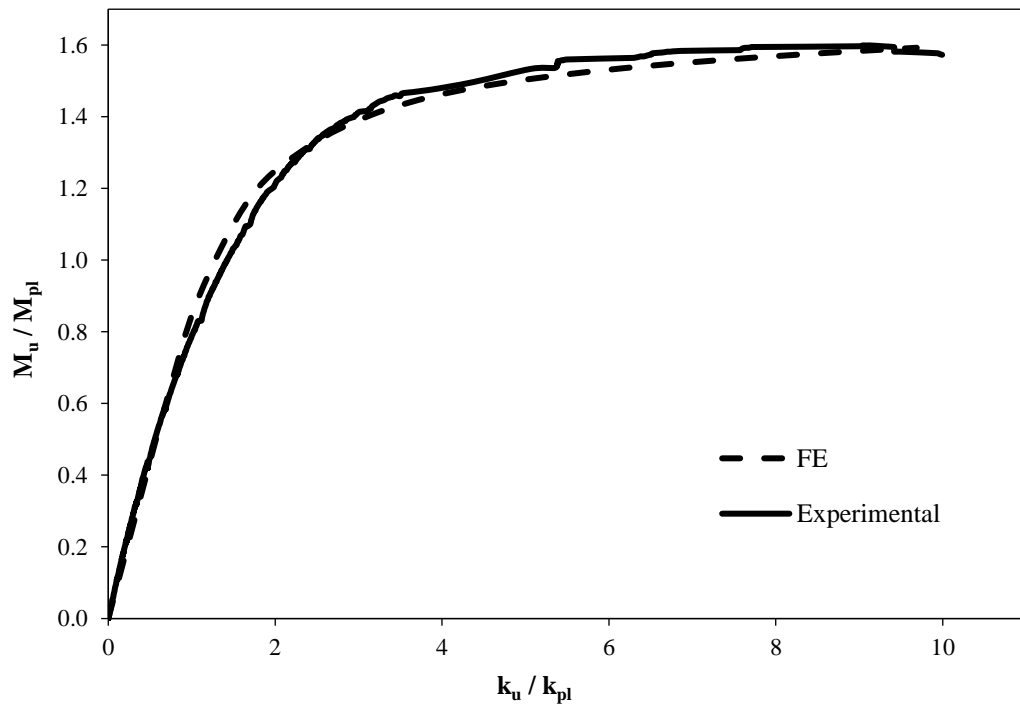


Fig. 4.12: Normalised moment-rotation curves for the section 100x50x5 4-point bending test

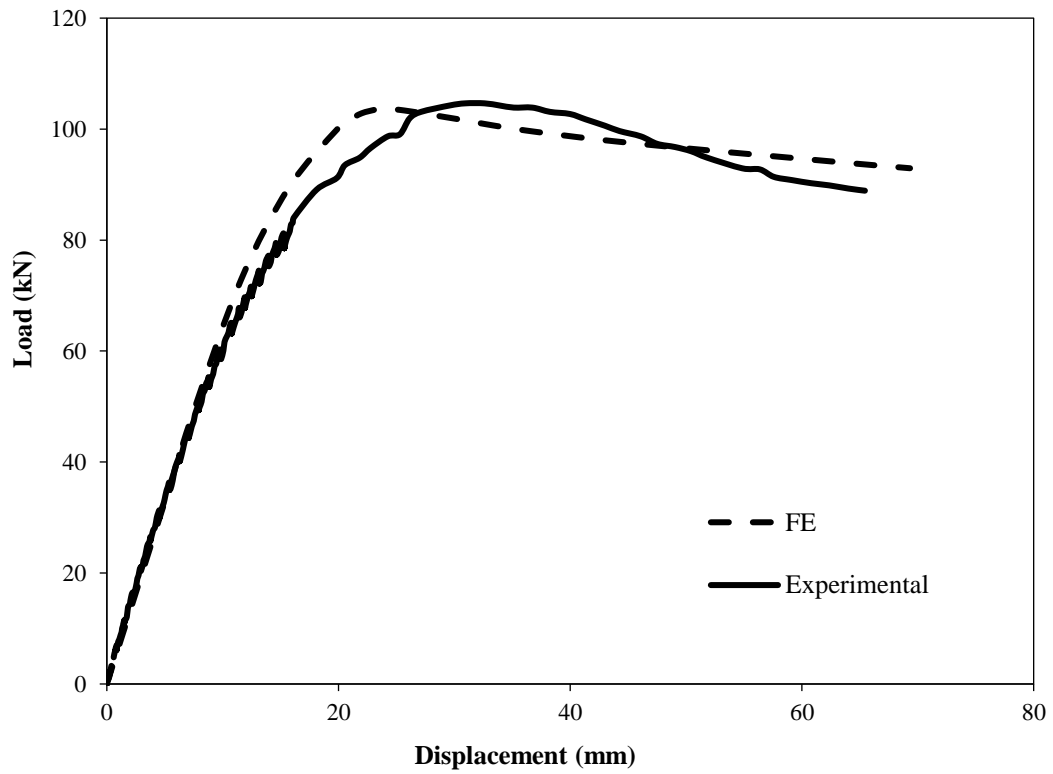
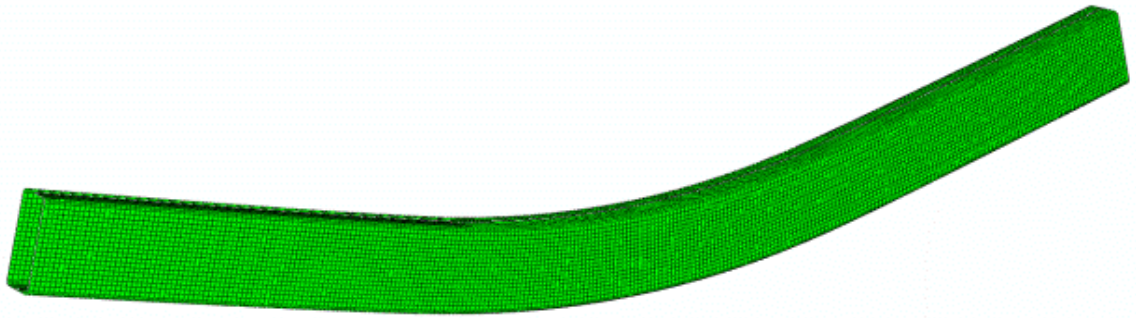


Fig. 4.13: Load – mid-span displacement response for the section 100×50×3-D continuous beam



a) RHS 100×50×2 3-point bending



b) RHS 100×50×5 4-point bending



c) RHS 100×50×5-D Continuous beams

Fig. 4.14: Comparison between experimental and numerical failure modes for simply supported and continuous beams

4.3. PARAMETRIC STUDIES

After the accurate replication of the experimental results reported by Gkantou et al. (2019) and Theofanous et al. (2014), the validated FE models were used to conduct parametric studies with the use of FE package ABAQUS (2007) version 6.14, in order to improve current understanding of the inelastic behaviour of stainless steel continuous beams. These parametric studies were carried out to expand the available structural performance data for various geometric parameters, such as cross-sectional slenderness, cross section aspect ratio, moment gradient and loading and structural arrangements, and to assess existing design codes (EN 1993-1-4+A1, 2015) and design recommendations for the design of continuous beams.

Initially, three cross-sections with aspect ratios equal to 1.0, 2.0 and 2.44 were considered, thus covering a wide range of aspect ratios. The aspect ratio of 2.44 is the limiting value beyond which the web subject to bending becomes more slender than the flange. For each of these models five thickness values, namely 2 mm, 3 mm, 4 mm, 6 mm and 8 mm, were considered to assess the effect of cross-section slenderness. For each section three span lengths, namely 1200 mm, 2400 mm and 2928 mm were considered. The five loading cases (LC1 to LC5) shown in Fig. 4.15 were considered for each of the 15 section geometries and 3 span lengths (P is the reference total load), thus resulting in a wide range of structural arrangements, moment gradients and required rotation capacities for a full moment redistribution, likely to occur in practice. Two sets of material properties defined in Table 4.4 are adopted, as representative for austenitic and lean duplex stainless steel grades. The mechanical properties were obtained, as a mean value from the pool of data reported by Groth

and Johansson (1990) and Theofanous et al. (2014) for austenitic and lean duplex stainless steel grades respectively.

Table 4.4: Material properties

Material	E (N/mm ²)	$\sigma_{0.2}$ (N/mm ²)	$\sigma_{1.0}$ (N/mm ²)	σ_u (N/mm ²)	n	n _{0.2,1.0}
Austenitic	200000	498	554	755	5.25	2.88
Lean Duplex	200000	693	743	797	7.9	3.67

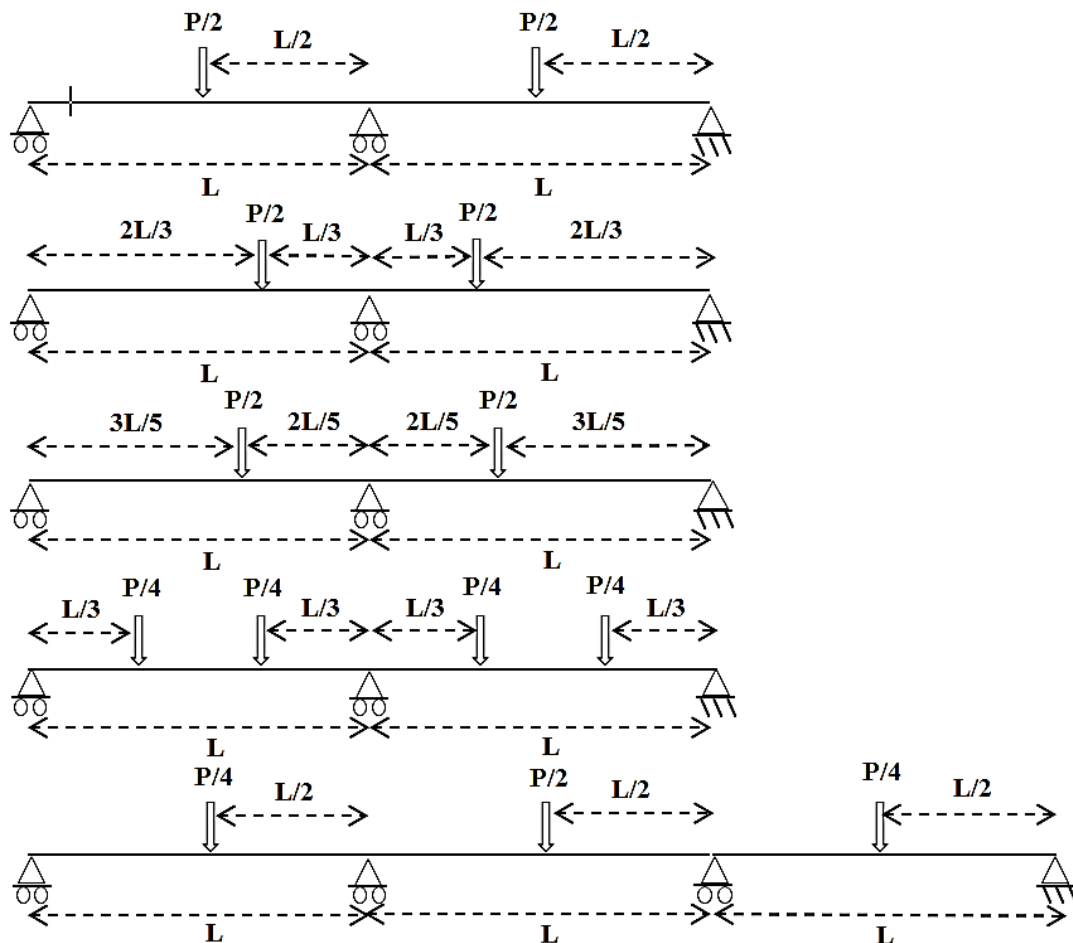
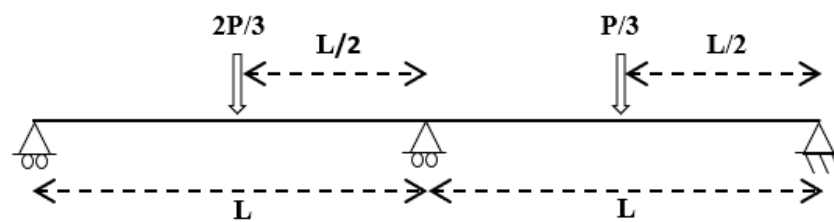


Fig. 4.15: Load cases considered in the parametric studies (LC1 to LC5)

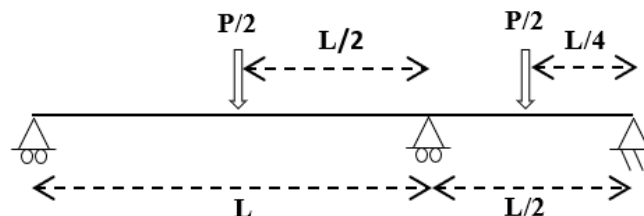
To further expand the available structural performance data, additional parametric studies were subsequently conducted, based on the material properties extracted from the tensile coupon tests, presented in Chapter 3 (Table 4.5). Three cross-sections aspect ratios, namely 1.0, 2.0 and 2.44, and four thicknesses, namely 2 mm, 3 mm, 4 mm and 5 mm, were considered. As it can be seen in Fig. 4.16, two load cases were considered (LC1.1 and LC2.1), where for LC1.1 it was decided to configure two equal spans of 2400 mm, with the one being doubly loaded compared to the other (one span loaded with a concentric load $P/3$ and the other one with $2P/3$). Contrary, in LC2.1 two unequal spans were considered (2400 mm and 1200 mm) with two equal loads ($P/2$) applied at mid spans.

Table 4.5: Material properties

Material	E (N/mm ²)	$\sigma_{0.2}$ (N/mm ²)	$\sigma_{1.0}$ (N/mm ²)	σ_u (N/mm ²)	n	$n_{0.2,1.0}$
Austenitic	197200	466	507	698.47	9.0	2.60
Duplex	200950	579	640	814.9	12	2.50



a) Load Case 1.1 (LC1.1)



b) Load Case 2.1 (LC2.1)

Fig. 4.16: Additional Load Cases considered in the parametric studies

For all models the introduced initial geometric imperfections corresponded to the lowest elastic buckling mode shape with an amplitude equal to $t/100$, which was shown to provide an excellent agreement with the experimental response. Based on the obtained ultimate capacity predictions, the accuracy of several design methods is assessed in Chapter 6.

CHAPTER 5

NUMERICAL INVESTIGATION OF STAINLESS STEEL PORTAL FRAMES

5.1. DEVELOPMENT OF MODEL

Most of the experimental data summarised in Chapter 2 for steel frames are too old and have not been reported in sufficient detail in terms of material properties, initial geometric imperfections and overall structural response; hence they cannot be utilized in this thesis. The most up-to-date experimental results of portal frames are reported by Walkinson and Hancock (1999), which are used for the validation of FE portal frames that will consequently be used for the conduction of parametric studies. In addition to being relatively recent, the three tests reported by Wilkinson and Hancock (1999) are on frames employing cold-formed RHS and consider the application of various ratios of horizontal to vertical loads to account for the effect of different combinations of snow and wind loading. Hence, they utilise members of similar geometry made of a nonlinear material, which exhibits similar behaviour to stainless

steels and are subjected to loading conditions relevant to the ones stainless steel are expected to experience. Moreover, the tests are reported in exceptional detail, give an accurate account of overall dimensions and cross-sectional dimensions, measured initial geometric imperfections, material properties for both flat and corner material and overall structural response until failure.

In this Chapter, finite element models of RHS portal frames are developed and validated against the aforementioned experimental tests (Wilkinson and Hancock, 1999). Upon successful validation, parametric studies are conducted on stainless steel portal frames of various geometric configurations. As for the FE modelling of the rest of the test conducted in this research, the finite element analysis package ABAQUS was used (2007). The use of both beam and shell elements was considered.

5.1.1. Modelling using beam elements

Beam elements are commonly used in engineering practice, due to their cost-effectiveness and ease of use. Facilitate code design checks since the obtained results are in terms of cross-sectional loads that can be easily used together with the code equations in an automated manner. The disadvantage of employing beam elements relate to their inability to obtain any information on cross-sectional deformation and local buckling, since the underlying assumption of beam elements is that cross-sections remain undeformed. However, if local buckling is not a major concern as would be the case for stocky cross-sections, FE models with beam elements can accurately predict the structural behaviour of portal frames by capturing global failure modes including member buckling and frame sway.

Three portal frames were modelled with the use of wire beam elements called B31, by incorporating the precise geometric dimensions reported by Walkinson and Hancock (1999). Each portal frame has a span of 7000 mm, a height at eaves of 3000 mm and a height at apex of 4000 mm. At the knee joints a 105° angle was employed between the steel column and the rafter. To incorporate the nonlinear material response of the Steel Grades used in the tests, namely C350 and C450 (Wilkinson and Hancock, 1999), the Von Mises criterion and isotropic hardening flow rule were assumed similar to Chapter 4. The exact cross-section geometries of the RHS 150×50×4 steel frames, reported in Table 5.1 (outer web depth d , outer flange width b , thickness t and external radius r_e), were replicated with the use of ABAQUS utility for defining beam profiles.

Table 5.1: Cross section geometries for portal frame tests (Walkinson and Hancock, 1999)

Frames	Cross-Section	Steel Grade	d (mm)	b (mm)	t (mm)	r_e (mm)
Frame 1	150×50×4	C350	150.5	50.4	3.94	7.5
Frame 2	150×50×4	C450	150.6	50.4	3.92	7.5
Frame 3	150×50×4	C450	150.6	50.4	3.92	7.5

With respect to the column base boundary conditions, in the experimental study (Wilkinson and Hancock, 1999), each column was pinned to two vertical steel plates through a 30 mm diameter high strength steel pin which was running through the neutral axis of the RHS. Each vertical steel plate was welded on top of a base plate which was fastened on the strong floor via high strength fully tensioned bolts. To best replicate the aforementioned experimental support conditions, pin support conditions were modelled in ABAQUS. Furthermore, three-point loads were applied for each frame, two equal vertical loads at the mid-span of each rafter

to represent the gravity load as a result of dead and snow load and one horizontal load applied on the column at a height 2000 mm, which represents the wind load and varies for each frame test in accordance with Table 5.2. The locations of the applied loads are depicted in Fig. 5.1 below and follow the description of the experimental tests.

To account for the effect of initial geometric imperfections in the numerical simulations, a linear buckling analysis was conducted, to extract the global buckling mode shape (Fig. 5.2), which was subsequently utilized in a RIKS nonlinear analysis. In order to assess which global imperfection amplitude will best replicate the experimental tests during the validation process, three different global imperfection amplitudes were considered, namely $h/200$, $h/1000$ and $h/2000$. The first amplitude value refers to the sway imperfection amplitude specified by EN 1993-1-1+A1 (2014) to account for the lack of verticality of the columns, $h/1000$ refers to a more realistic situation where sufficient care has been taken in the construction process, whilst $L/2000$ refers to a case with almost no sway imperfection and serves as a benchmark to assess the effect of sway imperfection on the structural response.

Fig. 5.2 depicts the relevant buckling mode shape associated with sway imperfections, which was scaled to the required amplitude as previously described in the subsequent RIKS analysis. It should be noted that ideally both global sway imperfections, which are associated with the out-of-verticality of the frame (i.e. imperfections at frame level, associated with the $P-\Delta$ effects) and local member imperfections associated with the out of straightness of the members (i.e. imperfections at member level relevant to column buckling and associated with the $P-\delta$ effects) should be considered. However, it was observed that due to the moment transfer between the beams and the columns, the rotation of the beam-column nodes caused

by the vertical loads resulted in a significant curvature of the columns that produced an out-of-straightness far beyond the imperfection amplitudes commonly assumed for column buckling ($L/1000$). Hence, since member imperfections had little effect and in the interest of computational efficiency, member imperfections were not considered in the modelling of the frames.

Table 5.2: Horizontal load for each portal frame test (Walkinson and Hancock, 1999)

Frames	Cross-Section	Steel Grade	Vertical over horizontal load ratio
Frame 1	150×50×4	C350	40
Frame 2	150×50×4	C450	40
Frame 3	150×50×4	C450	3.3

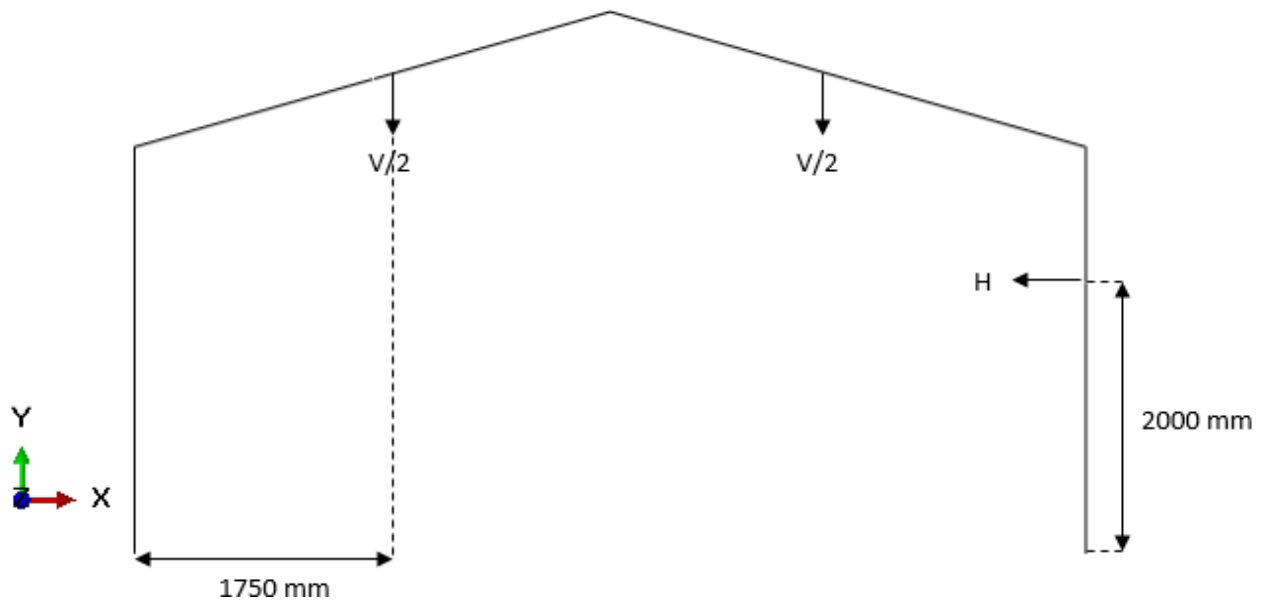


Fig. 5.1: Position of applied loads (dimensions in mm)

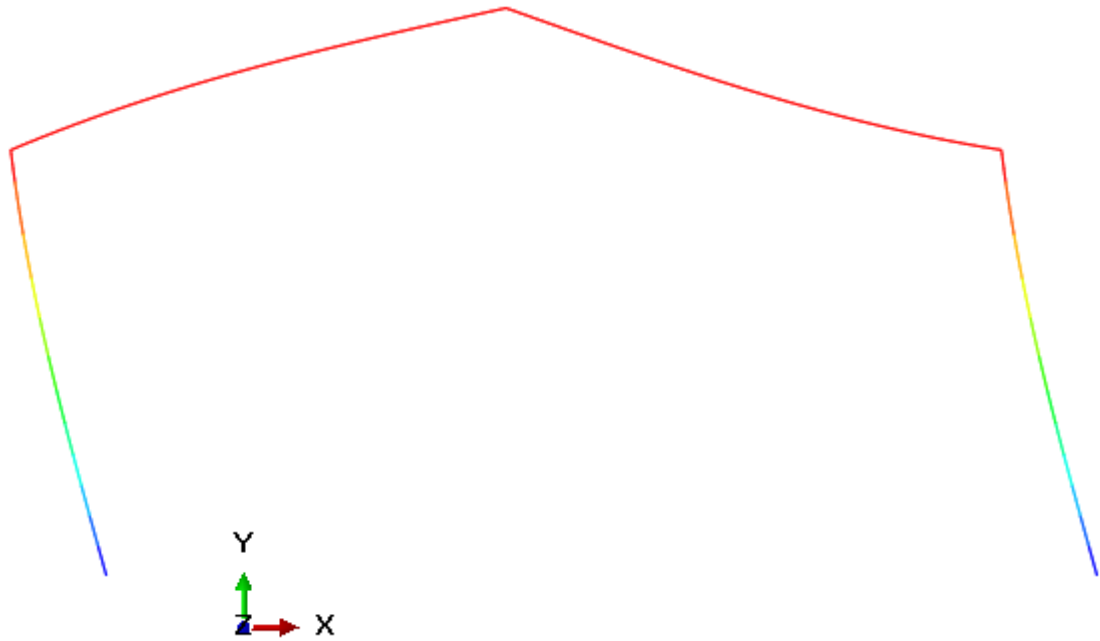


Fig. 5.2: Frame sway mode shape

5.1.2. Modelling using shell elements

To accurately capture local failure modes, shell elements were considered. Similar to the modelling of simply supported and continuous beams, S4R shell elements were utilized. Precise geometric and cross section dimensions were incorporated for each portal frame. To achieve the 105° angle at knee joints between the steel column and the rafter, both column and rafter were precisely profile cut at the same angle (Fig. 5.3), using the Merge / Cutting Instances technique (ABAQUS, 2007). 3D Deformable Solid-Extrude elements (C3D8R) steel connection plates were introduced at the knee joints (10 mm thick solid plates) and at the apex joint (20 mm thick solid plate), as the shell elements are susceptible to shear locking effects, which could lead to false results. To consider the nonlinear material response of the steel grades C350 and C450 the Von Mises yield criterion and an isotropic hardening rule

were utilized; the material properties were introduced in ABAQUS as multilinear curve, where detail approach on this method is provided in section 4.1. In accordance with the research conducted by Karren 1967 for cold-formed steel, the corner properties were extended to a distance equal the thickness of the section beyond the curved corner regions (Fig. 5.4). Material properties utilized for both flat and corner regions shown in Table 5.3 below.

Table 5.3: Material Properties (Walkinson and Hancock, 1999)

Steel Grade	Position	E (N/mm ²)	f _y (N/mm ²)	f _u (N/mm ²)	ε _f (%)
C350	Flat	207000	411	464	37
C350	Corner	200000	560	595	16
C450	Flat	207000	437	520	32
C450	Corner	204000	580	623	16

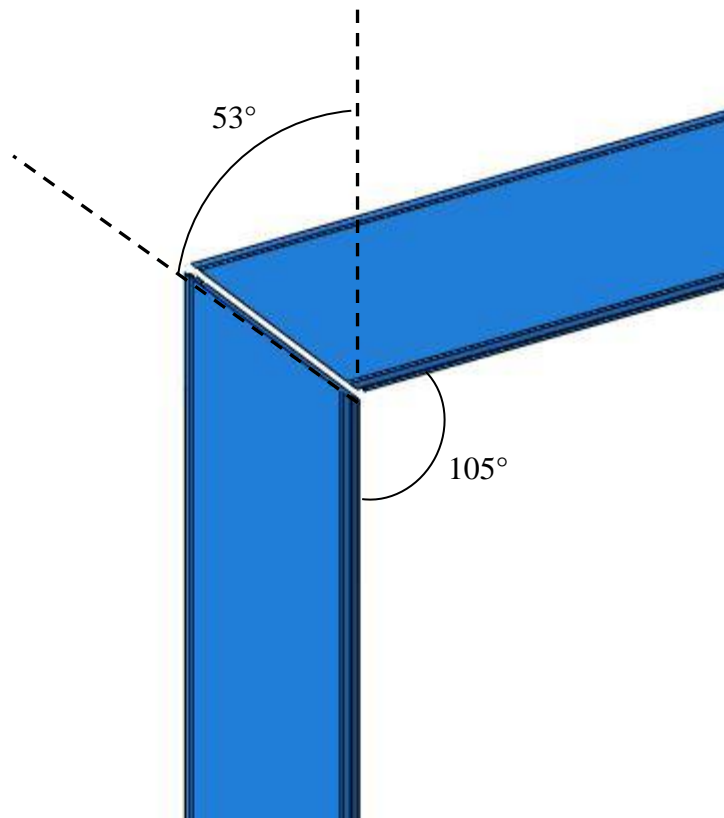


Fig. 5.3: Profile cut of cross sections at knee joints

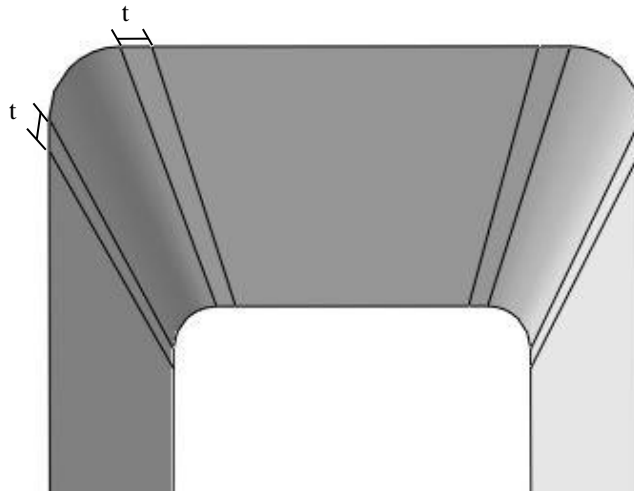


Fig. 5.4: Extended corner material properties

In order to avoid any deformations at column bases kinematic coupling was used as depicted in Fig. 5.5. As it was stated in section 5.1.1, a collar tie was used, in order to transfer the vertical tension force from the actuator to the mid-point of each inclined rafter; details on the loading method named gravity load simulator, presented by Wilkinson and Hancock (1999). To increase the strength of the RHS at loading points during the conduction of experimental tests, web stiffeners were introduced, which were approximated during the numerical modelling with the use of kinematic coupling, which prevented the deformation of the cross-section at the points of load introduction.

In accordance with construction industry, where frame out-of-plane defections are restrained in multi-bay portal frames with the use of bracing systems, Wilkinson and Hancock (1999) applied lateral restrains on the frame tests with the use of a system previously used during a research program conducted by the University of Lehigh (Yarimci et al., 1967). Lateral restrains were introduced, at the loading points, close to knee joints and at the South column only for Frame 2 and Frame 3 as is depicted in Fig. 2.17 (Chapter 2). The same rule was

applied during the numerical modelling of the frames by restraining the displacement along the x-axis at the specified locations highlighted as orange in Fig. 5.6.

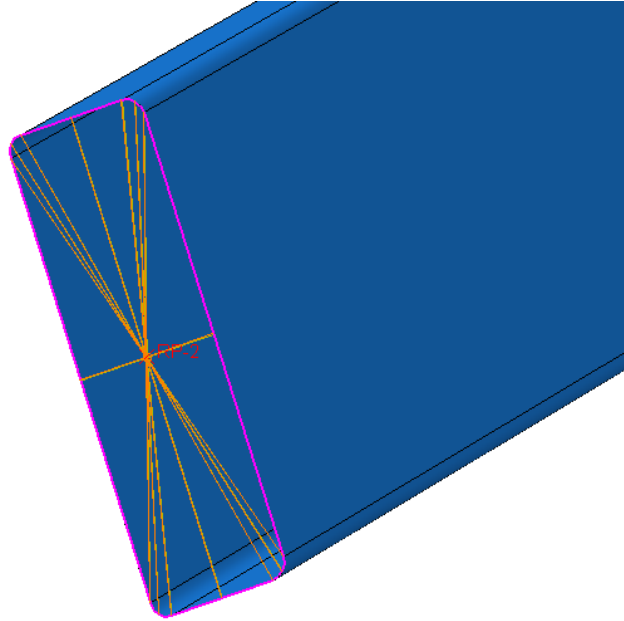


Fig. 5.5: Kinematic coupling applied at column bases

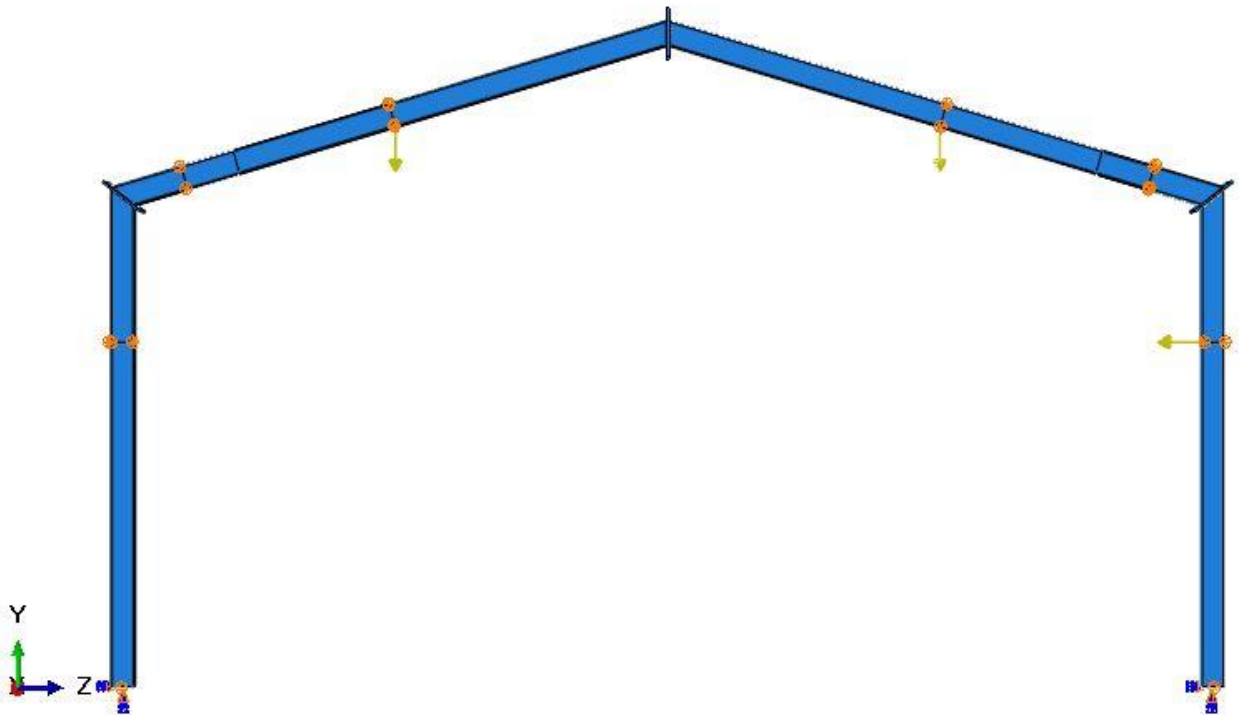


Fig. 5.6: Lateral restrain

Moreover, to fit in the pinned based conditions that were employed during the experimental tests, the required translational degrees of freedom were restrained at columns' bases allowing free rotations about their x-axis. To sufficient represent, the full penetration butt weld of rafters' and columns' ends on the 10 mm and 20 mm thick joint plates, the Tie Constrain method was utilized; the perimeter edges for both rafters and columns were set as the Slave surface and the top and bottom surfaces of the joint plate were set as the Master surface (Fig. 5.7). The two vertical and one horizontal point loads, were applied at the aforementioned locations depicted in Fig. 5.1, at the web top corner arc junction, which was proved to be the most efficient approach for the accurate replication of the experimental tests.

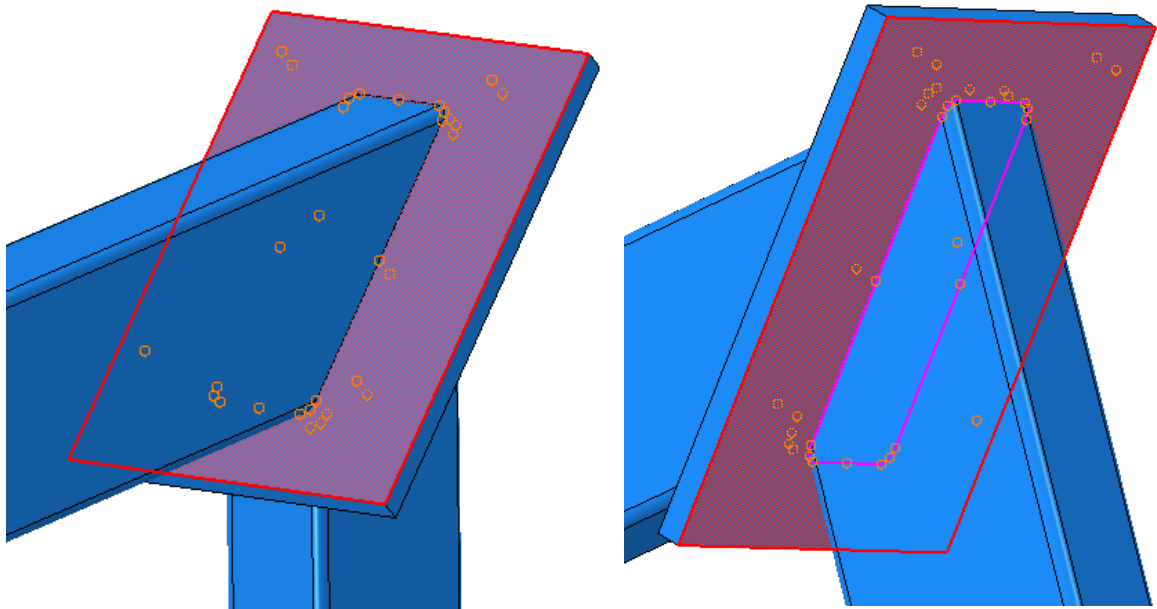


Fig. 5.7: Tie constrain

A uniform mesh density throughout the models is employed to ensure accurate results. As for the modelling of simply supported and continuous beams the mesh size varies between 4 mm and 6 mm, whilst a minimum of 4 elements were employed along each of the 4 curved quarter

circular corner regions of the cross-sections as shown in Fig. 5.8. Furthermore, a minimum of 3 elements was employed along the thickness of knee connection plates and a minimum of 6 elements along the thickness of apex connection plate (Fig. 5.9).

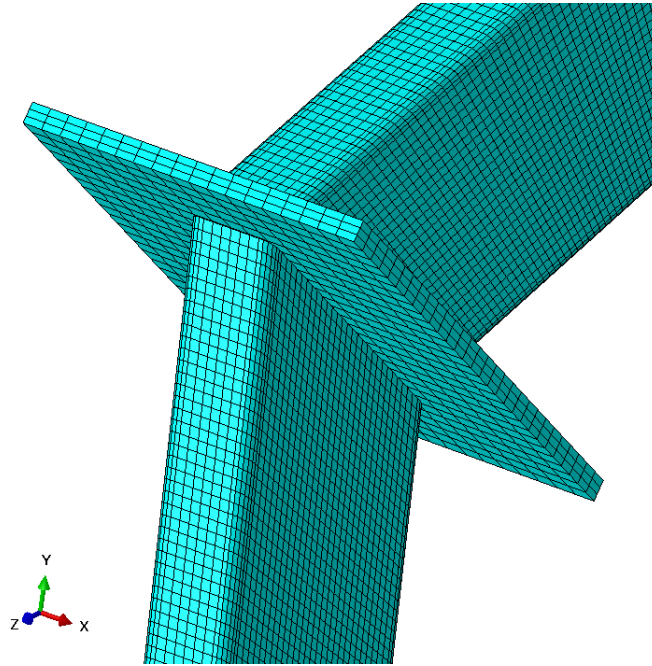


Fig. 5.8: RHS mesh configuration

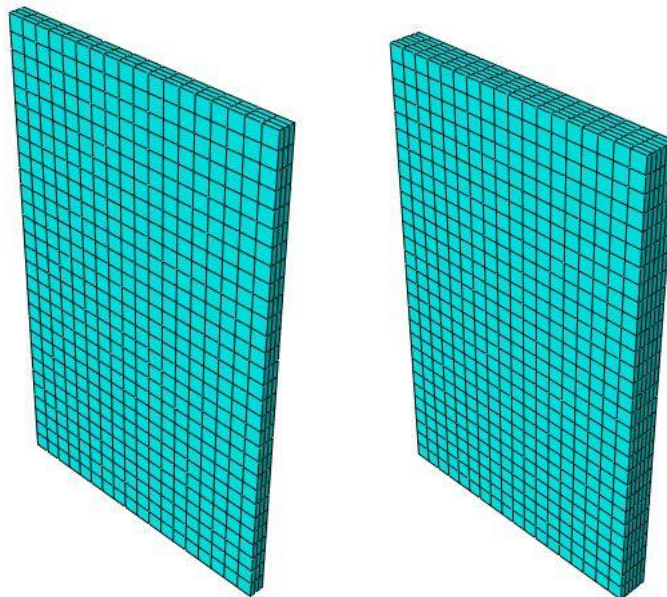


Fig. 5.9: Knee joint and apex joint connection plates mesh configurations

Similar to the previous modelling strategy where beam elements were employed for the discretisation of the frames, both linear and nonlinear analysis were conducted during the numerical simulation of shell element frames. Initially, to extract the local and global buckling mode shapes, a linear buckling analysis was conducted (Fig. 5.10, Fig. 5.11). Subsequently, the buckling mode shapes were utilized in a RIKS nonlinear analysis. The amplitude of local imperfection was considered as $t/100$ (t is the thickness of the cross section), according to the numerical study on stainless steel beams that reported in Chapter 4. Furthermore, during the validation of beam element frames against the experimental tests provided by Wilkinson and Hancock (1999), it was concluded that the global imperfection amplitude $h/200$ (EN 1993-1-1+A1, 2014) best replicates the experimental tests. Therefore, it was utilized during the RIKS analysis for shell element frames. Finally, in accordance with the simulation employing beam elements, member imperfections were not considered; only cross-sectional local imperfections pertinent to local buckling and frame sway imperfections, leading to $P-\Delta$ effects were explicitly modelled to ascertain the combined effect on the overall response. The validation of the models employing the two distinct modelling strategies (i.e. employing beam elements and employing shell elements) is discussed hereafter allows the importance of incorporating local buckling to be determined. A final point to note relates to the explicit incorporation of the enhanced corner properties in the numerical models. As beam elements do not allow varying material properties around the cross-section, the corner strength enhancements were ignored, whilst the models employing shell elements the strength enhancements were explicitly considered and assumed to extend up to a distance equal to t beyond the corner regions.

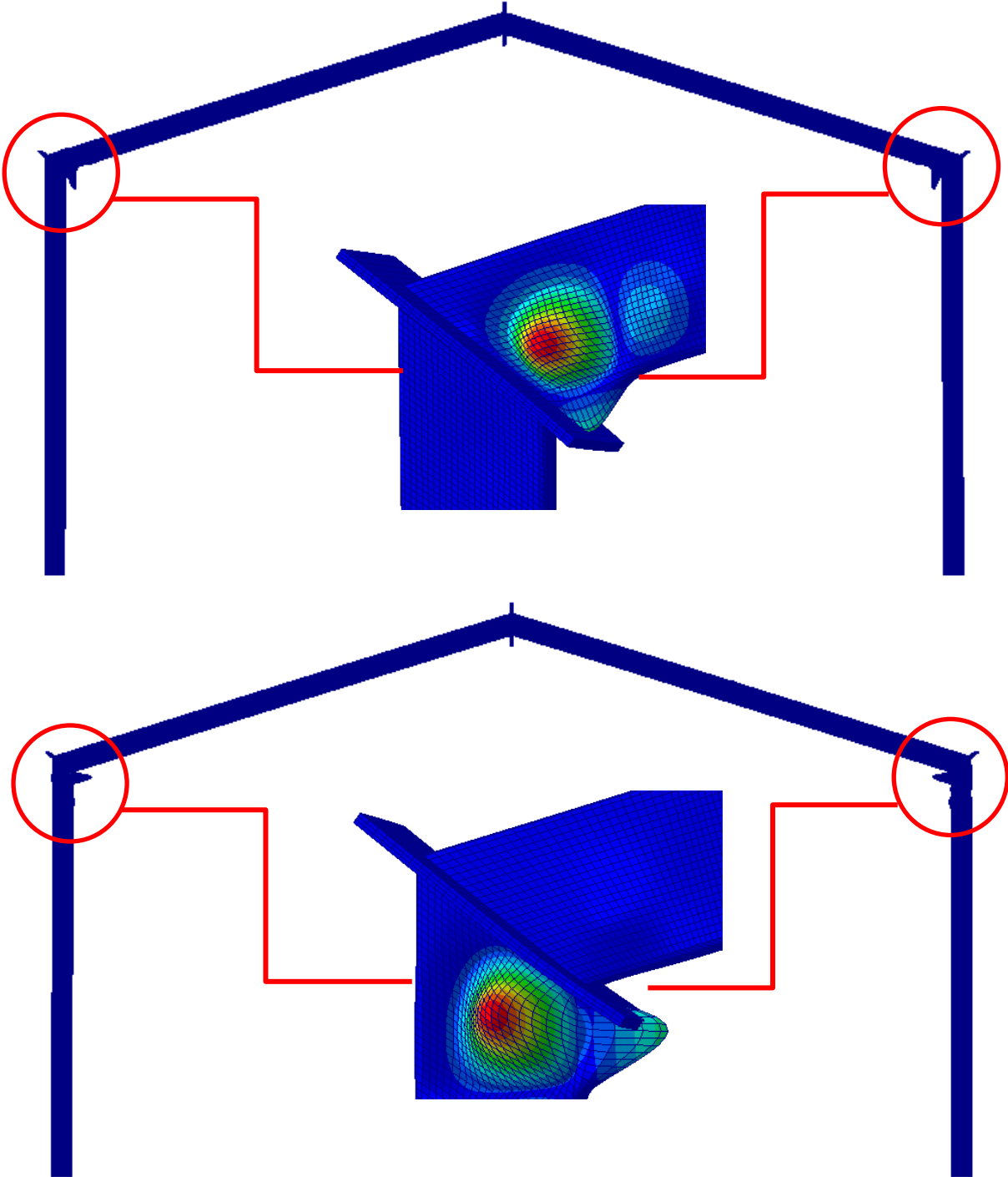


Fig. 5.10: Local buckling mode shapes

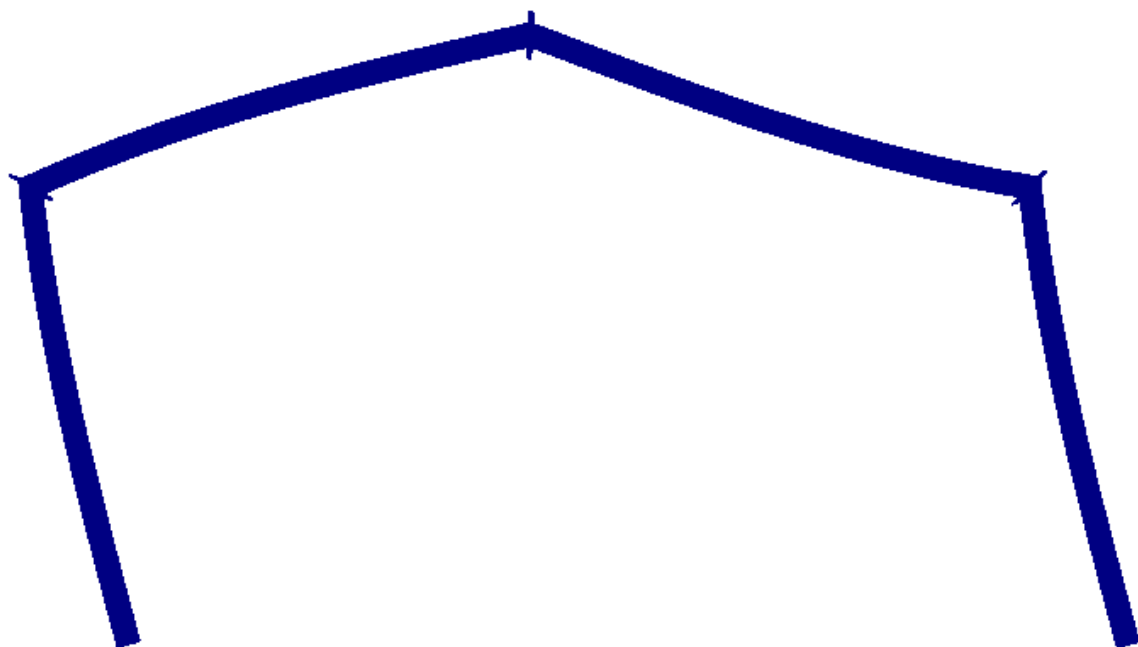


Fig. 5.11: Frame sway mode shape

5.2. VALIDATION

Herein, the numerical results are compared against the portal frames test results reported by Wilkinson and Hancock (1999). The accuracy of the models to replicate the experimental results and their suitability for performing parametric studies are assessed.

5.2.1. Beam elements

In this section, the Beam elements portal frames are compared against the experimental results. After, the FE models were accurately produced by following the modelling assumptions reported in section 5.1, the vertical load was plotted against the vertical displacement at apex and the horizontal displacement at North knee joint. The numerical and

the experimental graphs are illustrated in Fig. 5.12 to Fig. 5.17. For each frame three global imperfection amplitudes were considered; $h/1000$, $h/2000$ and $h/200$ where h is the height of the columns, in order to examine, which best replicates the experimental results.

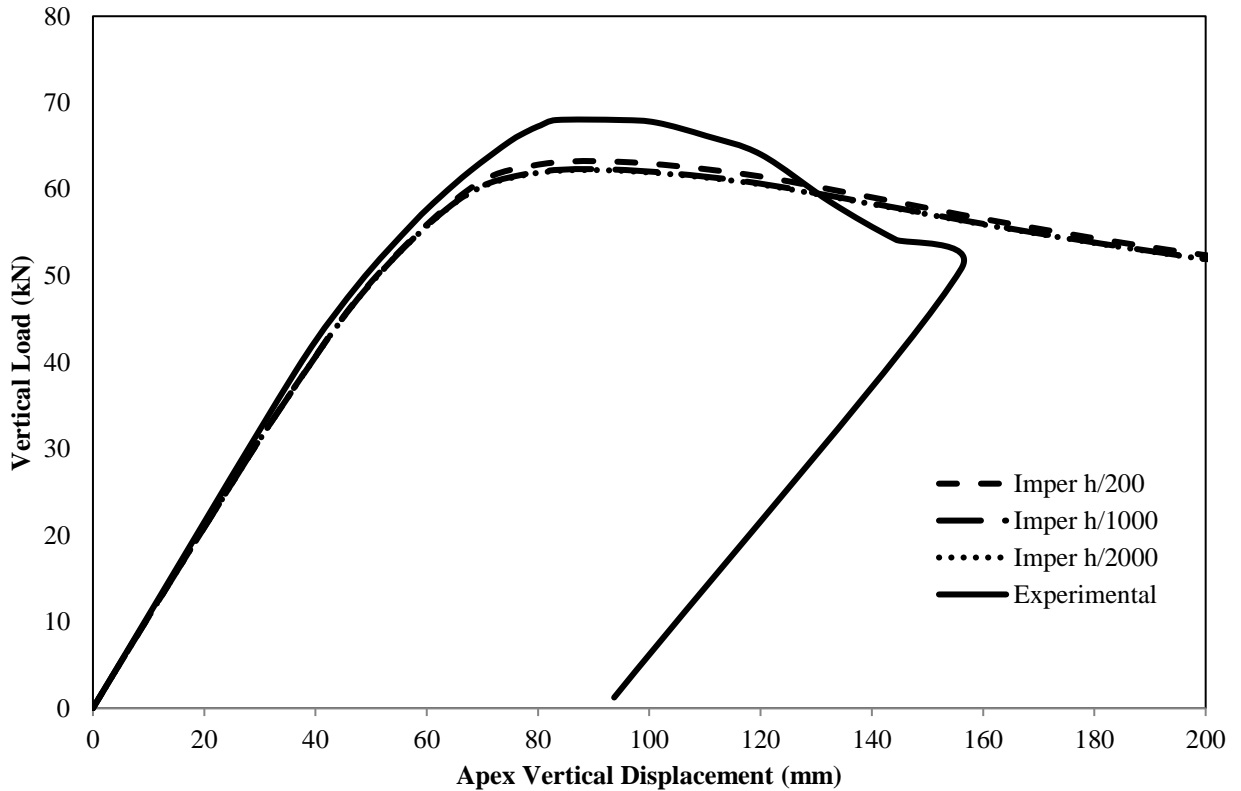


Fig. 5.12: Vertical load – vertical displacement apex for Frame 1

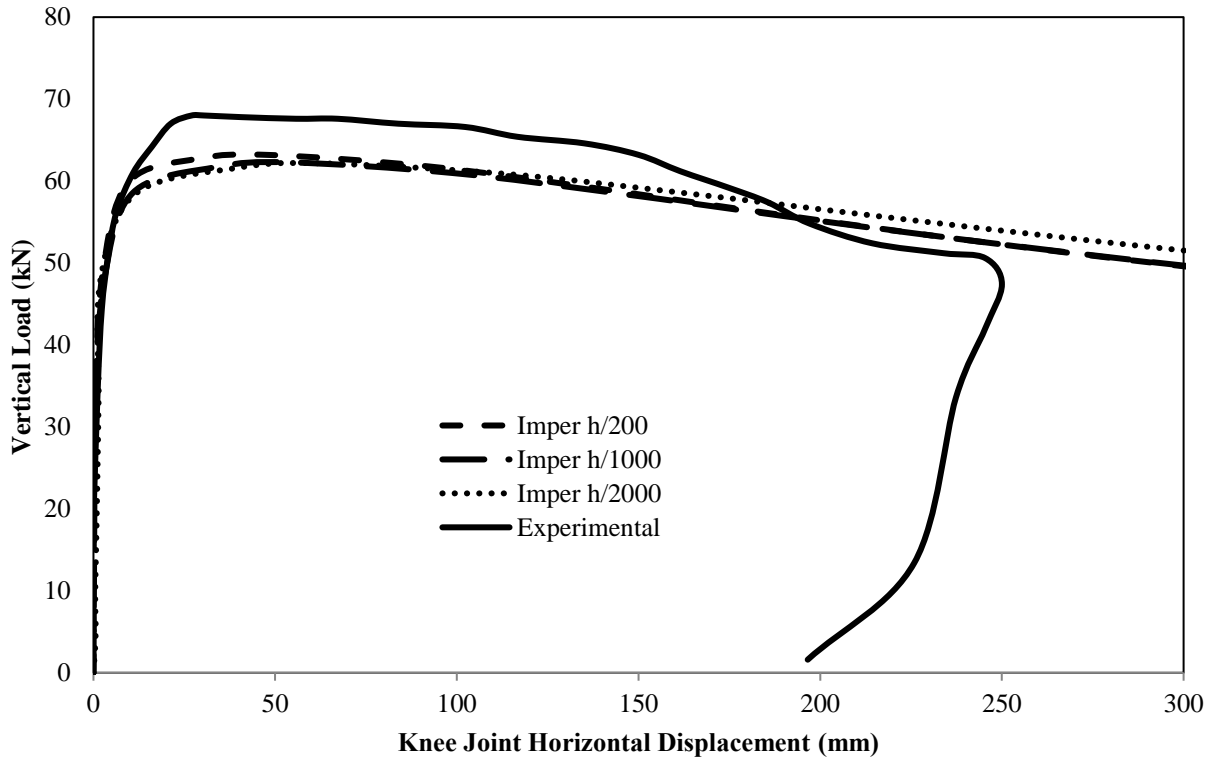


Fig. 5.13: Vertical load – horizontal displacement at North knee joint for Frame 1

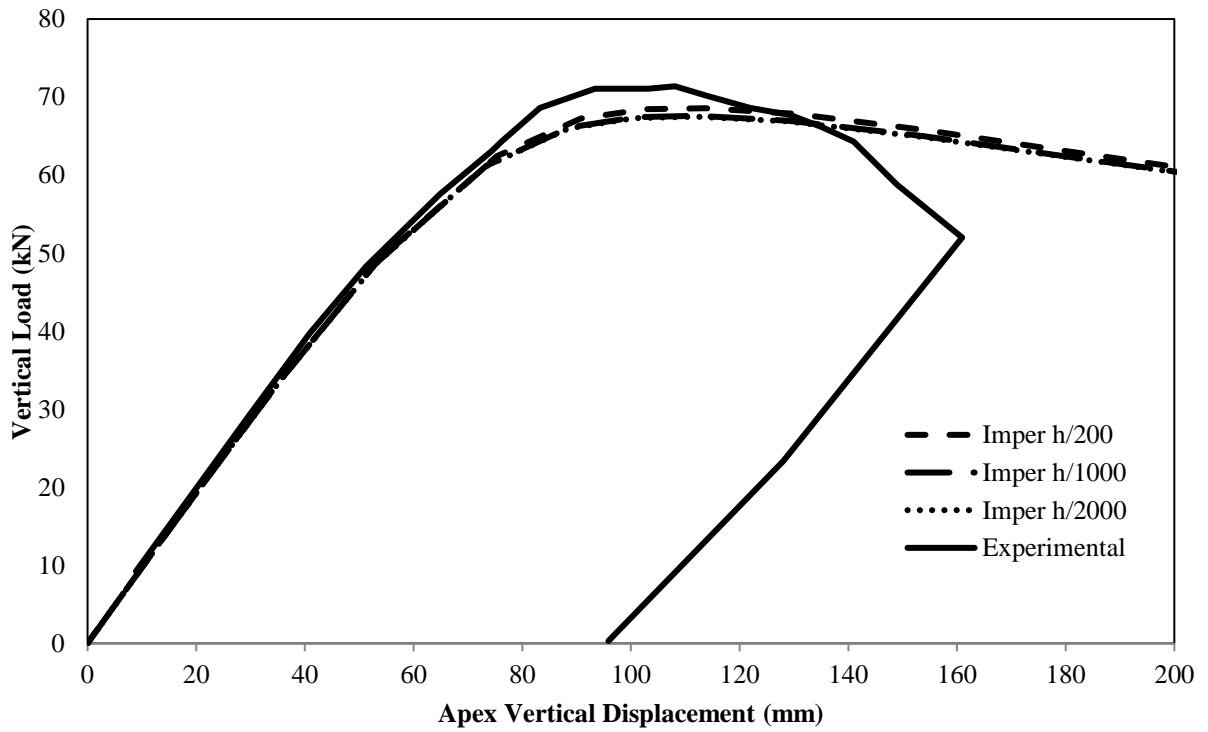


Fig. 5.14: Vertical load – vertical displacement apex for Frame 2

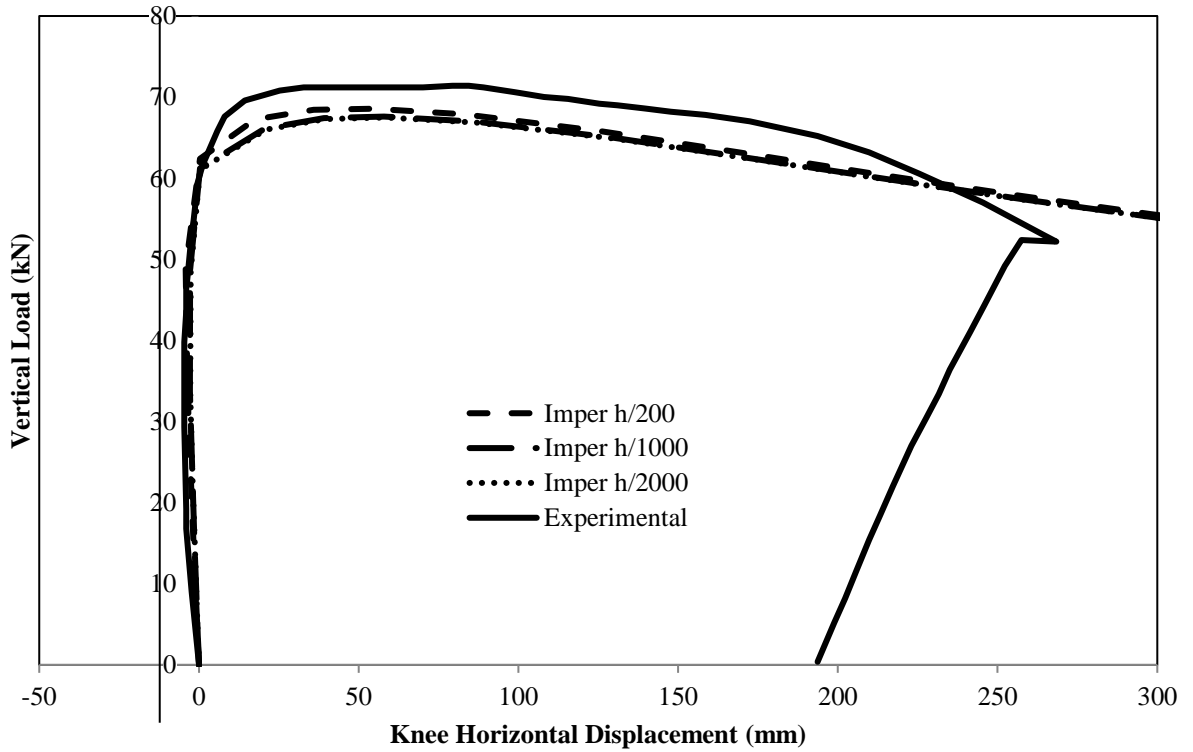


Fig. 5.15: Vertical load – horizontal displacement at North knee joint for frame 2

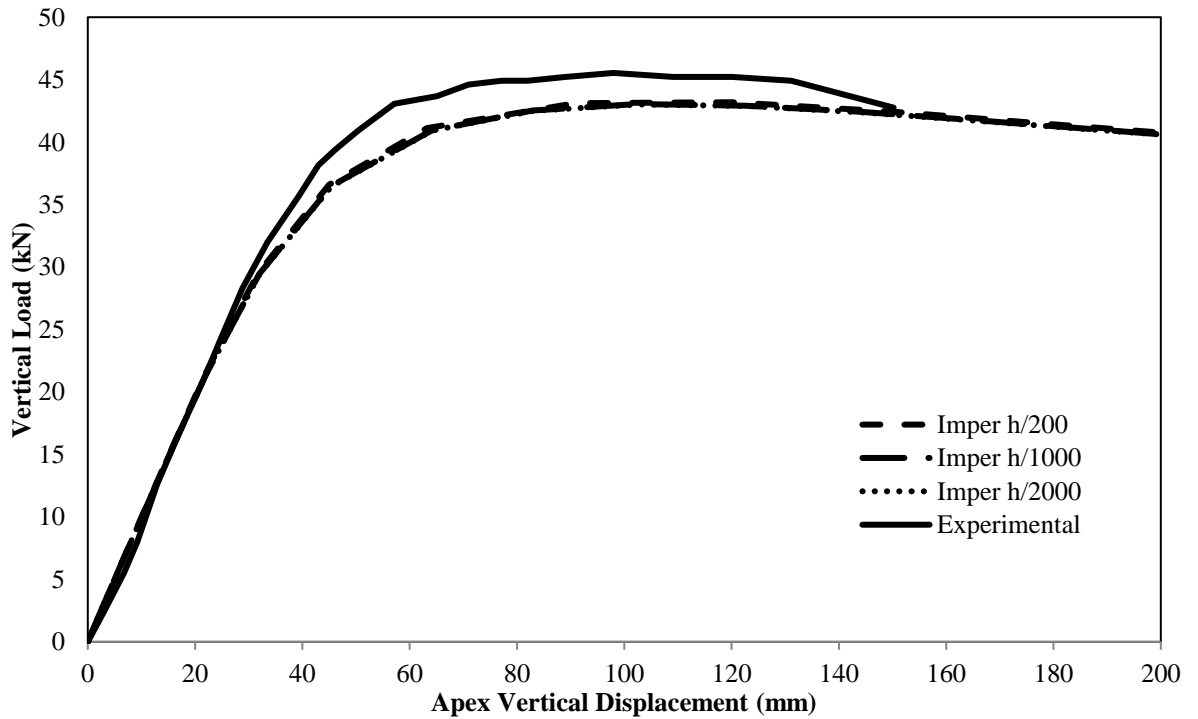


Fig. 5.16: Vertical load – vertical displacement apex for Frame 3

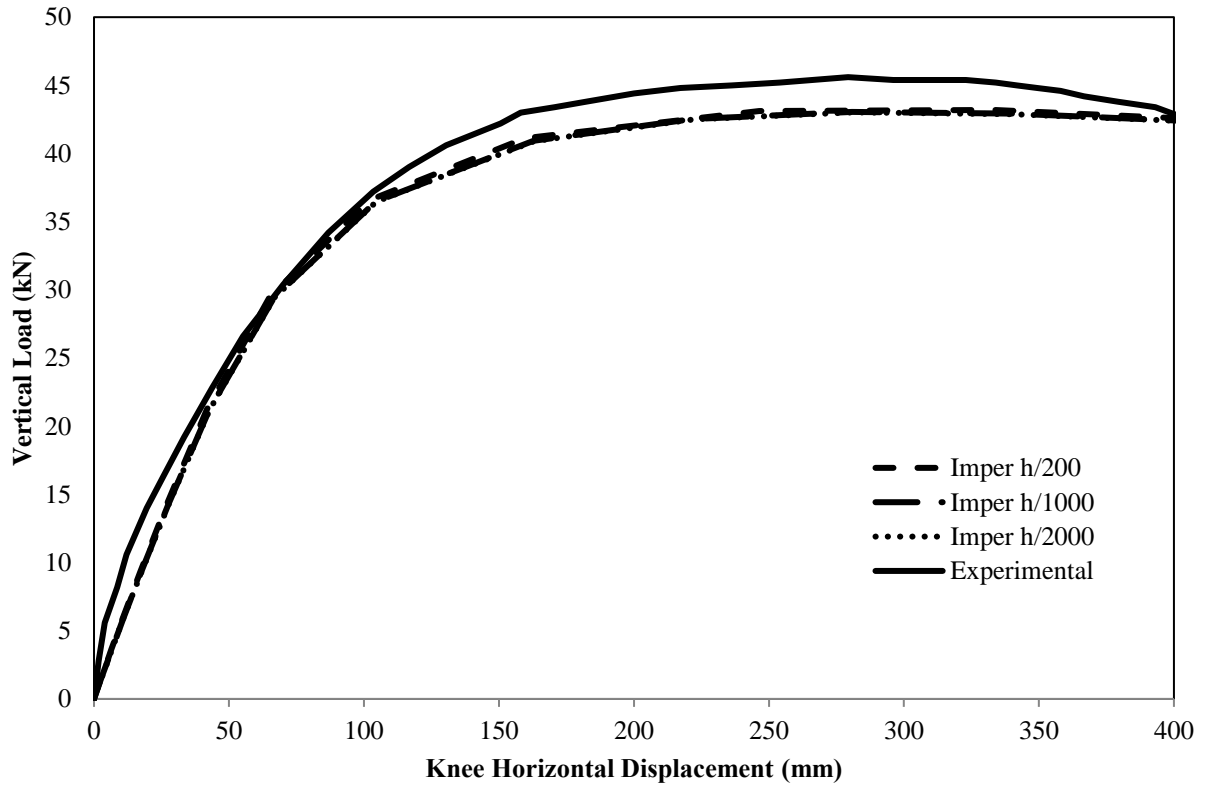


Fig. 5.17: Vertical load – horizontal displacement at North knee joint for Frame 3

In accordance with the above illustrated graphs, an overall good agreement between the experimental and numerical response in terms of initial stiffness, ultimate load and post ultimate response can be observed. It could be stated that slight underestimation of the ultimate load can be observed. To investigate this concern, numerical models of shell elements are validated against the experimental tests in the following section. Furthermore, the numerical over experimental ultimate load ratios were presented for each predicted global imperfection amplitude, $h/1000$, $h/2000$ and $h/200$ (Table 5.4). It was observed the favourable mean and coefficient of variation values are achieved for an initial global imperfection amplitude equal to $h/200$, which is utilized in section 5.2.2 for the replication of the experimental models using shell elements. The comparison between experimental and numerical failure modes is shown

in Fig. 5.18, where the beam rendering functionality of ABAQUS was utilized to facilitate a better visual comparison.

Table 5.4: $F_{u,FE}/F_{u,test}$ for the imperfection amplitudes considered

Tests	Material Grades	Sections	$F_{u,FE}/F_{u,test}$		
			h/1000	h/2000	h/200
Frame 1	C350	RHS 150×50×4	0.915	0.914	0.929
Frame 2	C450	RHS 150×50×4	0.947	0.945	0.961
Frame 3	C450	RHS 150×50×4	0.945	0.944	0.948
		Mean	0.936	0.934	0.946
		COV	0.019	0.018	0.017

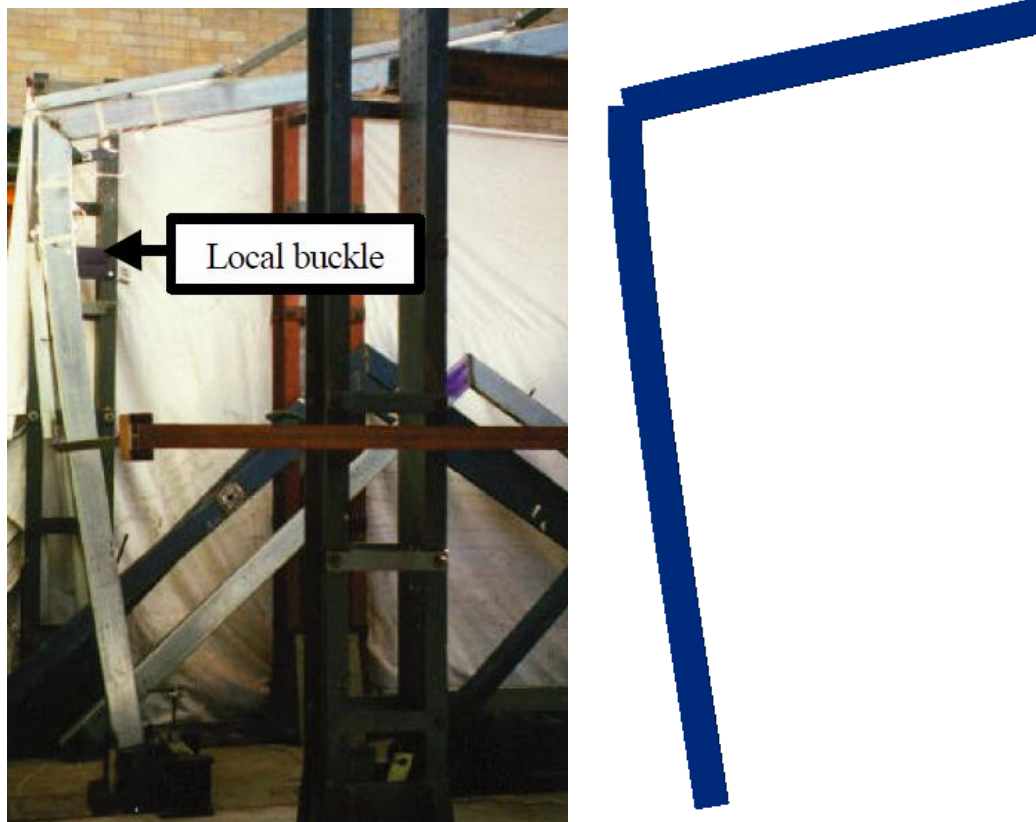


Fig. 5.18: Comparison between experimental and numerical failure mode for Frame 3

5.2.2. Shell elements

Shell elements were used for a more accurate replication of the experimental results (Wilkinson and Hancock, 1999), since FE models incorporating beam elements were slightly underestimate the ultimate load response for each frame. During the numerical simulation of the portal frames the local geometric imperfection amplitude $t/100$ and global imperfection amplitude $h/200$ were utilized based on previous conducted investigation in Sections 4.2.2 and 5.2.1 respectively. As for the models incorporating beam elements, the vertical load was plotted against the vertical displacement at apex and the horizontal at North knee Joint and compared versus the experimental results (Fig. 5.19 to Fig. 5.24).

By comparing the experimental with numerical results for the below illustrated figures, it is clear the excellent agreement achieved in terms of initial stiffness and ultimate load response. Furthermore, the importance of utilizing the corner material properties within the corner region of the cross section and beyond (Karren, 1967; Gardner and Nethercot, 2004; Ashraf et al., 2006) and the employment of kinematic coupling at the vertical applied loads is observed. The difference on the numerical over the experimental ultimate load ratios between the models utilizing beam and shell elements are presented in Table 5.6, where it is observed that the most favourable mean and coefficient of variation values are achieved for frames discretised with shell elements.

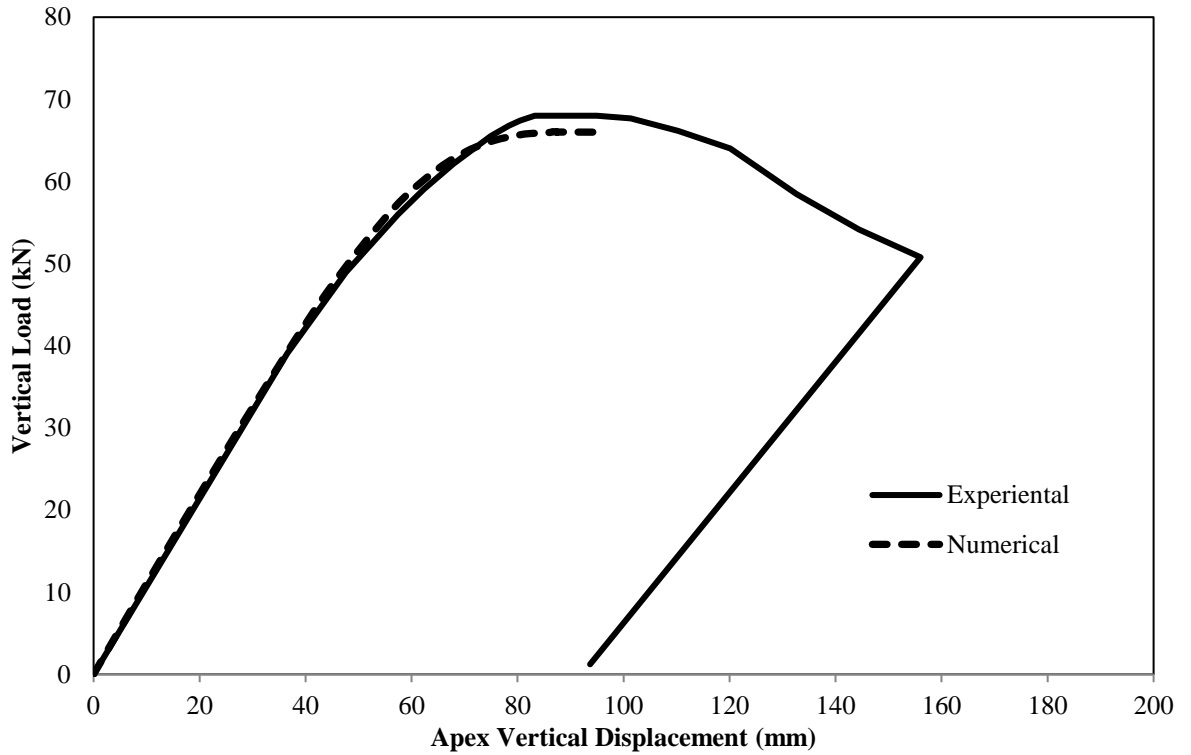


Fig. 5.19: Vertical load – vertical displacement apex for Frame 1

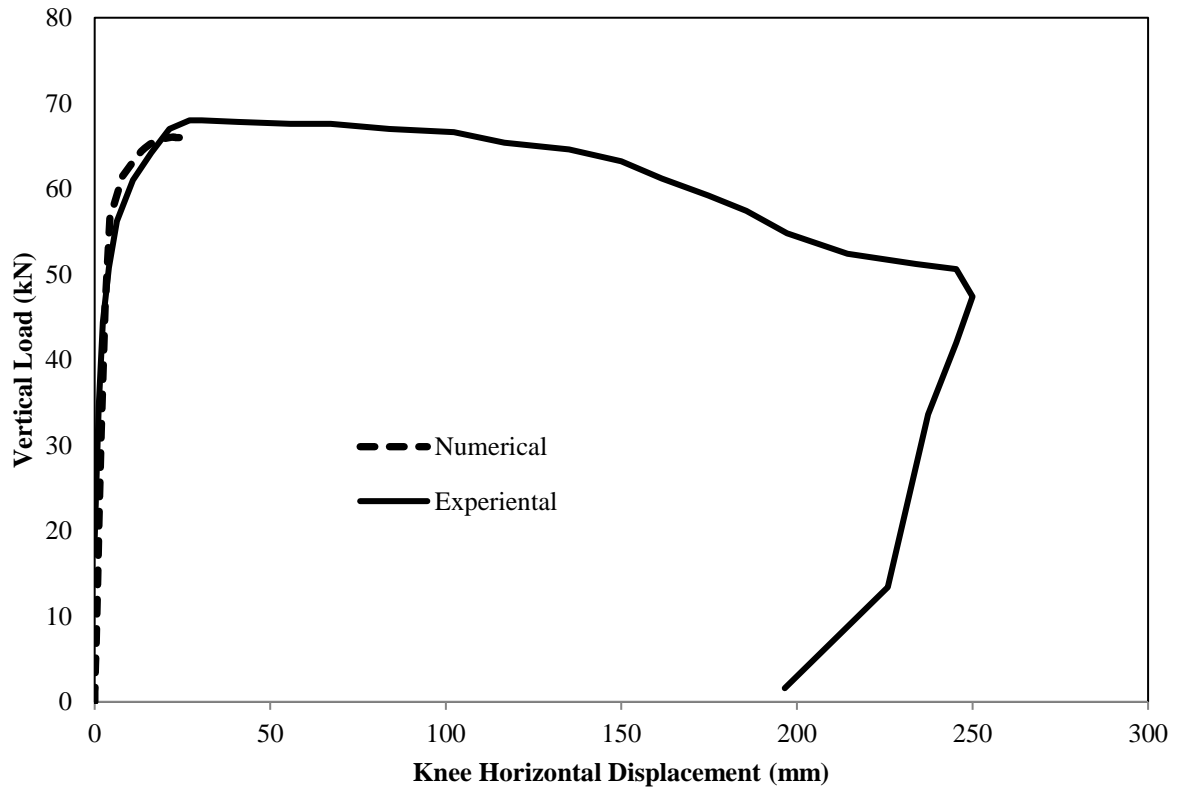


Fig. 5.20: Vertical load – horizontal displacement at North knee joint for Frame 1

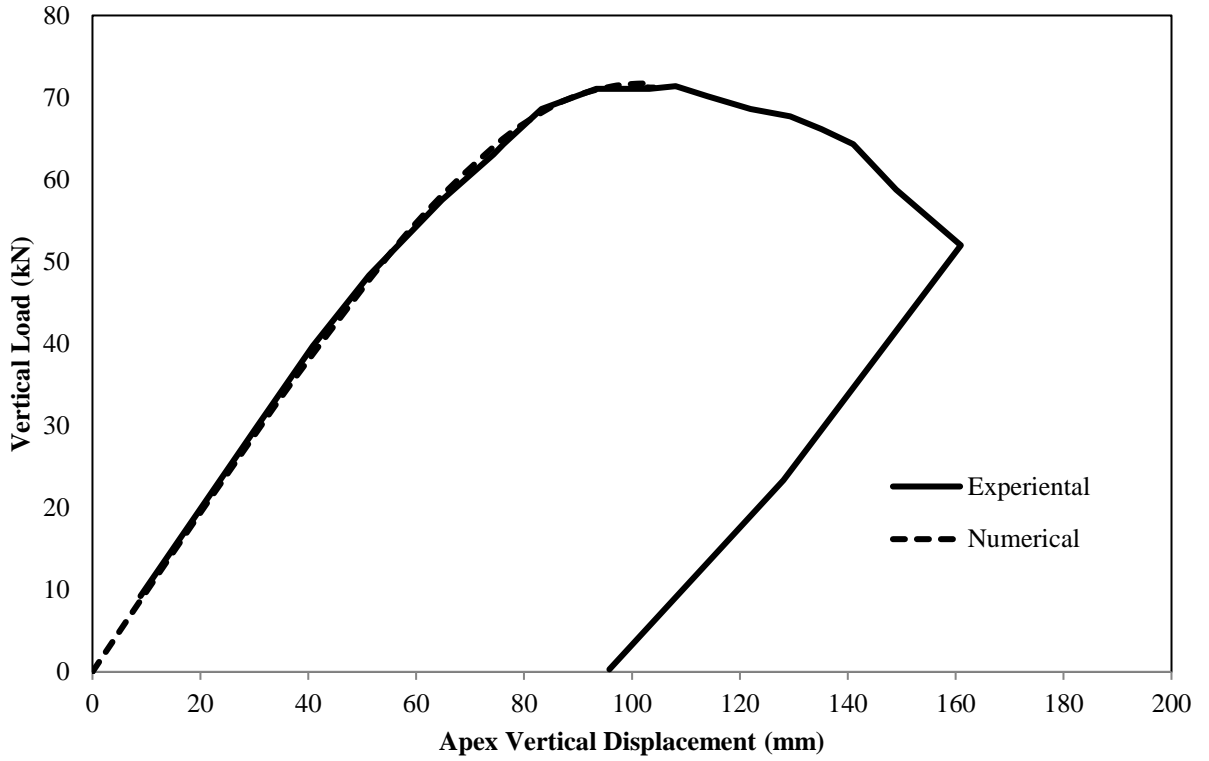


Fig. 5.21: Vertical load – vertical displacement apex for Frame 2

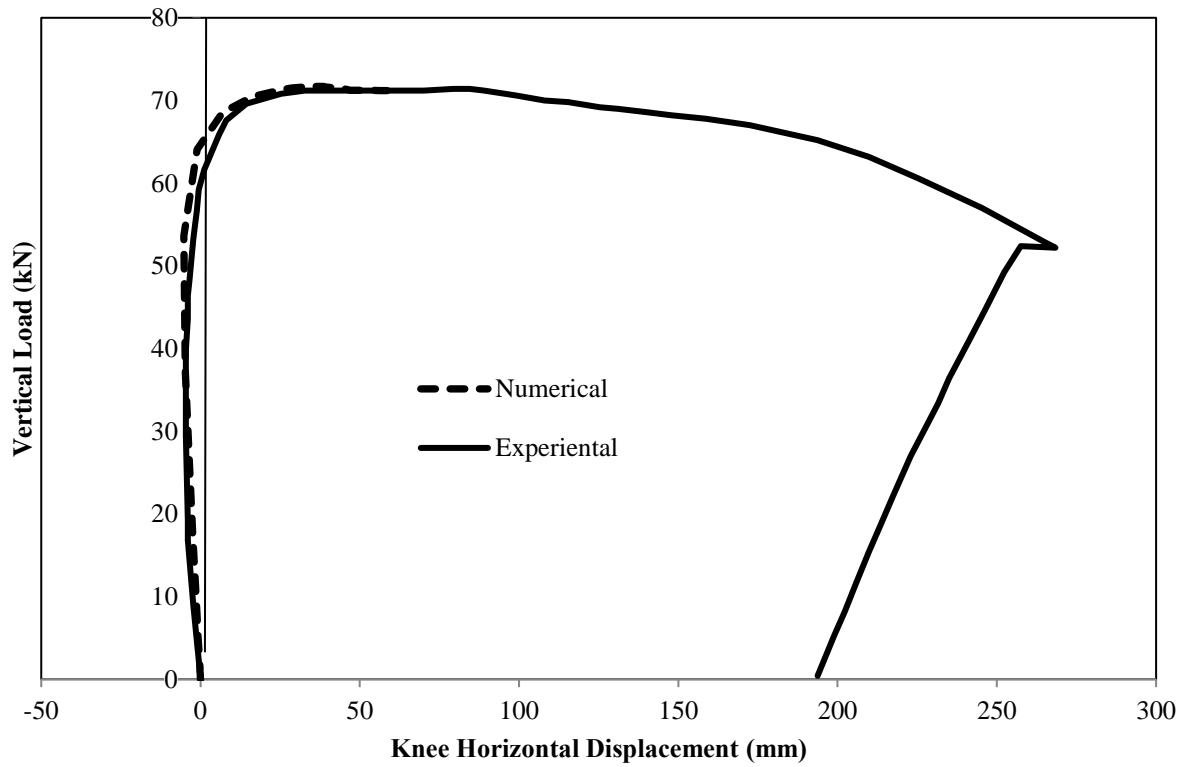


Fig. 5.22: Vertical load – horizontal displacement at North knee joint for Frame 2

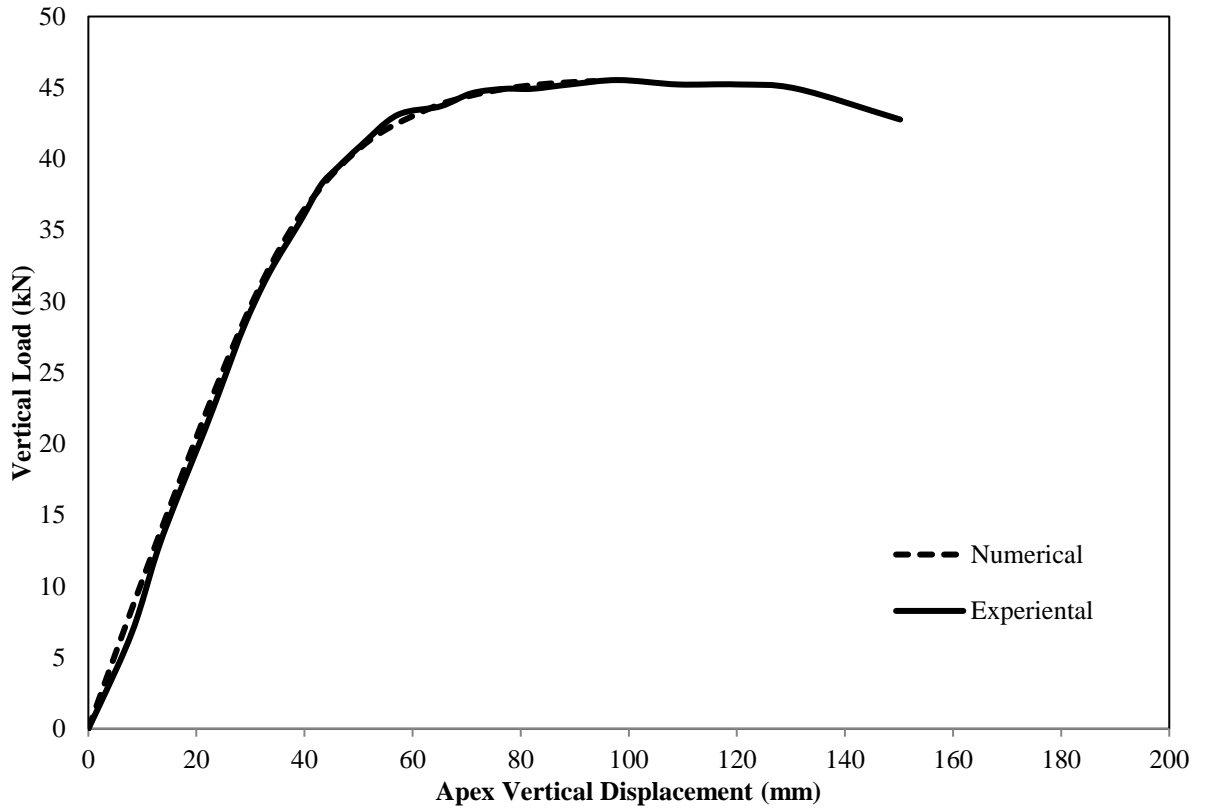


Fig. 5.23: Vertical load – vertical displacement apex for Frame 3

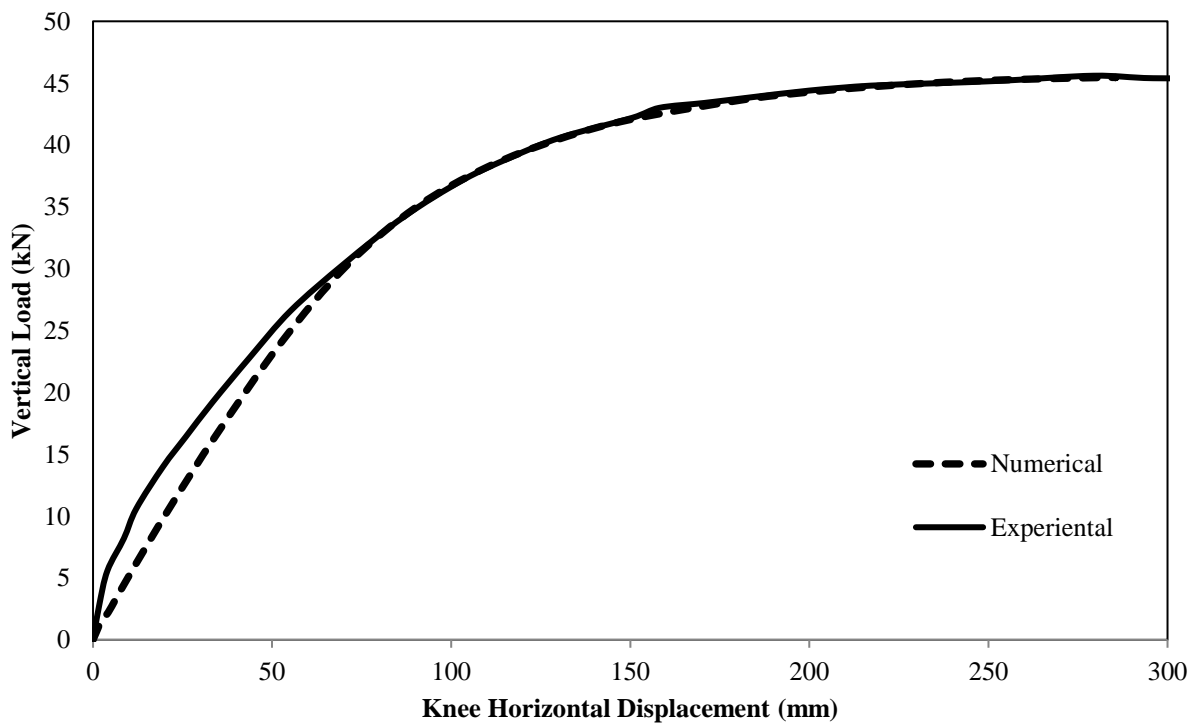


Fig. 5.24: Vertical load – horizontal displacement at North knee joint for Frame 3

Table 5.5: $F_{u,FE}/F_{u,test}$ for frames discretised with shell and beam elements

Tests	Material Grades	Sections	$F_{u,FE,beam}$	$F_{u,FE, shell}$
			elements/ $F_{u,test}$	elements/ $F_{u,test}$
			h/200	h/200
Frame 1	C350	RHS 150×50×4	0.929	0.972
Frame 2	C450	RHS 150×50×4	0.961	1.005
Frame 3	C450	RHS 150×50×4	0.948	0.986
Mean			0.946	0.987
COV			0.017	0.016

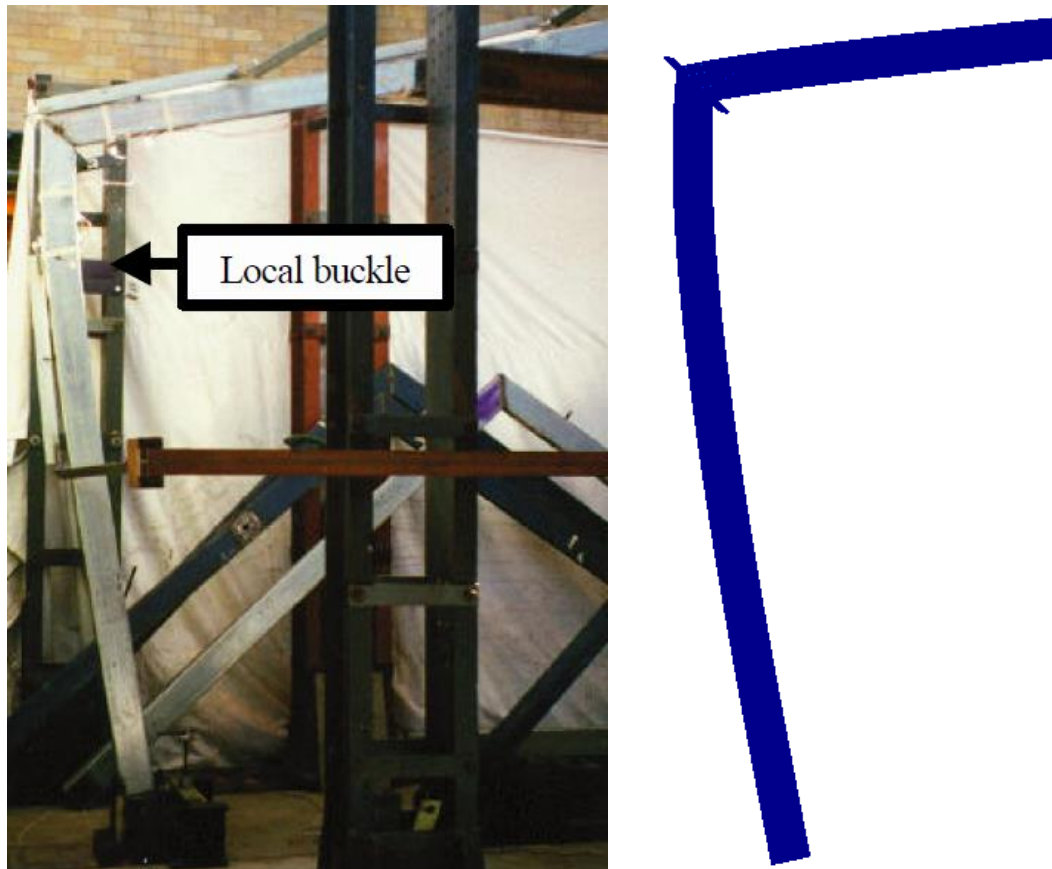


Fig. 5.25: Comparison between experimental and numerical failure mode for Frame 3

5.3. PARAMETRIC STUDIES

In section 5.2, the ability of the FE models utilizing shell elements to accurately replicate the portal frame test results was well proved for shell elements. Given that the importance of corner strength enhancements is expected to be higher for stainless steel cross-sections, the validated FE models using shell elements were used to conduct parametric studies, in order to expand the available structural performance data over a range of geometric parameters, such as cross-sectional slenderness, cross-section aspect ratio, span to column height ratio as well as to investigate the effect of the level of static indeterminacy by comparing the response of pinned-based and fixed-based frames. Two cross-section aspect ratios, namely 1.0 and 2.0, and three thicknesses, namely 2 mm, 3 mm, 4 mm, 5 mm, 6 mm and 10 mm were considered. In more detail, the thicknesses 2 mm, 3 mm and 5 mm were utilized for the SHS 50×50 and RHS 100×50, where for the SHS 100×100 and RHS 200×100, the thicknesses 4 mm, 6 mm and 10 mm were used. A span to column height ratio, equal to 3 was assumed in all studies, with the span (L) set equal to 9000 mm and the column height (h) equal to 3000 mm. It is also noted that only the in-plane behaviour of the frame is of interest.

In practice the portal frames are subjected to a combination of vertical gravity and horizontal wind loads. To capture the behaviour of stainless steel portal frames under this load combination, the loading arrangement presented in Fig. 5.26 was considered. Two equal vertical loads $V/2$ were applied at a distance equal to one-third of the span length from each end support and a horizontal load H at the top of the left-hand side column. For each FE model, two support conditions (Fix based and Pin based) and three horizontal to vertical load ratios, equal to 0, 0.1 and 0.2 were employed. The reasoning behind employing two different support

conditions relates to the obtaining results over a wider range of α_{cr} values, as well as to obtaining results for frames of different degrees of structural indeterminacy. The fixed-based frames have generally a higher α_{cr} value compared to their pinned-based counterparts, and generally require the formation of more plastic hinges for collapse to occur. The use of different section sizes for the same aspect ratio and cross-section slenderness (50×50 and 100×100, 100×50 and 200×100) also leads to different levels of α_{cr} and different column buckling resistances.

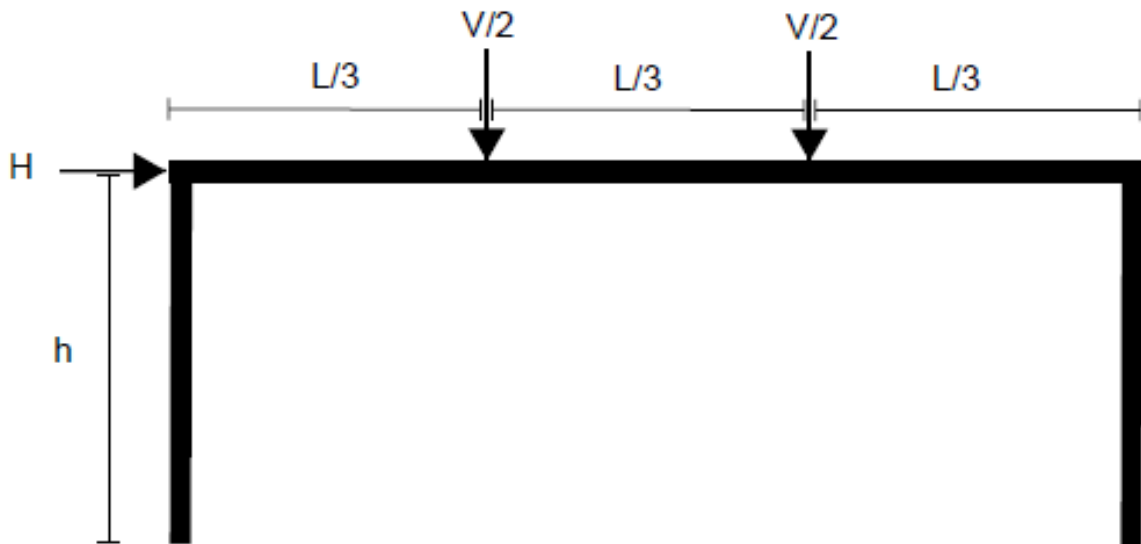


Fig. 5.26: Loading arrangement adopted in the parametric studies

To maintain consistency with the research conducted on simply supported and continuous stainless steel beams, the same material properties were utilized for the carrying out of parametric studies (Table 4.5). The local imperfection amplitude $t/100$ was implemented for all the models, which was shown to provide an excellent agreement with the experimental response during the validation of the beam tests. Moreover, a global initial sway imperfection equal to $h/200$ was considered, in accordance with the European structural design codes for

carbon steel (EN 1993-1-1+A1, 2014). A summary of the cross-section variations of the frame models considered together with the cross-section slenderness of each section and the expected compressive strain at cross-sectional failure depending on whether they were in the austenitic and duplex grade is given in Table 5.6. The obtained results are discussed in the following Chapter.

Table 5.6: Frame variation considered in the parametric studies

Section designation	Cross-section slenderness $\bar{\lambda}_p$ for the austenitic grade	Cross-section slenderness $\bar{\lambda}_p$ for the duplex grade	ϵ_{csm} for austenitic grade	ϵ_{csm} for duplex grade
50×50×2	0.58	0.64	1.83	1.28
50×50×3	0.38	0.41	8.48	5.93
50×50×5	0.22	0.24	14.08	10.05
100×50×2	0.57	0.63	1.85	1.30
100×50×3	0.38	0.41	8.49	5.94
100×50×5	0.22	0.24	14.08	10.05
100×100×4	0.58	0.64	1.83	1.28
100×100×6	0.38	0.41	8.48	5.93
100×100×10	0.22	0.24	14.08	10.05
200×100×4	0.57	0.63	1.85	1.30
200×100×6	0.38	0.41	8.49	5.94
200×100×10	0.22	0.24	14.08	10.05

CHAPTER 6

DISCUSSION OF RESULTS AND DESIGN RECOMMENDATIONS

6.1. DESIGN OF STAINLESS STEEL SIMPLY SUPPORTED BEAMS

EN 1993-1-4+A1 (2015) adopts the cross-section classification procedure for the treatment of local buckling of stainless steel sections. According to EN 1993-1-4+A1 (2015), Class 3 sections can reach their yield stress before the appearance of local buckling. The cross-sections which are capable of reaching their full plastic moment capacity are classified as Class 2 sections, while the Class 1 sections are characterized by their capability to reach and maintain their plastic moment capacity with sufficient deformation capacity and can therefore be used in plastic design. The classes of the tested cross-sections are shown in Table 6.1. Given that the present research focuses in the plastic design of indeterminate structures, most of the specimens have been selected to be Class 1, while only the specimen with nominal thickness 2 mm falling just about to Class 2.

The experimental results of the 3-point and 4-point bending tests are used to assess the current Eurocode slenderness limits for internal elements in compression, as well as the codified ultimate predicted capacities. Hence, the ratio of the moment resistance predicted by Eurocode (i.e. M_{pl} for Classes 1 and 2 sections) normalized by the ultimate moment M_u is shown in Table 6.1. As can be seen Eurocode predictions appear rather conservative and largely scattered, contrary to the moment resistance predicted by CSM method (M_{csm}) normalized by the ultimate moment M_u . This owes to the fact that the strain-hardening exhibited by stocky stainless steel sections is not accounted for by Eurocode.

In Fig. 6.1, the ultimate moment M_u normalized by the plastic moment M_{pl} is plotted against the flange slenderness $c/t\varepsilon$, where c and t are the plate width and thickness respectively and $\varepsilon=(235/\sigma_{0.2})^{1/2}$. The Class 2 limit of 35 is also specified, showing that the current limit is acceptable. In order to assess Class 1 limit, the deformation capacity R of the specimens that have failed upon reaching M_{pl} is plotted against the flange slenderness in Fig. 6.2. The current Class 1 limit for the part of the specimen subjected to compression is 33. Note that no rules for plastic global analysis are given in Eurocode (EN 1993-1-4+A1, 2015); hence there is an absence of codified deformation capacity requirement for Class 1 stainless steel cross-sections. Nevertheless, the deformation capacity requirement $R=3$ from carbon steel has been considered (Sedlacek and Feldmann, 1995). As it can be seen, most of the specimens have reached beyond the required deformation capacity, while the cross-sections 100×50×3 Duplex 3-point bending and 100×50×2 4-point bending tests fell below the deformation capacity requirement of 3. This is in a disagreement with EN 1993-1-3+A1 (2014) for carbon steel, which states that Class 1 cross-sections have sufficient deformation capacity to reach and maintain their cross-sectional plastic moment resistance. Overall the presented results show

that the carbon steel limits could be adopted for stainless steel, however further tests are required.

Table 6.1 Assessment of design methods for simply supported beams

Cross-section	Test configuration	EN 1993-1-4+A1, 2015		CSM	
		Class	M_{pl}/ M_u	$\bar{\lambda}_p$	M_{csm}/ M_u
RHS 100×50×2		2	1.04	0.58	1.03
RHS 100×50×3	3-point bending	1	0.78	0.39	0.89
RHS 100×50×5		1	0.55	0.23	0.81
RHS 100×50×3-D		1	0.83	0.44	0.95
RHS 100×50×2		2	0.91	0.58	0.90
RHS 100×50×3	4-point bending	1	0.80	0.39	0.91
RHS 100×50×5		1	0.61	0.23	0.90
RHS 100×50×3-D		1	0.83	0.44	0.94
Mean			0.79		0.92
COV			0.20		0.07

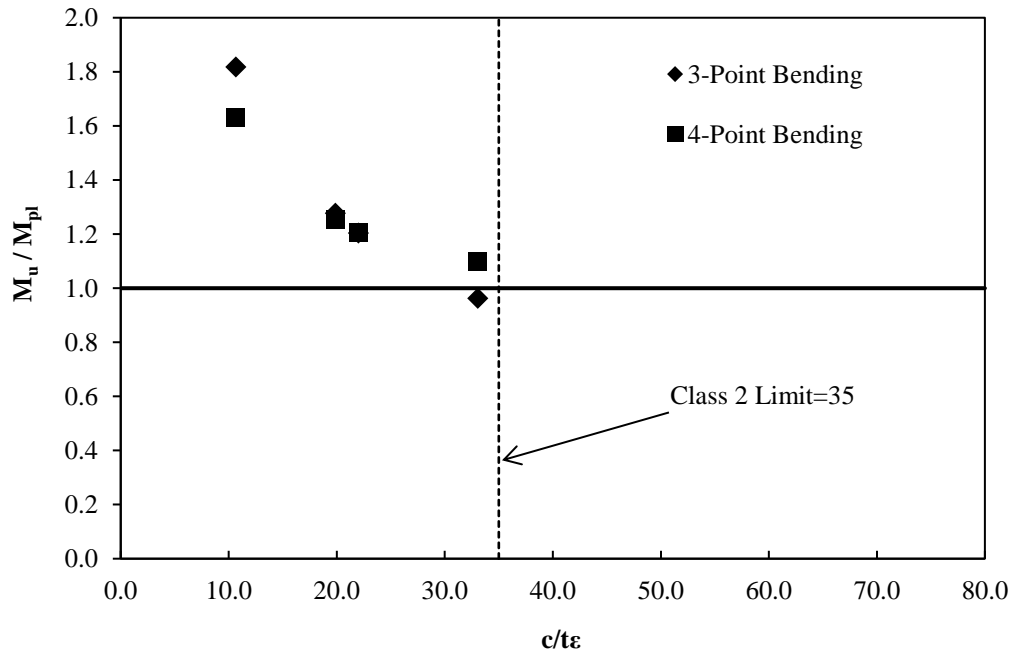


Fig. 6.1: Assessment of the Eurocode Class 2 slenderness limits for internal elements in compression (EN 1993-1-4+A1, 2015)

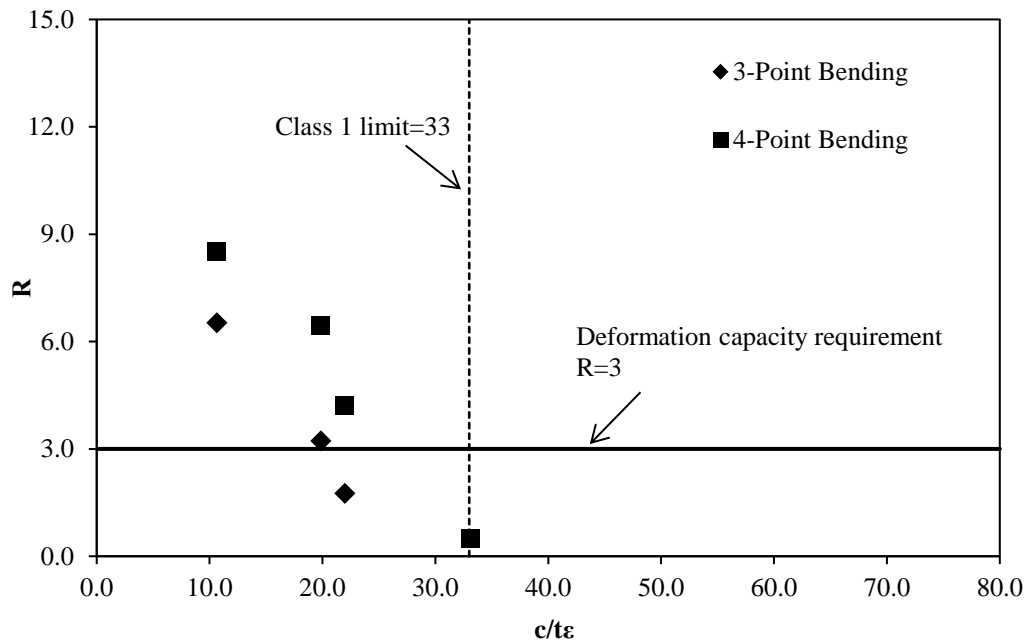


Fig. 6.2: Assessment of the Eurocode Class 1 slenderness limits for internal elements in compression (EN 1993-1-4+A1, 2015)

6.2. DESIGN OF STAINLESS STEEL CONTINUOUS BEAMS

In this section, the design methods for the behaviour and design of stainless steel continuous beams are discussed. In particular, the ultimate capacity predictions determined according to the four design methods outlined in Chapter 2 (i.e. Eurocode method without moment redistribution, Eurocode method with moment redistribution, CSM without moment redistribution, CSM with moment redistribution) are normalized by the ultimate experimental load and the results are reported in Table 6.2. Aiming to allow a general overview of plastic design for stainless steel structures, test data reported in the literature are also considered (Mirambell and Real, 2000; Real and Mirambell, 2005; Theofanous et al., 2014; Arrayago and Real, 2016). It can be seen that the Eurocode method, which allows for neither moment redistribution nor strain-hardening yields the most conservative design predictions. Improved

design predictions both in terms of accuracy (Mean closer to 1) and consistency (small COV) are obtained for both the variation of the Eurocode, which allows for moment redistribution and the CSM without moment redistribution. The significance of the recently adopted cross-sectional slenderness limits (EN 1993-1-4+A1, 2015) for an efficient design, was observed in the two SHS 80×80×3 tested by Mirambell and Real (2000), which were originally listed as Class 4 (EN 1993-1-4, 2006) not allow for CSM with moment redistribution to be utilized. Overall both the effect of strain-hardening and moment redistribution have to be taken into account, in order to obtain accurate predictions of the observed response and as expected the CSM for indeterminate structures results in most cases in the most accurate design predictions. However, it should be noted the CSM for indeterminate structures seems better suited for austenitic and duplex grades, which display a high level of strain-hardening whereas the predictions of the ultimate response of ferritic stainless steel continuous beams are overall unsafe.

Table 6.2: Assessment of design methods for plastic design of stainless steel continuous beams – experimental results

	Specimen	Grade	Class	EC3 no	EC3 with	CSM no	CSM with
				redistribution	redistribution	redistribution	redistribution
				F_{pred}/F_u			
Mirambell and Real, 2000; Real and Mirambell, 2005	SHS 80×80×3	1.4301	2	0.74	0.83	0.76	N/A
	SHS 80×80×3	1.4301	2	0.80	0.88	0.82	N/A
	RHS 120×80×4	1.4301	1	0.72	0.81	0.80	0.89
	RHS 120×80×4	1.4301	1	0.72	0.81	0.80	0.89
	I-100×100×8	1.4301	1	0.70	0.79	0.89	1.00
	SHS 50×50×3	1.4301/1.4307	1	0.60	0.68	0.81	0.91
	SHS 50×50×3	1.4301/1.4307	1	0.49	0.68	0.67	0.91
	SHS 60×60×3	1.4301/1.4307	1	0.64	0.72	0.83	0.93
	SHS 60×60×3	1.4301/1.4307	1	0.67	0.76	0.87	0.98
	SHS 100×100×3	1.4301/1.4307	4	0.71	0.71	0.85	N/A
	SHS 100×100×3	1.4301/1.4307	4	0.72	0.72	0.85	N/A
	RHS 60×40×3	1.4301/1.4307	1	0.56	0.63	0.75	0.84
	RHS 60×40×3	1.4301/1.4307	1	0.56	0.63	0.75	0.85
	RHS 60×40×3	1.4301/1.4307	1	0.61	0.69	0.75	0.84
	RHS 60×40×3	1.4301/1.4307	1	0.51	0.71	0.62	0.85
	I-200×140×6×6	1.4162	4	0.68	0.68	0.76	N/A
	I-200×140×8×6	1.4162	3	0.66	0.66	0.74	N/A
	I-200×140×10×8	1.4162	1	0.70	0.79	0.81	0.91
	I-200×140×12×8	1.4162	1	0.64	0.72	0.83	0.93
	I-200×140×6×6	1.4162	4	0.56	0.56	0.62	N/A
	I-200×140×8×6	1.4162	3	0.57	0.57	0.65	N/A
Theofanous et al., 2014	I-200×140×10×8	1.4162	1	0.60	0.84	0.70	0.95
	I-200×140×12×8	1.4162	1	0.59	0.82	0.77	1.02
	SHS 80×80×4	1.4003	1	1.06	1.20	1.07	1.20

	Specimen	Grade	Class	EC3 no	EC3 with	CSM no	CSM with
				redistribution	redistribution	redistribution	redistribution
				F_{pred}/F_u			
Arrayago and Real, 2016	SHS 80×80×4	1.4003	1	1.04	1.18	1.05	1.18
	SHS 60×60×3	1.4003	1	0.95	1.08	0.97	1.09
	RHS 80×40×4	1.4003	1	0.92	1.04	0.95	1.07
	RHS 80×40×4	1.4003	1	0.91	1.03	0.91	1.03
	RHS 120×80×3	1.4003	3	1.06	N/A	N/A	N/A
	RHS 120×80×3	1.4003	4	0.85	N/A	N/A	N/A
	RHS 70×50×2	1.4003	4	0.98	1.11	0.94	N/A
	RHS 70×50×2	1.4003	4	0.77	N/A	N/A	N/A
Gkantou et al., 2019	RHS 100×50×2	1.4301/1.4307	2	0.94	1.02	0.88	0.97
	RHS 100×50×3	1.4301/1.4307	1	0.90	0.97	1.01	1.13
	RHS 100×50×5	1.4301/1.4307	1	0.55	0.59	0.69	0.80
	RHS 100×50×3	1.4462	1	0.81	0.87	0.87	0.97
Mean		All		0.73	0.81	0.82	0.97
COV				0.22	0.21	0.14	0.11
Mean	Austenitic			0.68	0.76	0.80	0.91
COV				0.18	0.15	0.11	0.09
Mean	Duplex			0.65	0.72	0.75	0.96
COV				0.12	0.16	0.11	0.04
Mean	Ferritic			0.95	1.11	0.98	1.11
COV				0.10	0.06	0.07	0.07

* N/A = Not applicable for any of the listed design methods

The FE results obtained from the parametric studies, that were conducted after the accurate replication of the experimental models reported by Theofanous et al. (2014) and Gkantou et al. (2019), are analysed and discussed. Alike the test data reported in Table 6.2, the ultimate capacity predictions determined according to the four design methods outlined above, are normalized by the ultimate load obtained for each simulated beam from the FE analysis (Table 6.3). Similar conclusions are drawn from the results of the parametric studies for the seven load cases considered (LC1 to LC5; LC1.1 and LC2.1). In accordance with Table 6.3, significantly improved predicted capacities both in terms of efficiency and consistency are evident by the CSM considering-plastic-design. For LC2 and LC5, CSM for indeterminate structures seems to overestimate the ultimate capacity. This is likely due to the high shear forces that the plastic hinges are subjected to, which reduces the cross-section moment resistance.

Table 6.3: Assessment of design methods for plastic design of stainless steel continuous beams – numerical results

	Specimen	H/B ratio	Grade	Number of FE	EC3 no	EC3 with	CSM no	CSM with
					redistribu	redistribut	redistribut	redistribut
					F_{pred}/F_u			
LC1	SHS 100×100	1.0	1.4301/1.4307	5	0.78	0.83	0.88	0.99
	SHS 100×100	1.0	1.4162	5	0.81	0.91	0.90	0.95
	RHS 200×100	2.0	1.4301/1.4307	5	0.85	0.91	0.90	1.01
	RHS 200×100	2.0	1.4162	5	0.88	0.92	0.96	0.98
	RHS 244×100	2.44	1.4301/1.4307	5	0.86	0.90	0.92	1.02
	RHS 244×100	2.44	1.4162	5	0.93	0.97	0.90	1.01
LC2	SHS 100×100	1.0	1.4301/1.4307	5	0.69	0.84	0.73	0.98
	SHS 100×100	1.0	1.4162	5	0.74	0.94	0.86	0.94
	RHS 200×100	2.0	1.4301/1.4307	5	0.85	0.99	0.87	1.07
	RHS 200×100	2.0	1.4162	5	0.88	0.97	0.84	1.05
	RHS 244×100	2.44	1.4301/1.4307	5	0.87	0.97	0.92	1.21
	RHS 244×100	2.44	1.4162	5	0.90	1.10	0.94	1.08
LC3	SHS 100×100	1.0	1.4301/1.4307	5	0.73	0.83	0.80	0.95
	SHS 100×100	1.0	1.4162	5	0.77	0.97	0.86	0.92
	RHS 200×100	2.0	1.4301/1.4307	5	0.87	0.98	0.87	1.02
	RHS 200×100	2.0	1.4162	5	0.91	0.98	0.92	1.04
	RHS 244×100	2.44	1.4301/1.4307	5	0.88	0.95	0.91	1.02
	RHS 244×100	2.44	1.4162	5	0.94	1.02	0.96	1.00
LC4	SHS 100×100	1.0	1.4301/1.4307	5	0.70	0.81	0.84	0.95
	SHS 100×100	1.0	1.4162	5	0.73	0.93	0.93	0.94
	RHS 200×100	2.0	1.4301/1.4307	5	0.81	0.94	0.95	0.99
	RHS 200×100	2.0	1.4162	5	0.82	0.90	0.93	0.97
	RHS 244×100	2.44	1.4301/1.4307	5	0.83	0.92	1.01	1.01
	RHS 244×100	2.44	1.4162	5	0.90	1.00	1.03	1.08

LC5	SHS 100×100	1.0	1.4301/1.4307	5	0.70	0.83	0.80	0.95
	SHS 100×100	1.0	1.4162	5	0.75	0.94	0.86	0.93
	RHS 200×100	2.0	1.4301/1.4307	5	0.82	0.96	0.89	1.03
	RHS 200×100	2.0	1.4162	5	0.89	1.02	0.90	1.02
	RHS 244×100	2.44	1.4301/1.4307	5	0.81	0.90	0.88	1.05
	RHS 244×100	2.44	1.4162	5	0.90	1.06	0.97	1.20
LC1.1	SHS 50×50	1.0	1.4301/1.4307	4	0.77	0.83	0.88	1.01
	SHS 50×50	1.0	1.4462	4	0.77	0.81	0.84	0.96
	RHS 100×50	2.0	1.4301/1.4307	4	0.78	0.84	0.88	1.01
	RHS 100×50	2.0	1.4462	4	0.76	0.80	0.82	0.94
	RHS 122×50	2.44	1.4301/1.4307	4	0.76	0.81	0.89	1.03
	RHS 122×50	2.44	1.4462	4	0.75	0.79	0.86	0.97
LC2.1	SHS 50×50	1.0	1.4301/1.4307	4	0.80	0.83	0.91	1.02
	SHS 50×50	1.0	1.4462	4	0.80	0.81	0.87	0.97
	RHS 100×50	2.0	1.4301/1.4307	4	0.80	0.82	0.90	1.00
	RHS 100×50	2.0	1.4462	4	0.78	0.80	0.84	0.92
	RHS 122×50	2.44	1.4301/1.4307	4	0.79	0.80	0.91	1.02
	RHS 122×50	2.44	1.4462	4	0.77	0.79	0.88	0.95
	Mean		All	198	0.83	0.93	0.90	1.00
	COV				0.09	0.08	0.06	0.06

* N/A = Not applicable for any of the listed design methods

The predicted collapse load F_{pred} normalised by the numerically obtained collapse load F_u is plotted against the cross-section slenderness $\bar{\lambda}_p$ in Fig. 6.3 to 6.7 and Fig. 6.8 to 6.9 for the load cases LC1, LC3, LC4, LC1.1 and LC2.1 and LC2, LC5 respectively. The current Eurocode method significantly underestimates the strength of continuous beams, due to not allowing for the formation of successive plastic hinges and moment redistribution and not accounting for the significant strain-hardening exhibited by stocky stainless steel sections. This is evident by the very low F_{pred}/F_u observed in Fig. 6.3 to 6.7, which decreases with decreasing slenderness indicating the increasing conservatism for stocky sections. Allowing for moment redistribution for Class 1 sections, while still assuming an elastic-perfectly plastic material response, the accuracy of the results is partially improved. CSM without redistribution offers an improvement since strain-hardening is accounted for. Finally, CSM with moment redistribution yields the most accurate results.

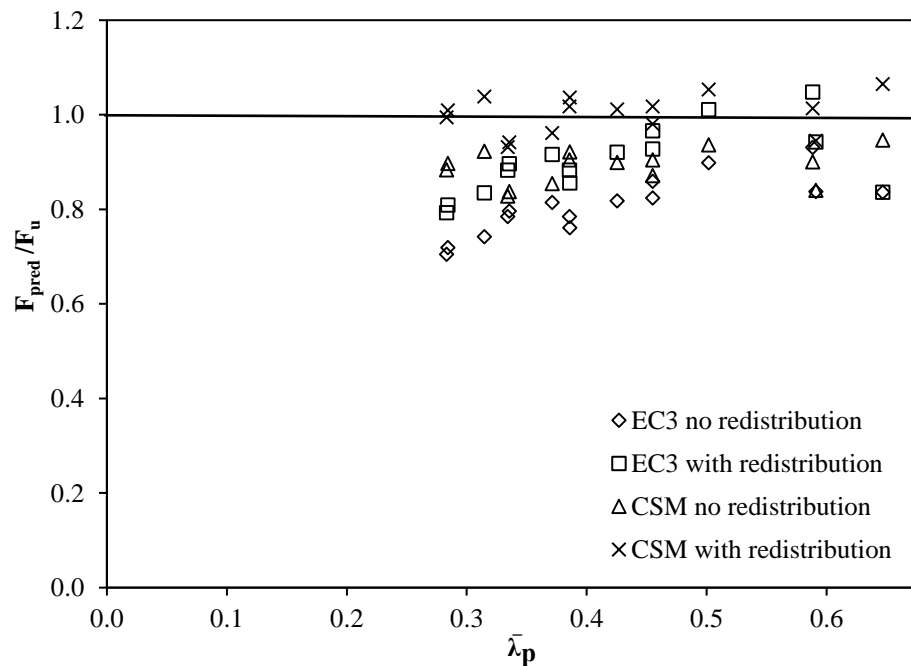


Fig. 6.3: F_{pred}/F_u against the $\bar{\lambda}_p$ for the four design methods for LC1

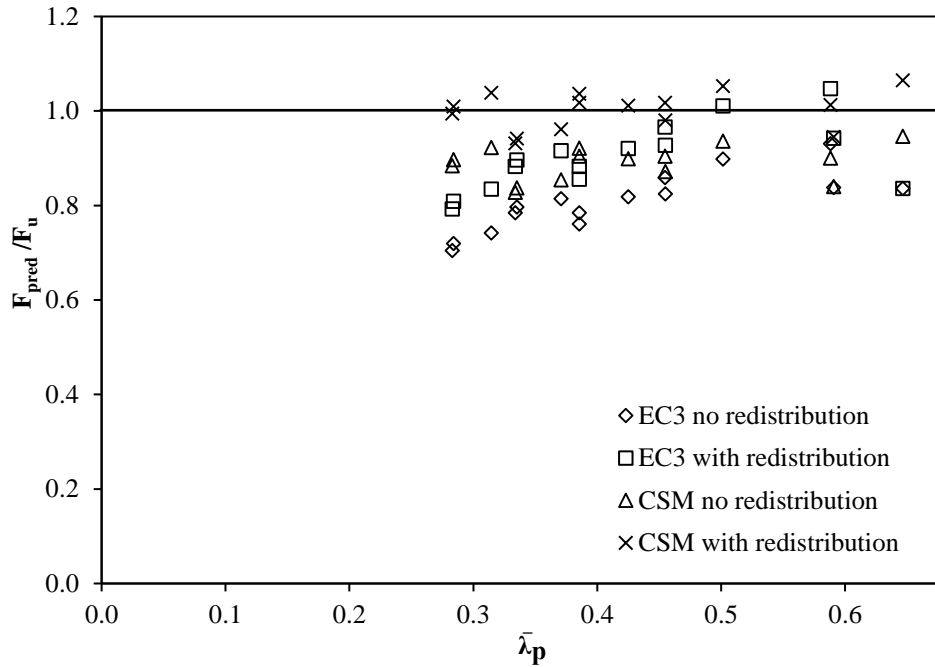


Fig. 6.4: F_{pred}/F_u against the $\bar{\lambda}_p$ for the four design methods for LC3

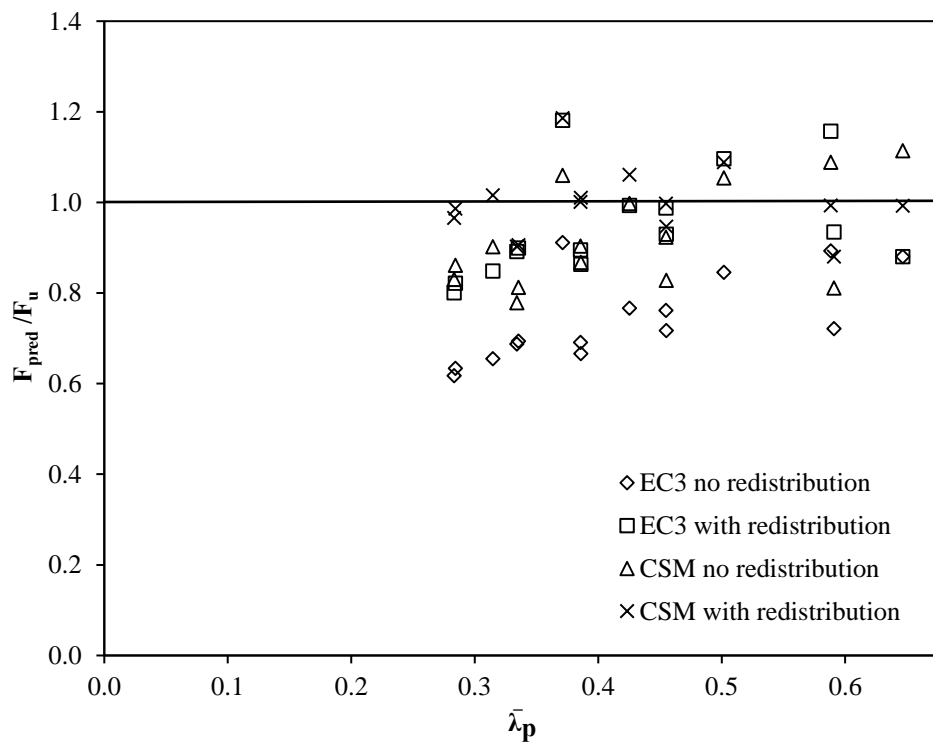


Fig. 6.5: F_{pred}/F_u against the $\bar{\lambda}_p$ for the four design methods for LC4

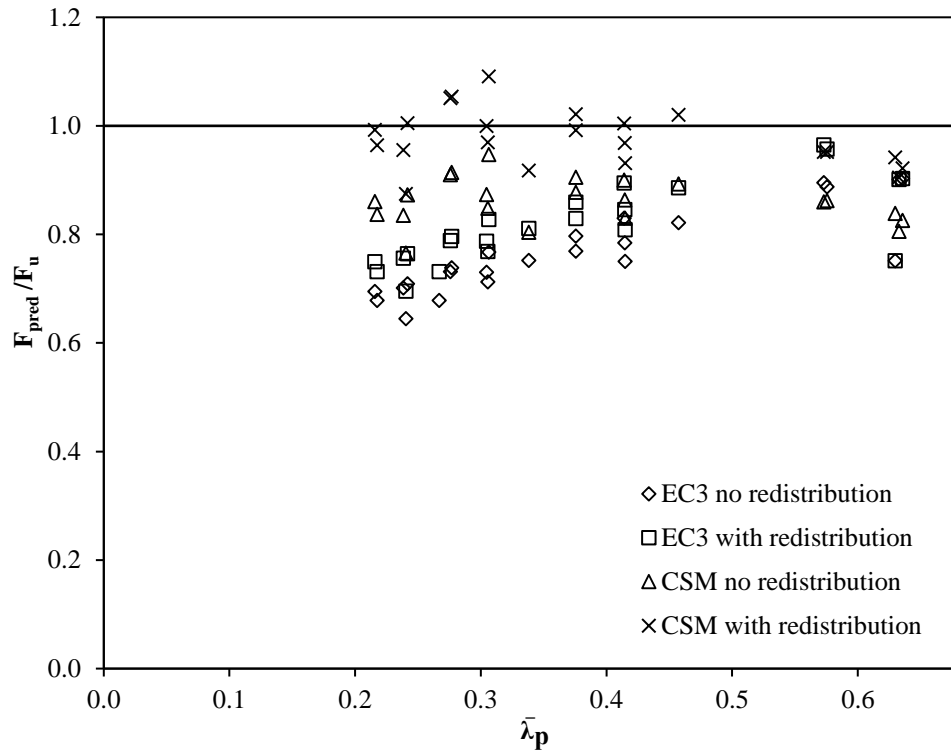


Fig. 6.6: F_{pred}/F_u against the $\bar{\lambda}_p$ for the four design methods for LC 1.1

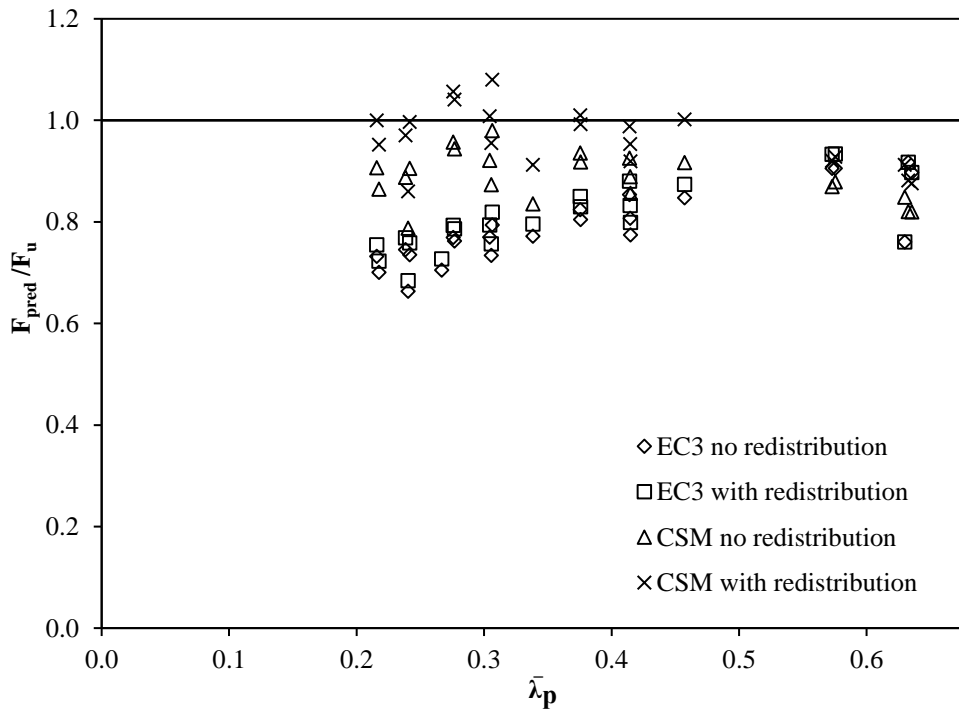


Fig. 6.7: F_{pred}/F_u against the $\bar{\lambda}_p$ for the four design methods for LC 2.1

Contrary to load cases LC1, LC3, LC4, LC1.1 and LC2.1, in load cases LC2 and LC5, CSM for indeterminate structures seems to overestimate the observed response as shown in Fig. 6.8 to 6.9. This is attributed to the higher shear stresses imposed on the plastic hinge locations, which decrease the moment resistance of those sections. It should be noted that for load combinations LC1, LC3, LC4, LC1.1 and LC2.1, shear stresses are lower due to the location of loads, whilst in the remaining load cases, the effect of shear is more pronounced.

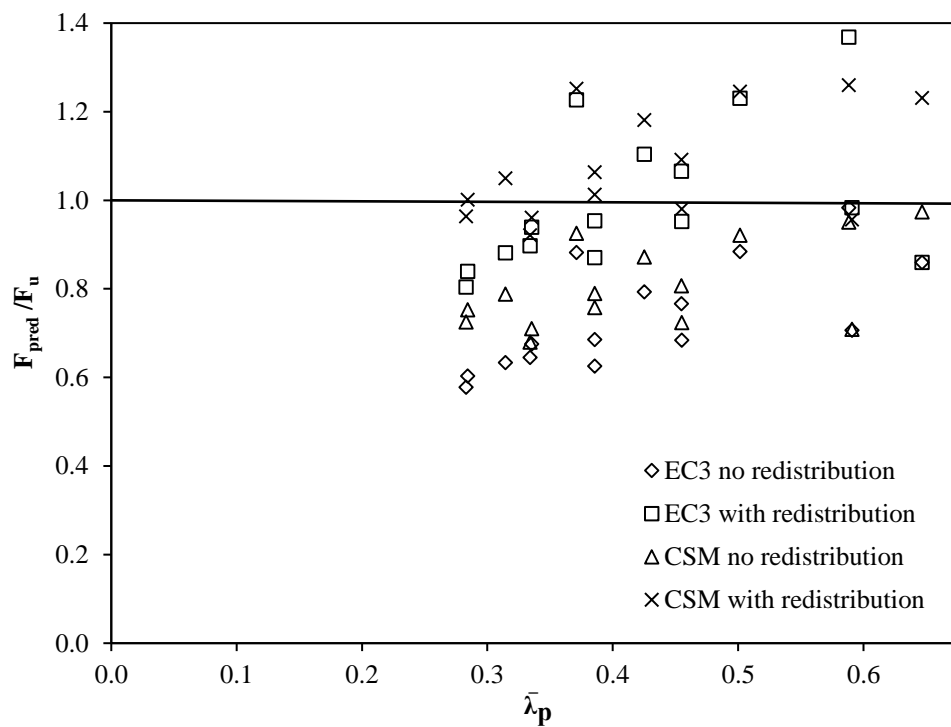


Fig. 6.8: F_{pred}/F_u against the $\bar{\lambda}_p$ for the four design methods for LC2

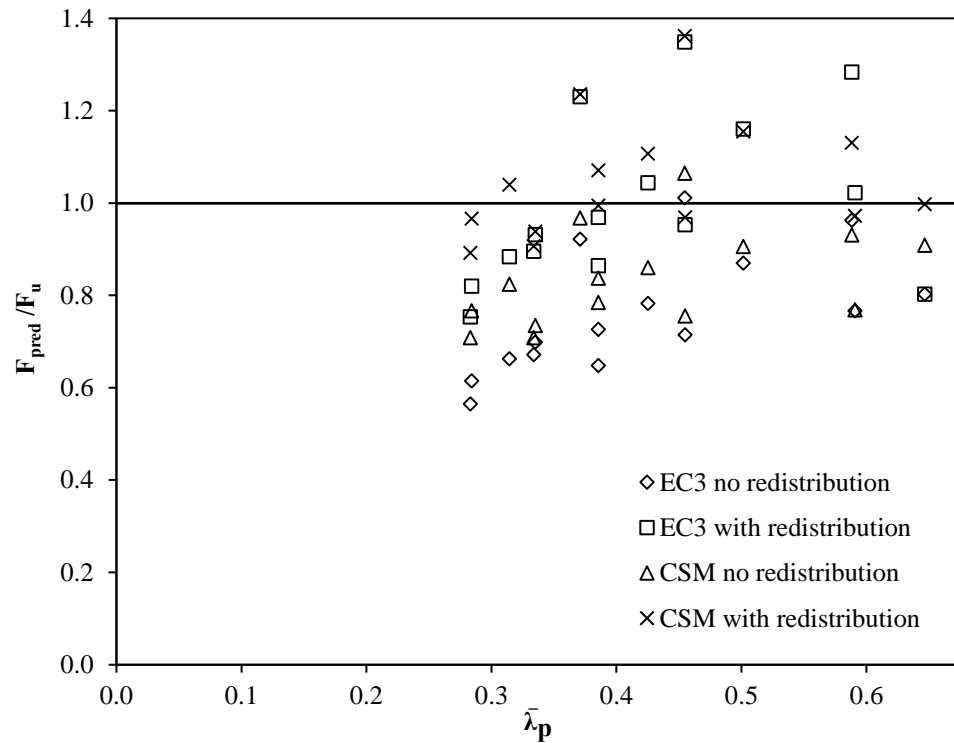


Fig. 6.9: F_{pred}/F_u against the $\bar{\lambda}_p$ for the four design methods for LC5

6.3. BEHAVIOUR AND DESIGN OF STAINLESS STEEL FRAMES

6.3.1. Levels of structural behaviour

The structural behaviour of a frame can be considered at different levels of response. These include the material response, the cross-sectional response, the member response and the system (structure) response. Each successive layer of response limits the structural behaviour of the frame and all 4 layers and their interactions need be considered for an efficient design.

The material response is limiting response of the structure if no other failure mode occurs at either cross-sectional, member or system level. In this study two material grades were considered, namely the austenitic and the duplex grades. Within the EN 1993-1-4+A1 (2015)

design framework a single parameter, namely the nominal yield strength f_y quantifies the material response, whilst the CSM takes into account in addition to the nominal yield strength the strain-hardening characteristics as quantified by the strain hardening stiffness E_{sh} .

The cross-sectional response refers to failure at cross-sectional level under the action of the applied loads. It limits the material response due to the potential occurrence of local buckling, thereby limiting the compressive and flexural resistance of a cross-section. Conventionally, the cross-sectional response is deduced from the class of the considered cross-section, depending on which different levels of cross-sectional resistances are considered in design in a discrete fashion (Gardner and Theofanous, 2008). The CSM offers an alternative design approach allowing for strain-hardening at cross-sectional level, thereby forming a continuous relationship between cross-sectional and material response.

The member response limits the cross-sectional response due to the occurrence of member instabilities. Hence the full strength of a cross-section may not be exploited if the member which the cross-section belongs to fails at lower load levels. In this study, all members of the frames are beam-columns and the relevant member instability failure mode involves buckling of a beam-column about the major axis. The minor axis response is not considered in this study. The structural behaviour and design of stainless steel beam-columns with RHS and SHS has been studied experimentally and numerically by Zhao et al. (2016; 2019) and is not explicitly considered in this study.

Finally, the system response refers to the interaction of all structural members and their connections to one another. The behaviour of stainless steel connections (Elflah et al., 2019

(a); Elflah et al., 2019 (b); Elflah et al., 2019 (c); Yuan et al., 2019) is beyond the scope of this research project. It is assumed that the connections possess adequate strength, stiffness and ductility not to affect the frame behaviour (i.e. they will not fail prior to the members). The behaviour at system level is associated with both frame instability, as quantified using the α_{cr} factor and moment redistribution for indeterminate structures with Class 1 sections, as quantified by the α_p factor. As previously stated, moment redistribution is not permitted in EN 1993-1-4+A1 (2015). Nonetheless, its application is considered and assessed herein.

The previous discussion is summarised in Table 6.4 where the relevant design parameters for the design procedures assessed herein are given for each of the four levels of structural response. In the next section the numerical results obtained from the parametric studies on stainless steel frames as discussed in Section 5.3 are utilized for the assessment of various design methods applicable to stainless steel frames. These include the currently applicable design methodology of EN 1993-1-4+A1 (2015), which does not permit the application of plastic design termed “EC3 no redistribution”, a variation of the method allowing for moment redistribution termed “EC3 with redistribution”, the CSM applied only at cross-sectional level “CSM” and the variation of the CSM for indeterminate structures “CSM with redistribution”. In general, the design methods assessed can be classified in two broad groups; those allowing for moment redistribution and assuming failure to occur when a mechanism occurs, and those not allowing for moment redistribution. In all cases second-order effects, cross-sectional behaviour and member behaviour need be considered.

Table 6.4: Design parameters for various levels of response and design methods.

Level of response	Design methods without moment redistribution		Design methods allowing for moment redistribution	
	EC3 no redistribution	CSM no redistribution	EC3 with redistribution	CSM with redistribution
Material	f_y	f_y, E_{sh}	f_y	f_y, E_{sh}
Cross-section	classification, $c/t\epsilon$	$\bar{\lambda}_p, \epsilon_{CSM}$	classification, $c/t\epsilon$	$\bar{\lambda}_p, \epsilon_{CSM}$
Member	$\lambda_y, k_y, M_{pl,y}, N_{b,y,Rd}$	$\lambda_y, k_y, M_{csm}, N_{b,y,Rd}$	$\lambda_y, k_y, M_{pl,y}, N_{b,y,Rd}$	$\lambda_y, k_y, M_{csm}, N_{b,y,Rd}$
System	α_{cr}	α_{cr}	α_{cr}, α_p	$\alpha_{cr}, \alpha_{csm}$

6.3.2. Numerical results and failure modes

Based on the modelled cross-section geometries, support conditions and ratio of applied horizontal over applied vertical loads (H/V), a wide range of structural responses and failure modes occurs, as well as different degrees of sensitivity to second order effects. A crucial parameter affecting the behaviour and failure mode relates to the slenderness of the (beam-column) of the frame. With increasing column slenderness, failure is due to member instability and occurs prior to the formation of a plastic hinge, or prior to local buckling of the most heavily stressed cross-sections. The effect of local slenderness (i.e. cross-section slenderness) is to limit the extent to which strain-hardening can be exploited at the most heavily stressed cross-sections; for high member slenderness values, the effect of cross-section slenderness is not important as failure is governed by member instability prior to the formation of a plastic hinge. Typical failure modes of a fixed-based frame employing a stocky member (i.e. RHS

200×100×10) and a slender member (i.e. RHS 100×50×3) are shown in Fig. 6.10 for a fixed-based frame subjected to vertical loads only. Clearly the frame with the higher member slenderness fails by member instability prior to the development of the plastic hinges, whilst the formation a local beam mechanism through the successive formation of plastic hinges can be seen for the frame employing the stockier member.

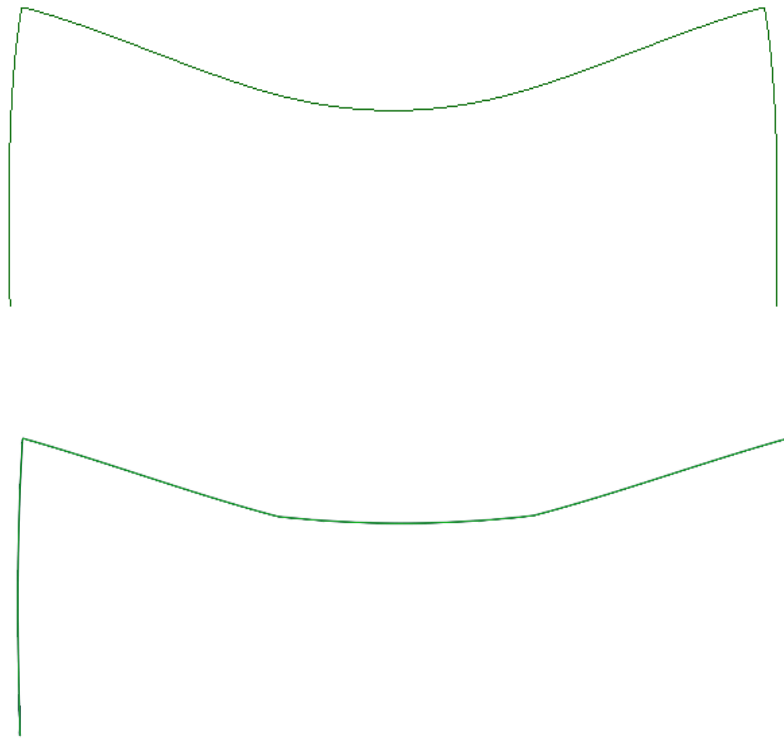


Fig. 6.10: Failure modes for frames employing slender (top) and stocky (bottom) beam-columns

The type of the plastic collapse mechanism at failure differs depending on the H/V ratio and whether the frame is pinned or fixed. For fixed-based frames and for pinned-based frames without any horizontal loads ($H/V=0$), a local beam collapse mechanism involving the formation of plastic hinges on the top of each column and within the beam length without any sway of the frame occurs. Contrary, a combined mechanism involving both sway and local

beam mechanism can be observed for pin-ended frames subjected to high lateral loads, a typical example of which is shown in Fig. 6.11.

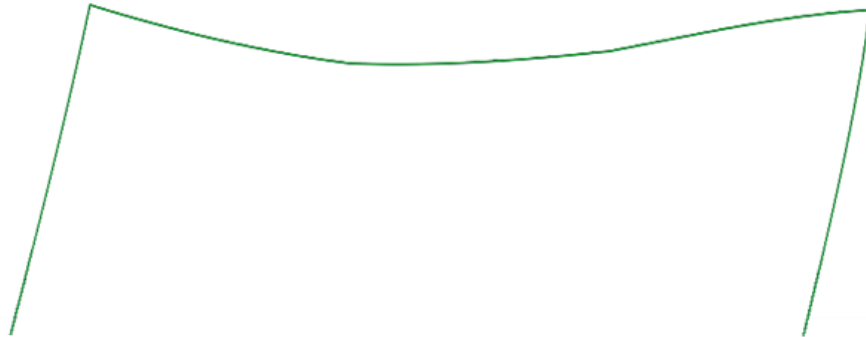


Fig. 6.11: Combined plastic mechanism of a pin-ended frame

Within the range of investigated parameters considered, the relevant collapse mechanisms obtained are reported in Table 6.5.

Table 6.5: Plastic mechanism for the support conditions and load patterns considered

Support conditions	Horizontal over Vertical load ratio (H/V)		
	0	0.1	0.2
Pinned	local beam mechanism	combined mechanism	combined mechanism
Fixed	local beam mechanism	local beam mechanism	local beam mechanism

It is noted that the collapse mechanisms referred to in Table 6.4 are the expected plastic collapse mechanisms that would develop if no member instability occurs, i.e. they should be regarded as the failure modes in the limiting case of the beam-columns of the frame being too

stocky to fail by member instability prior to the formation of a sufficient number of plastic hinges for a mechanism to occur. In most cases this is not the case and allowance for member instability is made by referring to the EN 1993-1-4+A1 (2015) beam-column check about the major axis, given in Eq. 26:

$$\frac{N_{Ed}}{N_{b,y,Rd}} + k_y \frac{M_{Ed}}{M_{pl,y,Rd}} \leq 1 \quad (26)$$

where N_{Ed} and M_{Ed} are the applied axial forces and bending moments, $N_{b,y,Rd}$ is the buckling resistance of the beam-column about the major axis and $M_{pl,y,Rd}$ is the plastic moment resistance about the major axis. The interaction factor k_y is defined in Eq. 27:

$$k_y = 1.0 + 2(\bar{\lambda}_y - 0.5) \frac{N_{Ed}}{N_{b,y,Rd}} \quad \text{but} \quad 1.2 \leq k_y \leq 1.2 + 2 \frac{N_{Ed}}{N_{b,y,Rd}} \quad (27)$$

For the determination of the interaction factor, the non-dimensional slenderness associated with major axis buckling needs to be determined, which in turn necessitates the estimation of the critical length of the column $L_{e,y}$. In this thesis the critical length of the column was back calculated from the F_{cr} values which were determined for each frame by means of linear eigenvalue buckling analysis, using Eq. 28:

$$L_{e,y} = \sqrt{\frac{\pi^2 EI}{F_{cr}}} \quad (28)$$

where F_{cr} is the elastic critical buckling load that causes global sway instability based on initial elastic stiffness.

Having discussed the importance of cross-sectional and member slenderness, frame sway instability and potential for moment redistribution, key parameters pertaining to all design methods assessed hereafter are reported in Tables 6.6 and 6.7 for fixed-based and pinned frames respectively. These include cross-sectional plastic moment resistance about the major axis $M_{pl,y}$, the corresponding moment resistance according to the CMS M_{CSM} , the non-dimensional slenderness of the beam-columns about their major axis λ_y corresponding to the effective buckling length $L_{e,y}$, the flexural buckling resistance about the major axis $N_{b,y}$ the $\alpha_{cr,1}$ factor, which is a measure of the susceptibility of the frames to 2nd order effects (P- Δ effects) and the $\alpha_{p,1}$ which is a measure of the potential for moment redistribution. It is noted that the calculation of both F_{cr} and $\alpha_{p,1}$ is based on an assumed reference load configuration involving 0.5 kN vertical load at each of the beam's third points, and a horizontal load based on an assumed ratio of the horizontal to total vertical loads and can hence take the values of 0, 100 N and 200 N for a total vertical load of 1 kN. It is clear that the fixed-based frames, as expected, have much lower susceptibility to 2nd order effects (higher F_{cr} values), whilst their potential for moment redistribution (higher $\alpha_{p,1}$ values) is also considerably higher due to the higher degree of static indeterminacy. Furthermore, due to the fixed-ended conditions the non-dimensional slenderness of the columns of the fixed-based frame is significantly smaller compared to that of the columns of the pinned frame. This clearly affects the level up to which strain-hardening can be exploited as will be discussed in the following sections.

Table 6.6: Key design parameters for fixed-based frames

Cross-section	f_y (N/mm ²)	H/V	$M_{pl,y}$ (kNm)	M_{CSM} (kNm)	$\bar{\lambda}_y$	$N_{b,y}$ (kN)	F_{cr} (kN)	$\alpha_{p,1}$
50×50×2	466	0	3.2	3.1	3.8	10.8	24.2	3.3
50×50×3	466		4.5	5.2	3.8	15.2	34.1	4.7
50×50×5	466		6.8	8.4	4.0	22.3	49.8	7.1
100×50×2	466		8.8	8.4	2.1	51.3	127.0	10.0
100×50×3	466		12.7	14.4	2.1	74.2	183.5	14.3
100×50×5	466		19.9	24.5	2.1	115.1	283.6	22.3
100×100×4	466		25.4	24.6	1.9	153.3	386.6	29.0
100×100×6	466		36.2	41.2	1.9	216.6	544.5	41.1
100×100×10	466		54.2	67.0	2.0	319.0	796.6	61.5
200×100×4	466		70.1	67.4	1.0	605.2	2022.3	82.9
200×100×6	466		101.8	115.5	1.0	879.5	2923.2	120.1
200×100×10	466		158.8	195.8	1.0	1373.5	4517.4	187.1
50×50×2	579		3.9	3.6	4.2	11.1	24.7	4.0
50×50×3	579		5.6	6.2	4.2	15.6	34.7	5.7
50×50×5	579		8.4	10.0	4.4	22.9	50.8	8.6
100×50×2	579		10.9	9.7	2.3	53.4	129.4	12.0
100×50×3	579		15.8	17.4	2.3	77.3	187.1	17.1
100×50×5	579		24.7	29.4	2.3	119.7	289.0	26.6
100×100×4	579		31.5	28.9	2.1	159.9	394.0	34.7
100×100×6	579		44.9	49.7	2.1	225.9	554.9	49.2
100×100×10	579	67.3	80.3	2.2	332.4	811.8	73.4	
200×100×4	579	87.1	78.0	1.1	661.8	2060.8	102.6	
200×100×6	579	126.5	139.4	1.1	960.9	2978.8	148.5	
200×100×10	579	197.4	234.8	1.2	1497.8	4603.3	231.0	
50×50×2	466	0.1	3.2	3.1	3.9	10.3	23.0	3.3
50×50×3	466		4.5	5.2	3.9	14.5	32.5	4.7
50×50×5	466		6.8	8.4	4.0	21.3	47.5	7.1

Cross-section	f_y (N/mm ²)	H/V	$M_{pl,y}$ (kNm)	M_{CSM} (kNm)	$\bar{\lambda}_y$	$N_{b,y}$ (kN)	F_{cr} (kN)	$\alpha_{p,1}$
100×50×2	466		8.8	8.4	2.1	49.2	121.1	9.9
100×50×3	466		12.7	14.4	2.1	71.2	175.0	14.2
100×50×5	466		19.9	24.5	2.1	110.3	270.4	22.2
100×100×4	466		25.4	24.6	1.9	147.1	368.8	28.8
100×100×6	466		36.2	41.2	2.0	207.8	519.4	40.9
100×100×10	466		54.2	67.0	2.0	306.0	759.9	61.2
200×100×4	466		70.1	67.4	1.1	587.9	1929.7	83.0
200×100×6	466		101.8	115.5	1.1	854.2	2789.2	120.0
200×100×10	466		158.8	195.8	1.1	1333.4	4310.2	187.1
50×50×2	579		3.9	3.6	4.3	10.6	23.5	4.0
50×50×3	579		5.6	6.2	4.3	14.9	33.1	5.7
50×50×5	579		8.4	10.0	4.5	21.9	48.4	8.6
100×50×2	579		10.9	9.7	2.3	51.2	123.4	12.0
100×50×3	579		15.8	17.4	2.3	74.0	178.4	17.0
100×50×5	579		24.7	29.4	2.4	114.7	275.6	26.6
100×100×4	579		31.5	28.9	2.1	153.3	375.8	34.6
100×100×6	579		44.9	49.7	2.2	216.5	529.3	48.9
100×100×10	579		67.3	80.3	2.2	318.5	774.3	73.1
200×100×4	579		87.1	78.0	1.2	640.9	1966.3	102.7
200×100×6	579		126.5	139.4	1.2	930.3	2842.3	148.4
200×100×10	579		197.4	234.8	1.2	1449.5	4392.2	231.0
50×50×2	466		3.2	3.1	4.0	9.8	22.0	3.3
50×50×3	466		4.5	5.2	4.0	13.9	31.0	4.7
50×50×5	466		6.8	8.4	4.1	20.4	45.4	7.0
100×50×2	466	0.2	8.8	8.4	2.2	47.1	115.5	9.9
100×50×3	466	0.2	12.7	14.4	2.2	68.2	167.0	14.2
100×50×5	466	0.2	19.9	24.5	2.2	105.7	257.9	22.1
100×100×4	466	0.2	25.4	24.6	2.0	141.1	351.7	28.8
100×100×6	466	0.2	36.2	41.2	2.0	199.3	495.3	40.7

Cross-section	f_y (N/mm ²)	H/V	$M_{pl,y}$ (kNm)	M_{CSM} (kNm)	$\bar{\lambda}_y$	$N_{b,y}$ (kN)	F_{cr} (kN)	$\alpha_{p,1}$
100×100×10	466		54.2	67.0	2.1	293.4	724.6	60.9
200×100×4	466		70.1	67.4	1.1	570.6	1840.5	83.1
200×100×6	466		101.8	115.5	1.1	828.8	2660.3	120.0
200×100×10	466		158.8	195.8	1.1	1293.0	4111.0	187.0
50×50×2	579		3.9	3.6	4.4	10.1	22.4	4.0
50×50×3	579		5.6	6.2	4.5	14.3	31.6	5.7
50×50×5	579		8.4	10.0	4.6	21.0	46.2	8.6
100×50×2	579		10.9	9.7	2.4	49.0	117.7	11.9
100×50×3	579		15.8	17.4	2.4	70.9	170.1	17.0
100×50×5	579		24.7	29.4	2.4	109.8	262.8	26.5
100×100×4	579		31.5	28.9	2.2	146.9	358.4	34.4
100×100×6	579		44.9	49.7	2.2	207.5	504.7	48.7
100×100×10	579		67.3	80.3	2.3	305.2	738.4	72.6
200×100×4	579		87.1	78.0	1.2	620.0	1875.5	102.8
200×100×6	579		126.5	139.4	1.2	899.8	2710.9	148.3
200×100×10	579		197.4	234.8	1.2	1401.5	4189.2	231.0

Table 6.7: Key design parameters for pinned-based frames

Cross-section	f_y (N/mm ²)	H/V	$M_{pl,y}$ (kNm)	M_{CSM} (kNm)	$\bar{\lambda}_y$	$N_{b,y}$ (kN)	F_{cr} (kN)	$\alpha_{p,1}$
50×50×2	466		3.2	3.1	7.1	3.3	7.0	4.2
50×50×3	466		4.5	5.2	7.1	4.7	10.0	6.0
50×50×5	466		6.8	8.4	7.3	6.8	14.6	9.0
100×50×2	466	0	8.8	8.4	3.8	16.5	37.2	11.7
100×50×3	466		12.7	14.4	3.8	23.9	53.7	17.0
100×50×5	466		19.9	24.5	3.9	37.0	83.0	26.5
100×100×4	466		25.4	24.6	3.5	49.9	113.2	33.8
100×100×6	466		36.2	41.2	3.6	70.4	159.4	48.2

Cross-section	f_y (N/mm ²)	H/V	$M_{pl,y}$ (kNm)	M_{CSM} (kNm)	$\bar{\lambda}_y$	$N_{b,y}$ (kN)	F_{cr} (kN)	$\alpha_{p,1}$
100×100×10	466		54.2	67.0	3.7	103.4	233.2	72.2
200×100×4	466		70.1	67.4	1.9	234.8	592.1	93.4
200×100×6	466		101.8	115.5	1.9	340.0	855.8	135.7
200×100×10	466		158.8	195.8	1.9	527.2	1322.5	211.8
50×50×2	579		3.9	3.6	7.7	3.4	7.2	5.3
50×50×3	579		5.6	6.2	7.9	4.8	10.2	7.5
50×50×5	579		8.4	10.0	8.1	7.0	14.9	11.2
100×50×2	579		10.9	9.7	4.2	17.0	37.9	14.5
100×50×3	579		15.8	17.4	4.2	24.6	54.7	21.1
100×50×5	579		24.7	29.4	4.3	38.1	84.6	32.9
100×100×4	579		31.5	28.9	3.9	51.5	115.3	42.0
100×100×6	579		44.9	49.7	3.9	72.6	162.4	59.9
100×100×10	579		67.3	80.3	4.0	106.5	237.6	89.7
200×100×4	579		87.1	78.0	2.1	244.9	603.3	116.1
200×100×6	579		126.5	139.4	2.1	354.5	872.1	168.7
200×100×10	579		197.4	234.8	2.1	549.5	1347.6	263.1
50×50×2	466		3.2	3.1	7.1	3.3	7.0	3.7
50×50×3	466		4.5	5.2	7.2	4.6	9.8	5.3
50×50×5	466		6.8	8.4	7.4	6.8	14.4	8.0
100×50×2	466		8.8	8.4	3.8	16.4	36.8	10.3
100×50×3	466		12.7	14.4	3.8	23.7	53.1	15.0
100×50×5	466		19.9	24.5	3.9	36.6	82.1	23.4
100×100×4	466	0.1	25.4	24.6	3.5	49.4	111.9	29.8
100×100×6	466		36.2	41.2	3.6	69.7	157.6	42.5
100×100×10	466		54.2	67.0	3.7	102.3	230.6	63.7
200×100×4	466		70.1	67.4	1.9	232.6	585.7	82.4
200×100×6	466		101.8	115.5	1.9	336.8	846.5	119.8
200×100×10	466		158.8	195.8	2.0	522.2	1308.2	186.9
50×50×2	579		3.9	3.6	7.8	3.4	7.1	4.6

Cross-section	f_y (N/mm ²)	H/V	$M_{pl,y}$ (kNm)	M_{CSM} (kNm)	$\bar{\lambda}_y$	$N_{b,y}$ (kN)	F_{cr} (kN)	$\alpha_{p,1}$
50×50x3	579		5.6	6.2	7.9	4.7	10.1	6.6
50×50×5	579		8.4	10.0	8.1	6.9	14.7	9.9
100×50×2	579		10.9	9.7	4.2	16.9	37.5	12.8
100×50×3	579		15.8	17.4	4.2	24.4	54.1	18.6
100×50×5	579		24.7	29.4	4.3	37.7	83.7	29.0
100×100×4	579		31.5	28.9	3.9	50.9	114.1	37.1
100×100×6	579		44.9	49.7	3.9	71.8	160.6	52.9
100×100×10	579		67.3	80.3	4.1	105.4	235.0	79.2
200×100×4	579		87.1	78.0	2.1	242.6	596.8	102.4
200×100×6	579		126.5	139.4	2.1	351.1	862.6	148.8
200×100×10	579		197.4	234.8	2.2	544.2	1333.1	232.2
50×50×2	466		3.2	3.1	7.1	3.2	6.9	3.3
50×50×3	466		4.5	5.2	7.2	4.6	9.8	4.8
50×50×5	466		6.8	8.4	7.4	6.7	14.3	7.1
100×50×2	466		8.8	8.4	3.8	16.2	36.4	9.2
100×50×3	466		12.7	14.4	3.9	23.4	52.5	13.4
100×50×5	466		19.9	24.5	3.9	36.3	81.2	20.9
100×100×4	466		25.4	24.6	3.5	48.9	110.7	26.7
100×100×6	466		36.2	41.2	3.6	69.0	155.9	38.1
100×100×10	466		54.2	67.0	3.7	101.2	228.1	57.0
200×100×4	466	0.2	70.1	67.4	1.9	230.3	579.2	73.8
200×100×6	466		101.8	115.5	1.9	333.5	837.2	107.2
200×100×10	466		158.8	195.8	2.0	517.1	1293.7	167.2
50×50×2	579		3.9	3.6	7.8	3.3	7.1	4.1
50×50×3	579		5.6	6.2	8.0	4.7	9.9	5.9
50×50×5	579		8.4	10.0	8.2	6.9	14.5	8.9
100×50×2	579		10.9	9.7	4.2	16.7	37.0	11.5
100×50×3	579		15.8	17.4	4.3	24.1	53.5	16.6
100×50×5	579		24.7	29.4	4.3	37.3	82.7	26.0

Cross-section	f_y (N/mm ²)	H/V	$M_{pl,y}$ (kNm)	M_{CSM} (kNm)	$\bar{\lambda}_y$	$N_{b,y}$ (kN)	F_{cr} (kN)	$\alpha_{p,1}$
100×100×4	579		31.5	28.9	3.9	50.4	112.8	33.2
100×100×6	579		44.9	49.7	4.0	71.1	158.9	47.3
100×100×10	579		67.3	80.3	4.1	103.8	231.4	70.8
200×100×4	579		87.1	78.0	2.1	240.2	590.2	91.7
200×100×6	579		126.5	139.4	2.1	347.7	853.1	133.2
200×100×10	579		197.4	234.8	2.2	538.8	1318.3	207.7

As evidenced from Tables 6.6 and 6.7, all cross-sections in austenitic grade are Class 1, whilst the thinner cross-sections in duplex grade (50×50×2, 100×50×2, 100×100×4 and 200×100×4) are marginally classified as Class 2. All of the sections have a cross-sectional slenderness λ_{CSM} smaller than 0.68, hence the CSM is applicable to all of them. Finally, the range of non-dimensional slendernesses varies between 1.9 and 8.2 for the pinned-based frames and between 1 and 4.6 for the fixed-based frames. Based on the numerical results obtained from the 144 FE parametric studies conducted, the four design methods discussed in Section 6.3.1 are assessed based on their ability to accurately predict the numerical failure load F_u .

6.3.3. Assessment of design methods without moment redistribution

Based on linear elastic analysis, the closed formed solutions for pinned and fixed-based frames given in the Steel Designers' Manual (Owens and Knowles, 1994) were utilized to determine the bending moment diagram, shear force diagram and axial force diagram for each of the modelled frames. For the load cases not involving horizontal loads both columns were equally loaded, whereas for the load cases involving horizontal loads, the right-hand side column was more heavily loaded both in terms of bending moment and axial force. Hence, for all cases

the maximum bending moment and axial force of the frames were deemed to occur at top of the right-hand column of the frame.

To determine the predicted failure load according to EN 1993-1-4+A1 (2015), the load factor $F_{EC3,1}$ required to cause the bending moment occurring at the top of the right-hand side column to be equal to $M_{pl,y}$ was initially determined based on 1st order analysis. It is noted that the term load factor instead of load is used herein as in general the frames were subjected to a combination of vertical and horizontal loads at a prescribed ratio. As the load factor $F_{EC3,1}$ is associated with a load pattern involving a total vertical load of 1 kN, it can be viewed as the total vertical load applied on the frame with a coexisting horizontal load of either 0, 0.1 $F_{EC3,1}$ or 0.2 $F_{EC3,1}$. Allowance for the effect of a coexisting axial compressive force on the moment capacity of a cross-section was not made, since the applied compressive forces were small compared to the cross-sectional capacity; in all cases the maximum applied force was less than 1.3% of the squash load of the sections considered. Allowance was however made for the effect of member instability (i.e. failure of beam-column about its major axis) through the use of Eq. 26. If the determined $F_{EC3,1}$ did not satisfy Eq. 26, a lower value was determined through an iterative process until the Eq. 26 was met.

To account for P- Δ effects, the amplification factor k_{amp} defined by Eq. 29 was utilized to amplify the 1st order bending moments where the α_{cr} value was less than 10. The α_{cr} value was estimated as the ratio of $F_{EC3,1}$ over F_{cr} and is included in Table 6.8 and 6.9, where the “EC3 no redistribution” and the CSM design approaches are assessed:

$$k_{amp} = \frac{1}{1 - \frac{1}{\alpha_{cr,EC3}}} \quad (29)$$

For the determination of the frame resistance according to the CSM without moment redistribution, an identical procedure to the one previously described was followed. The $M_{pl,y}$ values were replaced by the M_{CSM} values, and similarly the determination of the α_{cr} was based on $F_{CSM,1}$. The obtained results are given in Tables 6.8 and 6.9 for fixed-based and pinned-based frames respectively, where the ratio of the predicted frame resistance F_{EC3} and F_{CSM} over the numerically obtained failure load F_u is reported as a means to quantify the accuracy of the design method.

Table 6.8: Assessment of design methods without moment redistribution for fixed-based frames.

Cross-section	f_y (N/mm ²)	H/V	F_u (kN)	EC3 no redistribution		CSM no redistribution	
				$\alpha_{cr,EC3}$	F_{pred}/F_u	$\alpha_{cr,CSM}$	F_{pred}/F_u
50×50×2	466		3.3	11.6	0.63	11.3	0.61
50×50×3	466		4.7	11.5	0.63	13.2	0.72
50×50×5	466		6.8	11.2	0.65	13.9	0.81
100×50×2	466		9.4	17.6	0.77	16.9	0.74
100×50×3	466		14.9	18.1	0.68	20.5	0.77
100×50×5	466	0	22.9	17.9	0.69	22.1	0.85
100×100×4	466		29.2	18.3	0.72	17.8	0.70
100×100×6	466		42.6	18.3	0.70	20.9	0.80
100×100×10	466		61.8	18.0	0.72	22.2	0.89
200×100×4	466		84.1	31.9	0.75	30.7	0.72
200×100×6	466		135.3	32.0	0.68	36.3	0.77

Cross-section	f_y (N/mm ²)	H/V	F_u (kN)	EC3 no		CSM no	
				redistribution		redistribution	
				$\alpha_{cr,EC3}$	F_{pred}/F_u	$\alpha_{cr,CSM}$	F_{pred}/F_u
200×100×10	466		218.0	31.8	0.65	39.2	0.80
50×50×2	579		4.0	10.2	0.60	9.4	0.50
50×50×3	579		5.7	10.1	0.60	11.2	0.67
50×50×5	579		8.2	9.8	0.57	11.7	0.75
100×50×2	579		11.4	15.7	0.72	14.1	0.65
100×50×3	579		18.4	16.4	0.62	18.1	0.68
100×50×5	579		28.1	16.2	0.63	19.3	0.75
100×100×4	579		36.0	16.4	0.67	15.0	0.61
100×100×6	579		52.6	16.5	0.64	18.3	0.71
100×100×10	579		76.7	16.2	0.65	19.4	0.78
200×100×4	579		103.4	26.4	0.75	23.6	0.68
200×100×6	579		167.5	26.5	0.67	29.2	0.74
200×100×10	579		278.0	26.4	0.63	31.5	0.75
50×50×2	466		3.2	11.8	0.61	11.4	0.59
50×50×3	466		4.5	11.7	0.62	13.3	0.71
50×50×5	466		6.5	11.3	0.65	14.0	0.80
100×50×2	466		9.0	17.8	0.75	17.2	0.72
100×50×3	466		14.5	18.5	0.65	20.9	0.74
100×50×5	466		22.1	18.3	0.67	22.5	0.83
100×100×4	466		28.5	18.7	0.69	18.2	0.67
100×100×6	466	0.1	41.6	18.7	0.67	21.4	0.76
100×100×10	466		60.0	18.3	0.69	22.7	0.85
200×100×4	466		81.5	32.2	0.74	31.0	0.71
200×100×6	466		133.3	32.3	0.65	36.7	0.73
200×100×10	466		212.2	32.1	0.63	39.6	0.78
50×50×2	579		3.8	10.3	0.60	9.4	0.50
50×50×3	579		5.5	10.3	0.59	11.4	0.65

Cross-section	f_y (N/mm ²)	H/V	F_u (kN)	EC3 no		CSM no	
				redistribution		redistribution	
				$\alpha_{cr,EC3}$	F_{pred}/F_u	$\alpha_{cr,CSM}$	F_{pred}/F_u
50×50×5	579		7.8	9.9	0.56	11.8	0.75
100×50×2	579		10.7	15.9	0.73	14.2	0.65
100×50×3	579		17.7	16.7	0.60	18.4	0.66
100×50×5	579		27.0	16.5	0.62	19.6	0.74
100×100×4	579		34.7	16.7	0.65	15.3	0.59
100×100×6	579		51.0	16.9	0.61	18.7	0.68
100×100×10	579		74.0	16.6	0.63	19.8	0.75
200×100×4	579		99.0	26.6	0.75	23.9	0.67
200×100×6	579		165.3	26.8	0.64	29.6	0.71
200×100×10	579		269.0	26.7	0.61	31.8	0.73
50×50×2	466		3.1	11.9	0.59	11.6	0.58
50×50×3	466		4.4	11.8	0.60	13.5	0.68
50×50×5	466		6.4	11.5	0.62	14.3	0.76
100×50×2	466		8.6	18.1	0.74	17.4	0.71
100×50×3	466		14.0	18.8	0.64	21.3	0.72
100×50×5	466		21.3	18.6	0.65	22.9	0.80
100×100×4	466		27.1	18.9	0.69	18.3	0.67
100×100×6	466		40.2	19.0	0.65	21.7	0.74
100×100×10	466		58.0	18.6	0.67	23.0	0.83
200×100×4	466		73.5	32.2	0.78	31.0	0.75
200×100×6	466		129.8	32.6	0.63	36.9	0.71
200×100×10	466		209.8	32.4	0.61	39.9	0.75
50×50×2	579		3.7	10.4	0.58	9.5	0.48
50×50×3	579		5.2	10.3	0.59	11.4	0.65
50×50×5	579		7.5	10.0	0.56	11.9	0.74
100×50×2	579		10.4	16.2	0.70	14.5	0.63
100×50×3	579	0.2	17.1	16.9	0.59	18.6	0.65

Cross-section	f_y (N/mm ²)	H/V	F_u (kN)	EC3 no		CSM no	
				redistribution		redistribution	
				$\alpha_{cr,EC3}$	F_{pred}/F_u	$\alpha_{cr,CSM}$	F_{pred}/F_u
100×50×5	579		26.1	16.6	0.61	19.8	0.72
100×100×4	579		33.6	17.1	0.63	15.6	0.57
100×100×6	579		49.4	17.2	0.59	19.1	0.66
100×100×10	579		72.4	17.0	0.60	20.3	0.72
200×100×4	579		91.6	26.7	0.77	23.9	0.69
200×100×6	579		161.6	27.0	0.62	29.8	0.68
200×100×10	579		261.1	26.9	0.60	32.0	0.71
MEAN					0.65		0.71
COV					0.09		0.11

Table 6.9: Assessment of design methods without moment redistribution for pinned-based frames.

Cross-section	f_y (N/mm ²)	H/V	F_u (kN)	EC3 no		CSM no	
				redistribution		redistribution	
				$\alpha_{cr,EC3}$	F_{pred}/F_u	$\alpha_{cr,CSM}$	F_{pred}/F_u
50×50×2	466		3.2	1.8	0.55	1.9	0.53
50×50×3	466		4.5	1.8	0.55	1.6	0.62
50×50×5	466		6.4	1.8	0.56	1.4	0.69
100×50×2	466		9.7	3.5	0.79	3.6	0.76
100×50×3	466	0	14.4	3.5	0.77	3.0	0.87
100×50×5	466		22.0	3.4	0.78	2.8	0.96
100×100×4	466		29.3	3.6	0.77	3.8	0.75
100×100×6	466		41.4	3.6	0.77	3.2	0.88
100×100×10	466		60.0	3.5	0.79	2.8	0.98
200×100×4	466		86.2	6.9	0.85	7.2	0.82

Cross-section	f_y (N/mm ²)	H/V	F_u (kN)	EC3 no		CSM no	
				$\alpha_{cr,EC3}$	F_{pred}/F_u	$\alpha_{cr,CSM}$	F_{pred}/F_u
200×100×6	466		131.3	6.9	0.81	6.1	0.92
200×100×10	466		195.7	6.8	0.85	5.5	1.04
50×50×2	579		3.9	1.5	0.41	1.6	0.38
50×50×3	579		5.4	1.5	0.41	1.3	0.46
50×50×5	579		7.7	1.4	0.41	1.2	0.49
100×50×2	579		11.9	2.8	0.73	3.2	0.65
100×50×3	579		17.7	2.8	0.71	2.6	0.78
100×50×5	579		27.1	2.8	0.72	2.4	0.85
100×100×4	579		36.2	3.0	0.71	3.3	0.65
100×100×6	579		51.2	3.0	0.71	2.7	0.79
100×100×10	579		73.1	2.9	0.74	2.4	0.88
200×100×4	579		105.9	5.7	0.83	6.3	0.74
200×100×6	579		160.6	5.6	0.79	5.1	0.87
200×100×10	579		240.7	5.6	0.82	4.7	0.98
50×50×2	466		2.7	2.1	0.65	2.2	0.63
50×50×3	466		3.8	2.1	0.64	1.8	0.73
50×50×5	466		5.4	2.1	0.67	1.7	0.82
100×50×2	466		8.2	4.1	0.83	4.2	0.80
100×50×3	466		13.3	4.0	0.74	3.6	0.84
100×50×5	466		19.0	4.0	0.81	3.2	1.00
100×100×4	466	0.1	25.2	4.3	0.80	4.4	0.77
100×100×6	466		35.8	4.2	0.80	3.7	0.91
100×100×10	466		51.6	4.1	0.82	3.3	1.02
200×100×4	466		68.4	8.1	0.93	8.4	0.89
200×100×6	466		116.1	8.1	0.79	7.1	0.90
200×100×10	466		185.3	8.0	0.77	6.5	0.95
50×50×2	579		3.3	1.8	0.54	1.9	0.49

Cross-section	f_y (N/mm ²)	H/V	F_u (kN)	EC3 no		CSM no	
				redistribution		redistribution	
				$\alpha_{cr,EC3}$	F_{pred}/F_u	$\alpha_{cr,CSM}$	F_{pred}/F_u
50×50×3	579		4.6	1.7	0.54	1.6	0.60
50×50×5	579		6.5	1.7	0.55	1.4	0.65
100×50×2	579		9.9	3.3	0.79	3.7	0.71
100×50×3	579		15.3	3.3	0.75	3.0	0.82
100×50×5	579		23.3	3.3	0.76	2.8	0.90
100×100×4	579		30.9	3.5	0.75	3.8	0.69
100×100×6	579		44.0	3.5	0.75	3.1	0.83
100×100×10	579		63.5	3.4	0.77	2.8	0.92
200×100×4	579		86.8	6.6	0.88	7.4	0.79
200×100×6	579		145.0	6.6	0.76	6.0	0.84
200×100×10	579		232.0	6.5	0.74	5.5	0.89
50×50×2	466		2.4	2.4	0.70	2.5	0.68
50×50×3	466		3.4	2.4	0.70	2.1	0.79
50×50×5	466		4.8	2.4	0.73	1.9	0.90
100×50×2	466		7.2	4.6	0.85	4.8	0.82
100×50×3	466		12.5	4.6	0.71	4.1	0.81
100×50×5	466		17.0	4.6	0.82	3.7	1.01
100×100×4	466		22.2	4.9	0.81	5.0	0.79
100×100×6	466	0.2	31.9	4.8	0.80	4.2	0.92
100×100×10	466		46.1	4.7	0.83	3.8	1.02
200×100×4	466		59.8	9.2	0.93	9.6	0.90
200×100×6	466		102.7	9.2	0.79	8.1	0.90
200×100×10	466		164.0	9.1	0.77	7.4	0.95
50×50×2	579		2.9	2.0	0.61	2.2	0.56
50×50×3	579		4.1	2.0	0.60	1.8	0.67
50×50×5	579		5.8	1.9	0.63	1.6	0.75
100×50×2	579		8.6	3.8	0.83	4.2	0.75

Cross-section	f_y (N/mm ²)	H/V	F_u (kN)	EC3 no		CSM no	
				$\alpha_{cr,EC3}$	F_{pred}/F_u	$\alpha_{cr,CSM}$	F_{pred}/F_u
100×50×3	579		15.3	3.8	0.68	3.4	0.75
100×50×5	579		20.8	3.7	0.78	3.2	0.93
100×100×4	579		27.3	4.0	0.77	4.4	0.71
100×100×6	579		39.2	4.0	0.77	3.6	0.85
100×100×10	579		56.5	3.8	0.79	3.2	0.94
200×100×4	579		75.0	7.6	0.90	8.5	0.81
200×100×6	579		127.4	7.5	0.77	6.8	0.85
200×100×10	579		205.7	7.5	0.74	6.3	0.88
MEAN					0.74		0.80
COV					0.15		0.18

From tables 6.8 and 6.9 it becomes apparent that the allowing for strain-hardening at cross-sectional level leads to an increase of the design efficiency, albeit by only 6%. Furthermore, both design methods seem to provide significantly more consistent ultimate capacity predictions for the fixed-ended frames. This is due to the diminished influence of the second order effects, the presence of which contributes to the increase of scatter, as shown in Fig. 6.12, where the predicted over numerically obtained resistance of the modelled frames is plotted against the α_{cr} factor. It can be clearly seen that the predictions for the pinned-based frames, which possess low values of α_{cr} , display a higher scatter. Furthermore, with decreasing α_{cr} , the conservatism of the predictions increases, thus indicating that the amplification of bending moments to account for second-order effects may be inappropriate for very sway-sensitive frames. This is in accordance with the design recommendations of EN 1993-1-1+A1

(2014), which stipulates that second-order analysis should be used for the design of frames with α_{cr} values lower than 3.

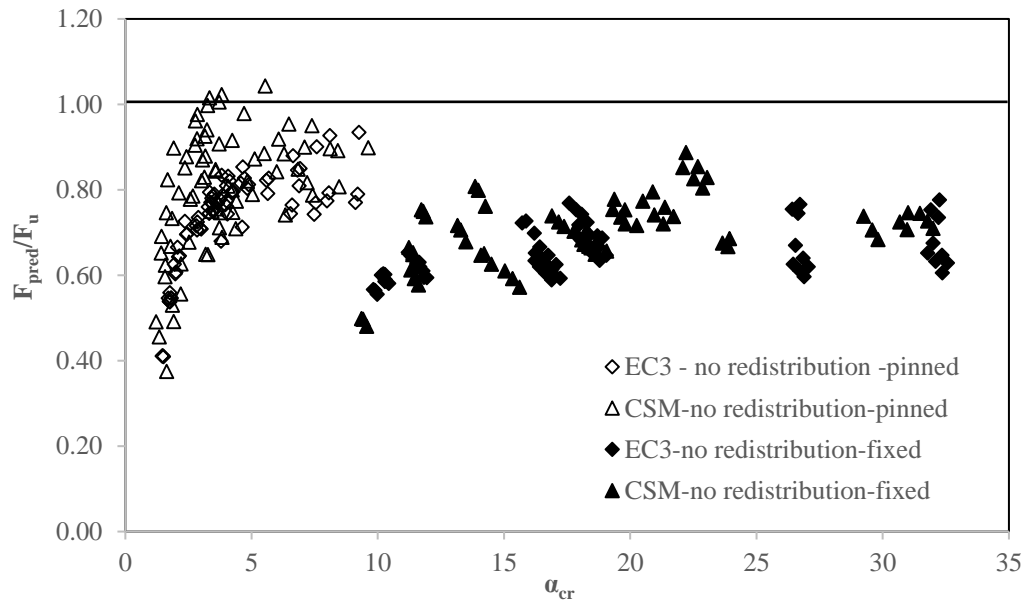


Fig. 6.12: Accuracy of design methods not allowing for moment redistribution as a function of α_{cr}

For both design methods, the ultimate capacity is significantly under-predicted, with the fixed-based frames being on average under-predicted by 29% and 35% based on the CSM and the EC3 design calculations respectively. As observed in the discussion on the design of continuous beams, this is due to the effect of element interaction, which in the case of frames, seems to be more important, as in general more plastic hinges have to form for collapse to occur and hence the potential for moment redistribution is higher. This is clearly depicted in Fig. 6.12, where fixed-based frames with similar α_{cr} values to those of pinned-based frames are considerably more under-predicted than their pinned-based counterparts. Hence, the need to incorporate the effects of moment redistribution in the design procedure emerges.

6.3.4. Assessment of design methods allowing for moment redistribution

Following the assessment of design methods based on elastic analysis (i.e. not accounting for moment redistribution), this section discusses the applicability of design methods incorporating explicitly the effects of moment redistribution, via employing plastic analysis procedures. As discussed earlier where various procedures for the design of continuous considered, plastic analysis is expected to result in a more rational design for structures employing sufficiently stocky sections.

The predicted resistance of a frame based on traditional plastic analysis (i.e. assuming a rigid-plastic material response) can be determined using the Rankine equation (Eq. 3), where α_{cr} and α_p are the F_{cr} and $\alpha_{p,1}$ factors reported in Tables 6.6 and 6.7. Thus the ultimate collapse factor of a frame can be explicitly determined from the results of a rigid plastic analysis and a linear eigenvalue buckling analysis. No further allowance of the P- Δ effects (sway effects) is required. However, after the collapse load factor of a frame has been determined, the stability of the beam-columns comprising the frames has to be verified using Eq. (26) and (27), to exclude member instability prior to the collapse load being obtained. Similarly, the CSM for indeterminate structures, in conjunction with the Rankine equation can be employed to predict the ultimate response of a frame allowing for the combined beneficial effects of strain-hardening at cross-sectional level and moment redistribution and the detrimental second-order effects. Both methods are assessed in Table 6.10.

Table 6.10: Assessment of design methods allowing for moment redistribution

Cross-section	f_y (N/mm ²)	H/V	EC3 with redistribution		CSM with redistribution	
			pinned-	fixed-	pinned-	fixed-
			based	based	based	based
			F_{pred}/F_u	F_{pred}/F_u	F_{pred}/F_u	F_{pred}/F_u
50×50×2	466	0	0.83	0.88	0.81	0.86
50×50×3	466		0.83	0.88	0.95	0.99
50×50×5	466		0.87	0.91	1.08	1.09
100×50×2	466		0.92	0.98	0.88	0.95
100×50×3	466		0.90	0.89	1.02	1.00
100×50×5	466		0.91	0.90	1.12	1.09
100×100×4	466		0.89	0.92	0.86	0.90
100×100×6	466		0.89	0.90	1.02	1.01
100×100×10	466		0.92	0.92	1.14	1.12
200×100×4	466		0.94	0.95	0.90	0.91
200×100×6	466		0.89	0.85	1.01	0.96
200×100×10	466		0.93	0.82	1.15	1.01
50×50×2	579		0.78	0.60	0.71	0.80
50×50×3	579		0.80	0.86	0.88	0.94
50×50×5	579		0.83	0.89	0.99	1.04
100×50×2	579		0.88	0.72	0.79	0.87
100×50×3	579		0.86	0.85	0.95	0.93
100×50×5	579		0.87	0.87	1.04	1.02
100×100×4	579		0.85	0.67	0.78	0.82
100×100×6	579		0.85	0.86	0.95	0.94
100×100×10	579	0.89	0.88	1.06	1.03	
200×100×4	579	0.92	0.75	0.82	0.85	
200×100×6	579	0.88	0.84	0.97	0.93	
200×100×10	579	0.91	0.79	1.09	0.93	

Cross-section	f_y (N/mm ²)	H/V	EC3 with redistribution		CSM with redistribution	
			pinned-	fixed-	pinned-	fixed-
			based	based	based	based
			F_{pred}/F_u	F_{pred}/F_u	F_{pred}/F_u	F_{pred}/F_u
50×50×2	466	0.1	0.90	0.90	0.88	0.88
50×50×3	466		0.91	0.91	1.03	1.02
50×50×5	466		0.95	0.94	1.17	1.13
100×50×2	466		0.98	1.02	0.94	0.98
100×50×3	466		0.88	0.91	1.00	1.02
100×50×5	466		0.96	0.93	1.18	1.12
100×100×4	466		0.94	0.94	0.91	0.91
100×100×6	466		0.94	0.91	1.07	1.03
100×100×10	466		0.97	0.94	1.20	1.15
200×100×4	466		1.06	0.98	1.02	0.94
200×100×6	466		0.90	0.86	1.03	0.97
200×100×10	466		0.88	0.85	1.09	1.03
50×50×2	579		0.86	0.60	0.79	0.84
50×50×3	579		0.88	0.88	0.97	0.96
50×50×5	579		0.91	0.93	1.09	1.08
100×50×2	579		0.96	0.73	0.86	0.92
100×50×3	579		0.90	0.88	1.00	0.96
100×50×5	579		0.92	0.90	1.10	1.05
100×100×4	579		0.91	0.65	0.83	0.84
100×100×6	579		0.90	0.88	1.00	0.96
100×100×10	579	0.93	0.90	1.11	1.06	
200×100×4	579	1.01	0.75	0.90	0.89	
200×100×6	579	0.88	0.85	0.96	0.94	
200×100×10	579	0.85	0.82	1.01	0.96	
50×50×2	466	0.2	0.94	0.92	0.91	0.90
50×50×3	466		0.94	0.93	1.07	1.04

Cross-section	f_y (N/mm ²)	H/V	EC3 with redistribution		CSM with redistribution	
			pinned-	fixed-	pinned-	fixed-
			based	based	based	based
			F_{pred}/F_u	F_{pred}/F_u	F_{pred}/F_u	F_{pred}/F_u
50×50×5	466		0.99	0.95	1.22	1.14
100×50×2	466		1.02	1.06	0.98	1.02
100×50×3	466		0.85	0.93	0.97	1.05
100×50×5	466		0.98	0.96	1.21	1.16
100×100×4	466		0.97	0.98	0.94	0.96
100×100×6	466		0.96	0.94	1.09	1.06
100×100×10	466		0.99	0.97	1.22	1.18
200×100×4	466		1.09	1.08	1.05	1.04
200×100×6	466		0.93	0.88	1.05	1.00
200×100×10	466		0.90	0.85	1.11	1.04
50×50×2	579		0.90	0.58	0.82	0.85
50×50×3	579		0.90	0.93	1.00	1.01
50×50×5	579		0.95	0.96	1.13	1.12
100×50×2	579		1.02	0.70	0.91	0.94
100×50×3	579		0.83	0.90	0.91	0.99
100×50×5	579		0.95	0.92	1.13	1.08
100×100×4	579		0.94	0.63	0.86	0.86
100×100×6	579		0.93	0.90	1.03	0.99
100×100×10	579		0.96	0.91	1.15	1.07
200×100×4	579		1.06	0.77	0.95	0.96
200×100×6	579		0.90	0.87	1.00	0.95
200×100×10	579		0.87	0.84	1.04	0.99
MEAN			0.92	0.87	1.00	0.99
COV			0.06	0.12	0.12	0.09

As expected, all design methods incorporating moment redistribution are more efficient compared to the ones based on elastic analysis. Furthermore, the scatter is reduced. Fig. 6.13 depicts the ratio of the predicted over numerical frame resistances plotted against the α_{cr} factor of the modelled frames, where α_{cr} was obtained as the ratio of F_{cr} over F_{pred} (i.e. the number by which the predicted load pattern at collapse has to be multiplied to cause sway instability of an idealised infinitely elastic frame). Contrary to the strong trend between α_{cr} and design predictions observed in Fig. 6.12 for elastic design methods, the explicit incorporation of the sway instability of the frame via the Rankine Eq. seems to provide consistent ultimate capacity predictions over the full range of α_{cr} values considered.

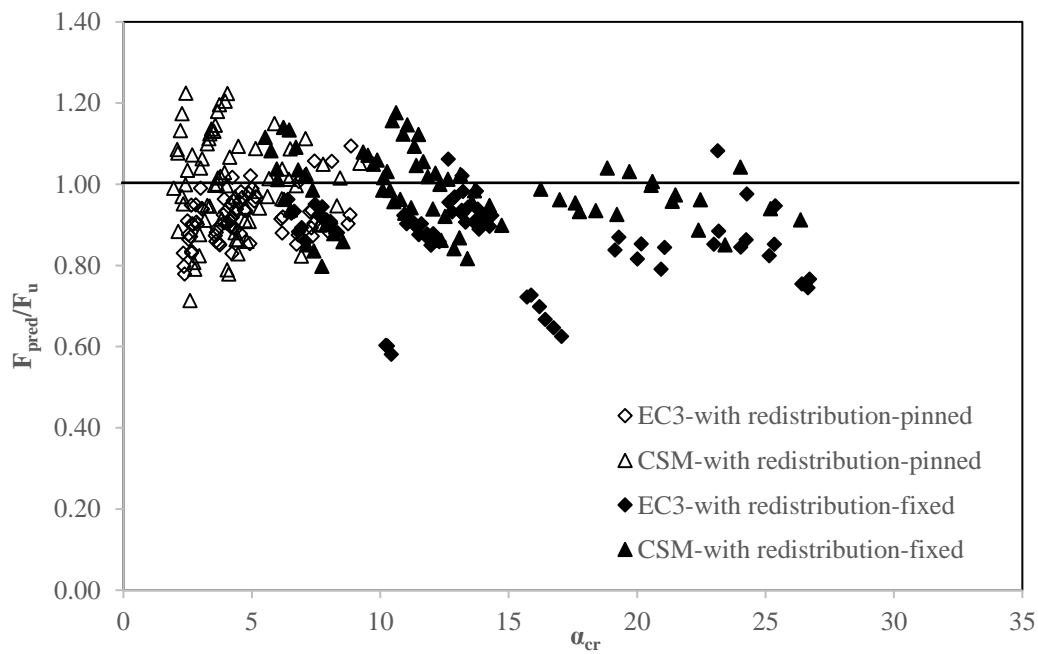


Fig. 6.13: Accuracy of design methods allowing for moment redistribution as a function of

α_{cr}

6.3.5. Design recommendations

Having conducted a comprehensive numerical study on the performance of stainless steel indeterminate structures, it was determined that incorporating both the effect of strain-hardening at cross-sectional level, where stocky cross-sections are employed, and the effect of moment redistribution are of paramount importance to accurately predict the ultimate response of stainless steel indeterminate structures.

For the design of continuous stainless steel beams, it can be concluded that the CSM for indeterminate structures is a simple to use and efficient design method that involves no additional complexity compared to traditional plastic analysis, yet it yields superior results in terms of design efficiency and consistency of the predictions. It is therefore proposed that it should be incorporated in future revisions of EN 1993-1-4+A1(2015) as it was demonstrated both experimentally and numerically that continuous stainless steel beams possess significant potential for moment redistribution. This recommendation comes with the caveat that the applied shear force is small enough not to diminish the moment resistance, as is usually the case for reasonably sized continuous beams, the span to depth of which leads to negligible shear forces.

The design of stainless steel frames is more complex and necessitates explicit consideration of second-order effects and additional member checks. It was demonstrated that, particularly for fixed-based frames, applying CSM with moment redistribution allows improved ultimate capacity predictions to be made. Furthermore, applying the plastic analysis and using the Rankine equation to allow for second-order effects can yield more accurate results compared

to elastic analysis using the k_{amp} method to allow for second-order effects and was also found to be simpler. Furthermore, significant gains can be made by applying traditional plastic analysis (i.e. without allowing for strain-hardening) and in anticipation of the CSM being adopted in EN 1993-1-4+A1 (2005), the traditional plastic analysis approach employed in conventional steel structures can be employed, provided that the connections are designed appropriately to allow plastic hinges to develop prior to their failure.

CHAPTER 7

CONCLUSION AND FUTURE RESEARCH

7.1. CONCLUSIONS

In this section the outcomes of this research project related to plastic design of stainless steel indeterminate structures are summarized. Future research suggestions are presented in the following section.

Eight experiments on simply supported beams employing RHS in austenitic and duplex stainless steels grades and four experiments on continuous beams of the same material were reported in Chapter 3. Flat and corner coupons were extracted and tested for each cross-section, in order to obtain their stress – strain responses, which were subsequently employed in Chapter 4 and 5 during the development of FE models and the carrying out of parametric studies. Key results, such ultimate moment (M_u), ultimate load (F_u), maximum displacement

(δ_u) and rotation (θ_u) are reported; result to a great contribution to the pool of available experimental data.

In Chapters 4 and 5, finite element models were developed and validated against the experimental data presented for simply supported, continuous beams (Gkantou et al., 2019; Theofanous et al., 2014) and portal frames (Wilkinson and Hancock, 1999). Furthermore, parametric studies were then conducted to further investigate the response of continuous beams and portal frames over a wide range of cross-section slenderness, cross-section aspect ratios, span lengths and loading arrangements. Recommendations for the numerical modelling of stainless steel continuous beams and frames were made and it was demonstrated that for structures employing stocky sections, traditional FE models with beam elements can yield results close to the ones provided by elaborate FE models with shell elements.

Eurocode design provisions (EN 1993-1-4+A1, 2015) and the strain-based design approach termed continuous strength method (Afshan and Gardner, 2013) were assessed in Chapter 6 for all the obtained experimental and numerical data of stainless steel continuous beams and portal frames. It was shown that the current Eurocode 3: Part 1.4+A1 (2015) approach significantly underestimates the strength of stainless continuous beams. This is because the formation of successive plastic hinges and moment redistribution in indeterminate structures with adequate deformation capacity, as well as the effect of strain-hardening at cross-sectional level, are not accounted for. Based on the collated test data on continuous stainless steel beams (Mirambell and Real, 2000; Real and Mirambell, 2005; Theofanous et al., 2014; Arrayago and Real, 2016) and the experimental and numerical results of the present study, it was shown that accounting for both strain-hardening and moment redistribution is of paramount importance

for the design. To this end, the continuous strength method, which rationally accounts for the local buckling at cross-section level, extended to the design of stainless steel indeterminate structures in order to consider the moment redistribution, provides the most accurate design estimations.

The aforementioned method was successfully extended to stainless steel portal frames. It was demonstrated that both second-order effects and moment redistribution can be easily incorporated in design by applying the well-established Rankine formula together with conventional plastic analysis, as modified to allow for the effects of strain-hardening. The CSM for indeterminate structures yielded results close to the numerically obtained ultimate load which were 35% and 53% higher compared to current design procedures for pinned-based and fixed-based frames respectively. Allowing for both moment redistribution and strain-hardening is expected to lead to result to significant material savings thus promoting the more widespread use of stainless steel in construction.

7.2. SUGGESTIONS FOR FUTURE RESEARCH

Important aspects of stainless steel design warrant further investigation and these are highlighted in this last section of the thesis. The further research required is both experimental and numerical and some of it has already been planned and is underway as can be seen in Appendix A.

The parametric studies conducted on stainless steel continuous beams yielded inconclusive results for beams subjected to high shear forces in conjunction with high bending moments. Both experimental and numerical research is required to quantify the effect of coexisting high

shear stresses on the moment resistance and potential for moment redistribution of continuous beams. For the vast majority of the applications involving beams, shear forces are rarely a concern, however, for completeness, a procedure to allow for the effect of shear on the CSM predictions is required.

The research reported herein on stainless steel frames was purely numerical, as limitations in available experimental resources did not allow some planned tests on stainless steel frames to be conducted. It is of utmost importance that experimental tests on stainless steel frames are performed so that experimental validation for the effects of moment redistribution on the response of frames becomes available and to provide a set of data against which numerical models can be validated. It is envisaged that the planned tests will be conducted soon. Furthermore, the behaviour of stainless steel frames employing other types of cross-sections typically used in practice such as I-sections should be investigated both experimentally and numerically. Special features commonly employed in portal frames such as haunches also warrant further investigation to allow stainless steel construction to develop further.

Key to the behaviour of frames is the response of the connections, which in this thesis was not considered (i.e. the connections were assumed to possess sufficient over-strength to be ignored). The structural behaviour of frames employing semi-rigid joints is another research topic requiring attention as semi-rigid joint can often lead to the most economic design solution.

Finally, all research reported herein was focusing on the static response of stainless steel structures under ambient temperatures. Clearly, the behaviour of continuous stainless steel

beams and frames at elevated temperatures (i.e. fire) and under cyclic (earthquake) and impact (explosion) loads warrants further research given the excellent material ductility from which applications subjected to extreme loads can benefit. Such applications relate to bridges and buildings in seismic areas, some critical components in the offshore industry and in general to critical infrastructure requiring long design lives where maintenance and inspection are costly and there is a risk of exposure to chlorides from salt water or de-icing salts.

Clearly all previously mentioned research topics are not limited to stainless steels but can also extend to structures employing other nonlinear structural materials of which the material behaviour displays an absence of a yield plateau, such as all structural aluminium alloys and some grades of high strength steels.

REFERENCES

ABAQUS. (2007) Analysis User's Manual I-V. Version 6.7-1 ABAQUS, Inc., Dassault Systemes. USA.

Abdella K. (2006) Inversion of a full-range stress-strain relation for stainless steel alloys. *International Journal of Non-linear Mechanincs*, 41(3): 456-463.

Afshan S. and Gardner L. (2013) Experimental Study of Cold-Formed Ferritic Stainless Steel Hollow Sections. *Journal of Structural Engineering*, 139: 43-49.

Afshan S. and Gardner L. (2013) The continuous strength method for structural stainless steel design. *Thin-Walled Structures*, 68: 42–9.

Afshan S., Rossi B. and Gardner L. (2013) Strength enhancements in cold-formed structural sections - Part I: Material testing. *Journal of Constructional Steel Research* 83: 177-188.

AISC Design Guide 27. (2013) *Structural Stainless Steel*. American Institute of Steel Construction (AISC).

Arrayago I. and Real E. (2016) Experimental study on ferritic stainless steel simply supported and continuous beams. *Journal of Constructional Steel Research*, 119: 50-62.

Ashraf M., Gardner L. and Nethercot D.A. (2006b) Finite element modelling of structural stainless steel cross-sections. *Thin Wall Structures*, 44(10): 1048-1062.

Ashraf M., Gardner L. and Nethercot D.A. (2005) Strength of the corner regions of stainless steel cross sections. *Journal of Constructional Steel Research*, 61(1): 37–52.

ASCE 8-02. (2002) Specification for the design of cold-formed stainless steel structural members. American Society of Civil Engineers (SEI/ASCE), Reston, VA.

AS 1163. (2016) Structural steel hollow sections. Standards Australia (AS), Sydney.

AS 4100. (2016) Steel structures. Standards Australia (AS), Sydney.

AS/NZS 4673. (2001) Cold-formed stainless steel structures. Standards Australia (AS/NZS), Sydney.

Baker J.F. (1954) *The Steel Skeleton Volume I: Elastic Behaviour and Design*. Cambridge University Press, United Kingdom.

Baker J.F. (1950) The Design of Steel Frames. *Journal Institute Structural Engineers*, 27: 397.

Baker J.F. and Eickhoff K.G. (1955) The behavior of saw-tooth portal frames. *Proceeding of the Conference on the correlation between calculated and observed stress and displacements in structures*. Institution of Civil Engineers.

Baker J.F. and Heyman J. (1950) Tests on Miniature Portal Frames. *Journal Institute Structural Engineers*, 28.

Bild S., Roik K., Sedlacek G., Stutzki C. and Spangemacher R. (1989) The b/t-ratios controlling the applicability of analysis models in Eurocode 3, Part 1.1. *Background Document*, 5.

Bruneau M., Uang C.M. and Whittaker A. (1998) Ductile design of steel structures. New York, McGraw-Hill.

Byfield M. and Nethercot D.A (1998) An analysis of the true bending strength of steel beams. Proceedings of the Institution of Civil Engineers-Structures and Buildings. 128:2, 188-197.

Cruise R.B and Gardner L. (2008) Strength enhancements induced during cold forming of stainless steel sections Journal of Construction Steel Research, 64(11): 1310-1361.

Chan T.M. and Gardner L. (2008) Bending strength of hot-rolled elliptical hollow sections. Journal of Construction Steel Research, 64: 971-986.

Design of steel structures: Part 1.1-General rules and rules for buildings. (1992). DD ENV. 1993-1-1, European Committee for Standardisation, Eurocode 3 Editorial Group, Brussels, Belgium. Dwyer, T.J., and Galambos, T.V. (1965). Plastic behavior.

Davies J.M. (1966) Frame instability and strain hardening in plastic theory. Journal of the Structural Division, American Society of Civil Engineers (ASCE). 92: ST3, 1-16.

Davies J.M. (2002) Second-order elastic-plastic analysis of plane frames. Journal of Constructional Steel Research. 58:10, 1315-1330.

Davies J.M. (2006) Strain hardening, local buckling and lateral-torsional buckling in plastic hinges. Journal of Constructional Steel Research. 62: 1-2, 27-34.

Elflah M., Theofanous M., Dirar S. and Yuan H.X. (2019a). Behaviour of stainless steel beam-to-column joints - Part 1: Experimental investigation. Journal of Constructional Steel Research 152: 183-193.

Elflah M., Theofanous M. and Dirar S. (2019b). Behaviour of stainless steel beam-to-column joints - Part 2: Numerical modelling and parametric study. *Journal of Constructional Steel Research* 152: 194-212.

Elflah M., Theofanous M., Dirar S. and Yuan H.X. (2019c). Structural behavior of stainless steel beam-to-tubular column joints. *Engineering Structures* 184: 158-175.

EN 1993-1-1 (2005) Eurocode 3. Design of Steel Structures: Part 1-1: General rules and rules for buildings, CEN.

EN 1993-1-1+A1 (2014) Eurocode 3. Design of Steel Structures: Part 1-1: General rules and rules for buildings, CEN.

EN 1993-1-4. (2006) Eurocode 3: Design of steel structures - Part 1.4: General rules - Supplementary rules for stainless steel, CEN.

EN 1993-1-4+A1. (2015) Eurocode 3: Design of steel structures - Part 1.4: General rules - Supplementary rules for stainless steel, CEN.

ESDEP. (1997) Comportement structural et dimensionnement des aciers inoxydables. Leçons 18, Cahiers de l'APK, 16: 126–150.

Gardner L. (2005) The use of stainless steel in structures. *Progress in Structural Engineering and Materials*, 7(2): 45–55.

Gardner L. (2008) The continuous strength method, *Proceedings of the institution of Civil Engineers-Structures And Buildings*, 161: 127-133, ISSN: 0965-0911.

Gardner L. and Ashraf M. (2006) Structural design for non-linear metallic materials, *Engineering Structures*, 926-934, ISSN: 0141-0296.

Gardner L. and Theofanous M. (2008) Discrete and continuous treatment of local buckling in stainless steel elements. *Journal of Constructional Steel Research*, 64: 1207–1216.

Gardner L. and Nethercot D.A. (2004a) Experiments on stainless steel hollow sections, Part 1: Material and cross-sectional behaviour. *Journal of Constructional Steel Research*, 60(9): 1291–1318.

Gardner L. and Nethercot D.A. (2004b) Experiments on stainless steel hollow sections, Part 2: Member behaviour of columns and beams. *Journal of Constructional Steel Research*, 60(9): 1319-1332.

Gardner L. and Nethercot D.A. (2004c) Numerical modelling of stainless steel structural components A consistent approach. *Journal of Structural Engineering, ASCEv*: 130(10): 1586_601.

Garden L., Saari N. and Wang F. (2010) Comparative experimental study of hot-rolled and cold-formed rectangular hollow sections. *Thin-Walled Structures* 48: 495–507.

Gardner L., Wang F. and Liew A. (2011) Influence of strain hardening on the behaviour and design of steel structures. *International Journal of Structural Stability and Dynamics*, 11(5): 855–875.

Gkantou M., Kokosis G., Theofanous M. and Dirar S. (2019) Plastic design of stainless steel continuous beams. *Journal of Constructional Steel Research*, 152: 1-322.

Hradil P., Talja A., Real E., Mirambell E. and Rossi B. (2013). Generalized multistage mechanical model for nonlinear metallic materials. *Thin-Walled Structures* 63: 63–69.

Hibbitt K. and Sorensen Inc. (2006) ABAQUS. ABAQUS/Standard user's manual volumes I-III and ABAQUS CAE manual. Version 6.6., Pawtucket, USA.

Hill H.N. (1944) Determination of stress-strain relations from the offset yield strength values. Technical Note No. 927, National Advisory Committee for Aeronautics, Washington, D.C.

Horne M.R. (1952) Experimental investigations into the behavior of continuous and fixed-ended beams. I. A. B. S. E. 4th Congress.

Karren K.W. (1967) Corner properties of cold-formed steel shapes. Journal of the Structural Division, ASCE, 93(1): 401–432.

Kemp A.R., Byfield M.P. and Nethercot, D.A. (2002) Effect of strain hardening on flexural properties of steel beams. The Structural Engineer, 80(8): 29–35.

Lechner A., Kettler M.R., Greiner R., Boissonnade N., Jaspart J.P. and Weynand K. (2008) Plastic capacity of semi-compact steel sections. Fifth International Conference on Coupled Instabilities in Metal Structures, Sydney, Australia 77-84.

Liew A. and Gardner L. (2015) Ultimate capacity of structural steel cross-sections under compression, bending and combined loading, Structures, 1: 2-11.

Li Z. and Schafer B.W. (2010) Buckling analysis of cold-formed steel members with general boundary conditions using CUFSM: Conventional and constrained finite strip methods. 20th International Specialty Conference on Cold-Formed Steel Structures, Missouri University of Science and Technology, Rolla, MO.

Lim J.B.P., King C.M., Rathbone A.J., Davies J.M. and Edmondson V. (2005) Eurocode 3 and the in-plane stability of portal frames. The Structural Engineer, 83: 21, 43-49.

Lindner J. (2016) Verification of flexural buckling according to Eurocode 3 part 1-1 using bow imperfections. Steel Construction, 9(4): 349-362.

Low M.W. (1959) Some model tests on multi-storey rigid steel frames, Proceedings of the Institution of Civil Engineers. 13:3, 287-298.

Mirambell E. and Real E. (2000) On the calculation of deflections in structural stainless steel beams: An experimental and numerical investigation. Journal of Constructional Steel Research, 54: 109–133.

Neal B.G. and Symonds P.S. (1952) The Calculation of Plastic Collapse Loads for plane frames. I. A. B. S. E. 4th Congress.

Owens G.W. and Knowles P.R (1994) Steel Designers Manual. The Steel Construction Institute, Ascot, England.

Quach W.M, Teng J.G. and Chung K.F. (2008) Three-stage full-range stress–strain model for stainless steels. Journal of Structural Engineering, 134: 1518–27.

Rasmussen K.J.R. (2003) Full-range stress–strain curves for stainless steel alloys. Journal of Constructional Steel Research, 59(1): 47–61.

Ramberg W. and Osgood W.R. (1943) Description of stress–strain curves by three parameters. Technical note no. 902. National Advisory Committee for Aeronautics, Washington (DC).

Rasmussen K.J.R. and Hancock G.J. (1993) Design of cold-formed stainless steel tubular members II: Beams. Journal of Structural Engineering, American Society of Civil Engineers (ASCE), 119(8): 2368-2386.

Real E. and Mirambell E. (2005) Flexural behaviour of stainless steel beams. Engineering Structures, 27(10): 1465-1475.

Rossi B., Afshan S. and Gardner L. (2013). Strength enhancements in cold-formed structural sections - Part II: Predictive models. Journal of Constructional Steel Research 83: 189-196.

Rossi B., Degee H. and Pascon F. (2009). Enhanced mechanical properties after cold process of fabrication of non-linear metallic profiles. *Thin-Walled Structures* 47(12): 1575-1589.

Schafer B.W. (2008) The Direct Strength Method of cold-formed steel member design. *Journal of Constructional Steel Research*, 64(7-8): 766-778.

Schafer B.W. and Pekoz T. (1998). Direct strength prediction of cold-formed steel members using numerical elastic buckling solutions. *Proceedings of the Fourteenth International Specialty Conference on Cold-Formed Steel Structures* St. Louis, Missouri, October 15-16.

Sedlacek G. and Feldmann M. (1995) The b/t-ratios controlling the applicability of analysis models in Eurocode 3, Part 1.1. *Background Document*, 5.

Seif M. and Schafer B.W. (2010) Local buckling of structural steel shapes. *Journal of Constructional Steel Research*, 66(10): 1232–1247.

Theofanous M. and Gardner L. (2012) Effect of element interaction and material non-linearity on the ultimate capacity of stainless steel cross-sections. *Steel and Composite Structures*, 12(1): 73–92.

Theofanous M. and Gardner L. (2010) Experimental and numerical studies of lean duplex stainless steel beams. *Journal of Constructional Steel Research*, 66: 816-825.

Theofanous M., Saliba N., Zhao O. and Gardner L. (2014) Ultimate response of stainless steel continuous beams. *Thin-Walled Structures*, 83: 115-127.

Von Kármán T., Sechler E.E. and Donnell L.H. (1932). *The Strength of Thin Plates In Compression*. *Transactions of the ASME*, 54: 53-57.

Wang F. (2011). *A deformation based approach to structural steel design*, PhD Thesis, Imperial College London, United Kingdom.

Walport F., Gardner L., Real E., Arrayago I. and Nethercot D.A. (2017) Effects of Material Nonlinearity on the Global Analysis and Stability of Stainless Steel Frames. *Journal of Constructional Steel Research*, 152: 173-182.

Wilkinson T. and Hancock G.J. (1998) Tests to examine compact web slenderness of cold-formed RHS. *Journal of Structural Engineering*, American Society of Civil Engineers (ASCE). 124: 10, 1166-1174.

Wilkinson T. and Hancock G.J. (1998) Tests of Portal Frames in cold-formed RHS. 8th International Symposium on Tubular Structures, VIII: 521-529.

Wilkinson T. and Hancock G.J. (1999) Tests of cold-formed rectangular hollow section portal frames. The University of Sydney, Department of Civil Engineering.

Winter G. (1947) Strength of Thin Steel Compression Flanges. *Transactions of American Society of Civil Engineers (ASCE)*, Paper No. 2305, Trans., 112, 1.

Wood R.H. (1958) The stability of tall buildings. *Proceedings of the Institution of Civil Engineers*. 11: 1, 69-102.

Yaramici E., Yura J.A., and Lu L.W. (1967) Techniques for Testing Structures Permitted to Sway. *Experimental Mechanics*, 321-331.

Young B. and Lui W.M. (2005) Behavior of cold-formed high strength stainless steel sections. *Journal of Structural Engineering*, American Society of Civil Engineers (ASCE), 131(11): 1738-1745.

Zhao O., Rossi B., Gardner L. and Young B. (2015) Behaviour of structural stainless steel cross-sections under combined loading – Part I: Experimental Study. *Engineering Structures*, 89: 236-246.

Zhou F. and Young B. (2005) Tests of cold-formed stainless steel tubular flexural members. *Thin Walled Structures*. 43(9): 1325-1337.

Zhou F., Tong L. and Chen Y. (2013) Experimental and numerical investigations of high strength steel welded h-section columns. *International Journal of Steel Structures*, 13: 209–218.

Zienkiewicz O.C. and Taylor R.L (2005). *The Finite Element Method for Solid and Structural Mechanics*. Published by Elsevier Ltd.

APPENDIX A

PLANNED TESTS ON STAINLESS STEEL PORTAL FRAMES

This appendix gives an overview of the planned experimental tests on stainless steel frames which were however not conducted due to restrictions associated with the availability of lab facilities and technicians. As this work was part of the present it is included in the thesis, however as it was not finished it is appended at the end. In the section on the suggestions for future research it is recommended that the tests are conducted provided that all lab-related limitations are overcome.

A1. FRAME LAYOUT

Four fixed-based stainless steel portal frames with a proposed loading arrangement similar to the 4-point bending configuration were prepared in the Structures Laboratory at the University of Birmingham. As for the simply supported and continuous beam tests, four RHS portal frames with a nominal outer web depth H and a nominal outer flange width B equal to 100

mm and 50 respectively, both for columns and beams were employed. Furthermore, the same nominal thickness (t equal to 2 mm, 3 mm and 5 mm) and material properties (three of the sections were cold-formed from Grade EN 1.4301/1.4307 austenitic stainless steel and one from Grade 1.4462 duplex stainless steel) were utilised. No need for additional tensile coupon tests was required, since all beam and column specimens for each section were cut from the same length of tubes, as for the simply supported and continuous beam specimens (refer to Table 3.2). Detailed mean measured dimensions (web depth, outer flange width, thickness and internal corner radius), for each cross section that was employed for the construction of portal frames, are previously defined in Table 3.1.

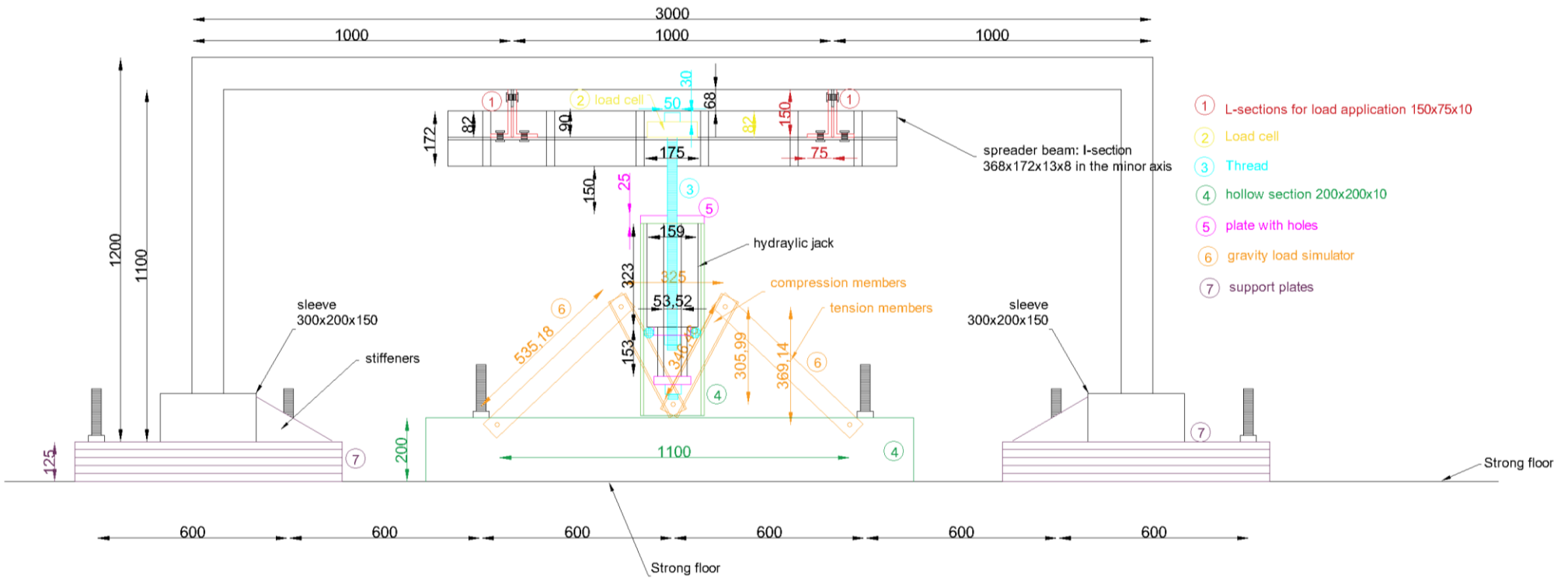


Fig. A.1: Portal frames layout (dimensions in mm)

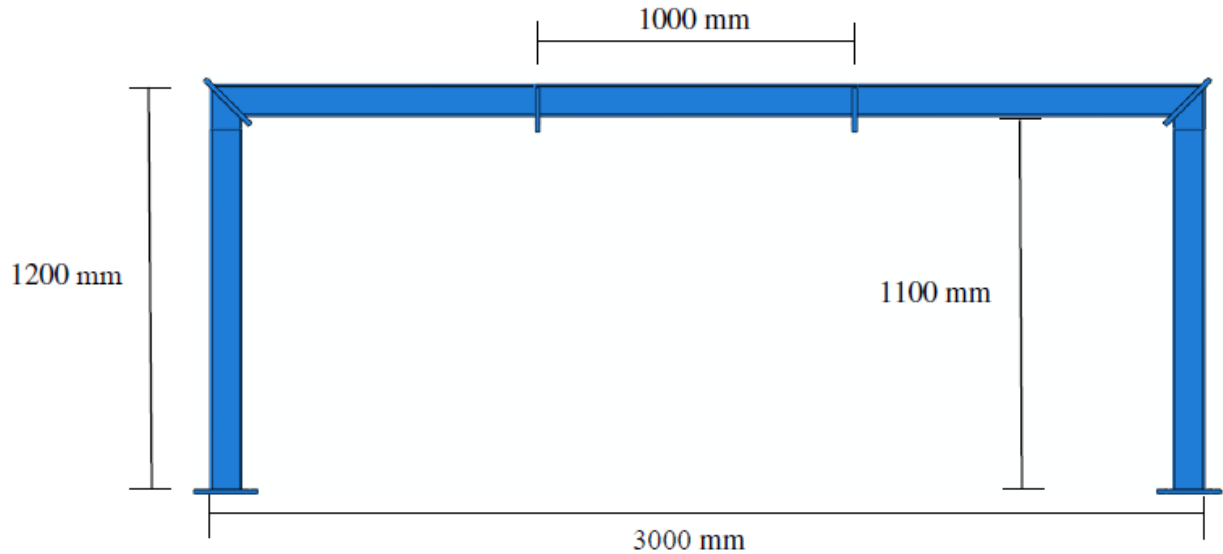


Fig. A.2: Overall setup for portal frames (dimensions in mm)

Detailed layout of the frames and a photograph that illustrates the overall set up for the future tests are shown above in Fig. A.1 and Fig. A.2 respectively. Each one of the portal frame specimens has a total height of 1200 mm and a span of 3000 mm. The columns of each frame were fix based and two point loads will be applied at a distance equal to one-third of the span length from each end column via an I section spreader beam. For the most efficient conduction of these tests, a unique loading configuration will be used, described as gravity load simulator (Yaramici et al., 1967). The gravity load simulator is consisted of two inclined members, pinned together by a rigid triangular unit. As the portal frame swayed, the two inclined arms move, in order to maintain the direction of the loads vertically. Thorough description of the various components that will be utilized for portal frames' design, provided further below.

A2. CONNECTIONS AND BASE

A total of four frames were fabricated according to specifications outlined herein. Each frame comprises the same RHS section for both columns and beam members. In portal frames plastic hinges tend to often form at the connection points between the span and the columns. For the joints to be able to achieve sufficiently large rotations at the plastic moment, stiffened welded connections were used. In construction industry, the most common used connection for portal frame is a typical nominally pinned-based connection, which is consisted by a single plate fillet welded to the end of the column and is connected with the concrete with holding down bolts; this approach was used for the design of column base connections, which were employed during the experimental tests. Furthermore, in order to connect the two specified loading points along the span of each portal frame specimen, with the underneath I section, which will used for the application of the two vertical loads, two welded plates were employed. The location of the welded connections is shown in Fig. A.3.

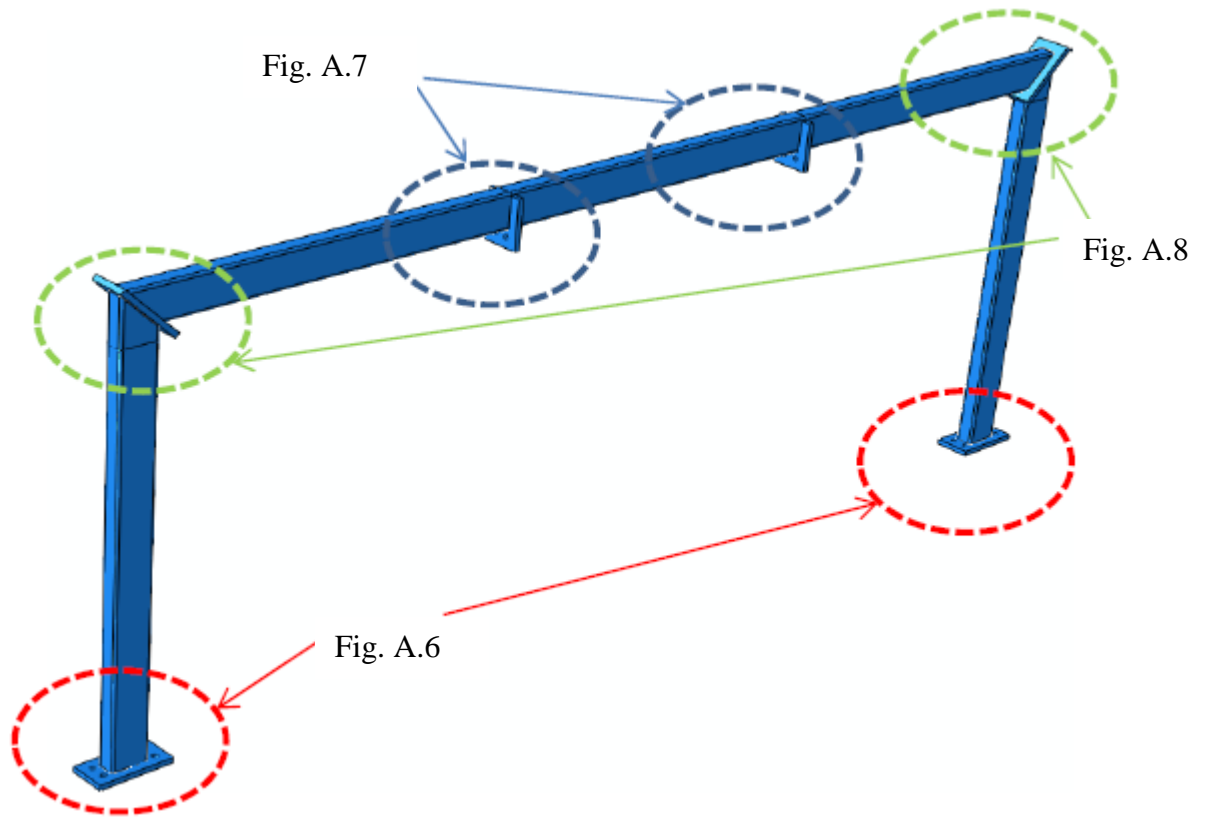


Fig. A.3: Location of connections

For the span to be perfectly attached with the column at each end, a miter joint was required. The two ends of each span were cut at 45° angle, to form a corner, as result the bottom flange was shorten by 50 mm from each span's end (Fig. A.4). In a similar way the columns were cut at one end at 90° angle plus the aforementioned cut angle that was used for span's ends, which reduce top flange's length by 100 mm (Fig. A.5).

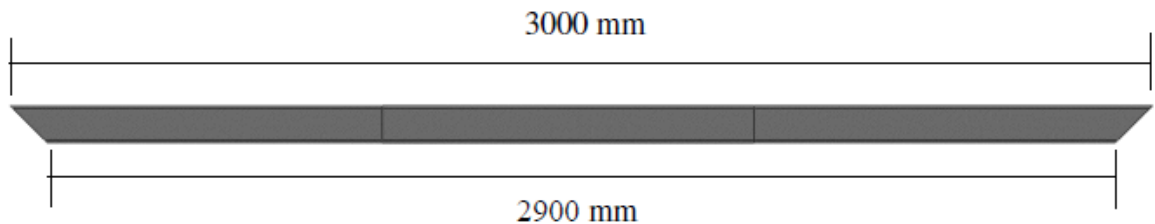


Fig. A.4: Cut requirements for beams (dimensions in mm)

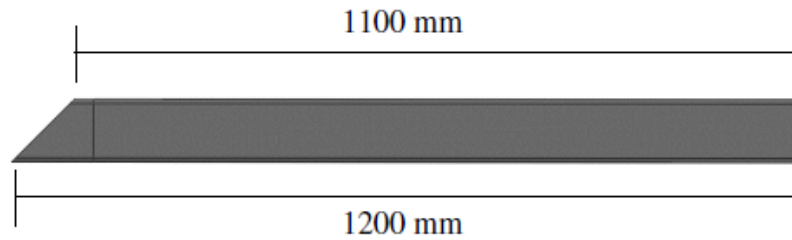


Fig. A.5: Cut requirements for columns (dimensions in mm)

As it was aforementioned a pin-based connection was originally used for portal frames. For the achievement of this connection, 8 mm thick base plates of Grade 1.4301 were employed (Fig. A.6). The RHS 100×50 columns were centrally located and fillet-welded with a 3 mm throat thickness all around the outer part of column base. Furthermore, four 18 mm diameter holes were utilized for each for each plate, in order the portal frames to be connected with the concrete strong floor with holding down bolts. At later stage, it was decided that the use of fixed-based columns would be more efficient, due to sway sensitivity of portal frames. For the transformation of pinned base columns to fixed base columns, four 300×100 steel channels of 150 mm height were employed Fig. A.7. The two channels were welded together with the use of two steel plates, to form a 300×200×150 mm sleeve. The RHS 100×50 columns were centrally placed inside the sleeve and steel plates were wedged, to achieve the fixation of the column base. Detailed illustration of the sleeve arrangement shown in Fig. A.8.

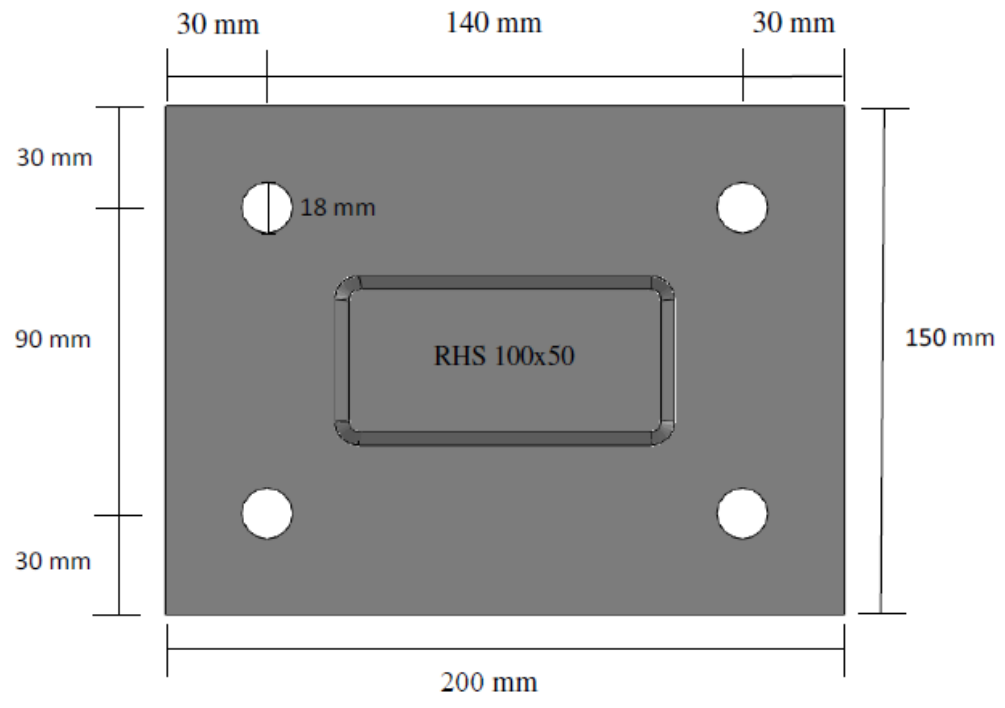


Fig. A.6: Base plate connection (dimensions in mm)



Fig. A.7: 300×100 steel channels

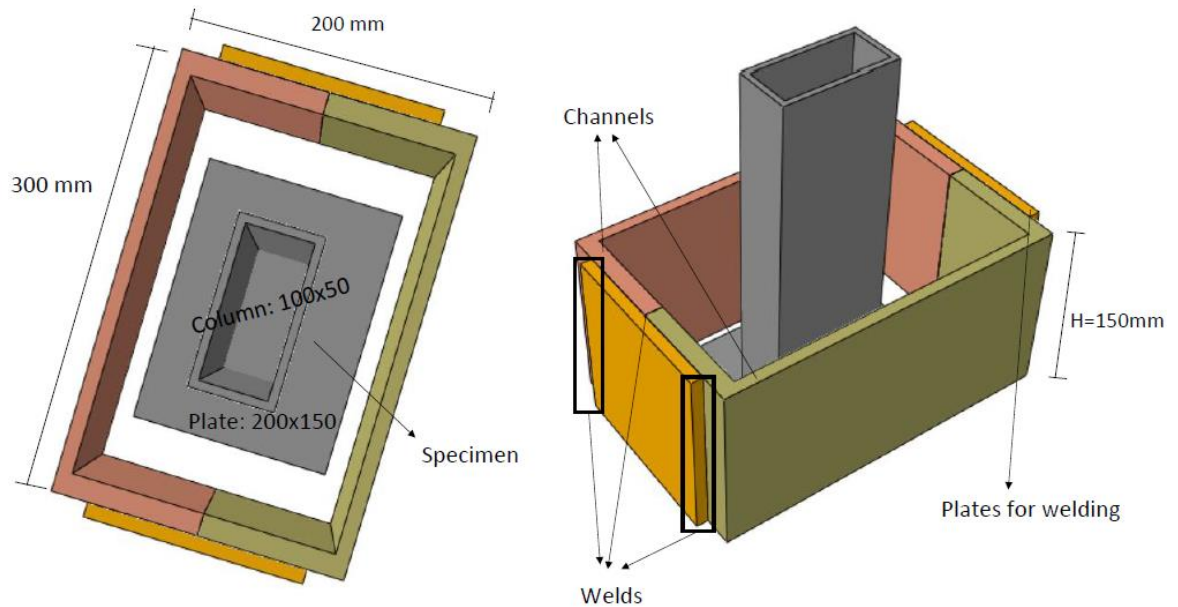


Fig. A.8: Column to sleeve arrangement

For the application of the two vertical loads at the previously specified locations along the span of the portal frames, an I section spreader beam will be utilized, which will be placed underneath the span of the portal frame. In order to attach the spreader beam to the span, one 6 mm thick steel plate of Grade 1.4301 was employed for each loading position. The RHS 100×50 beam was filler-welded with 5 mm throat thickness along the flat part of the web on both sides of the plate (Fig. A.9). The two loading plates, act as stiffeners, in order to avoid any early stage shear failure. Furthermore, two 18 mm diameter holes were located at a distance 30 mm from the edge of the loading plate, so that the spreader beam could be connected to the specimen via bolted L-sections. To increase the metal to metal contact area and to reinforce the 90° angle miter joint produced by cutting both beam and columns to the aforementioned angles, a 150×20×8 mm thick joint plate of Grade 1.4301 was employed for each connection point. Moreover, to transmit the full strength of the section, full penetration butt welds of beam and column ends were applied on the plate (Fig. A.10). Table A.1

summarizes all the sections sizes and plates that were employed for each frame during the fabrication process.

Table A.1: Section sizes and plates for each frame

Frame	Material Grade	Beam and columns section	Base plates	Loading plates	Plates at joints	Sleeves Fig.
Frame 1	EN 1.4301	RHS 100×50×2				
Frame 2	EN 1.4301	RHS 100×50×3	150×200 ×8 2 per frame	140×100 ×8 2 per frame	150×200 ×10 2 per frame	300×200 ×150 2 per frame
Frame 3	EN 1.4301	RHS 100×50×5				
Frame 4	EN 1.4162	RHS 100×50×3				

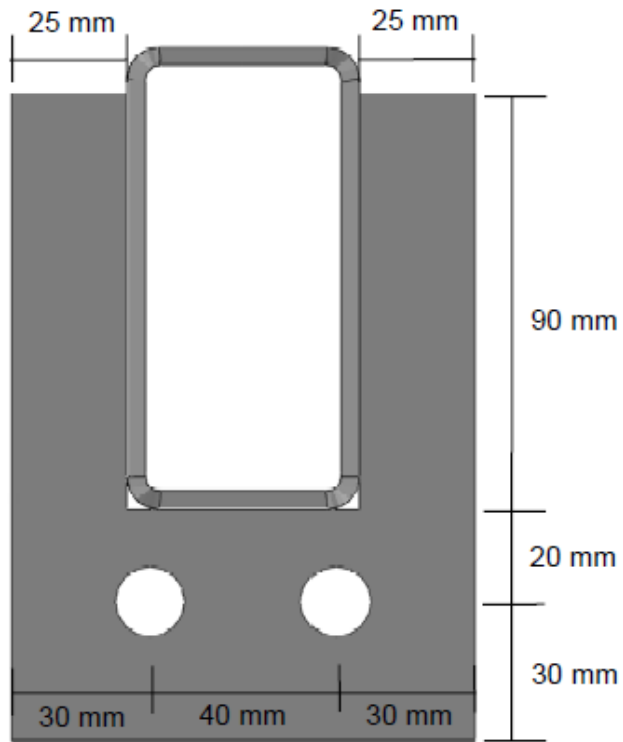


Fig. A.9: Loading plate arrangement (dimensions in mm)

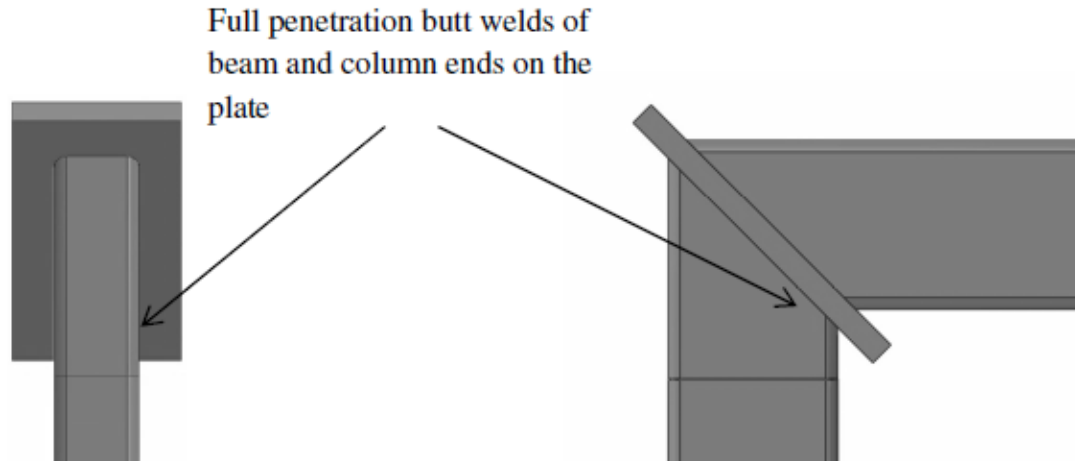


Fig. A.10: Butt welds

A3. CONSTRUCTION SEQUENCE

Both columns and beams were cut at the required length from the same tubes that were used for the 3-point 4-point bending tests. The requested drilling holes on the provided plates and the welding activities were conducted by the fabricator. Five plates of 25 mm thickness each will be placed below each column's location, in order to provide the appropriate height required for the Double-Acting ENERPAC Cylinder to reach its full stroke. For each steel support plate two 33 mm diameter holes will be drilled, in order to allow two M33 threads to be connected to the strong floor. The two 200×150 mm height sleeves, produced from four 300×100 steel channels and four welded steel plates, will be centrally located and fillet-welded to the upper base plate. To increase the rigidity of the column base, C section stiffeners will be cut to the appropriate triangular shape and will be placed to the inner side of the portal frames; they will be fillet-welded to the upper base plate and along the side of the sleeve (Fig. A.11). The RHS 100×50 columns will be centrally placed inside the sleeve and steel plates will be wedged, to achieve the fixation of the column base.

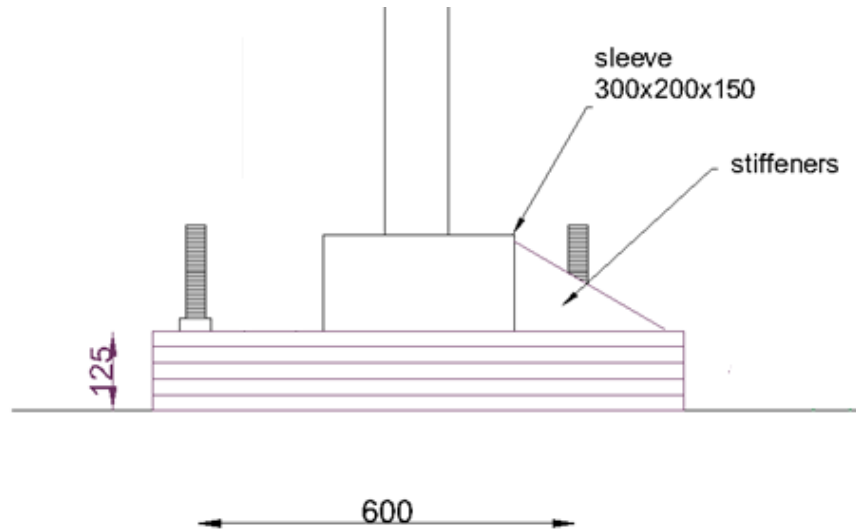


Fig. A.11: Column base arrangement

Once the portal frame will be moved and fixed in place with the use of a travelling crane inside the sleeves, two L sections 150×75×10 will be bolted with M18 bolts at each loading plate. Subsequently, the flange of each L section connection will be bolted on the web of the I section spreader beam (two 18 diameter holes at the web and two at the flange of each L section required). Detail illustration of the connection of the spreader beam to the specimen is provided in Fig. A.12. Last but not least, a vertical gravity load will be applied on the portal frames with the use of a unique loading configuration, described as gravity load simulator. Analytical description of this method which will be used in the future for the testing of the stainless steel portal frames, provided by Wilkinson and Hancock (1999).

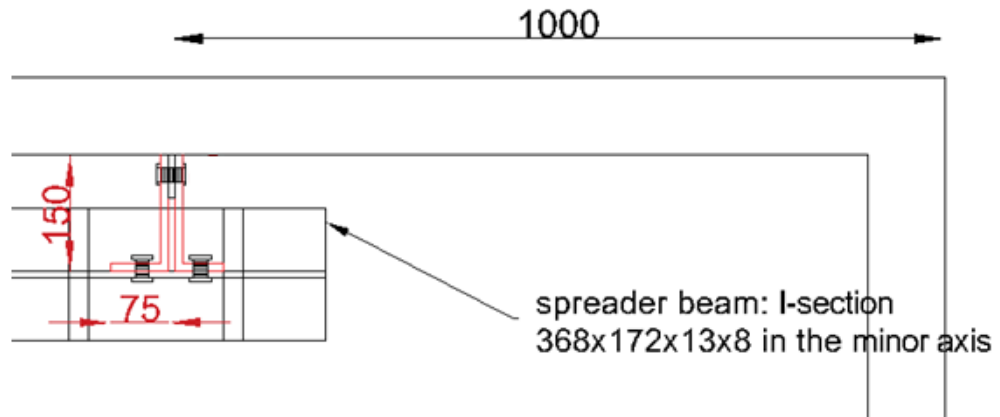


Fig. A.12: Connection of the spreader beam to portal frames (dimensions in mm)

A4. INSTRUMENTATION

For each of the four specimens, twenty-two strain gauges will be employed and placed at critical locations. Fig. A.13 shows the exact location along the span and the columns of each portal frame, where the gauges will be attached. At each location two strain gauges will be placed; one at the centre of the top flange and one at the centre of the bottom flange, in order to measure the extreme tensile and compressive strains that occur during the test. Furthermore, four LVDTs will be used; two will be located adjacent to the loading points to measure the vertical displacement of the span and one near each column to measure the horizontal displacement of the specimen. To measure the rotation of the specimen at the location of potential plastic hinges, six inclinometers will be employed. Moreover, for the application of the two vertical loads, a Double-Acting ENERPAC Cylinder is utilized. To connect the loading jack with the I-section spreader beam, a M36 threaded bar was used, which was passing through the centre of the full length of the cylinder to a 36 mm diameter hole at the web of the spreader beam. The M33 threaded bar will be fixed in place with the use of M33 nuts, one placed at the bottom of the cylinder and one at the top of the spreader's beam web.

Moreover, to measure the force that will be applied on the specimen via the cylinder, a hollow section load cell supported on the web of the spreader beam will be used. Detailed illustration of the load set up was illustrated in Fig. A.1. All the recording data, including reaction force (Load Cell), strains (Strain Gauges), rotations (Inclinometers) and displacements (LVDTs) will be extracted with the use of dataTaker DT800.

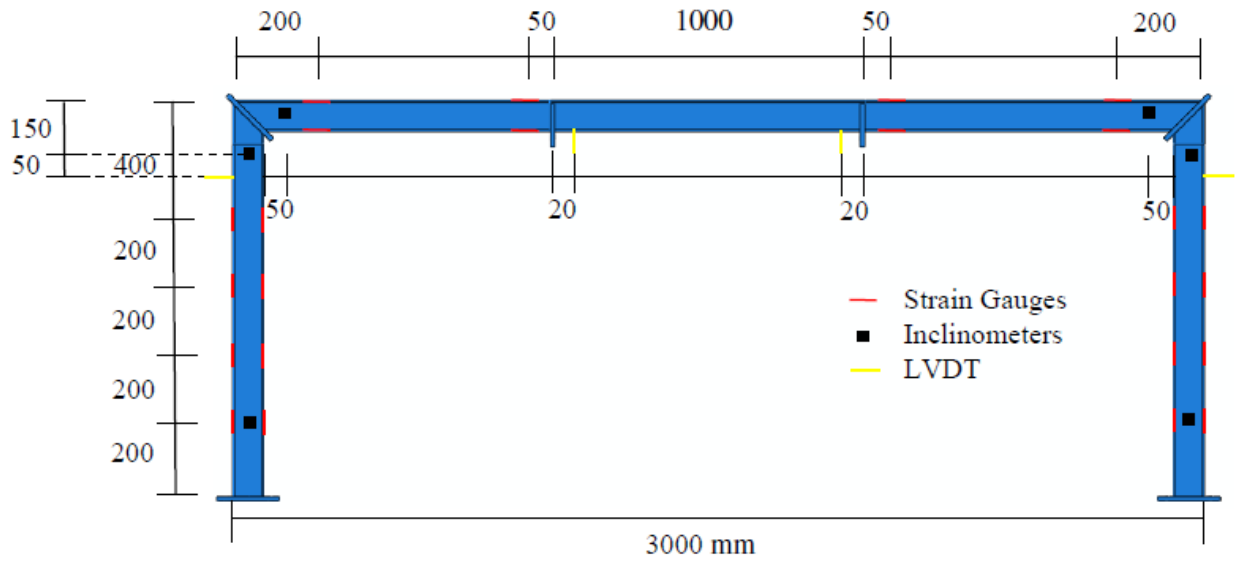


Fig. A.13: Location of Strain Gauges, LVDTs and Inclinometers (dimensions in mm)